Source of sulphur and the alteration footprint of the George Fisher Zn-Pb-Ag massive sulphide deposit, Australia

Dissertation

zur Erlangung des Grades eines

Doktors der Naturwissenschaften (doctor rerum naturalium)

am Fachbereich Geowissenschaften

der Freien Universität Berlin

vorgelegt von:

Philip Rieger

Berlin, October 2020

GFZ Helmholtz Centre Potsdam

Freie Universität Berlin

First reviewer (Erstgutachterin):

Prof. Dr. Sarah A. Gleeson

Department of Earth Sciences, Freie Universität Berlin
Inorganic and Isotope Geochemistry, GFZ German Research Centre of Geosciences

Second reviewer (Zweitgutachter):

Prof. Dr. Stephen Roberts

School of Ocean and Earth Science, National Oceanography Centre,
University of Southampton

Doctoral Committee (Promotionsausschuss):

Prof. Dr. Esther M. Schwarzenbach (Vorsitz)

Department of Earth Sciences, Freie Universität Berlin

Prof. Dr. Timm John

Department of Earth Sciences, Freie Universität Berlin

Prof. Dr. Sarah A. Gleeson

Department of Earth Sciences, Freie Universität Berlin
Inorganic and Isotope Geochemistry, GFZ German Research Centre of Geosciences

Prof. Dr. Stephen Roberts

School of Ocean and Earth Science, National Oceanography Centre,
University of Southampton

Dr. Joseph M. Magnall

Inorganic and Isotope Geochemistry, GFZ German Research Centre of Geosciences

Dr. J. Elis Hoffmann

Department of Earth Sciences, Freie Universität Berlin

Day of defense (Disputationsdatum):

26th of January 2021

Eidesstattliche Erklärung

Ich versichere hiermit an Eides Statt, dass diese Arbeit von niemand anderem als meiner Person verfasst worden ist. Alle verwendeten Hilfsmittel wie Berichte, Bücher, Internetseiten oder ähnliches sind im Literaturverzeichnis angegeben, Zitate aus fremden Arbeiten sind als solche kenntlich gemacht. Die Arbeit wurde bisher in gleicher oder ähnlicher Form keiner anderen Prüfungskommission vorgelegt. Die Teile der Arbeit die schon veröffentlicht oder eingereicht wurden, sind im Vorwort ("Preface") kenntlich gemacht. Weiterhin ist im Vorwort ("Preface") dargelegt, zu welchem Teil der Arbeit andere Wissenschaftler beigetragen haben.

Acknowledgments

To Joe and Sarah, there is so much that I want to thank you for, but most importantly, thanks for always being there to have my back: when I was melting away at >40 °C in the core yard at Mount Isa, when I had to get through the endless home office time this year, when deadlines for abstracts, paper submissions, or presentations came faster than expected, when I just needed to hear 'it's okay, you will get there', and in countless other occasions. You gave me both the guidance and the freedom that I needed. I have learnt so much from you on this journey, both as a scientist and as a person, and I was extremely lucky to have such great supervision.

Besides all the things I got to experience and learn throughout the last few years, by far the best was meeting, and becoming friends with, people from all parts of this world. You all left an impression on me, thank you.

To the geology teams at Mount Isa Mines Resource Development and at George Fisher, it seems like ages ago when you took me up in your midst. You made me feel welcome, and you shared your experience, your rocks, and your barbecues with me, what more could I have asked for. Amongst everyone else, I would like to thank Alphonse, Dan, Natasha, Nick, Michael, Michelle, Orla, Peter, Ray, Vincent, and William for the great time back in Mount Isa and at George Fisher and for the support even when I was >14 000 km away.

To Richard, thanks for getting things started and for giving us the opportunity to come to Mount Isa and to work on those brilliant rocks. One could really tell how much you love that place, thanks for sharing that enthusiasm with us.

To all my colleagues at GFZ who helped me to get through this thesis with all the small and big things that you may not have realized at the time. Thanks for the time you shared with me, no matter if it were weeks, months, or years: Alan, Alejandro, Alex, Anja, Bob, Christof, Dang, Franzi, Gregor, Hans-Martin, Haoyang, Hartmut, Haruna, Jess, Johannes, Julia, Kevin, Marcus, Maria, Marta, Marta, Martin, Mengdi, Merilie, Mohammed, Nicole, Oona, Peter, Philipp, Spyros, Svenja, Tine, Uwe, Volker, Yang, and Yufu.

To Mathias, Max, and Malte, thanks for all the fresh air and rehydration breaks, thanks for all the laughs and discussions (both scientific and nonsensical), thanks for being at my side both in euphoric and in hard times, and thanks for turning going to work into meeting some of your best friends. Thanks for letting me be part of your life.

To my friends and family, all of you have helped to get me here in one way or another. Thanks for all the laughs, the catch ups, the drinks, the food, the cultural holidays, the times kicking a ball, the chats, and, lately, the zoom or skype calls. All of you are more important to me than I could put in words here.

To Vera and Andi, you turned one of the most stressful times of my life into one of the happiest times. Thanks for putting Jakob into my life, I will always be there for him.

To Franzi, I do not even know where to start. Thanks for going through this with me. You had to do without many things, and I promise I will not do another PhD thesis. Thanks for being at my side with all your love.

Most importantly, to my parents, I cannot imagine where I would be without you. You have always encouraged me to follow my dreams, even when I decided to study rocks and when that took me half a world away from you. You are constantly showing everyone what it means to care for others, to be respectful, to be confident, to be optimistic, and to be great parents. I will always be grateful.

Finally, I had thought I will have a party with all of you to thank you for the part you played in my PhD journey and life over the course of the last few years. The virus has, however, made this impossible, or at least very irrational, for a while... So, if you find yourself mentioned above, either directly or indirectly, please feel hereby invited to claim a chat and a beverage of your choosing the next time you see me.

Summary

The George Fisher deposit is located in the northern Australian Carpentaria province, which is host to several of the world's largest Zn and Pb mineral deposits. The annual metal production from George Fisher is crucial in order to meet the global demand for Zn and Pb. The main ore minerals at George Fisher are sphalerite (ZnS) and galena (PbS), which occur in stratabound, and in discordant, massive sulphide ore bodies together with pyrite (FeS_2) and pyrrhotite (FeS). These massive sulphide ore bodies are hosted within carbonaceous, pyritic, calcareous, dolomitic siltstones and mudstones of the Paleoproterozoic Urquhart Shale Formation (ca. 1654 Ma), which is also host to two other world class base metal deposits (Mount Isa and Hilton). All three deposits are highly deformed, the textural relationships are complex, and there is a lack of indicator minerals to constrain the metamorphic grade of the Urquhart Shale. As a result, there has been considerable debate over (1) the processes that led to the accumulation of such huge amounts of base metal sulphides in the deposits of the area, and (2) the alteration footprint these processes have produced beyond the massive sulphide zones.

In this project, petrographic observations across several scales (drill core logging down to backscatter-electron microscopy) were combined with whole rock, and *in situ*, mineralogical, geochemical, and isotopic analyses of representative samples from (1) four drill holes that intersected the main ore bodies at George Fisher, and also from (2) a drill hole that intersected the barren Urquhart Shale Formation. These data were collected in order to constrain the background heterogeneity that is inherent to rocks of the Urquhart Shale Formation (e.g., from background diagenetic processes). Using this framework, the nature of some of the hydrothermal processes responsible for ore formation were constrained. Particular emphasis was put on constraining (1) the accumulation processes of reduced sulphur, (2) the ore forming processes, and (3) the mineralogical and geochemical alteration footprint of the George Fisher deposit.

In brief, the data from this study suggest that the Urquhart Shale Formation in the location we studied has not undergone regional greenschist metamorphism. The mineralogy and the paleoredox proxies (S-isotope data, Mo concentrations, rare earth

elements in carbonate minerals) from the barren Urquhart Shale sequence can, therefore, be interpreted in a sedimentary and diagenetic context; and those data concur with deposition of the Urquhart Shale Formation in a ferruginous, marine environment, which is consistent with the current understanding for the Paleoproterozoic oceans. Using this background composition as base line the petrographic, mineralogical, geochemical, and isotopic data from George Fisher suggest that (1) ore formation occurred in multiple events during diagenesis and later deformation, that (2) reduced sulphur in the deposit was likely derived via thermochemical sulphate reduction and the recycling of sulphur from pre-ore diagenetic pyrite, and that (3) fluid-rock interaction of hot (>200-250 °C), saline (Cl-rich), metal-bearing hydrothermal fluids with the Urquhart Shale Formation led to the dolomitization and replacement of pre-ore carbonate and the precipitation of base metal sulphides. Besides ore formation at George Fisher, these hydrothermal processes have resulted in mineralogical and bulk geochemical changes that include (1) albite, chlorite, and calcite depletion, (2) dolomite, phyllosilicate, and sulphide formation, (3) Na and Sr depletion, and (4) Tl and Mn enrichment relative to the barren host rocks. Furthermore, the fluid-rock interaction has led to light rare earth element (LREE) depletion in hydrothermal and hydrothermally altered carbonate minerals relative to whole rock and pre-ore carbonate LREE compositions.

Overall, this project has provided new constraints on background diagenetic and hydrothermal processes, and footprints, in the Urquhart Shale Formation at George Fisher. Moreover, the findings from this study can help to further refine exploration models for Zn-Pb deposits in one of the world's most important base metal provinces.

Zusammenfassung

Die Lagerstätte George Fisher befindet sich in der nordaustralischen Carpentaria-Provinz, in der mehrere der weltweit größten Zn- und Pb-Lagerstätten liegen. Die jährliche Metallproduktion aus George Fisher trägt erheblich dazu bei die weltweite Nachfrage nach Zn und Pb zu decken. Die wichtigsten Erzminerale in George Fisher sind Sphalerit (ZnS) und Galenit (PbS), die in schichtgebundenen und in diskordanten, Massivsulfiderzkörpern zusammen mit Pyrit (FeS_2) und Pyrrhotin (FeS) vorkommen. Diese Massivsulfiderzkörper befinden sich in kohlenstoffhaltigen, pyritischen, kalkhaltigen, dolomitischen Siltsteinen und Tonsteinen des paläoproterozoischen Urquhart Shales (ca. 1654 Ma). In dieser Formation liegen auch zwei weitere erstklassige Buntmetallvorkommen (Mount Isa und Hilton). Alle drei Lagerstätten sind stark deformiert, die strukturellen Beziehungen sind komplex, und es mangelt an metamorphen Indikatormineralien. Infolgedessen gab es Debatten über (1) die Prozesse, die zur Akkumulation solch riesiger Mengen an Buntmetallsulfiden in den Lagerstätten führten, und (2) den Alterationsfußabdruck, den diese Prozesse jenseits der Massivsulfiderzkörper erzeugt haben.

In diesem Projekt wurden petrographische Beobachtungen über mehrere Skalen (Bohrkernaufnahmen bis zur Elektronenmikroskopie) mit Gesamtgesteins- und *in situ*, mineralogischen, geochemischen sowie Isotopendaten repräsentativer Proben aus (1) vier Bohrlöchern, die die Haupterzkörper in George Fisher durchteuften, und auch aus (2) einem Bohrloch, das den unmineralisierten Urquhart-Shale durchteufte, kombiniert. Diese Daten wurden erhoben, um die Hintergrundheterogenität der Gesteine des Urquhart Shale zu verstehen (z.B. durch diagenetische Prozesse). Basierend auf diesen Daten wurden dann die erzbildenden hydrothermalen Prozesse untersucht. Ein besonderer Fokus lag auf der Untersuchung (1) der Akkumulationsprozesse des reduzierten Schwefels, (2) der Erzbildungsprozesse und (3) des mineralogischen und geochemischen Alterationsfußabdrucks der Lagerstätte George Fisher.

Zusammengefasst deuten die Daten dieser Studie darauf hin, dass der Urquhart Shale an dem von uns untersuchten Ort keine regionale grünschieferfazielle Metamorphose durchlaufen hat. Die Mineralogie und die Paläoredoxindikatoren

(S-Isotopendaten, Mo-Konzentrationen, Lanthanoide in Karbonaten) aus dem unmineralisierten Urquhart Shale können daher in einem sedimentären und diagenetischen Kontext interpretiert werden. Diese Daten sind konsistent mit der Sedimentation des Urquhart Shale in einer eisenhaltigen, marinen Umgebung. Ein solches Ablagerungsmilieu stimmt auch mit dem derzeitigen Wissensstand für die Ozeane des Paläoproterozoikums überein. Ausgehend von dieser Hintergrund-Zusammensetzung deuten die petrographischen, mineralogischen, geochemischen und Isotopendaten von George Fisher darauf hin, dass (1) die Erzbildung durch mehrere Ereignisse während der Diagenese und der späteren Deformation stattfand, und dass (2) die Akkumulation von reduziertem Schwefel in der Lagerstätte wahrscheinlich durch thermochemische Sulfatreduktion und das Recycling von Schwefel aus diagenetischem Pyrit stattfand, und dass (3) die Fluid-Gestein-Wechselwirkung von heißen (>200-250 °C), salzhaltigen (Cl-reichen), metallhaltigen hydrothermalen Fluiden mit dem Urquhart Shale zur Dolomitisierung und Verdrängung von diagenetischen Karbonaten und zur Ausfällung von Buntmetallsulfiden führte. Neben der Erzbildung in George Fisher haben diese hydrothermalen Prozesse zu mineralogischen und geochemischen Veränderungen geführt, die (1) Albit-, Chlorit- und Calcit-Verarmung, (2) Dolomit-, Phyllosilikat- und Sulfidbildung, (3) Na- und Sr-Verarmung und (4) Tl- und Mn-Anreicherung im Verhältnis zum unmineralisierten Wirtsgestein umfassen. Darüber hinaus hat die Fluid-Gesteins-Wechselwirkung zu einer Verarmung an leichten Seltenerdelementen (LREE) in hydrothermalen und hydrothermal alterierten Karbonaten geführt.

Insgesamt hat dieses Projekt neue Erkenntnisse für diagenetische und hydrothermale Hintergrundprozesse und Fußabdrücke im Urquhart Shale in und um George Fisher geliefert. Darüber hinaus können die Ergebnisse dieser Studie dazu beitragen, die Explorationsmodelle für Zn-Pb-Lagerstätten in einer der wichtigsten Buntmetallprovinzen der Welt weiter zu verfeinern.

Preface

This thesis is comprised of five chapters, which all individually concern the George Fisher massive sulphide Zn-Pb-Ag deposit and the Urquhart Shale Formation. Chapters 2, 3, and 4 are prepared to serve as independent stand-alone publications, which is why introductory material may be reiterated in the individual chapters. This preface will provide a short summary for each chapter and a declaration of personal contribution by the author and by colleagues and co-authors, who contributed in the individual chapters. Funding for this PhD project was provided by a Helmholtz recruitment initiative grant to S.A. Gleeson.

Chapter 1 provides the reader with an introduction of the importance of mining, mineral exploration, and mineral deposit research. Additionally, the reader is introduced to the Carpentaria province with a short summary of its geology and existing models of the Zn-Pb massive sulphide deposits that occur therein, together with the open research questions that are addressed in this thesis.

Chapter 2 has been published in Economic Geology. This chapter deals with the sulphide paragenesis and the sources of reduced sulphur for the Urquhart Shale formation and for the George Fisher deposit. The discussion of sulphur sources is based on *in situ* sulphur isotope analysis in paragenetically distinct generations of pyrite. The author conducted drill core logging and sampling supervised by J.M. Magnall and S.A. Gleeson, and supported by R. Lilly and the geology teams at Mount Isa Mines George Fisher operation and Mount Isa Mines Resource Development. Petrographic observations and sample selection were carried out by the author supported by discussions with J.M. Magnall and S.A. Gleeson. Thin section and mount preparation were carried out by U. Dittmann and E. Lewerenz. Backscatter electron imaging was carried out either by the author, or by F. Wilke or I. Schöppan in the author's presence, and was supported by F. Wilke, O. Appelt, S. Mayanna, and I. Schöppan. Sulphur isotope analysis was done using SIMS Cameca 1280 lab at GFZ Potsdam. F. Couffignal carried out instrument calibration. Analyses were done by the author with the support of F. Couffignal and A. Rocholl. Data processing and interpretation was carried out by the author in collaboration with J.M. Magnall, S.A. Gleeson, and A. Rocholl. C. Kusebauch

contributed the geochemical modelling and discussions on phase stabilities in the Fe-S-O system. J.M. Magnall and S.A. Gleeson supported the author with scientific discussions and guidance, and editing of the manuscript.

Chapter 3 has been submitted to Chemical Geology, and has been received with positive reviews by two expert reviewers. This chapter deals with the mineralogical and lithogeochemical footprint of the George Fisher Zn-Pb system in the Urquhart Shale formation. The author conducted drill core logging and sampling supervised by J.M. Magnall and S.A. Gleeson, and supported by R. Lilly and the geology teams at Mount Isa Mines George Fisher operation and Mount Isa Mines Resource Development. Petrographic observations and sample selection were carried out by the author supported by discussions with J.M. Magnall and S.A. Gleeson. Thin section preparation was carried out by U. Dittmann and E. Lewerenz. Whole rock sample preparation for X-ray diffraction (XRD) and lithogeochemical analysis was carried out by H. Liep and the author. Backscatter electron imaging was carried out either by the author, or by F. Wilke in the author's presence, and was supported by F. Wilke. X-ray diffraction mount preparation, analysis, data processing and interpretation was carried out by the author with the help of A.M. Schleicher and M. Bonitz. Lithogeochemical analysis was carried out at Bureau Veritas Minerals, Vancouver, Canada and data processing was carried out by the author. J.M. Magnall and S.A. Gleeson supported the author with scientific discussions and guidance, and editing of the manuscript.

Chapter 4 is an earlier version of a manuscript that has been submitted to Mineralium Deposita. This chapter concerns the rare earth element and yttrium systematics of diagenetic and hydrothermal processes preserved by carbonate minerals from the George Fisher deposit and the Urquhart Shale formation. The author conducted drill core logging and sampling supervised by J.M. Magnall and S.A. Gleeson, and supported by R. Lilly and the geology teams at Mount Isa Mines George Fisher operation and Mount Isa Mines Resource Development. Petrographic observations and sample selection were carried out by the author supported by discussions with J.M. Magnall and S.A. Gleeson. Thin section preparation was carried out by U. Dittmann and E. Lewerenz. Electron microprobe analyses and data reduction were carried out by the author, and by F. Wilke in the presence of the author. *In situ* analyses of carbonate

minerals were carried out in the LA-ICP-MS lab at GFZ Potsdam by M. Oelze in the author's physical, or virtual (due to Covid-19 restrictions), presence. Furthermore, M. Oelze supported the author with data processing, interpretation, and scientific discussions. J.M. Magnall and S.A. Gleeson supported the author with scientific discussions and guidance, and editing of the manuscript.

Chapter 5 concludes this thesis with a summary of the findings reported in Chapters 2 to 4 and an attempt to integrate the individual datasets amongst each other and with previous work.

Contents

1. Introduction

1.1. Why mining, mineral exploration, and mineral deposit research?

There is a rapidly growing demand for more sustainable raw materials to support the transformation to a carbon neutral, high-tech, society. While technological advances allow for a more effective use and recycling of raw materials (esp. metals), this can only partially supply the raw materials needed for a growing world population with increasing per capita wealth (Elshkaki et al. 2018). Therefore, in order to support the energy transition, mining plays a key role in the supply of the necessary raw materials. For example, Zn is used in a variety of different industrial sectors and is critical in modern infrastructure; the demand for Zn is, however, expected to exceed Zn resources (from mining and recycling) before 2040 (e.g., Elshkaki et al. 2018). So, new Zn resources will need to be discovered. Yet, few base metal discoveries are made at the surface, and, therefore, exploration for new mineral systems is increasingly challenging (Schodde 2017). For this reason, it is necessary to further constrain genetic models, which can be used in exploration in order to improve the efficiency of finding new, deeply covered mineral systems. In this context, mineral deposit research can contribute by developing new, and refining existing, ore formation models.

The majority of the global Zn resources are hosted in sediment-hosted mineral deposits and a large proportion of these resources are contained within a small number of supergiant clastic-dominated (CD-type) massive sulphide deposits (Fig. 1-1; Leach et al. 2005, 2010; Mudd et al. 2017). Several of the world's largest CD-type massive sulphide deposits are located in the northern Australian Carpentaria province, where, over the last century, a new world-class deposit has been discovered every 15-20 years (Mount Isa, Hilton, McArthur River, Lady Loretta, George Fisher, Century; McGoldrick et al. 2010). Consequently, this province is highly endowed and there is potential for future discoveries that will contribute significantly to the global Zn resources.

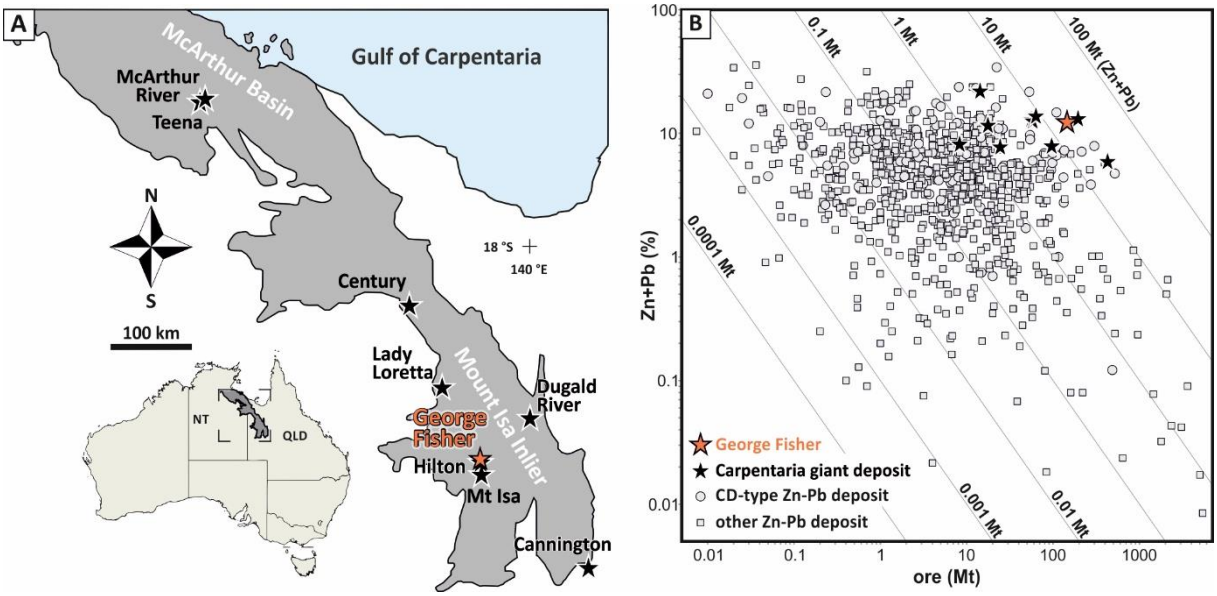

Fig. 1-1 (A) A map of the Carpentaria province. Stars annotate major Zn-Pb massive sulphide deposits. (B) Compilation of global resources for Zn and Pb; diagonal lines represent total contained metal (data from Mudd et al. 2017).

1.2. The Carpentaria CD-type massive sulphide deposits

The Carpentaria province is located in northern central Australia within Queensland and the Northern Territory. It comprises two Paleo- to Mesoproterozoic sedimentary basins: The Mount Isa Inlier and the McArthur Basin. These basins have formed in an intra-cratonic rift or continental back-arc setting, in which lithosphere underwent significant thinning (e.g., Giles et al. 2002; Gibson et al. 2012). Episodic extension, sag phases, and basin inversion led to the development of three superbasins: the Leichhardt, Calvert, and Isa superbasins (e.g., Jackson et al. 2000; Southgate et al.

2000; Gibson et al. 2016). After basin closure, the sedimentary rocks of these superbasins have undergone variable degrees of metamorphism and tectonic overprint, the intensity of which generally decreases from south-east to north-west (Blake 1987; Jackson et al. 1987). Besides world-class Zn-Pb deposits, the Carpentaria province is also host to substantial Cu, Au, and U resources (e.g., Williams 1998).

The Zn-Pb deposits of the district are generally classified as clastic-dominated (CD-type; Leach et al. 2010), shale-hosted (SHMS; Betts et al. 2003), or sedimentary-exhalative (SEDEX; Large et al. 2005) massive sulphide deposits. In this thesis, the CD-type classification is used, to prevent confusion with other sediment hosted massive sulphide deposits (cf. SHMS; e.g., Mississippi Valley Type; Leach et al. 2005), and to avoid using a name which implies a genetic process which may not occur in the deposits (cf. SEDEX; exhalation of hydrothermal fluids; Large et al. 1998). The Carpentaria CD-type massive sulphide systems generally comprise significant structural, paragenetic, geochemical, and mineralogical complexity. This is why, despite a century of research, there is no consensus on ore formation models. Ore formation models span across the range from syn-sedimentary exhalative (e.g., Mathias and Clark 1975; Large et al. 1998; Ireland et al. 2004), to syn-diagenetic or syn-inversion replacement (e.g., Broadbent et al. 1998; Painter 2003; Chapman 2004; Magnall et al. 2020b), or to syn-orogenic replacement (e.g., Perkins 1997; Davis 2004; Cave et al. 2020). In the Mount Isa area, developing ore formation models is further complicated by syn-orogenic Cu-mineralization (cf. Perkins 1997). For example, the Mount Isa deposit comprises both a world-class Zn-Pb and a world-class Cu deposit and, therefore, discussion has focussed on whether these have formed in a single-stage (Zn+Pb+Cu; e.g., Perkins 1997; Davis 2004; Cave et al. 2020), or a multi-stage system (Zn+Pb with later Cu±Zn±Pb; e.g., Andrew et al. 1989; Heinrich et al. 1989; Waring et al. 1998).

In general, the Carpentaria CD-type massive sulphide deposits are extremely large (ore >100 Mt at Zn+Pb >10 wt. %; Fig. 1-1) and the main sulphide minerals are sphalerite (ZnS), galena (PbS), pyrite (FeS_2), and pyrrhotite ($Fe_{1-x}S$). Therefore, these deposits represent anomalous concentrations of Zn (≥750 times average upper continental crust; Rudnick and Gao 2003), of Pb (≥3000), and also of reduced S (≥50).

The source of these metals and of the reduced sulphur is, however, only poorly constrained. Despite their large size, the alteration footprint of the CD-type systems is difficult to assess. This is, in part, due to the tectonic overprint of some systems, the fine-grained nature of the host lithologies, and the differing ore formation models, but also due to a lack of understanding concerning the background heterogeneity that is characteristic of the unmineralized host lithologies. Furthermore, historically assays in this area were limited to major elements, and therefore, there are few multi-element lithogeochemical data-sets available to assess possible alteration halos around the deposits.

Overall, the aim of this study was to identify the processes responsible for the accumulation of reduced sulphur in the George Fisher deposit and to constrain the mineralogical and geochemical footprint of the massive sulphide system. For this purpose, samples from drill-cores through the main ore bodies at the southern Carpentaria George Fisher deposit (165 Mt at 9.1 % Zn, 3.4 % Pb, and 55 g/t Ag; Glencore 2019) were studied in comparison with samples from a drill-hole that intersected unmineralized, correlative host lithologies (Urquhart Shale Formation). Following this introduction, the thesis is divided into four chapters:

In chapter 2, we focus on the accumulation processes of reduced sulphur. Previous sulphur isotope studies in the area have applied bulk analyses and analyses of mineral separates to constrain the accumulation of reduced sulphur. Pre-ore pyrite and ore-stage sulphides are, however, very fine grained and paragenetically complex. We have, therefore, used secondary ion mass spectrometry (SIMS) analyses of five generations of paragenetically constrained pyrite to assess the sulphur cycling through time in the Urquhart Shale Formation and at the George Fisher deposit. This chapter has been published in Economic Geology and further publication details are stated at the beginning of the chapter.

In chapter 3, we present a combined mineralogical and lithogeochemical study of samples from the unmineralized Urquhart Shale Formation and from the George Fisher deposit. The aim of this study is to assess if there is an alteration footprint around the George Fisher deposit, insights from which may be used in future exploration

programmes. This chapter is an earlier version of a manuscript published in Chemical Geology and further publication details are stated at the beginning of the chapter.

In chapter 4, we investigate the geochemistry of the carbonate minerals in the Urquhart Shale Formation and the George Fisher deposit. Previous studies have identified km-scale enrichments of major elements in carbonates around Carpentaria CD-type systems. It remains, however, untested if the carbonate-associated element anomalies are a result of diagenetic or hydrothermal processes. The aim of this study is to assess if (1) *in situ* trace element, particularly rare earth element and yttrium, geochemistry of carbonate mineral phases can be used to differentiate diagenetic and hydrothermal carbonates, and if (2) this can be used in future exploration programmes in carbonate-rich lithologies. This chapter is an earlier version of a manuscript that has been submitted to Mineralium Deposita.

In chapter 5, we provide a summary of the findings and interpretations in this thesis and the implications they may have (1) for mineralization at George Fisher and in the Carpentaria province, (2) for future research projects, and (3) for future exploration programmes.

2. Sources of reduced sulphur at the George Fisher deposit, Australia

Sulphur Isotope Constraints on the Conditions of Pyrite Formation in the Paleoproterozoic Urquhart Shale Formation and George Fisher Zn-Pb-Ag Deposit, Northern Australia

Rieger P.[1,2], Magnall J.M. [1], Gleeson S.A. [1,2], Lilly R. [3], Rocholl A. [1], Kusebauch C. [1]

[1]GFZ German Research Centre for Geosciences, Telegrafenberg, 14473 Potsdam, Germany
[2]Freie Universität Berlin, Institute for Geological Sciences, Malteserstraße 74-100, 12249 Berlin, Germany
[3]School of Earth and Environmental Sciences, University of Adelaide, Adelaide, South Australia 5005, Australia

Economic Geology (2020) vol. 115, p. 1003-1020.
https://doi.org/10.5382/econgeo.4726

2.1. Abstract

The Carpentaria province (McArthur basin and Mount Isa inlier) in northern Australia is one of the most important districts for clastic-dominated (CD-type) massive sulphide deposits. The George Fisher Zn-Pb-Ag deposit, located in this province, is hosted by the carbonaceous Urquhart Shale Formation (ca. 1654 Ma) in a region that has an active history of metamorphism and tectonism. In this study, paragenetically constrained pyrite in samples from the George Fisher deposit and unmineralized Urquhart Shale have been analysed *in situ* using secondary ion mass spectrometry (SIMS) of sulphur isotopes ($\delta^{34}S$ values). Samples were taken from four drill cores through the main orebodies at George Fisher and one drill core through correlative, unmineralized Urquhart Shale (Shovel Flats area). Five generations of pyrite were identified at George Fisher and record a protracted history of sulphate reduction under diagenetic and subsequent hydrothermal conditions: (1) fine-grained, subhedral-spheroidal pyrite (Py-0), (2) coarse-grained, anhedral pyrite (Py-1) associated with ore stage 1 sphalerite and galena, (3) coarse-grained, euhedral pyrite (Py-2) associated with ore-stage 2 sphalerite, galena, and pyrrhotite, (4) massive subhedral to euhedral pyrite (Py-3) associated with ore-stage 3 chalcopyrite, pyrrhotite, galena, and sphalerite, and (5) coarse-grained euhedral pyrite (Py-euh), which occurs only in unmineralized rocks. In the unmineralized Shovel Flats drill core, only Py-0 and Py-euh are present. Whereas pre-ore pyrite (Py-0) preserves negative $\delta^{34}S$ values (–8.1 to 11.8‰), the ore-stage pyrites (Py-1, Py-2, and Py-3) have higher $\delta^{34}S$ values (7.8–33.3, 1.9–12.7, and 23.4–28.2‰, respectively). The highest $\delta^{34}S$ values (7.2–33.9‰) are preserved in Py-euh. In combination with petrographic observations, the $\delta^{34}S$ values of pyrite provide evidence of three different processes responsible for the reduction of sulphate at George Fisher. Reduced sulphur in fine-grained pyrite (Py-0) formed via microbial sulphate reduction (MSR) under open-system conditions prior to the first generation of hydrothermal pyrite (Py-1) in ore-stage 1, which most likely formed via thermochemical sulphate reduction (TSR). During deformation, previously formed sulphide phases were then recycled and replaced during a second hydrothermal event (ore-stage 2), resulting in intermediate sulphur isotope values. Another syn-deformational hydrothermal Cu event, involving a

sulphate-bearing fluid, formed ore-stage 3 via TSR. This study demonstrates that the fine-grained pyrite formed pre-ore under conditions open to sulphate and outlines the role of multiple stages of sulphide formation in producing high-grade Zn-Pb-Ag orebodies in the Mount Isa inlier.

2.2. Introduction

Clastic-dominated (CD-type) massive sulphide deposits, sometimes referred to as sedimentary exhalative (SEDEX) deposits, constitute the majority of global reserves and resources for Zn and Pb (Mudd et al. 2017). One of the most important districts for CD-type Zn-Pb mineralization is the Paleoproterozoic to Mesoproterozoic Carpentaria province (McArthur basin and Mount [Mt.] Isa inlier), which is host to several of the world's largest deposits (George Fisher-Hilton, Mount Isa, McArthur River, Lady Loretta, and Century; Large et al. 2005). As a result of metamorphic and tectonic overprints, which increase from north to south in the Carpentaria province (Blake 1987), there has been much debate about the timing and genesis of the different CD-type deposits of this region.

Many genetic models for CD-type Zn-Pb deposits are developed around the paragenesis and distribution of pyrite, as it is the primary gangue sulphide mineral and occurs within pre-, syn-, and post-ore assemblages. In the Carpentaria province, the description of the relationship between Zn mineralization (sphalerite) and fine-grained (<10 μm), spheroidal pyrite (fg-py) differs between studies and, therefore, leads to different genetic models. For example, some models for the northern Carpentaria Zn-Pb-Ag deposits invoke SEDEX processes, which led to the coeval precipitation of sphalerite and fg-py within a sulphidic (euxinic) water column (e.g., Large et al. 1998), whereas others have argued that Zn mineralization occurred during diagenesis and, therefore, post-dated the formation of fg-py (Eldridge et al. 1993; Magnall et al. 2020b). In contrast, there is uncertainty concerning how much early formed sphalerite exists in some of the southern Carpentaria Zn-Pb-Ag deposits (e.g., Perkins and Bell 1998; Chapman 2004). For example, some models favour the introduction of base metals during later stages of sediment burial, whereupon fg-py forms as part of a hydrothermal halo around the deposit (e.g., Broadbent et al. 1998). There is also additional complexity

in the southern Carpentaria region, where some deposits such as Mount Isa preserve evidence of a separate, Cu-rich hydrothermal event that was superimposed during regional metamorphism and deformation on earlier Zn mineralization (e.g., Perkins 1984; Heinrich et al. 1989).

The timing of sulphide formation in CD-type deposits can provide valuable information on the nature of both the metal trap and the geodynamic setting. For example, in models involving mineralization via SEDEX or early diagenetic subseafloor replacement processes, the upflow of metal-bearing fluids to shallow levels of sedimentary basins is thought to be facilitated by high geothermal gradients in extensional, rift-related settings (e.g., Walsh et al. 2018); in terms of a metal trap, microbial sulphate reduction (MSR) is then considered to contribute a major proportion of reduced sulphur (e.g., Fallick et al. 2001). In contrast, it has been argued that CD-type mineralization can occur in compressional regimes, when faults intersect overpressured reservoirs, and mixing between hydrothermal and evolved basinal fluids results in thermochemical sulphate reduction (TSR; e.g. Broadbent et al. 1998).

The disparity between the different models for CD-type deposits is undoubtedly linked to the challenges associated with developing a robust paragenesis in these systems. The host rocks are typically fine-grained, fairly nondescript, organic-rich mudstones, making stratigraphic correlation particularly difficult in deformed units (e.g., Red Dog; Kelley et al. 2004). The sulphide mineralization in CD-type deposits is also commonly fine grained, and differentiating paragenetic relationships between diagenetic and hydrothermal mineral phases requires a combination of petrographic techniques, e.g., binocular, reflected-light, and scanning electron microscopy (SEM). Recently, the application of *in situ* techniques has helped to distinguish between sulphides that formed via diagenetic and hydrothermal sulphate reduction (e.g., Magnall et al. 2016b, 2020b). So far in the Carpentaria region, however, *in situ* studies have focused only on undeformed hydrothermal systems (e.g., Eldridge et al. 1993).

In this study, we report petrographic and pyrite sulphur isotope data ($\delta^{34}S$ values) for samples from the main orebodies of the George Fisher deposit. Currently, measured and indicated resources are 168 million tonnes (Mt) at 8.9% Zn, 3.5% Pb, and 55 g/t Ag

(224 Mt combined George Fisher and former Hilton deposit; Glencore 2018). We also report data generated on mudstone samples from the unmineralized Urquhart Shale Formation, which represents the host rock to the George Fisher deposit. For both sample suites, we present the results of combined SEM with high-resolution (spot size <5 µm) *in situ* secondary ion mass spectrometry (SIMS) in order to resolve microscale paragenetic features and differentiate between fg-py and ore-stage sulphides. In combining the petrographic and isotopic data, we establish a robust paragenesis for pyrite formation and associated sulphur cycling through the evolution of the George Fisher deposit, including a comparison with background processes in the Urquhart Shale Formation. In doing so, we answer the following questions:

1. Does fg-py represent a feature of the pre-ore environment, or can it be considered part of the mineralogical footprint of the hydrothermal system (e.g., Broadbent et al. 1998; Perkins 1998)?

2. How comparable was the metal trap at the George Fisher deposit to those of other CD-type Zn-Pb-Ag deposits in the Carpentaria province?

2.3. Geological Background

2.3.1. Mount Isa inlier and McArthur basin

The Paleoproterozoic to Mesoproterozoic Mount Isa inlier and McArthur basin (Fig. 2-1) preserve a protracted record (250 m.y.) of basin evolution in the eastern margin of the North Australian craton, following the assembly of the Columbia/Nuna supercontinent between 1880 and 1800 Ma (Betts et al. 2002, 2016). Basin evolution is split into three consecutive unconformity-bound superbasin cycles, in which sedimentation is interpreted to have occurred in a back-arc or intracontinental setting (Giles et al. 2002; references in Gibson et al. 2016). The superbasin cycles record multiple episodes of rifting, sag phases, and basin inversion, and comprise (1) the Leichhardt superbasin (1790–1740 Ma), consisting of continental tholeiites, felsic volcanic rocks, and fluviatile-lacustrine sedimentary rocks, (2) the Calvert superbasin (1730–1640 Ma), consisting of nonmarine red beds, fanglomerates, and basaltic lavas, followed by shallow marine conditions at the Lawn Hill platform and turbidites farther

to the east, and (3) the Isa superbasin (ca. 1640–1575 Ma), which consists of turbidites, carbonaceous mudstones, and dolomitic siltstones. In the Leichhardt River fault trough of the Mount Isa area, sections of two of these superbasins are preserved (Leichhardt superbasin and Calvert superbasin; Fig. 2-2).

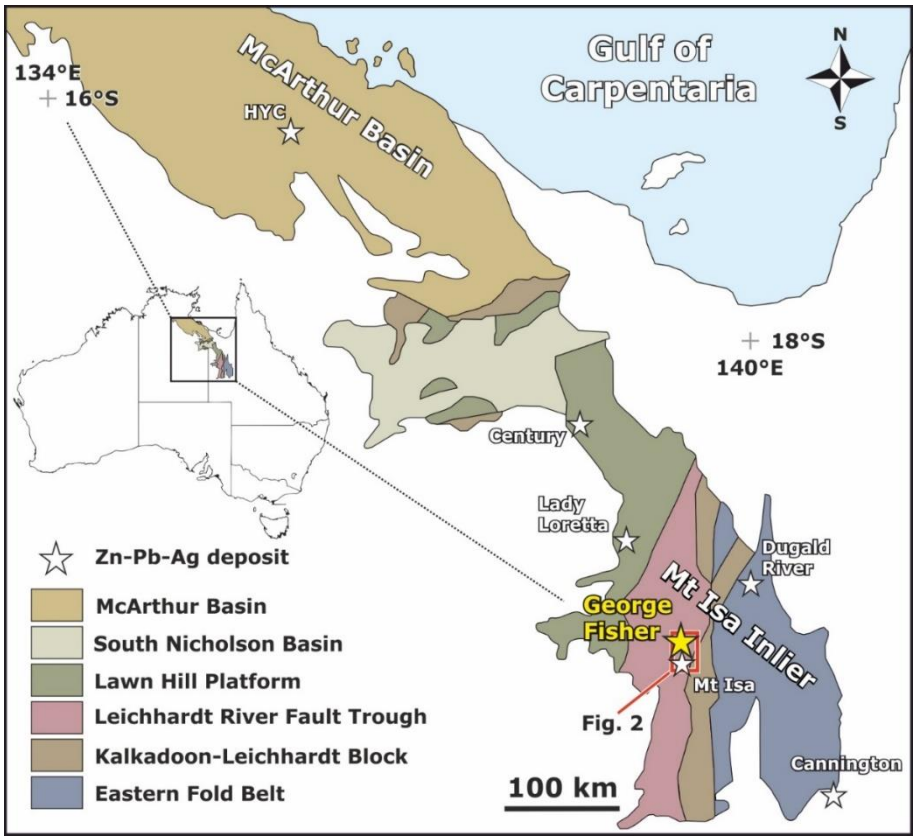

Fig. 2-1 A map of the Mount Isa inlier and McArthur basin (Gibson et al. 2017) showing tectono-stratigraphic subdivisions (Jackson et al. 2000) and seven major Zn-Pb-Ag deposits (asterisks). The George Fisher Zn-Pb-Ag deposit is highlighted in yellow, and the red rectangle outlines the Mount Isa region shown in Figure 2-2.

2.3.2. Mount Isa Group and Urquhart Shale Formation

The stratigraphic record of each superbasin cycle is subdivided into supersequences. The Mount Isa Group, which hosts the George Fisher and Mount Isa deposits, comprises the Gun and Loretta supersequences (Fig. 2-2). Whether the Mount Isa Group belongs to the Calvert or Isa superbasin is uncertain; for example, Southgate et al. (2000) proposed a stratigraphic position at the base of the Isa superbasin, whereas it was argued more recently that the Mount Isa Group should be placed at the top of the Calvert superbasin (Gibson et al. 2016).

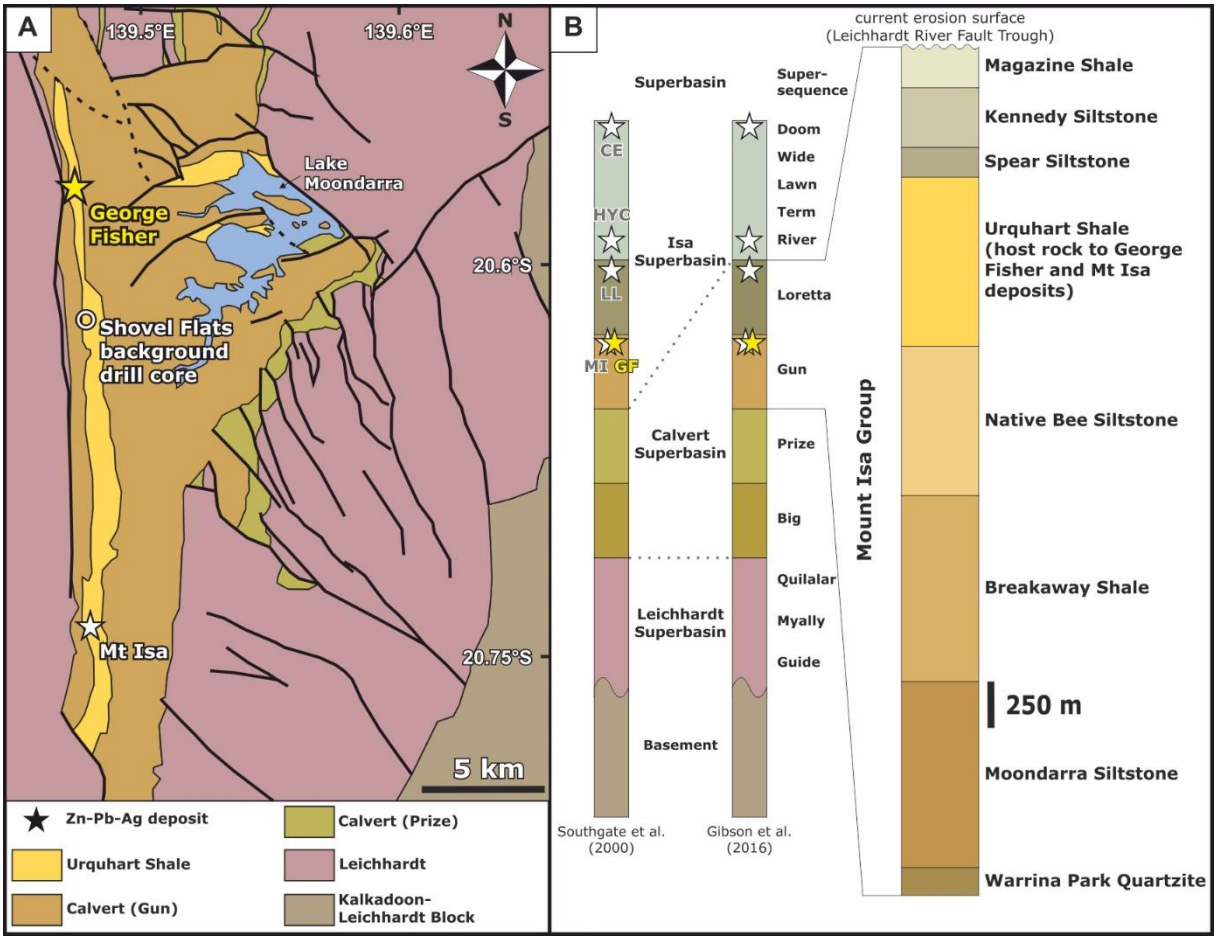

Fig. 2-2 (A) A map showing the bedrock geology of the Leichhardt River fault trough in the Mount Isa region (Gibson et al. 2017). The Mount Isa and George Fisher ore deposits are denoted by stars, along with a circle for the Shovel Flats background drill core. (B) A stratigraphic column showing the generalized superbasin stratigraphy for the Mount Isa inlier (after Southgate et al. 2000; Gibson et al. 2016). Also shown are approximate stratigraphic locations of George Fisher (GF), Mount Isa (MI), Lady Loretta (LL), HYC/McArthur River (HYC), and Century (CE) Zn-Pb-Ag deposits (asterisks). In the Mount Isa area, the Gun and Loretta supersequences are represented by the Mount Isa Group, which consists of eight clastic sedimentary formations (approximate formation thicknesses adapted from Neudert 1983).

The Mount Isa Group mainly consists of marine carbonates, siltstones, mudstones, and black, finely laminated carbonaceous siltstones, all of which were deposited between 1670 and 1650 Ma (Page et al. 2000; Neumann et al. 2006). The Urquhart Shale Formation (ca. 1654 ± 5 Ma; Page and Sweet 1998), the host rock to the George Fisher, Hilton (now mined in one operation together with George Fisher), and Mount Isa ore deposits, is part of the Mount Isa Group (Isa superbasin; e.g., Southgate et al. 2000; Calvert superbasin; Gibson et al. 2016, 2017; Fig. 2-2). There are two different interpretations concerning the depositional environment of the Urquhart Shale. Some authors have proposed deposition in a deep-water setting, based on the fine grain size

and high organic content of this formation (e.g., Mathias and Clark 1975). More specifically, Domagala et al. (2000) interpreted the Urquhart Shale to have been deposited via turbiditic flows in a relatively deep water, submarine fan setting. In contrast, other authors recognized evidence for a shallow water, hypersaline environment, such as pseudomorphs after sulphates, halite casts, and stromatolites (e.g., McClay and Carlile 1978; Neudert and Russell 1981). The dissolution of sulphate minerals has been linked to the formation of fine-grained pyrite in the Urquhart Shale Formation around the Mount Isa deposit; this pyrite is considered to have formed via TSR during burial diagenesis (Painter et al. 1999).

2.3.3. Deformation and metamorphism

The Mount Isa inlier has undergone a complex deformational history. Between ca. 1610 and 1510 Ma the rocks were folded and faulted during multiple events of north-south and east-west compression (Page and Bell 1986; Bell and Hickey 1998). Peak metamorphism is suggested to have taken place during the first phase of east-west compression, leading to sub-greenschist to amphibolite facies metamorphism in rocks west of the Mount Isa fault (Page and Bell 1986; Connors and Page 1995). In the Mount Isa area and at George Fisher, this complex deformational history resulted in folding and faulting (Chapman 2004; Murphy 2004). The metamorphic grade of the Urquhart Shale Formation and George Fisher deposit is, however, not well constrained. The only existing temperature constraints are derived from the reflectance of bituminous material in the Urquhart Shale Formation, which yield an estimated maximum burial temperature of approximately 200°C (Chapman 1999).

2.3.4. George Fisher deposit

The George Fisher deposit is located approximately 20 km north of the town of Mount Isa (Fig. 2-2). A total of nine domains are described by the Mount Isa Mines George Fisher operation nomenclature (A-I), which are further subdivided into unmineralized domains, consisting of barren mudstones and siltstones, weakly mineralized domains, and the main Zn-Pb orebodies. The mudstones are fine to medium bedded and consist of quartz, calcite, and ferroan dolomite with accessory mica, K-feldspar, and carbonaceous material; siltstones contain millimetre to sub-millimetre

laminae composed of quartz, ferroan dolomite, spheroidal pyrite, and carbonaceous material (Chapman 2004). The Urquhart Shale Formation at George Fisher has total organic carbon contents of 0.3 to 3.6 wt % (Chapman 1999). Chapman (1999, 2004) described multiple generations of sulphides in the George Fisher deposit: (1) spheroidal, fine-grained pyrite that formed prior to all other sulphides, (2) pre-deformation, vein-hosted stratabound sphalerite, (3) breccia-hosted, stratabound sphalerite associated with early stages of deformation, (4) later deformation-stage, vein-hosted galena and breccia-hosted galena and mixed sulphides, and (5) layer-parallel disseminated sphalerite interpreted as infill and alteration in host rocks proximal to mineralized zones. Additionally, Chapman (1999) described a later hydrothermal Cu event associated with vein infill or massive pyrrhotite breccias, which occurred after the main stage of Zn-Pb ore formation at temperatures of ~250° to 300°C (estimated by phyllosilicate mineral stabilities). Based on Pb model ages for galena, paragenetic observations, and metal distributions, (Chapman 1999, 2004) suggested that the bulk of the Pb (and Zn) mineralization at George Fisher took place syn-diagenetically at ca. 1653 Ma and, therefore, that most of the mineralization is pre-deformation in origin. Similarly, based on structural observations in the nearby Hilton deposit, Valenta (1994) concluded that stratiform Zn-Pb mineralization there predated deformation. In contrast, Murphy (2004) described four stages of ductile deformation (D1–4) and suggested that the main Zn-Pb-Ag hydrothermal event was syn-D4. A late-stage ore formation model is also favoured by Perkins (1998), who suggested fine-grained pyrite formed via post-diagenetic cleavage replacement in association with the ore-forming system at the Mount Isa deposit.

2.4. Methods and Samples

A total of five drill cores were sampled, including four from the George Fisher deposit that intersected domains A to E (Fig. 7-1), and one drill core (Shovel Flats) that intersected the unmineralized Urquhart Shale Formation (see Fig. 2-2 for location; Fig. 7-2). The drill cores were relogged for sedimentology, lithology, and alteration mineralogy prior to sampling (316 representative samples in total). There were difficulties in producing an exact stratigraphic correlation between the Shovel Flats drill-

hole and the George Fisher deposit, due to the complex structure of the area and the lack of suitable marker beds. As a result, the Shovel Flats drill core was sampled extensively (91 samples from 601.5 m with a sample resolution of ≤25 m) to cover any potential lithological and isotopic heterogeneity. The paragenetic relationships (Fig. 2-3) of sulphides within the samples were then evaluated using binocular and reflected-light microscopy, and multiple target areas (n = 49) with representative paragenetic stages of sulphides were drilled out using a diamond core drill bit (4 mm diameter). The micro-drilled cores were set in three epoxy mounts together with pyrite reference material (Balmat, Crowe and Vaughan 1996; S0302A, Magnall et al. 2016b) and coated in 30 nm of gold. Higher-resolution imaging was then produced using the SEM to evaluate possible compositional zonation (backscatter electron imaging [BSE]) and identify areas for isotopic analysis.

The $^{34}S/^{32}S$ ratios of pyrite were analysed by SIMS using the Cameca 1280-HR instrument at the GFZ German Research Centre for Geosciences (Potsdam, Germany). The three sample mounts were analysed over the course of several sessions (10 days). The instrument was operated at a mass resolution of M/dM ≈ 5,000. A ~100 to 150 pA, $^{133}Cs^+$ primary ion beam with a Gaussian energy distribution and an impact energy of 20 keV was focused to ≤5 µm on the polished sample surface. Low-energy, normal-incidence electron flooding was used in order to suppress charge build-up on the sample surface. Obtained count rates on the ^{32}S mass station typically ranged from 1 to 8 × 107 ions/s. Each analysis point was pre-sputtered for 100 s on a 15-µm raster, and data collection was then carried out for 100 s. The Balmat and S0302A pyrites ($\delta^{34}S$ = 15.1 and –0.2‰ respectively; Crowe and Vaughan 1996; Magnall et al. 2016b) were used as reference materials and for instrumental calibration, as drift monitors, and for data normalization.

Each analysis point (n = 1,657) was then imaged by BSE to identify the analysed phase(s). Areas containing very fine-grained pyrite or complex intergrowths of sulphide phases were analysed by transects of analytical spots with fixed spacing across several hundred microns (e.g., Fig. 2-4). The samples were then reimaged with an SEM, and the analysed spots were mapped. A total of 1,014 analyses were rejected on the basis of being

mixed phases (i.e., other sulphides or host rock). Over the course of the different sessions, 230 analyses were collected on the two reference materials, yielding a repeatability of 0.3 to 0.7‰ for S0302A (2 sd, n = 64) and 0.2 to 0.5‰ for Balmat (2 sd, n = 166).

The thermodynamic software package PHREEQC with the implemented llnl.dat database (Parkhurst and Appelo 2013) was used to calculate mineral stabilities in the Fe-S-O system. Phase stability fields were calculated for temperatures of 150°, 200°, and 250°C, 10 MPa, pH 6, sulphur activity ranging from 10–6 to 1 mol, and oxygen fugacities of –55 to –30 log fO2.

2.5. Results

2.5.1. Sulphide paragenesis

Three general sulphide assemblages are preserved in the George Fisher deposit: (1) pre-ore pyrite, (2) three different stages of hydrothermal sulphides, and (3) a generation of coarse-grained euhedral pyrite that occurs only in unmineralized rocks. In the correlative unmineralized stratigraphy (Urquhart Shale) of the background drill core, only pre-ore pyrite (1) and coarse-grained euhedral pyrite (3) are preserved. In the following section, individual stages are described in terms of the relative timing of sulphide formation (paragenesis; Fig. 2-3).

2.5.2. Pre-ore sulphides

The first generation of pyrite (Py-0) is predominantly found in the laminated, carbonaceous siltstone of the Urquhart Shale (Fig. 2-4, Fig. 2-5), both at George Fisher and in the Shovel Flats drill core. To a lesser extent, low abundances of Py-0 are also disseminated within organic-poor mudstone and siltstone. The siltstones are typically laminated, and pyrite is locally abundant (up to ~20 vol %) and occurs either as single grains or aggregates of grains that are concentrated along irregular (crinkly) laminae (Fig. 2-4, Fig. 2-5). Pyrite is typically spheroidal to subhedral and very fine grained (<10 µm) and can be split into two subtypes: Py-0a forms spheroidal to subspheroidal cores and is overgrown by Py-0b, which forms a porous, subhedral to euhedral overgrowth.

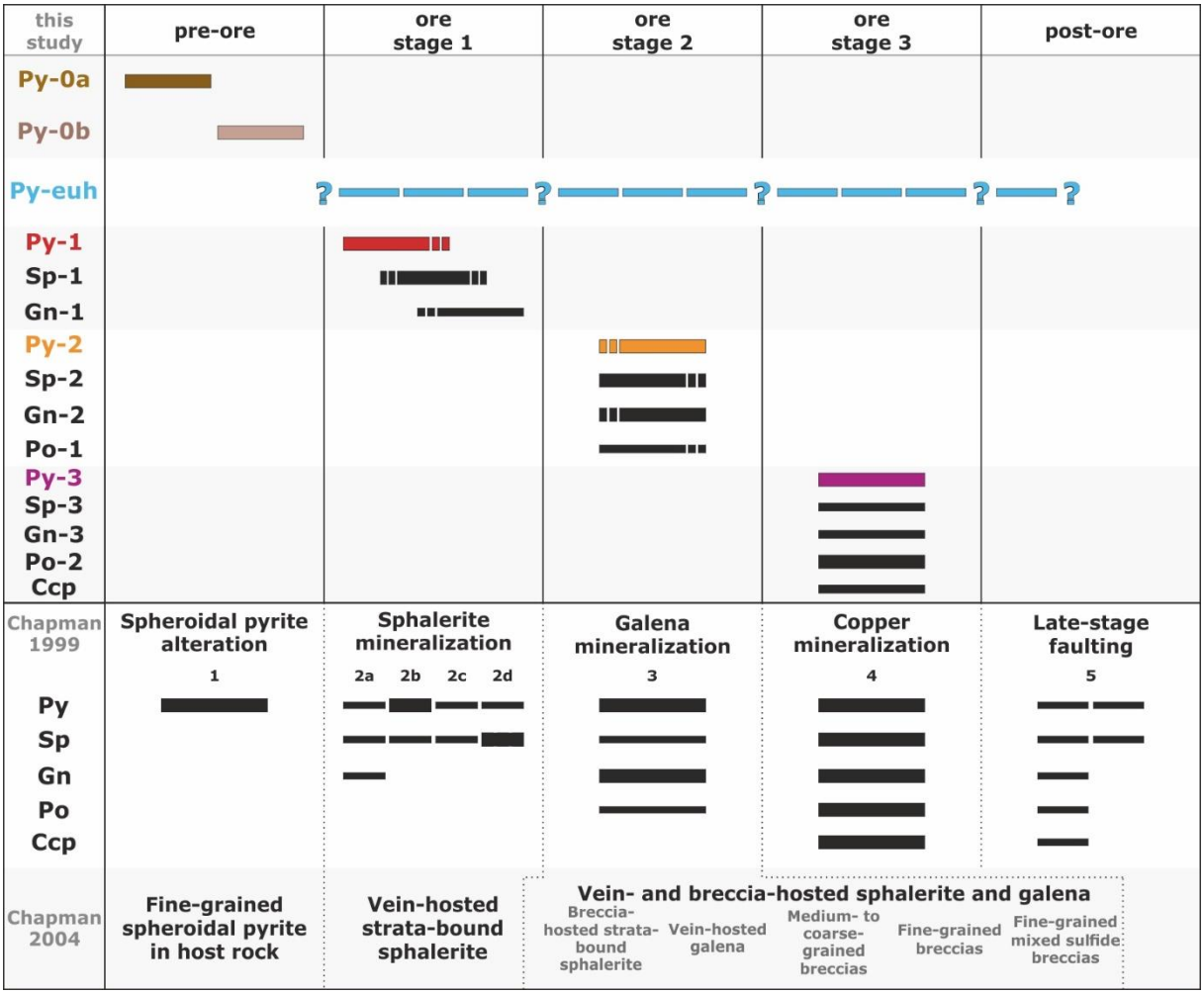

Fig. 2-3 The paragenetic sequence observed at George Fisher and in samples from the barren Urquhart Shale. Ore-stages 1 to 3 only occur at George Fisher; representative pyrite generations for each stage are highlighted in different colours. Euhedral pyrite (Py-euh) is only found in the barren Urquhart Shale samples and has not been observed with ore-stage sulphides; therefore, the possible time span for Py-euh formation is indicated by question marks and dashed lines. Also shown is sulphide paragenesis for George Fisher deposit reported by Chapman (1999, 2004). Mineral abbreviations: Ccp = chalcopyrite, Gn = galena, Po = pyrrhotite, Py = pyrite, Sp = sphalerite.

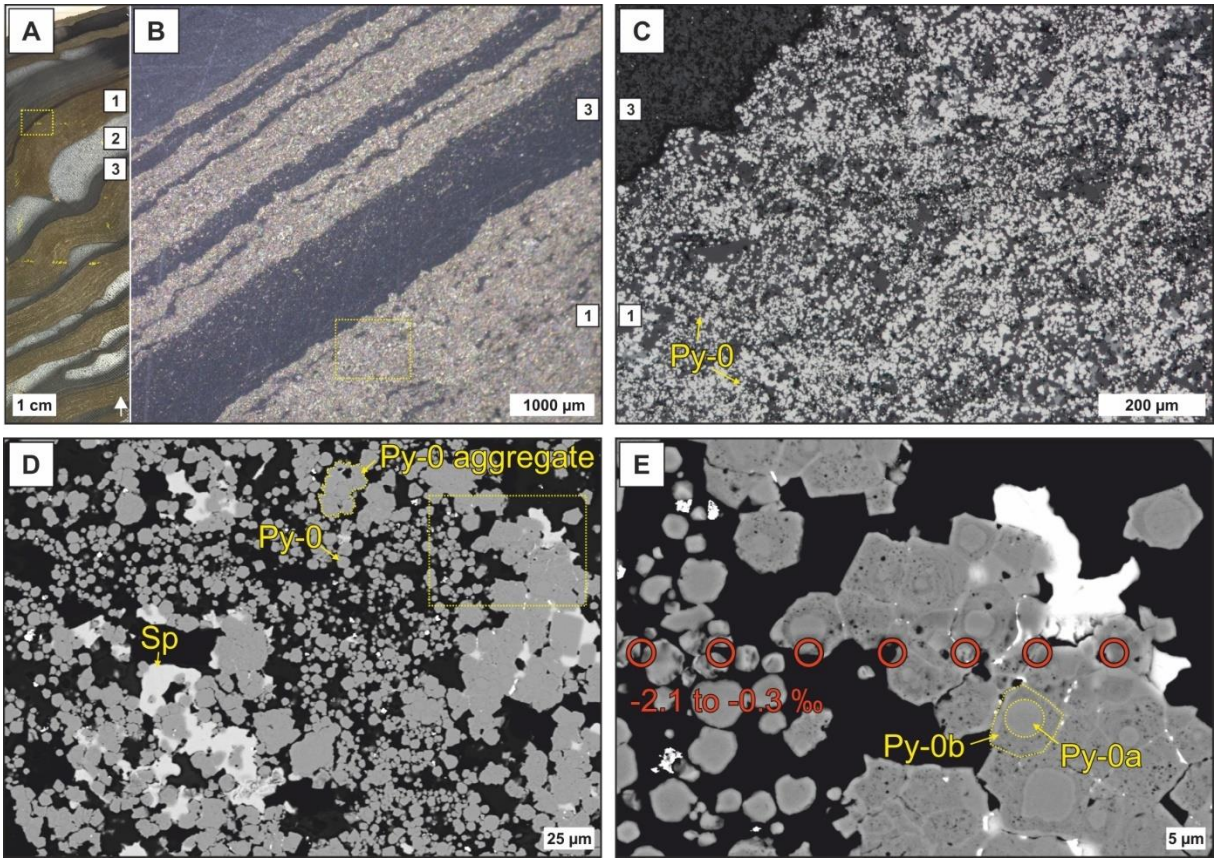

Fig. 2-4 (A) A photograph of a hand specimen from the George Fisher deposit comprising pyritic, carbonaceous siltstone (1), dolomitic mudstone (2), and carbonaceous mudstone (3). The yellow rectangle outlines the area shown in B, and the white arrow indicates uphole direction. (B) A binocular photomicroscope image of pyritic, carbonaceous siltstone (1) and carbonaceous mudstone (3). The yellow rectangle outlines the area shown in C. (C) A reflected-light photomicrograph of pyritic, carbonaceous siltstone (1) and carbonaceous mudstone (3) in which pyrite-0 (Py-0) grains are indicated by yellow arrows. (D) A backscatter electron (BSE) image of pyritic, carbonaceous siltstone in which Py-0 forms single grains or aggregates and sphalerite (Sp) forms around and interstitial to some Py-0 grains. The yellow rectangle outlines the area shown in E. (E) A high-resolution BSE image of Py-0 grains and aggregates in which Py-0 consists of spheroidal core (Py-0a) and subhedral overgrowth (Py-0b). Red circles indicate SIMS analysis spots and respective $\delta^{34}S$ values. Sample PRK751003, domain E George Fisher deposit, drill core 201012252 (A-D).

2.5.3. Ore-stage sulphides

Hydrothermal sulphides clearly replace and overgrow pre-ore pyrite (Fig. 2-6, Fig. 2-7) and can be differentiated in terms of texture, grain-size, and phase abundance. There are three generations of ore sulphides (ore-stages 1, 2, and 3), which comprise different proportions of pyrite, sphalerite, galena, pyrrhotite, and chalcopyrite. Additionally, ore-stages 1 and 2 are locally associated with fine-grained, stratabound sphalerite (e.g., Fig. 2-6).

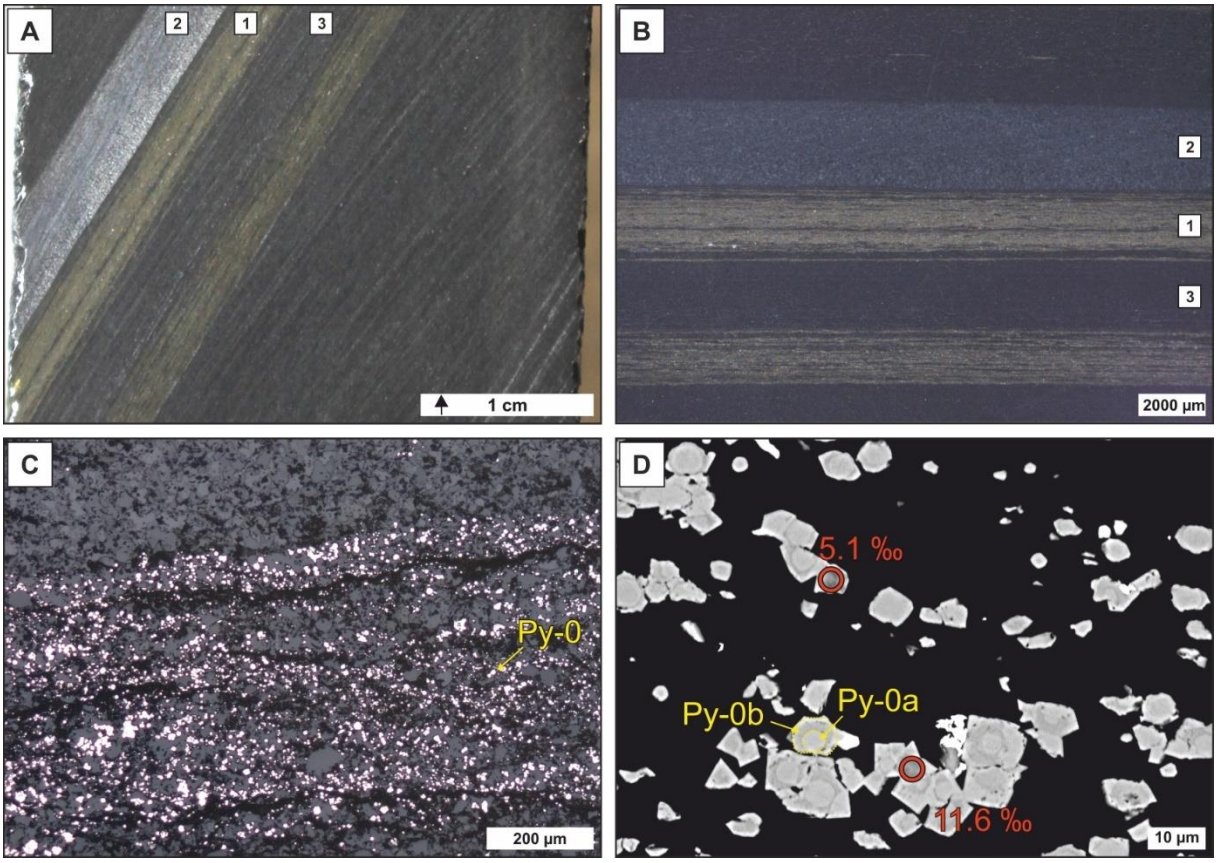

Fig. 2-5 A hand specimen photograph (A) and binocular photomicroscope image (B) showing laminations of pyritic, carbonaceous siltstone (1), dolomitic mudstone (2), and carbonaceous mudstone (3). The black arrow indicates uphole direction shown in A. (C) A reflected-light photomicrograph of pyritic, carbonaceous siltstone, with individual Py-0 grains indicated by the yellow arrow. (D) A backscatter electron image of pyrite-0 (Py-0) grains and aggregates where Py-0 consists of spheroidal core (Py-0a) and subhedral overgrowth (Py-0b), and red circles indicate SIMS analysis spots and respective $\delta^{34}S$ values. Sample PR832SF040, Shovel Flats drill core (A-D).

Ore-stage 1: This stage of sulphides is stratabound and occurs mostly in laminated, carbonaceous siltstone and postdates Py-0 (Fig. 2-6). It consists of anhedral to subhedral pyrite (Py-1; ≤ several hundred µm), anhedral sphalerite (Sp-1; grain size up to several hundred µm), and locally fine grained (≤ several tens of µm), anhedral galena (Gn-1). The sulphides occur together with coarse-grained (≥100 µm) ferroan dolomite and locally calcite. Of these sulphide phases, Py-1 is the earliest in ore-stage 1 and is typically observed in nodules or layers. Galena-1 is the latest sulphide phase in ore-stage 1 and commonly forms small veinlets. Locally, Py-0 is replaced by Sp-1 or Gn-1, resulting in atoll textures (Fig. 2-6).

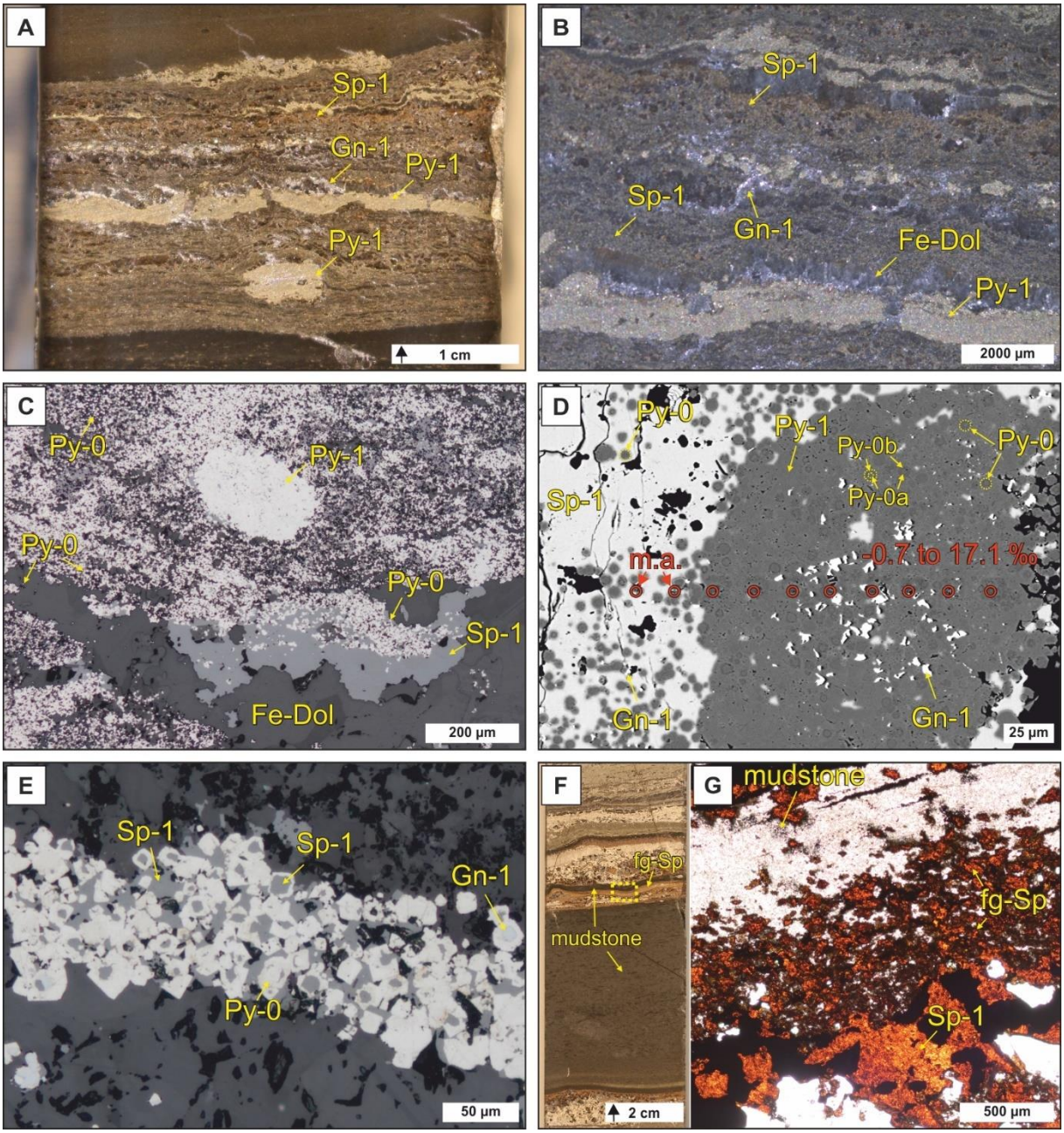

Fig. 2-6 (A) Hand specimen photograph and (B) binocular photomicrograph of ore-stage 1, pyrite-1 (Py-1) occurring in nodules or layers, sphalerite-1 (Sp-1) as stratabound, anhedral grains together with anhedral ferroan dolomite (Fe-Dol), galena-1 (Gn-1) as small veinlets across strata; black arrow indicates uphole direction. (C) Reflected-light photomicrograph of ore-stage 1 showing disseminated aggregates of pyrite-0 (Py-0) that are partially overgrown by sphalerite (Sp-1) and ferroan dolomite (Fe-Dol) and a nodule of Py-1. (D) A backscatter electron image of a Py-1 nodule and anhedral Sp-1 overgrowing Py-0a and Py-0b grains in which Gn-1 occurs as fine-grained infill to Py-1 and Sp-1. Red circles indicate SIMS analysis spots and respective $\delta^{34}S$ values. Mixed analyses (m.a.) of Py-0 and Sp-1 were rejected during data quality control. (E) A reflected light photomicrograph of ore-stage 1, showing atoll textures in which Sp-1 and Gn-1 have replaced Py-0. (F) Hand specimen photograph and (G) transmitted-light photomicrograph of ore-stage 1 showing stratabound sulphides, typical for ore-stage 1, and fine-grained sphalerite (fg-Sp), which replaces mudstone adjacent to more massive, stratabound sulphides (e.g., Sp-1). The yellow rectangle in F represents area shown in G. Samples PRK798C014, domain A George Fisher deposit, drill core 201512102 (A-C, E); PRK7952009, domain D George Fisher deposit, drill core 201601212 (D); PRK798C007, domain A George Fisher deposit, drill core 201512102 (F, G).

Ore-stage 2: This generation of sulphides (Fig. 2-7) occurs as veins and breccias that cut and replace the host rocks and previous sulphide phases. The breccias are 1 to >10 cm thick and contain a matrix of mostly galena (Gn-2), sphalerite (Sp- 2) with minor pyrite (Py-2), and pyrrhotite (Po-1). Within these breccias, there are host-rock fragments and quartz and carbonate as gangue minerals. Where host-rock clasts are preserved, Py-0 is selectively replaced by Sp-2 and Gn-2, resulting in atoll textures (Fig. 2-7). Py-2 is typically euhedral and 50 to 500 µm in size.

Ore-stage 3: This generation of sulphides forms either stratabound, massive units or veins and breccias that cut previous sulphide phases and bedding in the host rock (Fig. 2-8). Ore-stage 3 is associated with a buff-coloured phyllosilicate alteration assemblage of the host rock (Fig. 2-8). Pyrite (Py-3) and pyrrhotite (Po-2) are the main sulphides in ore-stage 3. Sphalerite (Sp-3), galena (Gn-3), and chalcopyrite (Ccp) form minor constituents during this stage. Sphalerite-3 occurs within the breccias, and Gn-3 and Ccp form veinlets within buff-coloured, phyllosilicate-altered host rocks. Pyrite (Py-3) is typically subhedral to euhedral and several tens of microns in size. Pyrrhotite (Po-2) is subhedral to anhedral and occurs interstitial to Py-3. Within mudstones, Po-2 forms porous, anhedral nodules several millimetres in size. Ore-stage 3 is chiefly present in the uppermost orebodies of the deposit.

2.5.4. Coarse-grained, euhedral pyrite

Euhedral pyrite (Py-euh; Fig. 2-9) forms overgrowths on Py-0a and Py-0b but lacks spatial or temporal relationship to the other generations of sulphides. Py-euh is coarse grained (up to several mm) and euhedral, occurs in carbonate beds or nodules (mostly calcite), and is present in both the Shovel Flats drill core and George Fisher deposit. Py-euh can be distinguished from euhedral pyrite in ore-stage 2 or 3 (Py-2 or Py-3) by a coarser grain size, mineral assemblage, and texture. Specifically, Py-2 and Py-3 only occur together with other sulphide minerals (Sp-2, Gn-2, Po-1, Sp-3, Gn-3, Po-2, Ccp) in veins or breccias, whereas Py-euh is not associated with other sulphides and commonly is stratabound together with carbonate phases.

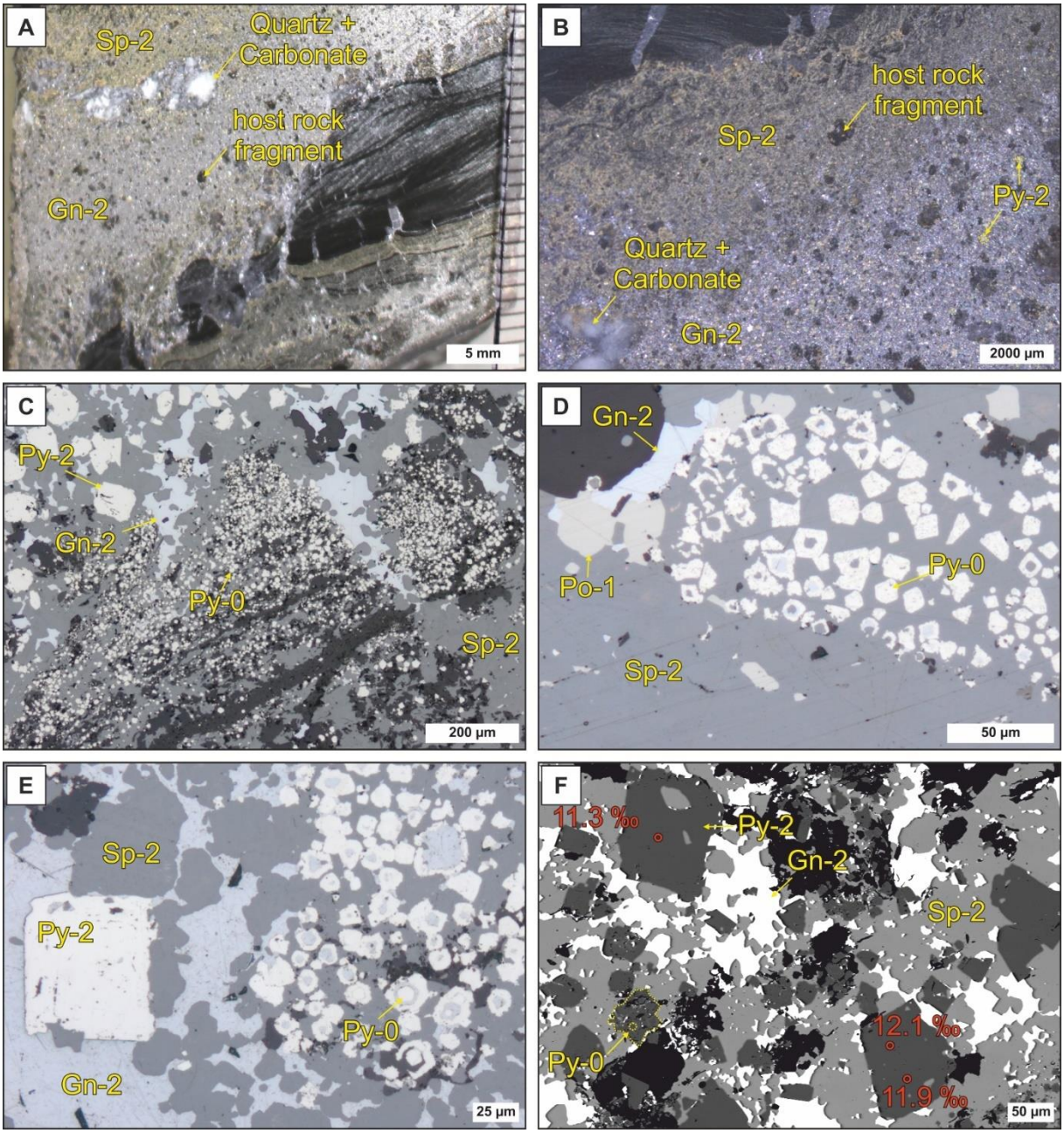

Fig. 2-7 (A) Hand specimen photograph and (B) binocular photomicrograph of ore-stage 2, showing galena-2 (Gn-2) and sphalerite-2 (Sp-2) breccias and veinlets, which cut and replace host-rock types; note quartz and carbonate as gangue minerals and host-rock fragments in breccias. (C-E) Reflected-light photomicrographs of pyrite-0 (Py-0) cut by Gn-2 (C), overgrown by Gn-2 and Sp-2 (C-E), and replaced by Gn-2 and Sp-2 (D, E); pyrite-2 (Py-2) forms euhedral crystals together with Sp-2 and Gn-2 (C, E). Note the atoll textures of Py-0 being replaced by Gn-2 and Sp-2 (D, E), which are in equilibrium with pyrrhotite-1 (Po-1; D). (F) A backscatter electron image of Py-0 aggregates and Py-2 in Gn-2 and Sp-2 breccia; red circles indicate SIMS analysis spots and respective $\delta^{34}S$ values. Samples PRK751025, domain C George Fisher deposit, drill core 201012252 (A-C, E, F); PRK751024, domain C George Fisher deposit, drill core 201012252 (D).

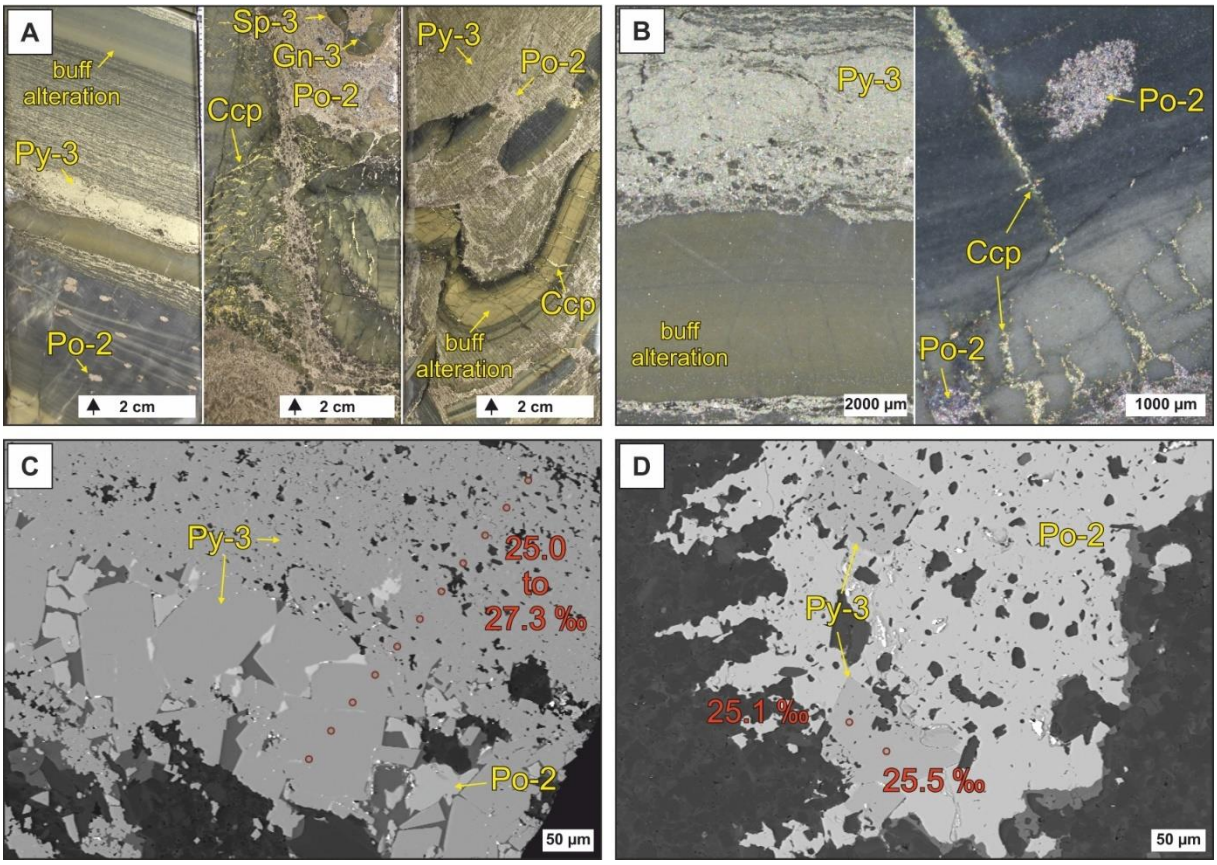

Fig. 2-8 (A) A hand specimen photographs of ore-stage 3 showing massive stratabound pyrite-3 (Py-3) alteration and pyrrhotite-2 (Po-2) nodules (left) and Po-2, galena-3 (Gn-3), sphalerite-3 (Sp-3), and Py-3 breccias replacing deformed host rock and chalcopyrite (Ccp) veinlets crosscutting and replacing deformed host rock (middle and right). Note the buff phyllosilicate alteration assemblage in the host rock associated with ore-stage 3. The black arrows indicate uphole direction. (B) Binocular photomicrographs of massive, stratabound Py-3 and buff altered host rock (left) and of a Po-2 nodule and Ccp and Po-2 veinlets. (C, D) Backscatter electron images of massive, stratabound Py-3 with Po-2 and of a Po-2 nodule together with Py-3; red circles indicate SIMS analysis spots and respective $\delta^{34}S$ values. Samples PRK751044, domain A George Fisher deposit, drill core 201012252 (A left, B left, C, D); PRK751049, domain A George Fisher deposit, drill core 201012252 (A middle); PRK751050, domain A George Fisher deposit, drill core 201012252 (A right, B right).

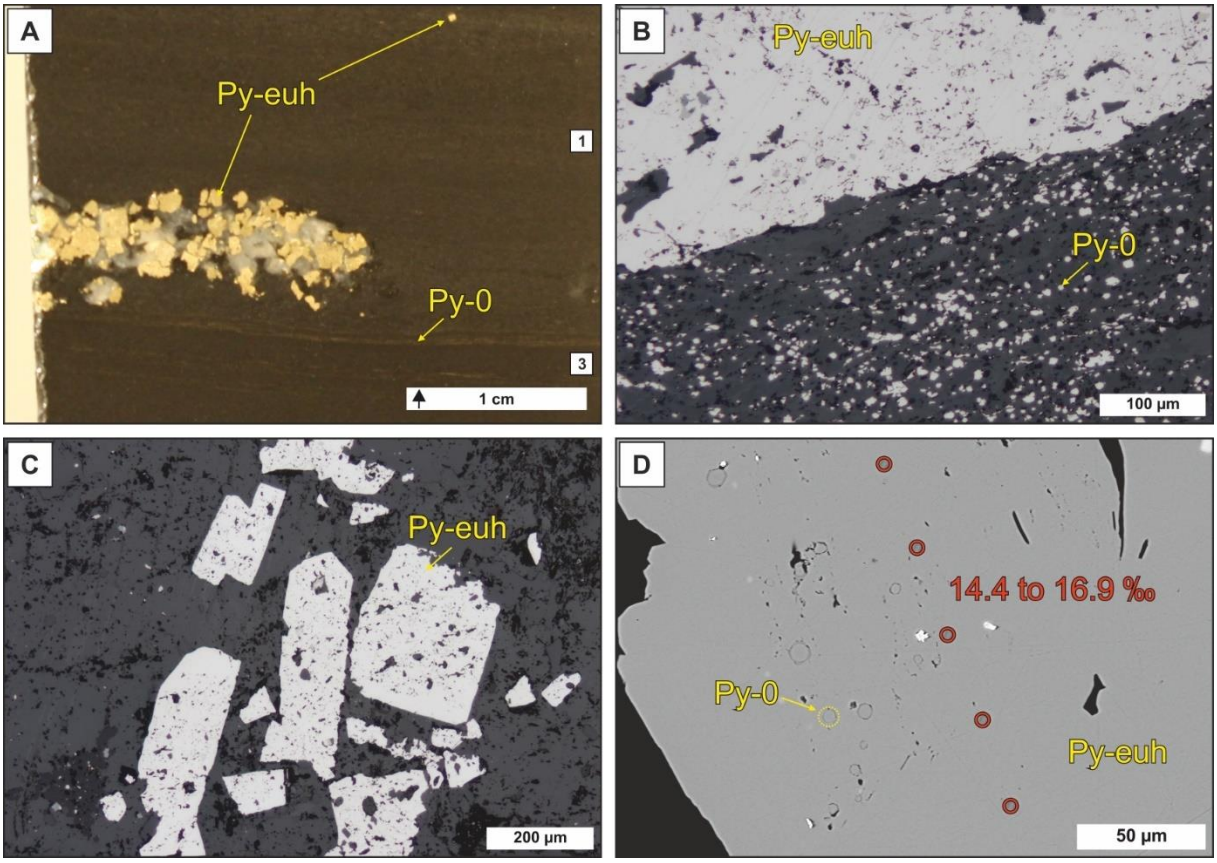

Fig. 2-9 (A) A hand specimen photograph of coarse-grained, euhedral pyrite (Py-euh), carbonaceous mudstone (3), and pyritic, carbonaceous siltstone (1) containing pyrite-0 (Py-0). The black arrow indicates uphole direction. (B, C) Reflected-light photomicrographs of Py-euh (B, C) and Py-0 (B). (D) Backscatter electron images of Py-euh. Note the Py-0 grains being overgrown by Py-euh; red circles indicate SIMS analysis spots and respective $\delta^{34}S$ values. Sample PR832SF008, Shovel Flats drill core (A); PR832SF040, Shovel Flats drill core (B, D); PR832SF086, Shovel Flats drill core (C).

2.5.5. Sulphur isotope composition ($\delta^{34}S$) of pyrite

The $\delta^{34}S$ values of 643 analyses of pyrite from the George Fisher deposit and the Shovel Flats drill core are summarized in Fig. 2-10 and Appendix Table A1.

Pyrite from the George Fisher deposit has $\delta^{34}S$ values between –8.1 and 33.9‰ (n = 446). Py-0a and Py-0b preserve $\delta^{34}S$ values of –8.1 to 2.7‰ (n = 116; five samples) and –4.1 to 5.4‰ (n = 44; four samples), respectively. The different generations of ore-stage pyrite have $\delta^{34}S$ values from 7.8 to 33.3‰ (Py-1; n = 75; four samples), 1.9 to 12.7‰ (Py-2; n = 155; four samples), and 23.4 to 28.2‰ (Py-3; n = 38; two samples). The $\delta^{34}S$ values of Py-euh are distributed between 7.2 and 33.9‰ (n = 18; two samples).

The $\delta^{34}S$ values of pyrite from the Shovel Flats drill core are 1.0 to 31.0‰ (n = 197). Compared to George Fisher, Py-0a and Py-0b have slightly higher $\delta^{34}S$ values of 1.0 to

11.8‰ (n = 24; five samples) and 6.5 to 11.6‰ (n = 2; two samples), respectively. Py-euh preserves $\delta^{34}S$ values of 10.3 to 31.0‰ (n = 171; eight samples).

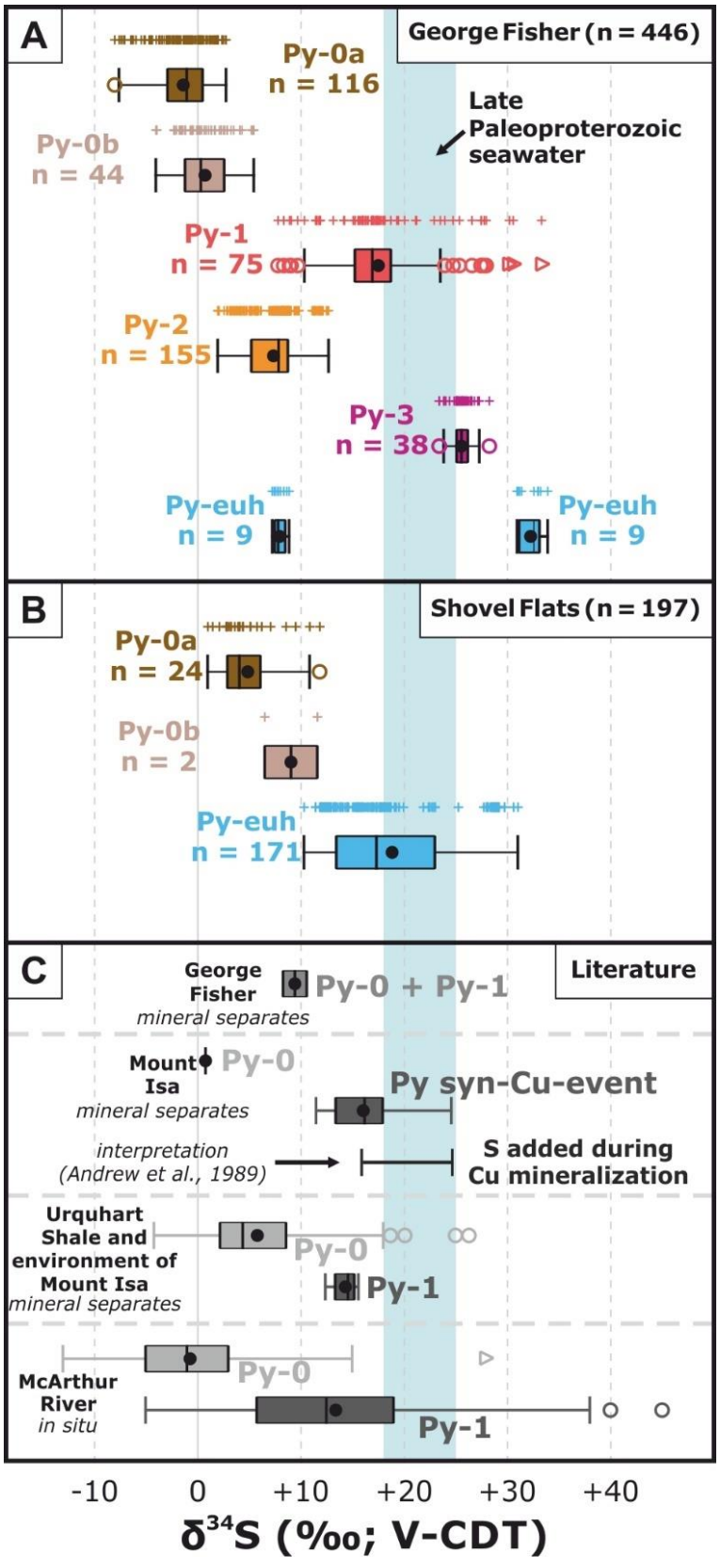

Fig. 2-10 Box and whisker plots showing the $\delta^{34}S$ (‰; Vienna-Canyon Diablo Troilite [V-CDT]) values of pyrite (Py-0a, Py-0b, Py-1, Py-2, Py-3, and Py-euh) from George Fisher (A), background Urquhart Shale (B), and from pyrite analyses of previous studies (C) in the Carpentaria province (George Fisher, Chapman 1999; Mount Isa, Andrew et al. 1989; Urquhart Shale and environment of Mount Isa, Painter et al. 1999; McArthur River, Eldridge et al. 1993). The pyrite nomenclature from these studies has been converted to that used in this study in order to simplify comparison. The $\delta^{34}S$ value of barite has been used as an approximation for late Paleoproterozoic seawater (Strauss 1993). Symbols above individual box and whisper symbols indicate individual data points of the respective pyrite generation.

2.6. Discussion

2.6.1. Pre-ore pyrite

At George Fisher, Py-0a and Py-0b are overgrown (Fig. 2-6, Fig. 2-7, Fig. 2-9) or replaced (Fig. 2-6, Fig. 2-7) by the ore-stage sulphides. As Py-0 is preserved at both George Fisher and in the barren Urquhart Shale, it is very likely that Py-0 formed in a pre-ore environment. Similarly, comparable fine-grained, stratiform pyrite has been documented in a number of other unmineralized, carbonaceous, fine-grained siliciclastic sequences of Proterozoic age (e.g., Schieber 1989; Painter et al. 1999; Lyons et al. 2000). In some of these settings, the concentration of fine-grained pyrite along crinkly laminations has been linked to the formation of microbial mats and diagenetic sulphide formation unrelated to hydrothermal activity (Schieber 1990). In contrast, it has also been proposed that fine-grained pyrite can form at higher temperatures via TSR during burial diagenesis (e.g., Painter et al. 1999). At ambient temperatures there are two main pathways by which seawater sulphate is microbially reduced to sulphide in anoxic marine sediments: (1) MSR and (2) sulphate-driven via anaerobic oxidation of methane (SD-AOM). The hydrogen sulphide produced reacts with reactive Fe to precipitate diagenetic pyrite by a series of iron sulphide precursor phases (Sweeney and Kaplan 1973; Raiswell and Berner 1985).

A large kinetic fractionation is associated with MSR ($\varepsilon^{34}S = \delta^{34}S_{SO_4} - \delta^{34}S_{H_2S}$), meaning that pyrite typically preserves $\delta^{34}S$ values that are considerably offset ($\Delta^{34}S = \delta^{34}S_{seawater} - \delta^{34}S_{pyrite}$) from those of coeval seawater sulphate (e.g., Kaplan et al. 1963; Kaplan and Rittenberg 1964). The δ^{34}Spyrite value will depend, therefore, both on $\varepsilon^{34}S$ and the initial $\delta^{34}S_{SO_4}$ value; however, there are no precise constraints on $\delta^{34}S_{SO_4}$ for the late Paleoproterozoic during the deposition of the Urquhart Shale (ca. 1654 Ma). On a regional scale, a wide range of $\delta^{34}S_{SO_4}$ values (14.1–37.2‰) are reported for slightly younger sedimentary units derived from the analyses of carbonate-associated sulphate (CAS) in the Paradise Creek Formation (McNamara Group, Lawn Hill platform, ca. 1650 Ma; Gellatly and Lyons 2005), which on a more global scale overlaps $\delta^{34}S_{CAS}$ values for samples of diagenetic carbonate in the Chuanlinggou Formation (Yanshan basin, North

China; ca. 1650 Ma; 27.3–40.2‰; Li et al. 2015). Nevertheless, $\delta^{34}S_{CAS}$ values can exceed that of coeval seawater ($\delta^{34}S_{SO_4}$) due to modification by MSR in diagenetic pore fluids (e.g., Present et al. 2015). A narrower range of $\delta^{34}S$ values (18–25‰) is recorded in bedded barite from the McArthur Group (McArthur basin; Strauss 1993). These units are slightly younger but broadly time correlative to the Mount Isa Group and may, therefore, provide a more conservative estimate for the isotopic composition of seawater sulphate. In the following discussion of $\delta^{34}S_{pyrite}$ values, therefore, $\delta^{34}S_{seawater}$ value of 18 to 25‰ will be used as a general reference.

The $\delta^{34}S_{Py\text{-}0}$ values represent a large offset from the estimated composition of coeval seawater sulphate ($\Delta^{34}S$ = 6.2–33.1‰; Fig. 2-10), and the lowest $\delta^{34}S_{Py\text{-}0}$ values overlap with the lowest reported $\delta^{34}S_{pyrite}$ values in samples from this time period (e.g., Canfield and Farquhar 2009; Fike et al. 2015). Development of more positive $\delta^{34}S$ values, perhaps approaching coeval $\delta^{34}S_{SO_4}$, typically occurs under sulphate-limited conditions. Importantly, sulphate limitation can occur at different scales: for example, progressive consumption of sulphate via MSR and SD-AOM can produce large isotopic gradients within diagenetic pore fluids (e.g., Jørgensen et al. 2004), which has been linked to highly variable $\delta^{34}S_{pyrite}$ values at a hand sample scale (e.g., Borowski et al. 2013; Magnall et al. 2016b). In contrast, it is generally accepted that sulphate limitation may also occur when MSR consumes high proportions of seawater sulphate in the water column of euxinic basins, which has been used to explain the preservation of highly positive $\delta^{34}S_{pyrite}$ values at a broader basin scale (e.g., Lyons et al. 2000).

The observed high $\Delta^{34}S$ values ($\delta^{34}S_{SO_4,seawater} - \delta^{34}S_{Py\text{-}0}$) are typical of MSR in relatively open system conditions when sulphate is not completely consumed (Gomes and Hurtgen 2015). Open-system conditions actually represent the vast majority of early pyrite formation in marine environments, normally within diagenetic pore waters below the sediment-water interface (e.g., Rudnicki et al. 2001). Open-system sulphate reduction may also develop locally within euxinic water columns with a high initial concentration of seawater sulphate (e.g., Lyons 1997), but without additional paleo-redox indicators it is not possible to differentiate between the different modes of open-system pyrite formation in the geologic record. The trend toward slightly more positive

$\delta^{34}S$ values in Py-0b, which forms euhedral overgrowths on Py-0a, is evidence of pyrite formation under increasingly sulphate limited conditions. Compared to Py-0a, formation of Py-0b likely occurred within slightly more restricted diagenetic pore fluids, with a common source of reduced sulphur derived from MSR. Indeed, pyrite that forms in modern marine sediments deposited under non-euxinic conditions preserves similar morphologies of euhedral overgrowths of earlier, fine-grained pyrite (South China Sea; Lin et al. 2016).

When comparing samples from the George Fisher deposit and the Shovel Flats drill hole, a small difference in $\delta^{34}S_{Py\text{-}0}$ values (Fig. 2-10) may also provide evidence of slightly more sulphate-limited conditions in the unmineralized samples. Yet it is notable that no highly positive $\delta^{34}S_{Py\text{-}0}$ values (>15‰) exist in any of the samples, unlike the diagenetic pyrite analysed in other Proterozoic sedimentary basins (e.g., Strauss and Schieber 1990; Lyons et al. 2000; Magnall et al. 2020b). The absence of such highly positive $\delta^{34}S_{Py\text{-}0}$ values demonstrates that pyrite did not form in highly sulphate limited conditions in the Urquhart Shale, either in unmineralized or mineralized samples.

Altogether, the pre-ore timing of Py-0, combined with overlapping $\delta^{34}S_{Py\text{-}0}$ values between unmineralized and mineralized samples (Fig. 2-10), suggests that MSR in relatively open system conditions resulted in extensive diagenetic pyrite formation before the onset of hydrothermal activity.

2.6.2. Sulphide paragenesis

Due to morphological and textural similarities, pre-ore Py-0 in this study may be the equivalent of early diagenetic fine-grained Py-1 as described at the McArthur River deposit (e.g., Eldridge et al. 1993). For the Mount Isa deposit, Perkins (1998) and Perkins and Bell (1998) reported morphologically similar zoned fine-grained pyrite, which they interpreted to have formed via post-diagenetic cleavage replacement. Such a relationship to post-diagenetic cleavage replacement has not been observed in this study.

The overall paragenesis of ore-stage sulphides at George Fisher described in this study (Fig. 2-3) is broadly consistent with the relative timing of sulphide minerals described by Chapman (1999, 2004). Stratabound sulphide mineralization is typical of

the ore at George Fisher and is described as ore-stage 1 (this study) and as pre-deformation vein-hosted stratabound sphalerite by Chapman (2004). Furthermore, fine-grained stratabound sphalerite adjacent to high-grade ore zones is described in both studies (Chapman 2004; Fig. 2-6), and has been interpreted to form as an alteration feature in the host rock (Chapman 2004). The subdivision of breccia-hosted Zn-Pb-Ag mineralization into different generations of successive ore breccias (Fig. 2-7; breccia-hosted stratabound sphalerite, vein- and breccia-hosted galena, and fine-grained mixed sulphide breccias; Chapman 2004) is here simplified into ore-stage 2, because (1) clear crosscutting relationships between different ore breccias could not be discerned, (2) pyrite morphologies are very similar throughout ore-stage 2, and (3) $\delta^{34}S_{Py\text{-}2}$ values display a narrow range in all analysed ore-stage 2 samples (1.9–12.7‰; 155 analyses of four individual samples).

2.6.3. Interpreting $\delta^{34}S$ values in ore-stage pyrite

Pyrite from ore-stage 1 (Py-1) preserves a broad distribution of $\delta^{34}S$ values (7.8–33.3‰) that is a typical result of *in situ* analyses of ore-stage sulphides in CD-type deposits (e.g., Eldridge et al. 1993; Kelley et al. 2004; Magnall et al. 2016b; Gadd et al. 2017). The heterogeneity of $\delta^{34}S_{Py\text{-}1}$ values is at the hand sample scale, which is common in systems that are transport limited, i.e., where variability exists in the rate of sulphate replenishment relative to reduction (e.g., Goldhaber and Kaplan 1975; Riciputi et al. 1996). Importantly, pyrite from ore-stage 1 is isotopically distinct from pre-ore pyrite (Fig. 2-10), providing evidence that ore-stage sulphur may not have evolved from open- to closed-system conditions via progressive sulphate depletion during MSR. Rather, it is more likely that Py-1 formed from reduced sulphur derived by a separate process.

Highly positive $\delta^{34}S$ values are typical of more closed-system sulphate reduction and are a feature of all CD-type deposits (e.g., Eldridge et al. 1988; Magnall et al. 2016b; Gadd et al. 2017). Recently, it has been shown how positive $\delta^{34}S$ values developed within pre-ore diagenetic environments via SD-AOM, prior to sulphide mineralization in CD-type Zn-Pb deposits from the Selwyn basin (Magnall et al. 2016b; Johnson et al. 2018). The Shovel Flats drill hole, however, does not preserve stratiform pyrite that is

comparable to Py-1, in terms of either morphology or $\delta^{34}S$ values. This result would imply that another sulphate reduction process was responsible for Py-1 formation.

Under hydrothermal conditions (>100°C), sulphate reduction can proceed via an abiotic pathway given the availability of an appropriate reductant (e.g., organic matter), in a reaction described as TSR (Machel 2001):

Hydrocarbons + SO_4^{2-} → altered hydrocarbons + solid bitumen + H_2S + CO_2 + H_2O

The TSR reaction does, however, require a catalyst (e.g., H_2S; Toland 1960; Goldhaber and Orr 1995), which at George Fisher could have been derived from reduced sulphur produced by MSR and/or SD-AOM. The other components required for TSR were readily available within the Mount Isa Group. For example, preservation of substantial amounts of organic carbon has also been reported for sedimentary rocks in the northern Mount Isa inlier (total organic carbon up to 6.9 wt %; McNamara Group; Glikson et al. 2000) and for the Urquhart Shale at George Fisher (total organic carbon up to 3.6 wt %; Chapman 1999). In terms of sulphate availability, this is typically sourced from seawater sulphate or the dissolution of sulphate-bearing mineral phases (Machel 2001). In the Mount Isa Group there is evidence of local gypsum and anhydrite, which via dissolution could have provided a direct source of sulphate or alternatively might represent the end product of sulphate-rich evaporitic brines in the basin (e.g., McClay and Carlile 1978; Neudert and Russell 1981).

Under open-system conditions, there is a temperature-dependent kinetic fractionation associated with TSR (Kiyosu and Krouse 1990): $\varepsilon^{34}S$ = 20‰ (at 100°C), 15‰ (at 150°C), and 10‰ (at 200°C). As stated previously, however, the wide range of observed $\delta^{34}S_{Py\text{-}1}$ values provides evidence of transport limitation and Rayleigh fractionation effects that resulted from a restricted supply of sulphate. This distribution of $\delta^{34}S$ values in early ore-stage sulphides appears to be consistent with those of other CD-type deposits for which TSR has been proposed (e.g., Kelley et al. 2004; Magnall et al. 2016a; Gadd et al. 2017). It is also worthwhile drawing comparison to studies of TSR in natural gas reservoirs, where H_2S is produced by the thermal alteration of hydrocarbons in combination with the dissolution of sulphate mineral phases (e.g., Riciputi et al. 1996; Cai et al. 2003; King et al. 2014). In fact, the offset from respective

seawater sulphate values ($\Delta^{34}S$) measured for H_2S (Cai et al. 2003; Zhu et al. 2005) and for pyrite (Riciputi et al. 1996; Zhu et al. 2005; King et al. 2014) from these reservoirs is very similar to the offset determined herein for Py-1 from ore-stage 1 at George Fisher. Overall, the availability of organic matter and sulphate in the Urquhart Shale, together with $\Delta^{34}S$ values similar to those of TSR-produced ore-stage sulphides in other CD-type deposits (e.g., Kelley et al. 2004; Magnall et al. 2016a; Gadd et al. 2017) and natural gas reservoirs (e.g., Riciputi et al. 1996; Zhu et al. 2005; King et al. 2014), is consistent with reduced sulphur being derived from TSR during ore-stage 1 at George Fisher.

The $\delta^{34}S$ values of pyrite from ore-stage 2 (Py-2; Fig. 2-10) are intermediate between and overlap those of pre-ore pyrite (Py-0) and ore-stage 1 pyrite (Py-1). Slightly higher $\Delta^{34}S$ values associated with ore-stage 2 pyrite (Fig. 2-10) may have resulted from TSR that occurred at lower temperatures or involved a different source of sulphate. Alternatively, the replacement of fine-grained pyrite by ore-stage sulphides could also have provided a source of reduced sulphur within the highly mineralized ore zones, as suggested by previous authors for Mount Isa (Blanchard and Hall 1937; Grondjis and Schouten 1937; Solomon 1965; Finlow-Bates et al. 1977), George Fisher (Chapman 1999), and McArthur River (Williams and Rye 1974). At the George Fisher deposit the pyrrhotite (Po-1) that is more abundant in ore-stage 2 (Fig. 2-7) could have derived from the transformation of pyrite and involved a corresponding release of sulphur ($FeS_2 = FeS + ½ S_2$; Toulmin III and Barton Jr 1964). An important question remains, therefore, as to what physicochemical conditions were responsible for the transition between sphalerite + galena + pyrite (ore-stage 1) to sphalerite + galena + pyrrhotite ± pyrite (ore-stage 2).

A rigorous assessment of peak metamorphic conditions has not been conducted at the George Fisher deposit. The only existing temperature constraints are derived from the reflectance of bituminous material (~200°C) and a phyllosilicate assemblage that provides evidence that temperatures may have reached 300°C (Chapman 1999), which both correspond with sub-greenschist facies metamorphic conditions. This temperature regime is also broadly consistent with maximum temperatures (200°–350°C) derived from fluid inclusions in dolomite and quartz associated with syn-deformational Cu ore formation at the Mount Isa deposit (Heinrich et al. 1989; Kendrick et al. 2006). Using

these temperature constraints, thermodynamic modelling shows that small changes in temperature, sulphur activity, and oxygen fugacity could have affected the stability of pyrite and pyrrhotite (Fig. 2-11). An increase in temperature (arrow A in Fig. 2-11), decrease in sulphur activity (B), or decrease in oxygen fugacity (C) could have resulted in a shift toward the stability field of pyrrhotite at the expense of pyrite (e.g., Craig and Vokes 1993). In contrast, a decrease in temperature (A), increase in sulphur activity (B), or increase in oxygen fugacity (C) could have stabilized pyrite and destabilized pyrrhotite (e.g., Craig and Vokes 1993). One of these processes or the interplay of them may, indeed, explain why (1) earlier generations of pyrite at George Fisher are replaced by sphalerite and galena (Fig. 2-7) and (2) both pyrrhotite and pyrite occur in ore-stage 2 (Po-1 and Py-2; Fig. 2-7). Using this model of sulphide replacement, the fact that $\delta^{34}S_{Py-2}$ values are intermediate between those of $\delta^{34}S_{Py-0}$ and $\delta^{34}S_{Py-1}$ (Fig. 2-10) may indicate that similar proportions of pre-existing pyrite were involved in the replacement process. Overall, the interpretation that reduced sulphur for ore-stage 2 was derived from previous generations of pyrite is consistent with pyrite replacement textures (Fig. 2-7), increasing pyrrhotite abundance (Fig. 2-7), and intermediate $\delta^{34}S_{Py-2}$ values (Fig. 2-10) in ore-stage 2.

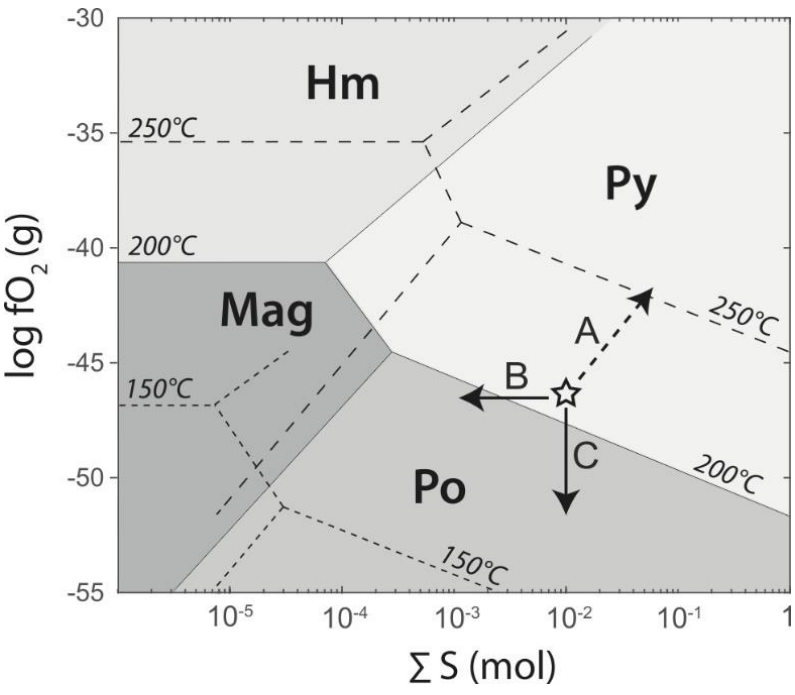

Fig. 2-11 A phase diagram for system Fe-S-O at pH = 6 showing stability fields for magnetite (Mag), hematite (Hm), pyrrhotite (Po), and pyrite (Py) for three different temperatures (150°C dashed lines; 200°C solid lines; 250°C dashed lines), and variable oxygen fugacity and sulphur activity. The asterisk and three arrows represent three scenarios under which Py is destabilized and Po becomes stable (A = increased temperature; B = decreasing sulphur activity; C = decreasing oxygen fugacity). The thermodynamic software package PHREEQC with the implemented llnl.dat database (Parkhurst and Appelo 2013) was used to calculate mineral stabilities in the Fe-S-O system.

The modelled temperatures are also below the threshold at which isotopic equilibration between other mineral phases is expected to be a factor. For example, previous work has shown that primary $\delta^{34}S$ values are retained in pyrite at temperatures below 350°C (Cook and Hoefs 1997; Wagner and Boyce 2006; Cloutier et al. 2015), which is the uppermost temperature constraint for the George Fisher deposit. Such temperatures are below the brittle-ductile transition for pyrite, unlike the other sulphide mineral phases present at George Fisher (galena, sphalerite, pyrrhotite) that preserve signs of ductile deformation (Marshall and Gilligan 1987). Indeed, it has been suggested that galena and sphalerite accommodated most of the deformation at the George Fisher deposit (Chapman 2004).

Pyrite in ore-stage 3 (Py-3) has a narrow distribution of $\delta^{34}S$ values, similar to those of late Paleoproterozoic seawater (Fig. 2-10). Following previous arguments, ore-stage 3 could potentially be the product of recycling of ore-stage 1; however, the broad distribution of $\delta^{34}S_{Py\text{-}1}$ values makes a formation by recycling of sulphur from ore-stage 1 unlikely, because a similar distribution is not preserved in the $\delta^{34}S_{Py\text{-}3}$ values. Different conditions of pyrite formation are perhaps more likely, considering that chalcopyrite also occurs in the ore stage 3 assemblage at George Fisher (Fig. 2-8) and is associated with buff-coloured phyllosilicate-altered host rocks (Fig. 2-8). Temperature constraints for ore-stage 3 are also high (250°–300°C; Chapman 1999), which could have resulted in minimal fractionation during TSR. It therefore seems possible that ore-stage 3 developed as a separate hydrothermal event that overprinted previous ore stages (Fig. 2-3). Indeed, a similar model has been proposed for the Mount Isa deposit, involving a Cu-rich, syn-metamorphic/syn-deformational, hydrothermal event being superimposed on pre-existing Zn-Pb mineralization (e.g., Andrew et al. 1989; Heinrich et al. 1989). Notably, the $\delta^{34}S_{Py\text{-}3}$ values overlap with $\delta^{34}S$ values reported at Mount Isa (Fig. 2-10), albeit skewed toward slightly more positive values at George Fisher.

2.6.4. Coarse-grained euhedral pyrite

The $\delta^{34}S$ values of Py-euh from the Shovel Flats drill hole form a broad distribution with a median close to those $\delta^{34}S$ values constrained for late Paleoproterozoic seawater sulphate (Fig. 2-10). In contrast, the $\delta^{34}S_{Py\text{-}euh}$ values of two

samples from the George Fisher deposit show a bimodal distribution, which is similar to the highest and lowest $\delta^{34}S_{Py\text{-}euh}$ values from the Shovel Flats drill hole. Such values can be produced by MSR under sulphate-limited conditions (e.g., Strauss and Schieber 1990; Lyons et al. 2000), TSR (Machel et al. 1995), or SD-AOM (e.g., Borowski et al. 2013). The presence of Py-euh in samples from the unmineralized Shovel Flats drill core means a hydrothermal origin is unlikely, but whether this pyrite formed during a later stage of diagenesis than Py-0 or during regional metamorphism is unknown.

The $\delta^{34}S_{Py\text{-}euh}$ values are significantly more positive than, and do not overlap with, the $\delta^{34}S_{Py\text{-}0}$ values. This suggests that this generation of pyrite is unlikely to have formed along a single closed-system trend. The broad distribution and highly positive $\delta^{34}S_{Py\text{-}euh}$ values (7.2–33.9‰) may, however, reflect TSR under transport-limited conditions—i.e., where variability exists in the rate of sulphate replenishment relative to reduction (e.g., Goldhaber and Kaplan 1975; Riciputi et al. 1996). Alternatively, highly positive $\delta^{34}S$ values are also commonly produced via SD-AOM at the sulphate-methane transition zone (e.g., Borowski et al. 2013). TSR and SD-AOM may, therefore, both be responsible for formation of the reduced sulphur in Py-euh.

2.6.5. Comparisons between George Fisher and other CD-type deposits in the Carpentaria province

There are notable similarities between the morphology and $\delta^{34}S$ values of the earliest stage of pyrite from this study and the major CD-type deposits in the Carpentaria province, irrespective of the metamorphic grade and tectonic overprint. For example, fine-grained pyrite within the host units to the McArthur River (Py-1; Eldridge et al. 1993), Teena (Py-1; Magnall et al. 2020b), Mount Isa (fine-grained pyrite; Painter et al. 1999), and George Fisher (Py-0; this study) deposits are texturally and isotopically indistinguishable. Such similarities in diagenetic pyrite could be evidence of broadly comparable paleoenvironments during deposition of the respective host rocks, even though they occur at different stratigraphic positions within the Gun and River supersequences (Fig. 2-2). Unlike genetic models for other deposits where it is considered a syn-ore phase (Broadbent et al. 1998; Large et al. 1998), Py-0 is most likely part of the pre-ore assemblage at the George Fisher deposit. A pre-ore timing of

isotopically very similar fine-grained pyrite in the Urquhart Shale Formation has previously been reported by Painter et al. (1999), who, however, favoured a late diagenetic source of reduced sulphur for pyrite formation via TSR rather than early diagenetic formation via MSR. As a result, even though some fine-grained pyrite may have formed due to post-diagenetic cleavage replacement (Perkins 1998; Perkins and Bell 1998), Py-0 should not *per se* be linked to a hydrothermal pyrite halo around the deposit (cf. Broadbent et al. 1998; Perkins 1998).

Overall, the $\delta^{34}S$ values of hydrothermal pyrite at the George Fisher deposit encompass a range similar to those of other CD-type deposits in the Carpentaria province (e.g., McArthur River; Fig. 2-10). Nevertheless, there is no evidence of any fine-grained, interstitial sphalerite cement at George Fisher, which in other deposits (e.g., McArthur River) has been interpreted to have formed during the earliest stages of sedimentation and diagenesis (Large et al. 1998). The key difference between the CD-type deposits of the northern and southern Carpentaria province is the much higher degree of deformation in the south, which has been interpreted to be responsible for recycling of reduced sulphur and the formation of high-grade ore zones in deposits of the Mount Isa inlier (e.g., Grondjis and Schouten 1937; Solomon 1965; Chapman 1999).

In the Mount Isa inlier deposits, it has been proposed that (1) ore-stage breccias formed during metamorphic modification of earlier sulphides (Chapman 2004) and that (2) increased abundance of pyrrhotite is due either to a higher metamorphic grade or to higher temperatures associated with later Cu ore formation (Large et al. 2005). At the George Fisher deposit, the bulk of the pyrite, sphalerite, and galena mineralization is restricted to stratabound veins (ore-stage 1) and breccias (ore stages 2 and 3). The pyrrhotite from both ore-stages 2 (Pb-Zn) and 3 (Cu) formed in response to changes in temperature, sulphur activity, and oxygen fugacity during hydrothermal activity (Fig. 2-11). Replacement textures and intermediate $\delta^{34}S$ values of pyrite (Py-2) in ore-stage 2 at the George Fisher deposit also provide evidence for sulphur recycling during the formation of high-grade ore zones.

The controls on fluid flow during ore formation are not well constrained at George Fisher; however, the proposed role of TSR is similar to the model proposed for

the Century deposit (see Broadbent et al. 1998; Broadbent 2002). At Century, TSR caused by reaction of hydrocarbons in the host rock with a hot, metal-bearing hydrothermal fluid coincident with the onset of basin inversion has been interpreted to be the responsible sulphate reduction process for stratabound ore formation (Broadbent et al. 1998). This interpretation may also be applied to George Fisher, where the mineralization both occurs in organic-rich rocks with altered hydrocarbons (Chapman 1999) and shows a fractionation of sulphur isotopes in ore-stage 1 similar to the H_2S produced via TSR in natural gas reservoirs (e.g., Cai et al. 2003; Zhu et al. 2005). Therefore, pre-existing pyrite, combined with sulphides formed via TSR, are most likely important parameters for ore formation at George Fisher, both by providing a source of reduced sulphur and by focusing deformation due to the rheological contrast with the host rock (Chapman 2004).

2.7. Conclusions

The formation of pre-ore, fine-grained pyrite, both in samples from the George Fisher deposit and an unmineralized sequence of the host rock from the Urquhart Shale Formation, preserves a record of open-system MSR during the late Paleoproterozoic. This fine-grained pyrite is morphologically and isotopically similar to pyrite that formed in Paleoproterozoic strata throughout the Carpentaria province and is a feature of the broader paleoenvironment in which the host rock was deposited. The formation of hydrothermal sulphide mineralization at George Fisher occurred during three distinct stages, which involved TSR and replacement of pre-existing sulphides under increasing temperatures and reduced oxygen fugacities. There is no evidence for any early formed syn-sedimentary sphalerite mineralization, which is more commonly described in deposits from the northern Carpentaria province. Instead, the George Fisher deposit may have formed during the onset of basin inversion, with stratiform ore formation (ore-stage 1) postdating the formation of fine-grained early diagenetic pyrite (Py-0) yet predating the onset of deformation of the Urquhart Shale Formation. Indeed, existing models for Zn-Pb deposits in the southern Carpentaria province involve ore formation from hydrothermal fluids driven by basin inversion, which may have occurred due to east-west crustal shortening associated with supercontinent assembly. Despite the

contrast in the overall timing of mineralization for different genetic models, $\delta^{34}S$ values preserved by the combined pre-ore and ore-stage sulphide assemblages are broadly comparable across the different Carpentaria Zn-Pb-Ag deposits, highlighting the importance of *in situ* microanalysis to provide additional context for rigorously interpreting sulphur isotope data.

2.8. Acknowledgments

We would like to thank the geology teams at Mount Isa Mines George Fisher operation and Mount Isa Mines Resource Development for support during field work and for access to drill cores. Funding for this project was provided by a Helmholtz recruitment initiative grant to S. Gleeson. Furthermore, we acknowledge U. Dittmann and E. Lewerenz for sample preparation; O. Appelt, S. Mayanna, I. Schöppan, and F. Wilke for assistance with BSE imaging; and F. Couffignal for his technical support in the SIMS laboratory at GFZ Potsdam. Thoughtful and thorough reviews by J. Slack and R. Large significantly improved the manuscript and are greatly appreciated. Moreover, we would like to thank L. Meinert for editorial handling of the manuscript.

3. Lithogeochemical and mineralogical footprint of the George Fisher deposit, Australia

The mineralogical and lithogeochemical footprint of the George Fisher Zn-Pb-Ag massive sulphide deposit in the Proterozoic Urquhart Shale Formation, Queensland, Australia

Rieger P.[1,2], Magnall J.M.[1], Gleeson S.A.[1,2], Schleicher A.M.[1], Bonitz M.[1,3] Lilly R. [4]

[1]GFZ German Research Centre for Geosciences, Telegrafenberg, 14473 Potsdam, Germany
[2]Freie Universität Berlin, Institute for Geological Sciences, Malteserstraße 74-100, 12249 Berlin, Germany
[3]University of Potsdam, Institute of Earth Sciences, Karl-Liebknecht-Straße 24/25, 14476 Potsdam, Germany
[4]School of Earth and Environmental Sciences, University of Adelaide, Adelaide, South Australia 5005, Australia

This chapter is the submitted version of a manuscript that is now published in Chemical Geology (2021) vol. 560, article 119975.
https://doi.org/10.1016/j.chemgeo.2020.119975

3.1. Abstract

The Proterozoic Carpentaria Province (McArthur basin and Mount Isa Inlier) in northern Australia comprises a number of world class clastic dominated (CD-type) Zn-Pb massive sulphide deposits, formally known as SEDEX deposits. In order to identify the geochemical footprint of any mineralizing system it is necessary to characterize compositional variability of the host-rock to mineralization. In the southern Carpentaria, establishing the baseline composition of the host rock is complicated by varying degrees of tectonic overprint, a lack of metamorphic indicator minerals, and the overall size of the ore forming systems. In this study, samples from drill-holes intersecting the main ore bodies at the world class George Fisher CD-type massive sulphide deposit have been compared to samples from a drill-hole intersecting barren, correlative lithologies of the Urquhart Shale Formation (ca. 1654 Ma). Bulk rock lithogeochemical (X-ray fluorescence, inductively coupled plasma mass spectrometry and LECO) and mineralogical (X-ray diffraction) analyses have been combined with petrographic observations to (1) establish the baseline composition of the Urquhart Shale Formation and (2) determine the geochemical and mineralogical footprint of the CD-type system at George Fisher. The absence of metamorphic indicator minerals, combined with the preservation of illite in unmineralized Urquhart Shale, suggests that in this part of the Mount Isa area, the host rocks did not reach greenschist facies conditions (>300 °C). Chlorite in the unmineralized Urquhart Shale is very fine grained (≤ 10 μm) within interstitial pore spaces with other phyllosilicates (e.g., illite), and is interpreted to be diagenetic in origin. Relative to the unmineralized Urquhart Shale, the first stage of sulphide mineralization (Zn-dominated, stratabound) at George Fisher is associated with decreased abundances of albite, chlorite, and calcite, and higher abundances of dolomite and phyllosilicates (muscovite and phlogopite). These mineralogical transformations are associated with strong minor and trace element depletion (Sr and Na) and enrichment (Tl and Mn). An element index based on this suite of elements (GF index = 10((400Tl+Mn)/(10Sr+Na))) is highly effective in differentiating between the background Urquhart Shale Formation and the alteration footprint at George Fisher and may provide an additional tool for geochemical exploration

programmes in the Mount Isa area. This study affirms the benefit of combining lithogeochemical, mineralogical, and petrographic data in order to understand the host rock baseline composition and the alteration footprint of Carpentaria CD-type massive sulphide systems.

3.2. Introduction

The Proterozoic Urquhart Shale Formation is host to three world class base metal deposits (Mount Isa, Hilton, and George Fisher), which collectively have a pre-mining resource of >370 Mt (10 wt. % Zn, 5.6 wt. % Pb, and 120 g/t Ag; Large et al. 2005). These clastic dominant (CD-type) deposits, formerly known as sedimentary exhalative (SEDEX) deposits, have accounted for a significant proportion of global Zn and Pb production and have been crucial in satisfying demand of these base metals for the global economy (Leach et al. 2005, 2010). Future demand will only be met through the discovery of new CD-type Zn-Pb massive sulphide deposits, although exploration models are currently limited by an incomplete understanding of the geochemical and mineralogical footprints of the Carpentaria CD-type deposits.

The Mount Isa, Hilton, and George Fisher deposits are located in close proximity (ca. 20 km) in the Mount Isa Inlier, which is broadly time correlative with the McArthur basin (both basins comprise the Carpentaria Zn Province; Fig. 3-1). The tectonic and metamorphic gradient increases towards the south of the Carpentaria Province, which has resulted in considerable debate over the genetic model for the Carpentaria CD-type deposits; specifically, debate has mostly focused on the relative contribution of sedimentary exhalative (SEDEX; e.g., Lambert and Scott 1973; Large et al. 1998), subseafloor diagenetic replacement processes (e.g., Eldridge et al. 1993; Painter et al. 1999; Chapman 2004), or syn-deformational replacement (e.g., Perkins 1997; Perkins and Bell 1998; Cave et al. 2020).

The host rock to the Carpentaria deposits can be broadly characterized as a fine-grained, variably pyritic and dolomitic carbonaceous siltstone (Leach et al. 2005, 2010). Fine-grained siliciclastic rocks often appear to be relatively homogenous at the hand specimen scale, but they can preserve considerable compositional heterogeneity due to

the variability of detrital, biogenic and authigenic components (e.g., Vine and Tourtelot 1970; Aplin and Macquaker 2011).

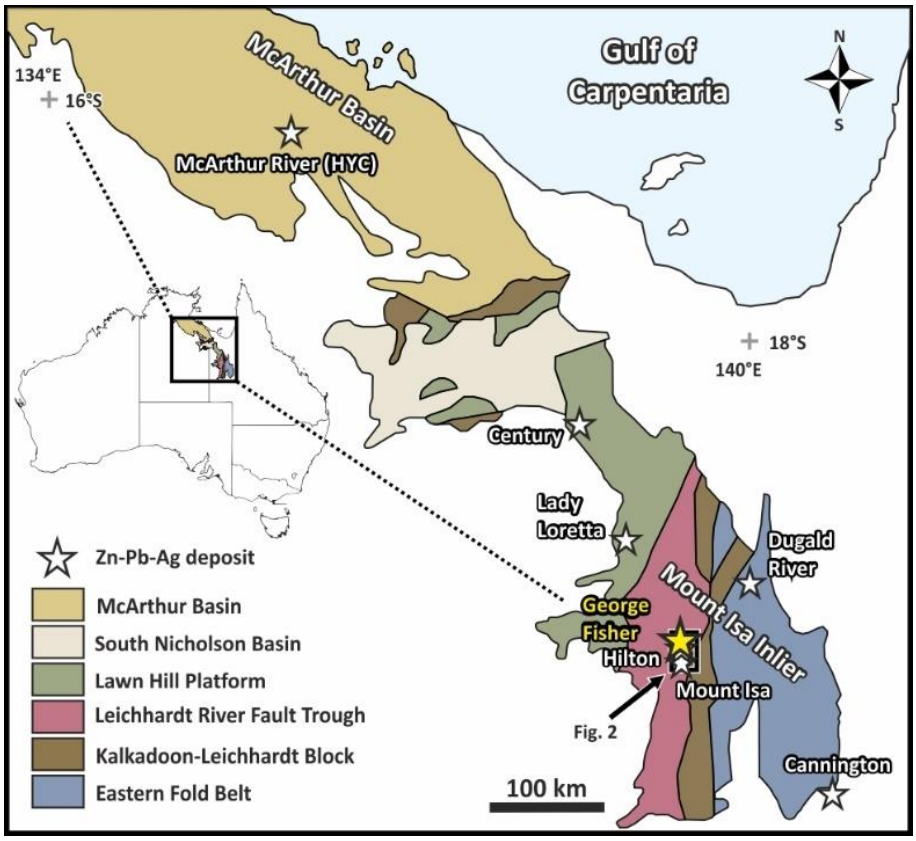

Fig. 3-1 Tectono-stratigraphic map of the Mount Isa Inlier and the McArthur basin with major Zn-Pb-Ag deposits marked by asterisks (Jackson et al. 2000; Gibson et al. 2017). The black rectangle indicates the Mount Isa region shown in Figure 3-2.

Published lithogeochemical alteration models for the Carpentaria deposits have so far mostly been informed by the SEDEX model. For example, the enrichment of several elements (Co, Fe, Tl, Zn, Pb, and Mn) in dolomite and pyrite in correlative stratigraphy to the McArthur River and Lady Loretta deposits has been linked with dispersion of trace elements into seawater following hydrothermal venting (Lambert and Scott 1973; Large and McGoldrick 1998; Large et al. 2000). As a result, a number of element ratios and threshold values have been proposed to vector laterally towards CD-type massive sulphide systems in the Carpentaria province (Tab. 1).

Tab. 1 Alteration indices and element ratios for the Carpentaria Province.

Element abundance / alteration index	Formula	Threshold	Reference
Relative abundance of Co and Ni	Co/Ni	>1	Lambert and Scott (1973)
Widely dispersed trace metal enrichment	Tl, Pb and Zn	Tl >4 ppm, Pb >100 ppm, Zn >1,000 ppm	Large and McGoldrick (1998)
SEDEX metal index (SEDEX MI)	Zn + 100Pb + 100 Tl	>10,000	Large and McGoldrick (1998)
Manganese content of dolomite (MnO_d)	(MnO x 30.41)/CaO	>1.0 wt%	Large and McGoldrick (1998)
SEDEX alteration index (SEDEX AI)	$\frac{100(FeO + 10\,MnO)}{FeO + 10MnO + MgO}$	>60	Large and McGoldrick (1998)
SEDEX alteration index 3 (AI mark 3)	$\frac{100(FeO + 10\,MnO)}{FeO + 10MnO + MgO + Al_2O_3}$	>30	Large et al. (2000)
SEDEX alteration index 4 (AI mark 4)	$\frac{100(FeO + 10\,MnO)}{FeO + 10MnO + MgO + 0.1 * SiO_2}$	-	Large et al. (2000)
Isa vector	$\frac{Tl(FeO_{dol} + 10\,MnO_d)}{Ge}$	-	Painter (2003)

One of the major caveats of existing alteration indexes is a sensitivity to compositional variability that is inherent to the host rock (Large et al. 2000). The challenge, therefore, is to develop alteration models that are able to discriminate between compositional heterogeneity that is inherent to background processes (detrital, diagenetic, metamorphic) and those derived from hydrothermal input. In the deposits of the deformed Mount Isa Inlier, establishing a baseline protolith composition is complicated by (1) the varying degrees of tectonic overprint, (2) the lack of indicator minerals to constrain metamorphic grades, and (3) the enormous size of the mineralizing systems (e.g., Painter et al. 1999). These three aspects limit the availability of suitable correlative protolith lithologies, which are fundamental for developing geochemical and mineralogical exploration models.

In this study, we report bulk rock lithogeochemical and mineralogical data from (1) drill core samples through the main ore bodies at the George Fisher deposit (165 Mt at 9.1 % Zn, 3.4 % Pb, and 55 g/t Ag; Glencore 2019) and (2) from a correlative, barren drill core through mudstones and siltstones of the Urquhart Shale Formation (Shovel Flats drill-hole), which is the host rock to the George Fisher, Hilton (now mined in one operation with George Fisher) and Mount Isa deposits. We present a suite of compositional and mineralogical data using X-ray fluorescence (XRF; major elements),

inductively coupled plasma mass spectrometry (ICP-MS, minor and trace elements), LECO (total organic carbon and sulphur) and X-ray diffraction (XRD; mineralogy) analyses. In combination with petrographic observations, we have evaluated the baseline lithological and compositional variability within the Urquhart Shale Formation and investigated the mass transfer and mineralogical transformations that may have been associated with ore formation and contributed to the alteration footprint in this part of the George Fisher deposit.

3.3. Geological background

3.3.1. Mount Isa Inlier, McArthur basin and superbasin cycles

The Mount Isa Inlier and McArthur Basin formed in an intracontinental setting during the Paleo- to Mesoproterozoic (Fig. 3-1; Betts et al. 2002, 2016; Giles et al. 2002). Basin formation was initiated during the late Paleoproterozoic (ca. 1790 Ma) and was followed by several episodes of rifting, sag phases and inversion, which are recorded by sedimentary rocks that can be separated into 3 unconformity bound superbasin sequences (Leichhardt Superbasin, Calvert Superbasin and Isa Superbasin; Southgate et al. 2000; Giles et al. 2002; Gibson et al. 2016). Basin closure then corresponded with the onset of the Isan orogeny (ca. 1600 Ma; Page et al. 2000).

Based on lithostratigraphic and chronostratigraphic correlations, these superbasins sequences are further subdivided into 12 correlated supersequences (e.g., Jackson et al. 2000; Page et al. 2000; Southgate et al. 2013). The Calvert and Isa Superbasins, which host the Mount Isa, George Fisher – Hilton, Lady Loretta, McArthur River and Century deposits, consist of the Big and Prize Supersequences (Calvert Superbasin; Southgate et al. 2000) and the Gun, Loretta, River, Term, Lawn, Wide and Doom Supersequences (Isa Superbasin; Southgate et al. 2000). In the Mount Isa area, there has been debate over whether the host rocks to the Mount Isa and George Fisher – Hilton deposits (Fig. 3-2; Gun Supersequence) belong to the Isa Superbasin (Southgate et al. 2000) or to the Calvert Superbasin (Gibson et al. 2016).

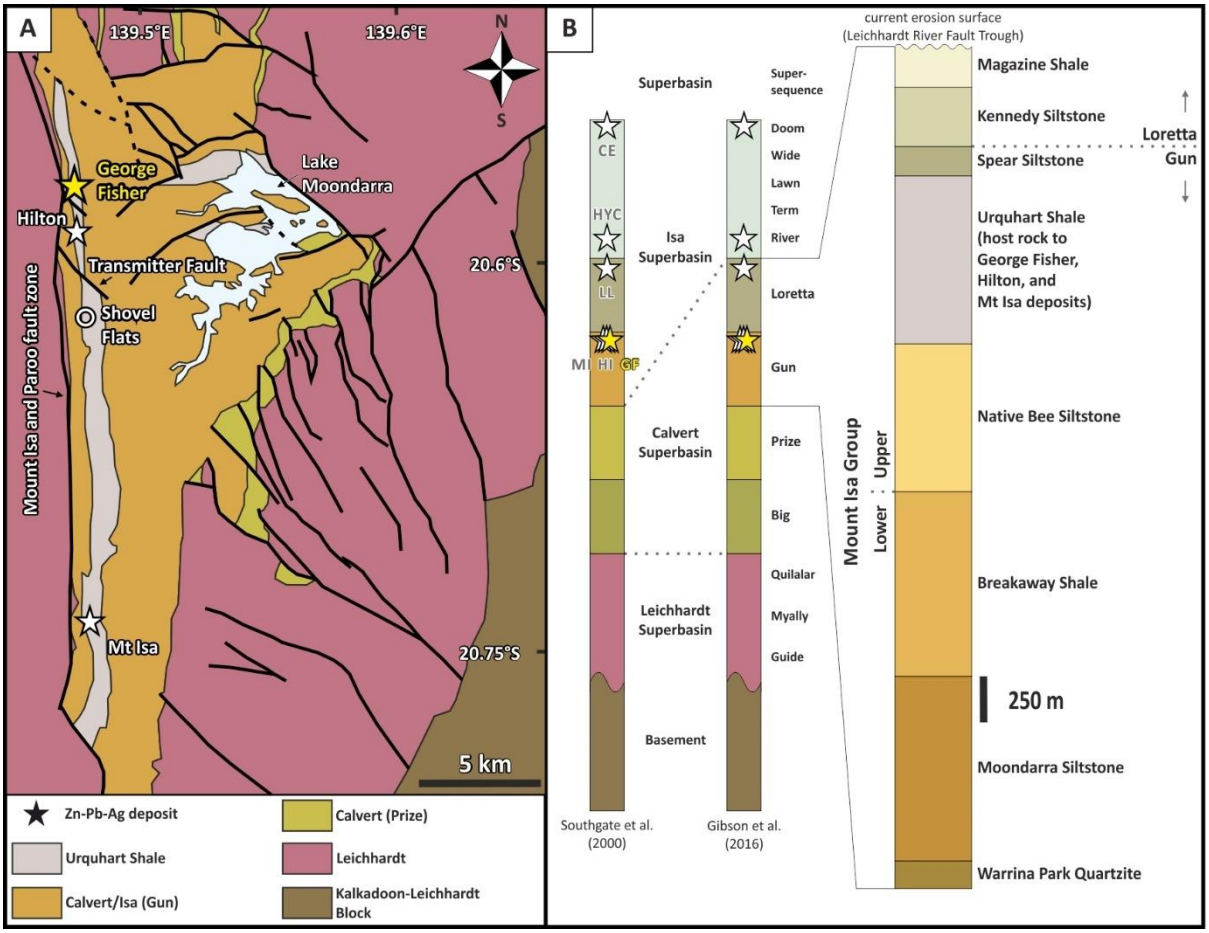

Fig. 3-2 (A) Geological map of the Leichhardt River Fault Trough in the Mount Isa area (after Gibson et al. 2016, 2017). The Mount Isa, Hilton, and George Fisher deposits and Shovel Flats drill-hole are marked by asterisks and a circle respectively. (B) A stratigraphic chart for the Mount Isa Inlier showing superbasins and supersequences (after Southgate et al. 2000; Gibson et al. 2016). The approximate stratigraphic locations of the Mount Isa (MI), Hilton (HI) George Fisher (GF), Lady Loretta (LL), and Century (CE) Zn-Pb-Ag deposits are denoted by asterisks. In the Mount Isa area, the Gun and Loretta supersequences are represented by the Mount Isa Group, which is subdivided into the upper and lower Mount Isa Group with approximate formation thickness adapted from Neudert (1983).

3.3.2. Mount Isa Group

The Mount Isa Group comprises a series of fine-grained, clastic sedimentary rock formations that belong to both the Gun and Loretta Supersequences (Fig. 3-2B). Sedimentation was interpreted to have occurred during transgressive and highstand conditions on a gently inclined shelf in the Leichhardt River Fault Trough, which resulted in deposition of siliciclastic and carbonate facies (Southgate et al. 2013). The formations of the Mount Isa Group can be further separated into the Lower and Upper Mount Isa Group by an unconformity between the Breakaway Shale and the Native Bee Siltstone (Fig. 3-2; van den Heuvel 1969; Mathias and Clark 1975). There is an overall

decrease in grain size through the Lower Mount Isa Group, with near-shore deposition of conglomerates and sandstones of the Warrina Park Quartzite transitioning to finer-grained deeper water siltstones and mudstones of the Moondarra Siltstone and Breakaway Shale (Derrick 1974; Mathias and Clark 1975; Domagala et al. 2000). The Upper Mount Isa Group (Fig. 3-2B) is composed mainly of siltstones and mudstones, which are mostly thinly bedded and comprise dolomite, quartz, K-feldspar, albite, muscovite, phlogopite and chlorite with minor calcite, pyrite, siderite, tourmaline, zircon, rutile and carbonaceous matter (Neudert 1983).

3.3.3. Urquhart Shale Formation

The Urquhart Shale Formation mostly comprises laminated to bedded siltstones and mudstones and has a gradational contact with the underlying Native Bee Siltstone Formation and the overlying Spear Siltstone Formation (Bennett 1965; Neudert 1983). The Urquhart Shale is siliceous to dolomitic, variably pyritic and carbonaceous and can generally be distinguished from the Native Bee Siltstone and Spear Siltstones by a much higher abundance of pyrite (Neudert 1983). The depositional ages of the Urquhart Shale Formation at the Mount Isa and George Fisher-Hilton deposits have been determined via U-Pb dating of zircons from interbedded tuff beds (1652 ± 7 Ma and 1654 ± 5 Ma respectively; Page and Sweet 1998; Page et al. 2000).

Several sedimentary facies have been identified in the Urquhart Shale Formation, which have generally been linked to sabkha or playa environments and emergent to semi-emergent conditions in the lower Urquhart Shale and a more distal, carbonate slope to basin environment in the upper Urquhart Shale (Neudert 1983). Further facies analysis refined this model and identified three dominant sedimentary facies in the Urquhart Shale Formation (Painter et al. 1999; Painter 2003): (1) a rhythmite facies, comprising fining-upwards sequences of interlaminated mudstones and siltstones, with abundant nodular carbonates as pseudomorphs after sulphate evaporites in the siltstones; notably, this facies comprises the bulk of the Zn-Pb mineralization at the Mount Isa deposit; (2) a carbonate cemented siltstone facies, which consists mostly of barren, massive calcareous and dolomitic siltstones with minor mudstones; and (3) cross-laminite facies, comprising cross-laminated siltstones and fine sandstones with

minor mudstones. Based on these sedimentary facies, the overall depositional environment of the Urquhart Shale was interpreted to resemble sedimentation on a carbonate slope proximal to a saline mudflat or sabkha environment (Painter 2003). Alternatively, sedimentary features, which were previously interpreted to represent evaporitic processes (e.g., nodular carbonates), were interpreted as diagenetic precipitates and overall the Urquhart Shale was considered to have been deposited as rhythmites in a deeper water environment (Domagala et al. 2000).

Previous lithogeochemical studies on the Urquhart Shale Formation have focused on drill core samples from between the Mount Isa deposit and the Transmitter Fault (Painter 2003; Fig. 3-2). Painter (2003) suggests that the Urquhart Shale is generally depleted in silicate-associated elements (Si, Al, Ti, Na, ± K) and enriched in carbonate-associated elements (Ca, Mg, Mn, ± Fe) relative to Post-Archean-Australian-Shale (PAAS; Nance and Taylor 1976). Furthermore, this author suggests that late diagenetic Zn-Pb mineralization has resulted in the enrichment (Mn, Fe, Pb, Zn, Ag, Tl, Ge, S, Cd, As, and Sb), depletion (Ca, Mg, Na, and Sr), and dilution (Si, Ti, Al, K, Zr, and Y) of several elements from un-/weakly-mineralized Urquhart Shale to the Mount Isa deposit. Based on these element changes, an alteration vector was formulated, which results in increasing values towards the Mount Isa deposit (Isa vector; Tab. 1; Painter 2003). The mineralogical changes towards the Mount Isa deposit were reported to be preserved by higher abundances of sulphide (pyrite, sphalerite, galena, and pyrrhotite) and ferromanganese carbonate minerals (dolomite and ankerite) relative to un-/weakly-mineralized Urquhart Shale (Painter 2003).

3.3.4. Deformation and Metamorphism of the western Mount Isa Inlier

The Mount Isa Inlier has been affected by multiple stages of deformation and varying degrees of metamorphism (Blake 1987). During the Isan orogeny (ca. 1610 to 1510 Ma), polystage deformation resulted in folding and faulting, and peak metamorphic conditions (sub-greenschist to amphibolite facies) have been constrained to the first phase of E-W compression (Page and Bell 1986; Connors and Page 1995; Bell and Hickey 1998). In the Mount Isa and George Fisher area, the highest metamorphic grades (greenschist to amphibolite facies) are located west of the Mount Isa – Paroo Fault Zone

and east of the Sybella batholith (ca. 1670 Ma; Page and Bell 1986; Wyborn et al. 1988; Connors and Page 1995). In the uppermost section of the Eastern Creek Volcanics, which are located in the footwall of the Paroo Fault at the Mount Isa deposit, temperatures of 325 °C ± 50 °C were reached during regional metamorphism (Hannan et al. 1993). There is a sharp contrast in metamorphic grade (amphibolite to sub-greenschist conditions) from uplifted rocks west of the Mount Isa – Paroo Fault zone to the sedimentary rocks of the Mount Isa Group in the east of the fault zone, where a lack of metamorphic indicator minerals complicate the determination of metamorphic grades (Valenta 1994). The only proposed metamorphic indicator minerals in the Mount Isa Group are chlorite (Wilson 1972; Rubenach 1992) and stilpnomelane (Heinrich et al. 1989), which would indicate lower greenschist metamorphic conditions. Hydrothermal chlorite is also part of the alteration assemblage associated with high temperature Cu-mineralization at George Fisher, Hilton, and Mount Isa (Fig. 3-3; Valenta 1988; Waring 1990; Chapman 1999; Cave et al. 2020). There are fewer temperature constraints for the unmineralized Urquhart Shale Formation, but bitumen reflectance and illite crystallinity indicate maximum burial temperatures of ca. 200 °C (McClay 1979; Chapman 1999), which are significantly lower than greenschist metamorphic conditions (≥300 °C; Fig. 3-3).

3.3.5. George Fisher Deposit

The George Fisher deposit is located approximately 20 km north of Mount Isa (Fig. 3-2). The ore bodies are hosted by mudstones and siltstones of the Urquhart Shale Formation. There are 9 ore domains (A to I, Fig. 7-3), which are further subdivided into unmineralized domains of barren mudstones and siltstones, weakly mineralized domains, and the main Zn-Pb ore bodies. Multiple generations of sulphides have been described at the George Fisher deposit (Chapman 1999, 2004; Murphy 2004; Rieger et al. 2020), which are broadly sub-divided into (0) fine-grained pyrite, (1) stratabound sphalerite + pyrite ± galena, (2) breccia-hosted galena + sphalerite + pyrite + pyrrhotite and (3) vein and breccia-hosted pyrite + pyrrhotite + chalcopyrite ± galena and sphalerite.

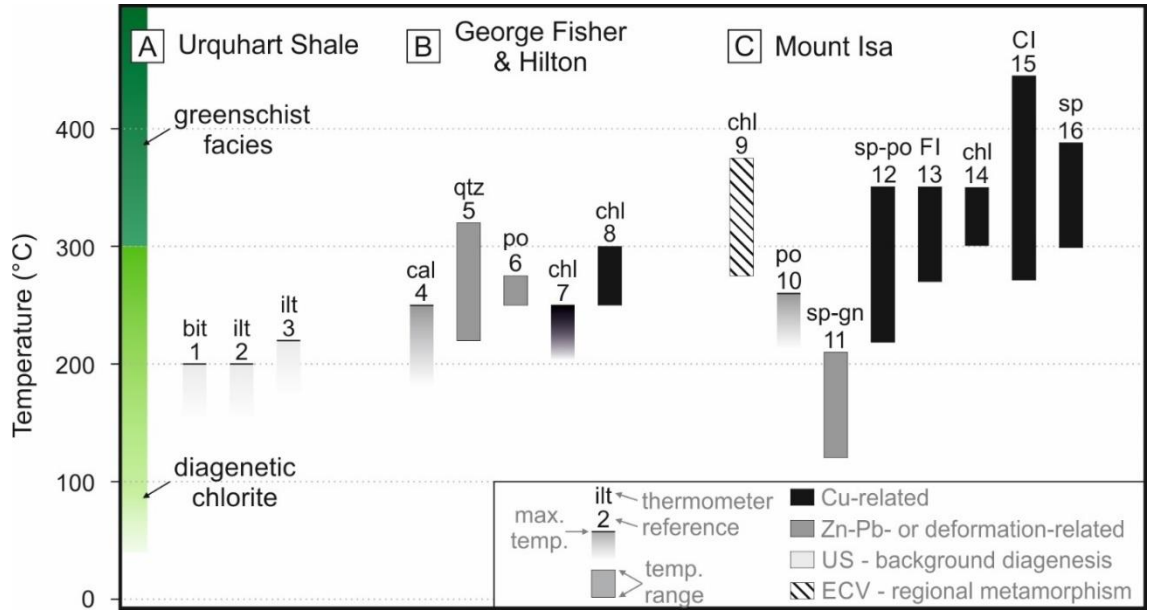

Fig. 3-3 Temperature constraints for (A) the Urquhart Shale Formation, (B) the George Fisher and Hilton deposits, and (C) the Mount Isa deposit. The green bars indicate temperatures of diagenetic chlorite formation and of greenschist facies metamorphic conditions. Individual temperature constraints are derived from: (1) bitumen reflectance (Chapman 1999), (2) illite crystallinity (McClay 1979), (3) maximum burial temperature derived from clay fraction analysis (this study), (4-6) calcite twinning, fractal analysis of quartz and from pyrrhotite twinning (Murphy 2004), (7) alteration associated with Cu-mineralization derived from chlorite stability (Chapman 2004), (8) alteration associated with Cu-mineralization derived from chlorite stability (Valenta 1988), (9) regional metamorphism in the Eastern Creek Volcanics derived from chlorite-quartz isotopic equilibrium (Hannan et al. 1993), (10) crystal structure of pyrrhotite (van den Heuvel 1969), (11-12) temperature of Zn-Pb and Cu mineralization derived from sphalerite-galena and sphalerite-pyrrhotite S-isotope equilibrium respectively (Painter et al. 1999), (13) fluid inclusion homogenization temperatures in Cu mineralization (Heinrich et al. 1989), (14) chlorite alteration associated with Cu-mineralization (Waring 1990), (15) clumped isotopes in carbonates associated with Cu-mineralization (Mering et al. 2018), and (16) sphalerite thermometry (Cave et al. 2020). Temperature constraints are grouped by their relationship to regional metamorphism (Eastern Creek Volcanics), diagenesis (Urquhart Shale), Zn-Pb mineralization, deformation, or Cu-mineralization.

There are different genetic models for the mineralization at George Fisher. For example, Murphy (2004) interpreted structural and paragenetic data to suggest a late stage, syn-tectonic (D4) origin for the mineralization at temperatures of 200-300 °C (Fig. 3-3). In contrast, a combination of paragenetic data, Pb-model ages, and metal distributions have been interpreted to support a model in which the bulk of the Zn-Pb mineralization at George Fisher and Hilton formed syn-diagenetically and pre-deformation, with Cu (± Zn-Pb) mineralization linked to a later hydrothermal event (e.g., Valenta 1994; Chapman 1999, 2004). The latter model is supported by more recent work that reported *in situ* sulphur isotope analyses of pyrite (Rieger et al. 2020), which interpreted: 1) formation of fine-grained pyrite by microbial sulphate reduction during

early diagenesis (pre-ore); 2) stratabound Zn mineralization (ore stage 1) during burial diagenesis with S derived from thermochemical sulphate reduction (TSR), and; 3) later Zn-Pb (ore stage 2) and Cu (ore stage 3) mineralization, with reduced sulphur derived from recycling of earlier sulphides and TSR. Precise constraints for the timing of individual ore forming events are, however, lacking and structural observations can be interpreted in support of a variety of relative timings (cf. contrasting interpretations by Chapman 1999, 2004, and Murphy 2004). Nonetheless, there is general agreement that Cu-mineralization at the George Fisher deposit is paragenetically late and was associated with the highest temperature hydrothermal event (see references in Fig. 3-3).

Multiple phases have been linked to alteration at the George Fisher deposit, including ferroan dolomite, quartz, K-feldspar, pyrite, hydrophlogopite, and Ba(-K)-feldspar (Chapman 1999, 2004). Zones of intense Ba(-K)-feldspar alteration were reported in the deeper parts of the deposit and Ba was interpreted to be derived from the hydrothermal fluid (Chapman 1999). In contrast, Painter (2003) suggested that Ba-feldspar formed due to diagenetic replacement and pseudomorphism of carbonate and feldspar after barite in the unmineralized Urquhart Shale near Mount Isa. Later syn-tectonic Cu-mineralization at George Fisher was associated with siderite, ferroan ankerite, biotite, chlorite, muscovite and magnetite alteration (Chapman 1999, 2004). Unlike other deposits of the Carpentaria Province (e.g., Lady Loretta, Large and McGoldrick 1998; McArthur River, Large et al. 2000; Mount Isa, Painter 2003; Century, Whitbread 2004) there has been no previously published investigation of the bulk rock lithogeochemistry at George Fisher.

3.4. Methods and Samples

3.4.1. Sampling and petrography

A total of 91 representative samples were selected from the Shovel Flats drill core, which intersects ca. 900 m of the unmineralized Urquhart Shale Formation (Fig. 3-2, Fig. 7-4). A total of 225 samples were taken from 4 drill-holes that intersected the main ore bodies at the George Fisher deposit (8C K751, n = 61; 10C K795, n = 77; 10C K798, n = 57; 12C I797, n = 30). Samples from the George Fisher deposit comprise representative examples from the main ore bodies, from weakly mineralized sections, and from barren

siltstones and mudstones between the ore bodies, and the hanging wall stratigraphy. Particular emphasis was given to sampling from drill-hole 10C K795, as it preserves 300 m of stratigraphy through the domains A-E and 100 m through unmineralized hanging wall Urquhart Shale (Fig. 3-4).

Petrographic examination of the samples was conducted using a desktop binocular microscope and key samples (n = 90) were selected for transmitted light and reflected light microscopy. A subset of 41 representative samples from the background drill-hole and 70 representative samples from the George Fisher deposit were then selected for X-ray diffraction and lithogeochemical analyses.

3.4.2. Bulk rock lithogeochemistry and mineralogy

The samples were crushed and powdered to a grain size of < 62 µm and whole rock geochemical analysis was carried out by Bureau Veritas Minerals (BVM) in Vancouver, Canada. Major, minor and trace element concentrations were analysed by ICP-MS of lithium borate fused rock powders. Trace metal concentrations (Mo, Cu, Pb, Zn, Ni, As, Cd, Sb, Bi, Ag, Au, Hg, Tl, and Se) were determined by ICP-ES/MS of aqua regia digested rock powders (upper detection limit for Zn and Pb = 10,000 ppm). Lithium borate fused samples with over limit Zn and Pb concentrations were analysed by X-ray fluorescence. Concentrations of total S, total C, TOC (total organic carbon), C_{gra} (graphitic carbon), and CO_2 were determined by a LECO analyser. Low total concentrations in some samples are due to incomplete combustion of sulphide minerals. In addition to internal measures (duplicates, blanks, and reference materials) for assessing accuracy and precision of the analyses at BVM, blanks (quartz sand) and blind reference materials were routinely run for data quality control. Analyses of the SBC-1 (n = 7) reference material (USGS) had median uncertainties of 1.2 % for element oxides and of 2.4 % for trace elements for certified values; median uncertainties for recommended values for ShBOQ-1 (USGS; n = 12) were 1.3 % and 4.2 % for element oxides and trace elements respectively. Median uncertainties for certified values were 1.0 % and 2.3 % for the massive sulphide standards (ORE Research & Exploration Pty Ltd) OREAS 131a (n = 3) and OREAS 134a (n = 3) respectively.

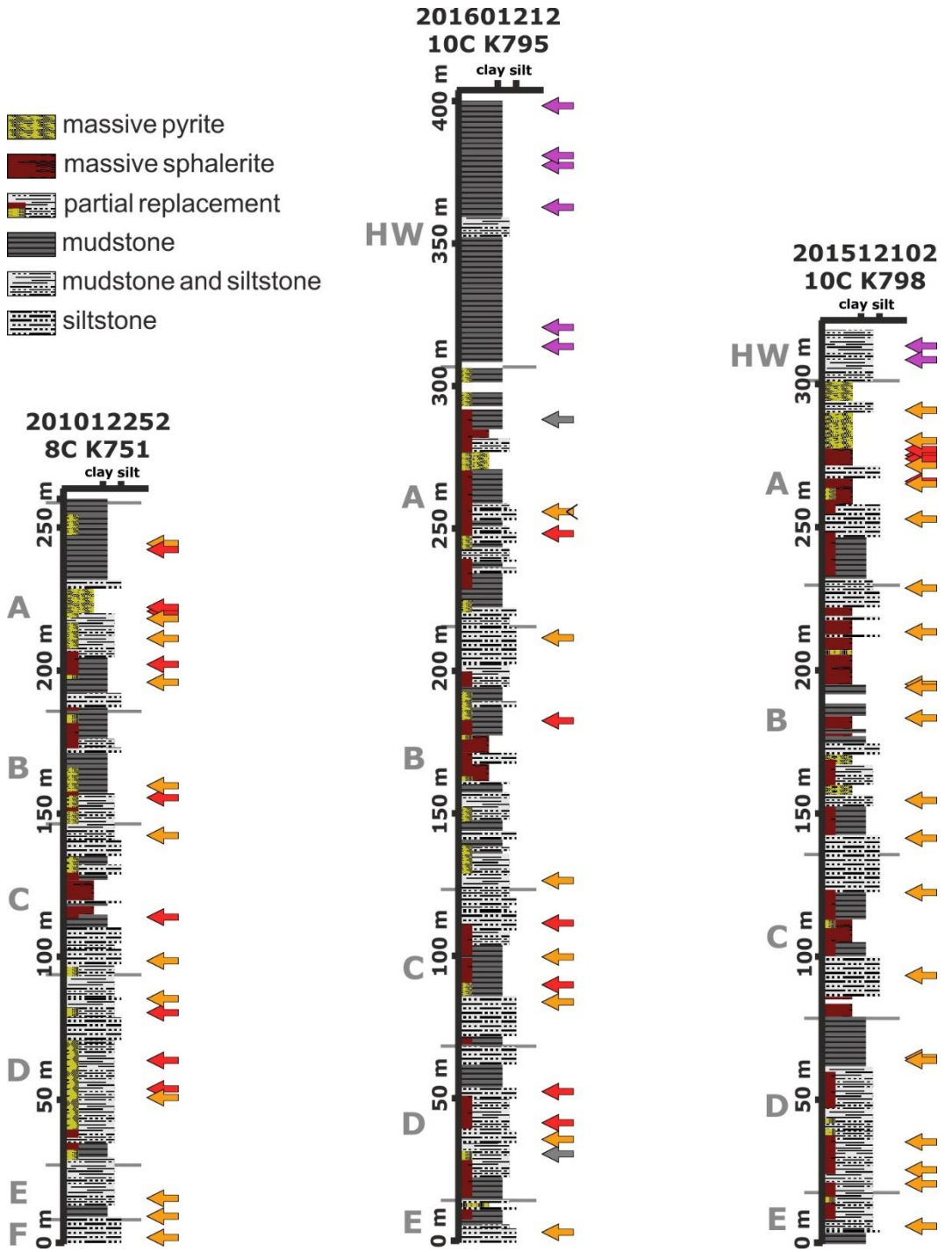

Fig. 3-4 Lithological logs of drill cores 8C K751, 10C K795 and 10C K798 from the George Fisher deposit. The drill-holes intersected mine nomenclature domains A-F (grey labels; George Fisher operations, Mount Isa Mines). The samples analysed in this study are hanging wall Urquhart Shale (purple), inter-mineralisation Urquhart Shale (orange) and massive sulphides (red).

Quantification of the bulk rock mineralogical composition was determined using a PANalytical Empyrean X-ray diffractometer (GFZ Potsdam). Splits of the lithogeochemistry samples were further homogenized to < 10 µm with a micronizing

mill. The measurements were performed at 40 mA and 40 kV with CuKα radiation and a step size of 0.013 °2Θ with 60sec/step from 4.6 to 75 °2Θ. The mineralogy was determined with the EVA software (version 11.0.0.3) by Bruker. Rietveld refinement for quantitative mineralogy was performed using the program BGMN and the graphical user interface Profex (Doebelin and Kleeberg 2015) calibrated for the used diffractometer. The uncertainty of the quantitative analyses is ≤ 3 wt.% for individual phases. High Pb and Zn concentrations in 7 samples resulted in overlapping signals between sphalerite and galena with carbonate mineral phases (calcite and dolomite) during Rietveld refinement resulting in an overestimation of carbonate concentrations (the mineralogical composition of these samples is not reported). To determine the pyrite abundance of these samples, Pyrite abundance was calculated on the basis of molar fractions of S, Pb, and Zn from the lithogeochemistry dataset. Therefore, sphalerite- and galena-bound S was subtracted from total S; these S values were then used to calculate the total S and Fe contained in pyrite. The clay-size (< 2 µm) fraction of Shovel Flats (n = 10) and George Fisher samples (n = 7) was prepared from separate rock chips that were mechanically crushed and separated following the analytical methods described by (Moore and Reynolds 1997). Air-dried and ethylene-glycol solvated oriented mounts were scanned from 2 ° to 35 ° at 0.01 °2Θ intervals.

3.4.3. Statistical analysis

The Gresens' method was used to quantify mass change between unaltered and altered samples. This analysis is based on the calculation of the *isocon*, which is defined by the ratio of immobile elements in the altered rock relative to its unaltered equivalent (Grant 1986). As summarised by Grant (2005), this ratio of immobile elements can be determined by using (1) the clustering of element ratios (concentration altered / concentration unaltered), (2) a best fit line (*isocon* line) through the origin and immobile elements in an *isocon* diagram (Grant 1986), (3) the pre-selection of immobile elements, or (4) the assumption of constant mass or constant volume during alteration processes.

For the graphical presentation of this method, major, minor and trace element concentrations have to be arbitrarily scaled in order to plot on one graph. As a result of

arbitrary scaling the apparent distance of an element to the *isocon* is strongly dependent on the scaling factor (Humphris et al. 1998). To eliminate this scaling effect, a modified *isocon* diagram can be formulated by consistently scaling all the data to plot on a circle with distance of 1 to the origin (sums of squares of each element = 1; Humphris et al. 1998). In this modified *isocon* diagram, groups of elements that behave similarly (e.g., immobile elements) will group together on one segment of the circle. This may simplify the selection of immobile elements in order to define the *isocon* (zero mass change).

After determination of the immobile elements, the bulk mass loss or gain (ΔM, in percent) of the altered rock relative to the unaltered rock can be calculated using (e.g., Wilkinson et al. 2011):

$$\Delta M = 100 * \left[\frac{c_{i\_altered} - c_{i\_un-altered}}{c_{i\_altered}}\right]$$

where $c_{i\_altered}$ and $c_{i\_unaltered}$ are the concentrations of one or multiple immobile elements in the altered and unaltered rock respectively. Furthermore, the addition or loss of an element (ΔE, in percent) in the altered sample relative to the unaltered sample is given by:

$$\Delta E = 100 * \left[\frac{c_{altered}}{\left(\frac{c_{i\_altered}}{c_{i\_un-altered}}\right) * c_{un-altered}} - 1\right]$$

where $c_{altered}$ and $c_{unaltered}$ are the concentrations of an element in the altered and unaltered sample respectively.

In this study the immobile elements were determined by combining the modified graphical approach developed by Humphris et al. (1998) and the clustering of element ratios (Grant 2005). Only elements that group together using both methods for both precursor sub-groups were considered immobile, which was further evaluated using the chemical index of alteration (Nesbitt and Young 1982). Immobile element ratios were then used to calculate median values, mean values and standard deviations for the *isocon*. To account for any compositional heterogeneity inherent to the unmineralized Urquhart Shale samples, only elements with a slope greater or smaller than two standard deviations of the *isocon* were considered to be either enriched or depleted at the George

Fisher deposit. To avoid overestimation of median values by removing below detection limit data, these data were imputed as 0.5 * detection limit values (e.g., Na2O, detection limit = 0.01 wt.%, value imputed for data below detection limit = 0.005 wt.%).

3.5. Results

3.5.1. Lithological logs

The Shovel Flats drill core preserves a long section of unmineralized Urquhart Shale Formation (ca. 900 m). The upper 300 m of the drill-hole intersected a deep regolith profile and only 300 to 900 m are shown in Fig. 7-4. The Urquhart Shale Formation primarily comprises interbedded mud- and siltstone (Fig. 3-5) with intervals of massive siltstone, and thinner intervals of more homogenous mudstone, siltstone, or nodular carbonate. Nodular carbonate beds, which are typically ≤ 10 cm thick, are not resolved at the scale of logging (Fig. 7-4), and are typically interbedded with pyritic carbonaceous siltstones (Fig. 3-6). The carbonate nodules are up to several cm in the lateral dimension and ≤ 2 cm thick. The samples preserve no well-developed foliation or deformation fabric at the hand specimen or thin section scale, although there has been some localized deformation associated with discrete fractures or small shear zones.

The drill-holes from the George Fisher deposit intersected the same lithologies as at Shovel Flats (Fig. 3-4). The Urquhart Shale Formation between the intervals of massive sulphide mainly comprises interbedded mud- and siltstones and intervals with more homogeneous mudstones, siltstones, or nodular carbonates. In all 4 drill cores, the ore stage 1 mineralization is stratabound in mostly laminated, carbonaceous siltstones and in nodular carbonates. Subsequent ore stage 2 and 3 mineralization is more independent of lithology and commonly crosscuts several individual lithologies in massive ore breccias or ore veins. There is a minor fault followed by 100 m of hanging-wall stratigraphy to ore domain A preserved in drill core 10C K795, which consists mostly of homogeneous mudstone.

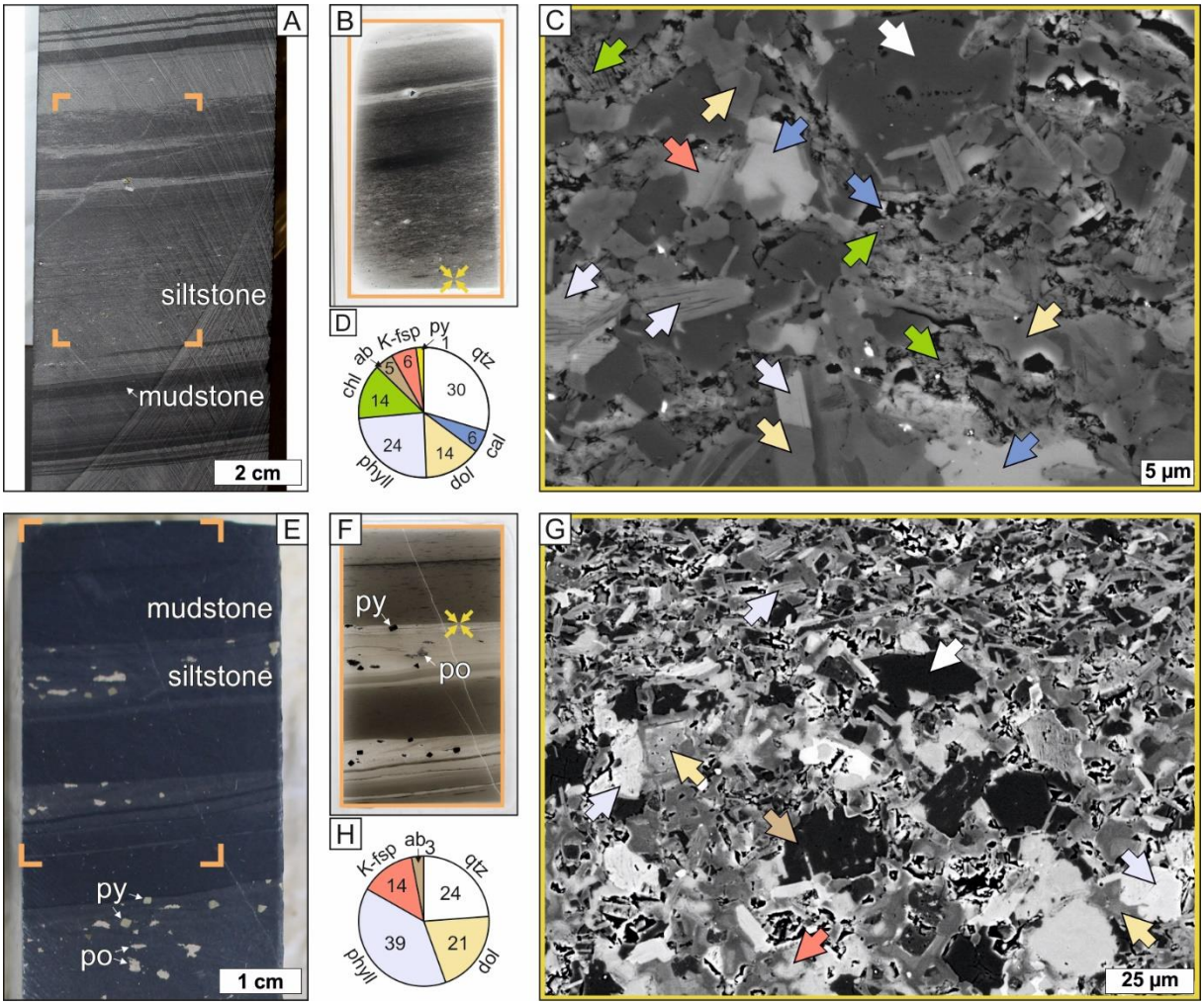

Fig. 3-5 (A-D) Interbedded mudstone and siltstone (sample PR832SF012) from Shovel Flats drill core. (A) Hand specimen photograph with mudstone (dark) and siltstone (grey); the orange rectangle indicates location of B. (B) Thin section photograph with mudstone and siltstone; the yellow arrows indicate the location of C. (C) Backscatter electron (BSE) image of siltstone; the arrows indicate individual mineral phases, see D for colour code. (D) Bulk-rock mineralogical composition (qtz = quartz, cal = calcite, dol = dolomite, phyll = phyllosilicate, chl = chlorite, ab = albite, K-fsp = K-feldspar, py = pyrite). (E-H) Interbedded mudstone and siltstone (sample PRK7952001) from drill core 10C K795. (E) Hand specimen photograph with mudstone (dark) and siltstone (grey) with pyrite and pyrrhotite; the orange rectangle indicates location of F. (F) Thin section photograph with carbonaceous mudstone and dolomitic siltstone; the yellow arrows indicate the location of G. (G) BSE image of dolomitic siltstone; the arrows indicate individual mineral phases, see H for colour code. (H) Bulk-rock mineralogical composition (qtz = quartz, dol = dolomite, phyll = phyllosilicate, K-fsp = K-feldspar, ab = albite).

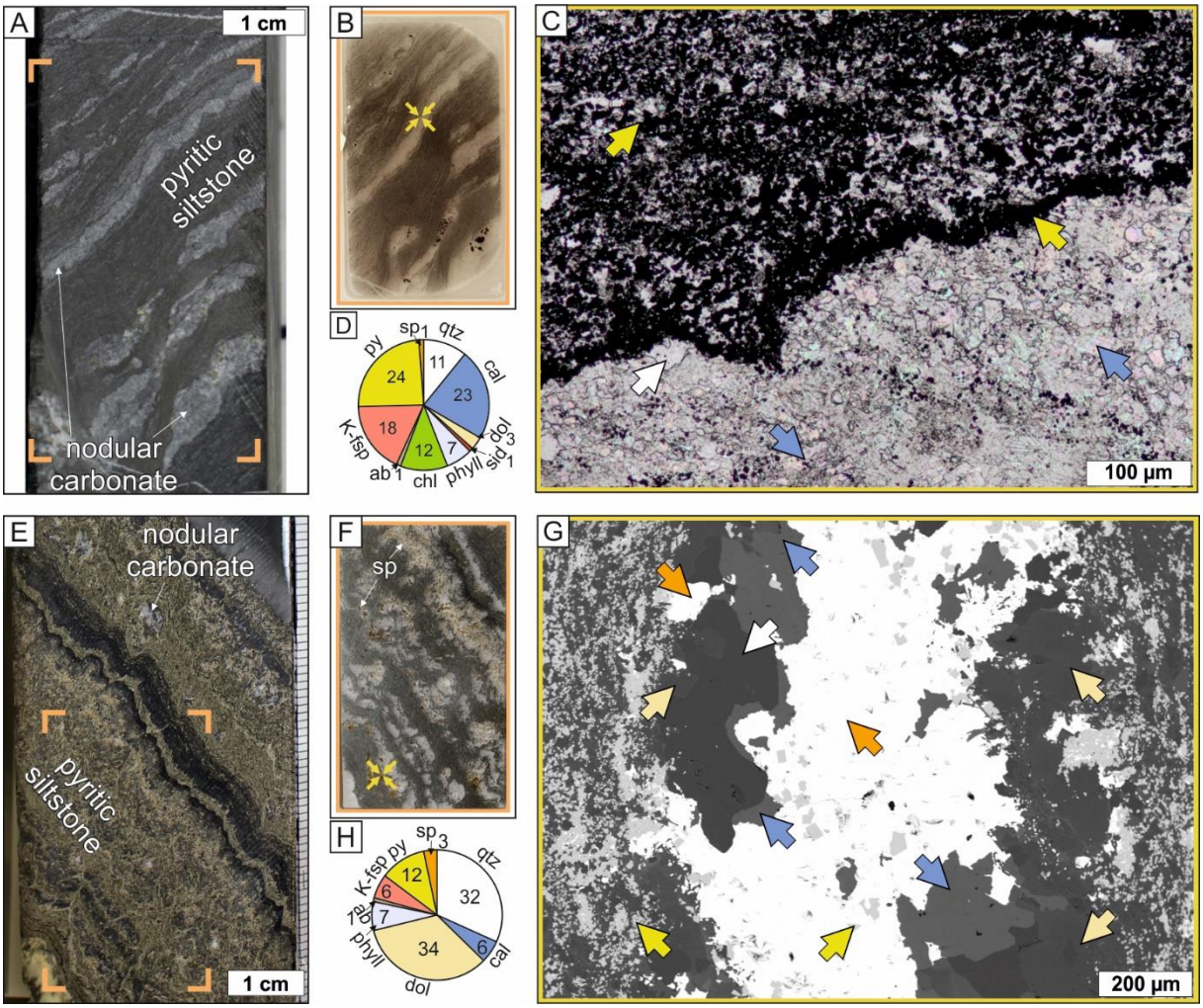

Fig. 3-6 Nodular carbonate and pyritic siltstone samples (Shovel Flats A-D, sample PR832SF080; George Fisher E-H, sample PRK751017). (A) Hand specimen photograph; the orange rectangles indicates location of B. (B) Thin section photograph of nodular carbonate and pyritic siltstone; the yellow arrows indicate the locations of C. (C) Transmitted light photomicrograph of nodular carbonate and pyritic siltstone; the arrows indicate individual mineral phases, see D. for colour code. (D) Bulk-rock mineralogical composition (qtz = quartz, cal = calcite, dol = dolomite, sid = siderite, phyll = phyllosilicate, chl = chlorite, ab = albite, K-fsp = K-feldspar, py = pyrite, sp = sphalerite). (E) Hand specimen photograph; the orange rectangles indicates location of F. (F) Thin section photograph of nodular carbonate and pyritic siltstone; note sphalerite in nodular carbonates; the yellow arrows indicate the locations of G. (G) Backscatter electron image of sphalerite replacing nodular carbonate; the arrows indicate individual mineral phases, see H. for colour code. (H) Bulk-rock mineralogical composition (qtz = quartz, cal = calcite, dol = dolomite, phyll = phyllosilicate, ab = albite, K-fsp = K-feldspar, py = pyrite, sp = sphalerite).

3.5.2. Mineralogy

Shovel Flats samples

The main mineral phases (median ≥ 1 wt. %) in Urquhart Shale samples from the Shovel Flats drill core are quartz, calcite, dolomite, phyllosilicates (muscovite, phlogopite, illite), chlorite, albite, K-feldspar, and pyrite (Fig. 3-7). The samples can be grouped according to mineralogical endmembers of (1) carbonates, (2) quartz and feldspars, and (3) phyllosilicates, which then corresponds with a rock type classification of calcareous/dolomitic mudstones and siltstones, siliceous marlstones and siliceous mudstones and siltstones (Fig. 3-8).

Chlorite typically occurs as clay-sized particles together with fine-grained illite in interstitial pore spaces in silicate and carbonate minerals (Fig. 3-5). Most Shovel Flats samples contain relatively low abundances of pyrite (< 5 wt. %), although high concentrations (< 37 wt. %) are preserved in some samples of nodular carbonate interbedded with laminated carbonaceous siltstones.

George Fisher samples

The unmineralized samples from between the ore bodies at the George Fisher deposit contain similar proportions of the main mineral groups to the samples from Shovel Flats (Fig. 3-7, Fig. 3-8). In contrast, the samples from the hanging wall stratigraphy in 10C K795 generally preserve higher and lower abundances of silicate and carbonate minerals respectively. The abundances of quartz, K-feldspar and pyrite are relatively consistent between the Shovel Flats samples and those from the George Fisher deposit. Compared to the Shovel Flats samples, dolomite and phyllosilicate phases are more abundant in the George Fisher samples, whereas calcite, chlorite and albite are less abundant to absent (Fig. 3-7, Fig. 3-8).

Ore samples from George Fisher preserve higher abundances of all sulphide minerals and generally lower abundances of all other minerals, the only exception being higher median calcite contents compared to George Fisher Urquhart Shale samples (Fig. 3-7).

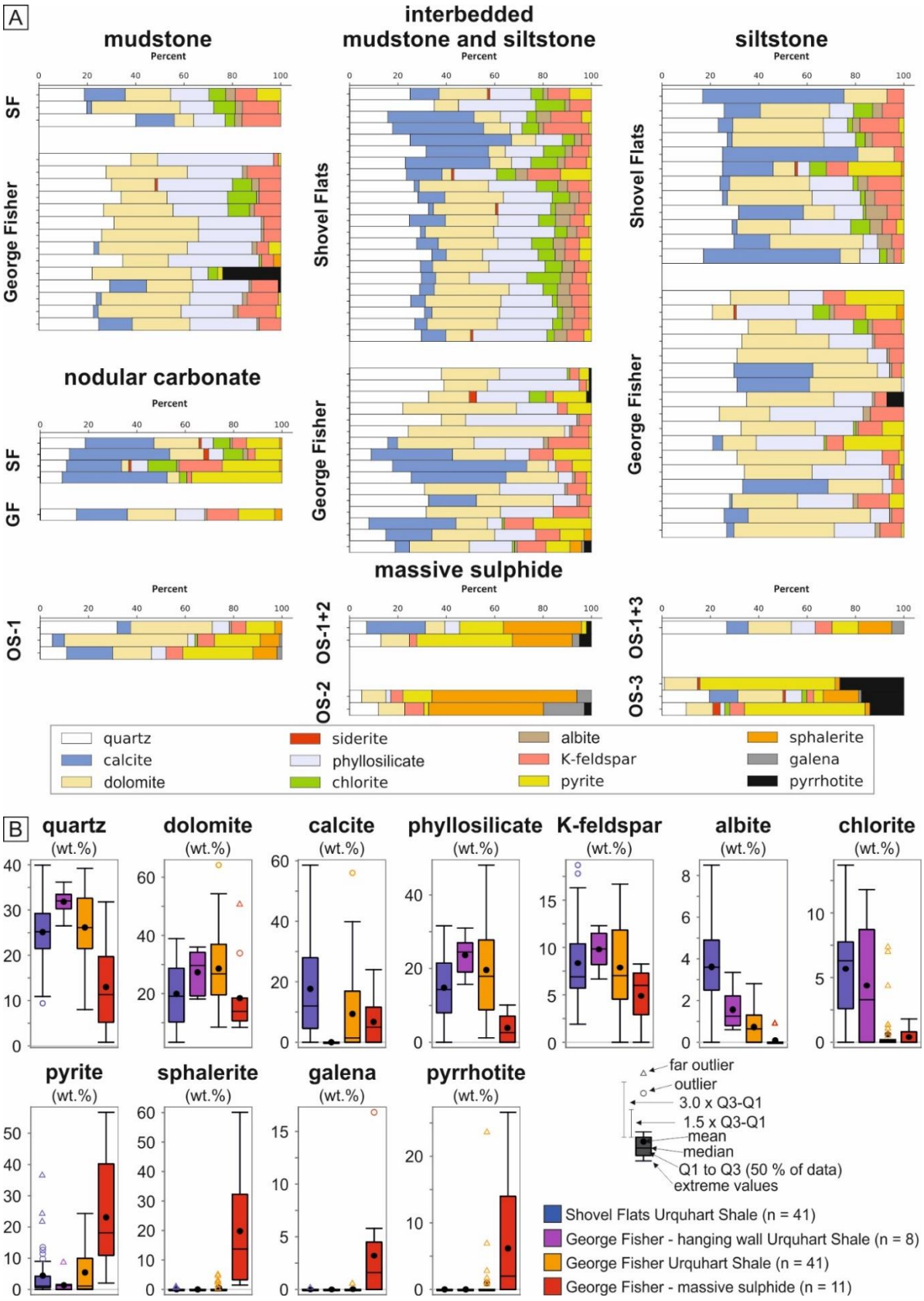

Fig. 3-7 Mineralogical composition of samples from the Shovel Flats drill core and the George Fisher deposit. (A) Bar plot of individual samples split by lithology. (B) Box and whisker plots for individual mineral phases split by location and details of the statistical method of box and whisker plots used in this study.

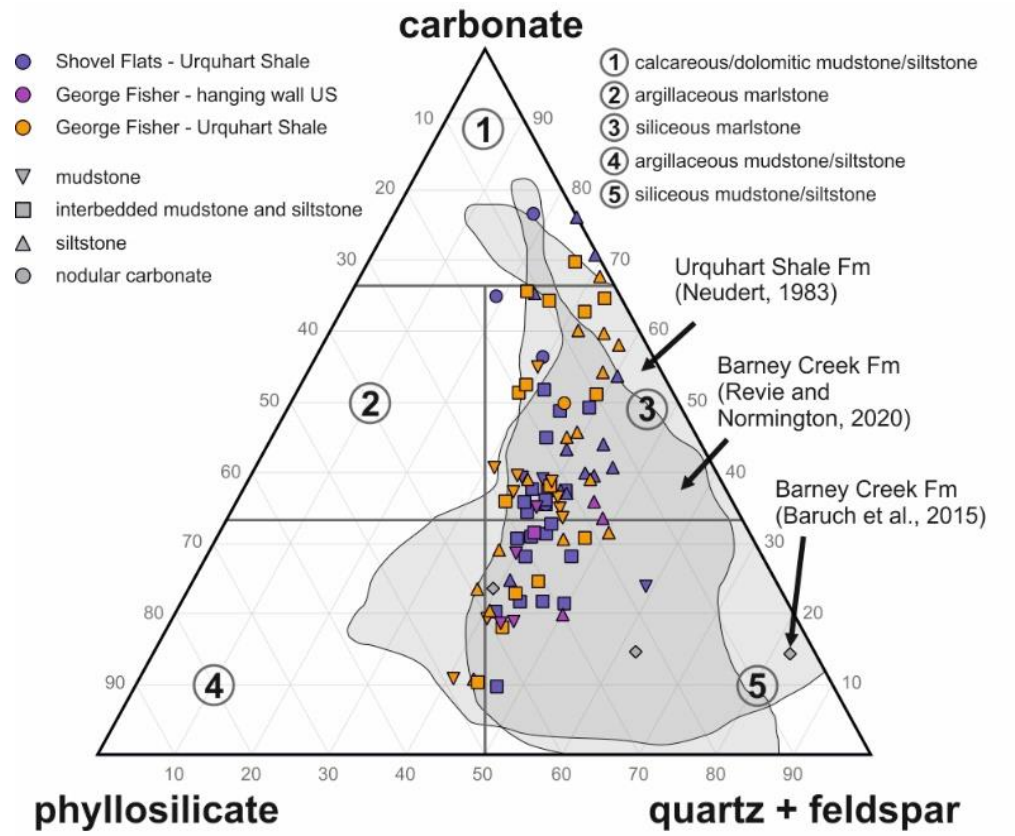

Fig. 3-8 Ternary diagram of three main mineral groups (carbonate, phyllosilicate and quartz + feldspar) plotting individual samples from the Shovel Flats drill core and from the George Fisher deposit and literature data for the Urquhart Shale Formation (Neudert 1983) and the Barney Creek Formation (Baruch et al. 2015; Revie and Normington 2020).

Clay-fraction mineralogy of the Urquhart Shale Formation (Shovel Flats and George Fisher)

All samples from Shovel Flats and George Fisher preserve illite and muscovite in the clay fraction (Fig. 7-5). The main difference between the two groups of samples is the absence of chlorite from most of the George Fisher samples. The same results are produced when the samples are treated with ethylene glycol, which indicates there is little smectite in the samples. The first basal reflection for illite in samples from George Fisher is generally narrower and has a higher intensity than in Shovel Flats samples, which is indicative of the illite to muscovite transition (Fig. 7-5).

3.5.3. Bulk rock geochemistry

The bulk rock compositional data of all samples is presented in the electronic appendix and the chemostratigraphic logs for some of the key analytes are presented in Fig. 3-9.

Fig. 3-9 Chemostratigraphic logs for the Shovel Flats drill core (A) and for drill core 10C K795 from the George Fisher deposit (B) with the downhole variation of Zn, Pb, Na, Sr, Mn, Tl, SEDEX alteration index values and the George Fisher Index (10[400Tl+Mn]/[10Sr+Na]). Zinc and Pb plots include mine assay data (red line = Zn; grey line = Pb). The blue lines show the median values of individual element of Urquhart Shale samples from Shovel Flats. The samples in B are grouped by colour: red = massive sulphide; orange = inter-mineralisation Urquhart Shale; purple = hanging wall Urquhart Shale.

Major element and base metal composition

Most samples from George Fisher contain very little Na and plot between Al and K in a ternary diagram of these 3 components, whereas samples from Shovel Flats preserve a similar range of K/Al ratios but plot towards higher Na concentrations (Fig. 3-10A). The samples from George Fisher that are located in the hanging wall sequence to massive sulphide mineralization are intermediate between the two groups (Fig. 3-10A). In terms of Ca, Mg and Fe concentrations, samples mostly plot between the calcite, dolomite, and pyrite end-members (Fig. 3-10C). In comparison to Shovel Flats, the George Fisher samples contain elevated Mn and the sub-group from the ore lenses plot towards the Fe end-member (Fig. 3-10C).

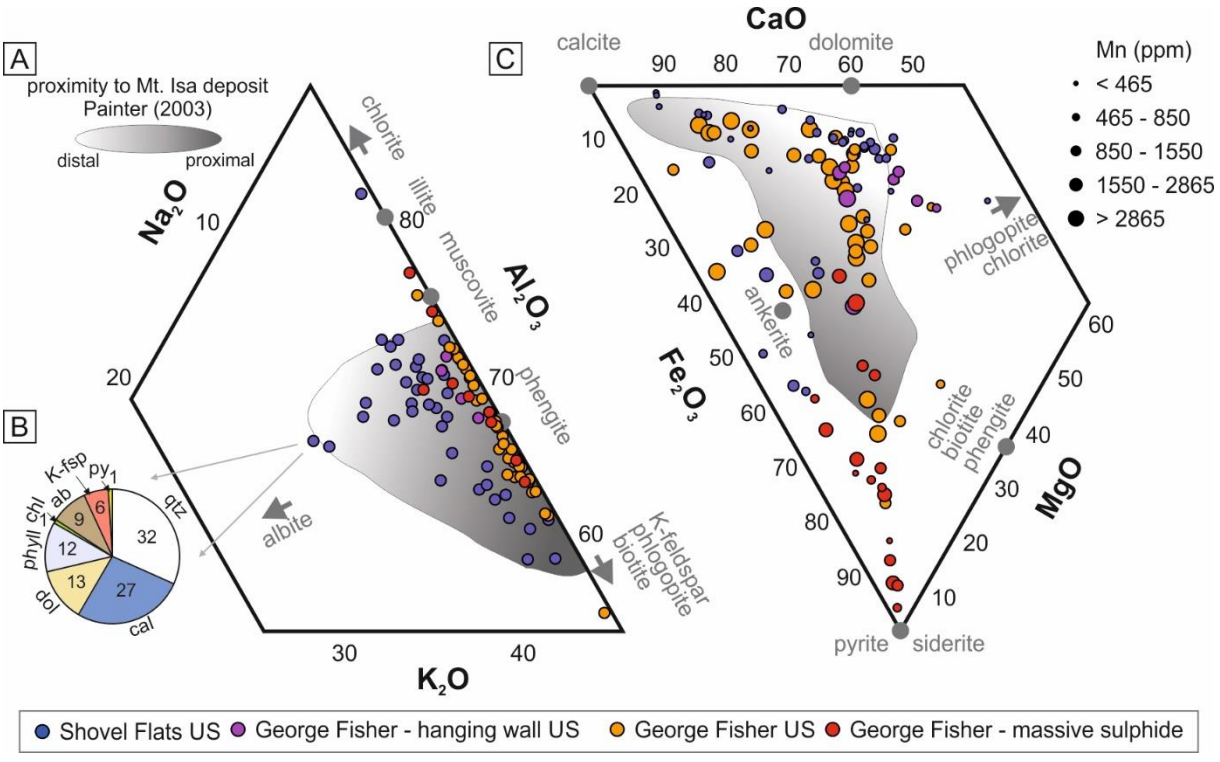

Fig. 3-10 (A) Na2O, K2O and Al2O3 ternary diagram for samples from the Shovel Flats drill core and the George Fisher deposit. End-member compositions of selected mineral phases are shown in grey. The grey field represents Urquhart Shale samples distal (white) to proximal (dark grey) to the Mount Isa deposit (data from Painter 2003). (B) Bulk-rock mineralogical composition of sample PR832SF035 from the Shovel Flats drill core (qtz = quartz, cal = calcite, dol = dolomite, phyll = phyllosilicate, chl = chlorite, ab = albite, K-fsp = K-feldspar, py = pyrite). This sample preserves the highest albite content in the XRD data set. (C) CaO, MgO and Fe2O3 ternary diagram for samples from the Shovel Flats drill core and the George Fisher deposit. End member compositions of selected mineral phases are shown in grey. The grey field represents Urquhart Shale samples distal (white) to proximal (dark grey) to the Mount Isa deposit (data from Painter 2003).

Base metal concentrations and total S can vary between the ore stages (Fig. 3-11A-D). Samples from ore stage 2 contain the highest Zn and Pb concentrations; ore stages 1 and 3 contain relatively lower Zn and Pb but are still highly enriched relative to unmineralized samples from George Fisher and Shovel Flats (Fig. 3-11A-D).

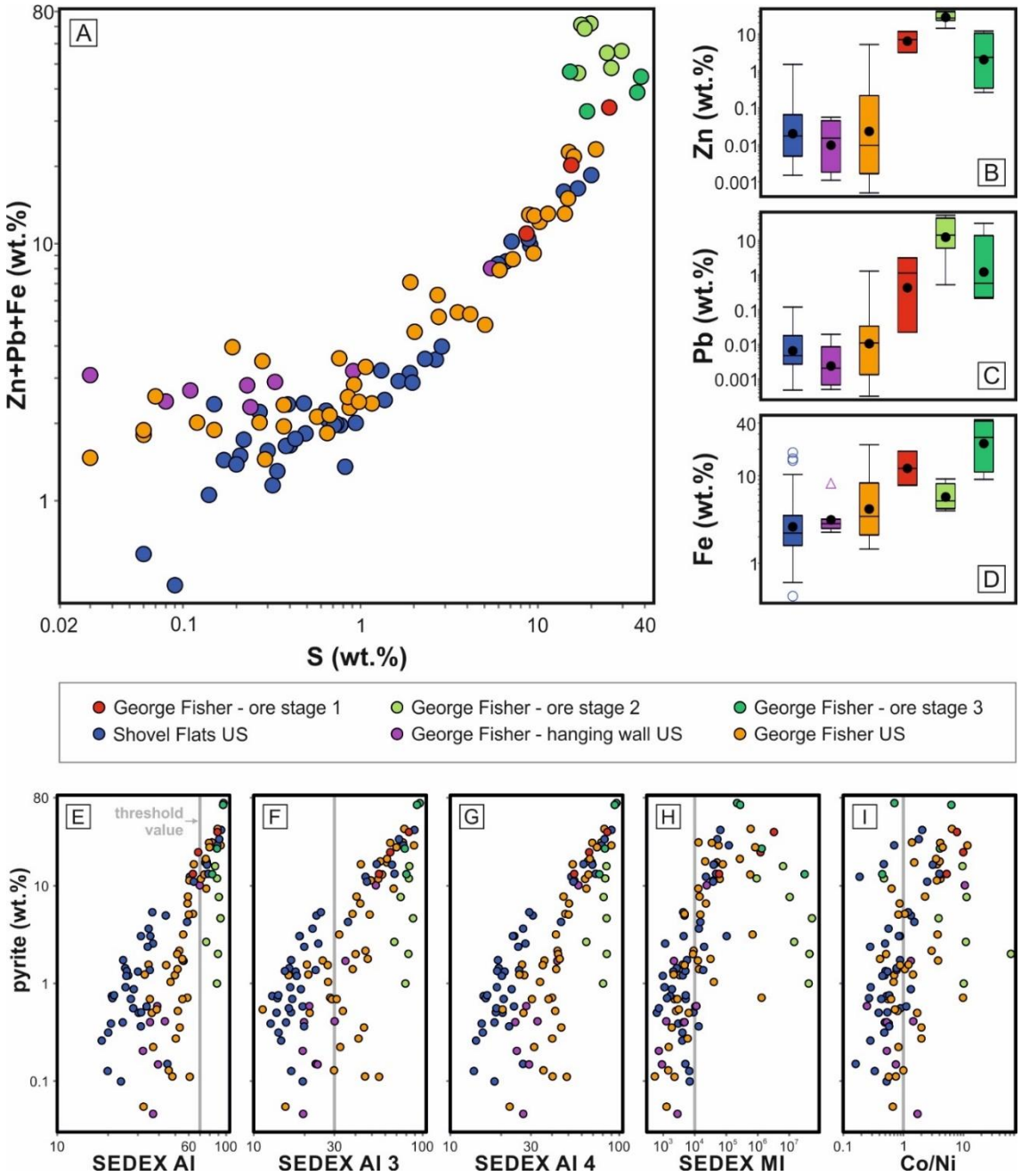

Fig. 3-11 (A-D) Sulphur and base metal concentrations for samples from the Shovel Flats drill core and the George Fisher deposit. (A) Sulphur vs. combined Zn-Pb-Fe. (B) Box and whisker plot for Zn concentrations. (C) Box and whisker plot for Pb concentrations. (D) Box and whisker plot for Fe concentrations. For details of the statistical method for box and whisker plots see Fig. 3-7B. (E-I) Literature alteration indexes vs. pyrite abundance for samples from the Shovel Flats drill core and the George Fisher deposit. (E) SEDEX alteration index. (F) SEDEX alteration index mark 3. (G) SEDEX alteration index mark 4. (H) SEDEX metal index. (I) Cobalt/Ni ratio.

In contrast, samples from Shovel Flats and the unmineralized samples from George Fisher have broadly overlapping total S and base metal concentrations. In the 10C K795 drill core at George Fisher, the Zn and Pb concentrations of the Urquhart Shale samples from the hanging wall and from in between the ore bodies are scattered around the median concentrations from the Shovel Flats drill core. In terms of alteration indexes, the values for the SEDEX AI, SEDEX AI 3, SEDEX AI 4, the SEDEX metal index and the Co/Ni ratio are highest in the ore samples (Fig. 3-11E-I). A total of 21 of the 41 Shovel Flats samples are below the suggested threshold values for CD-type massive sulphide deposits in the Carpentaria province (Table 1). Ten samples are above threshold values for less than four of these indices and another 10 samples are above threshold values for four or more indexes. All samples with pyrite contents of more than 10 wt. % fall into this category (Fig. 3-11). Molybdenum concentrations are generally low (Fig. 3-12; 62 samples < 2 ppm; 39 samples 2 to 10 ppm; 4 samples 10 to 25 ppm).

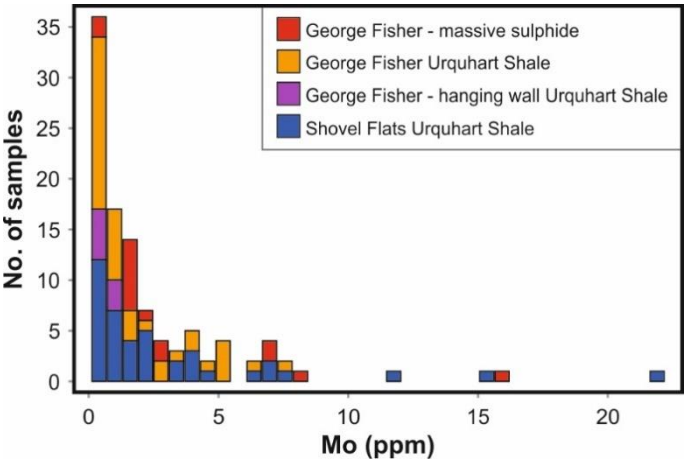

Fig. 3-12 Molybdenum concentrations for samples from the Shovel Flats drill core and the George Fisher deposit (bin width = 0.6 ppm).

Comparing Shovel Flats and George Fisher samples

The Shovel Flats samples (n = 21) that have below threshold values for the SEDEX alteration indexes were used as a reference for the unaltered protolith composition of the Urquhart Shale. The samples were further subdivided into two groups according to lithology: (1) siltstones (n = 9) and (2) mudstone and interbedded mudstone-siltstones (n = 12).

To evaluate relative mass changes, and element losses and gains median values for major, minor, and trace elements of each sub-group were compared (Fig. 3-13).

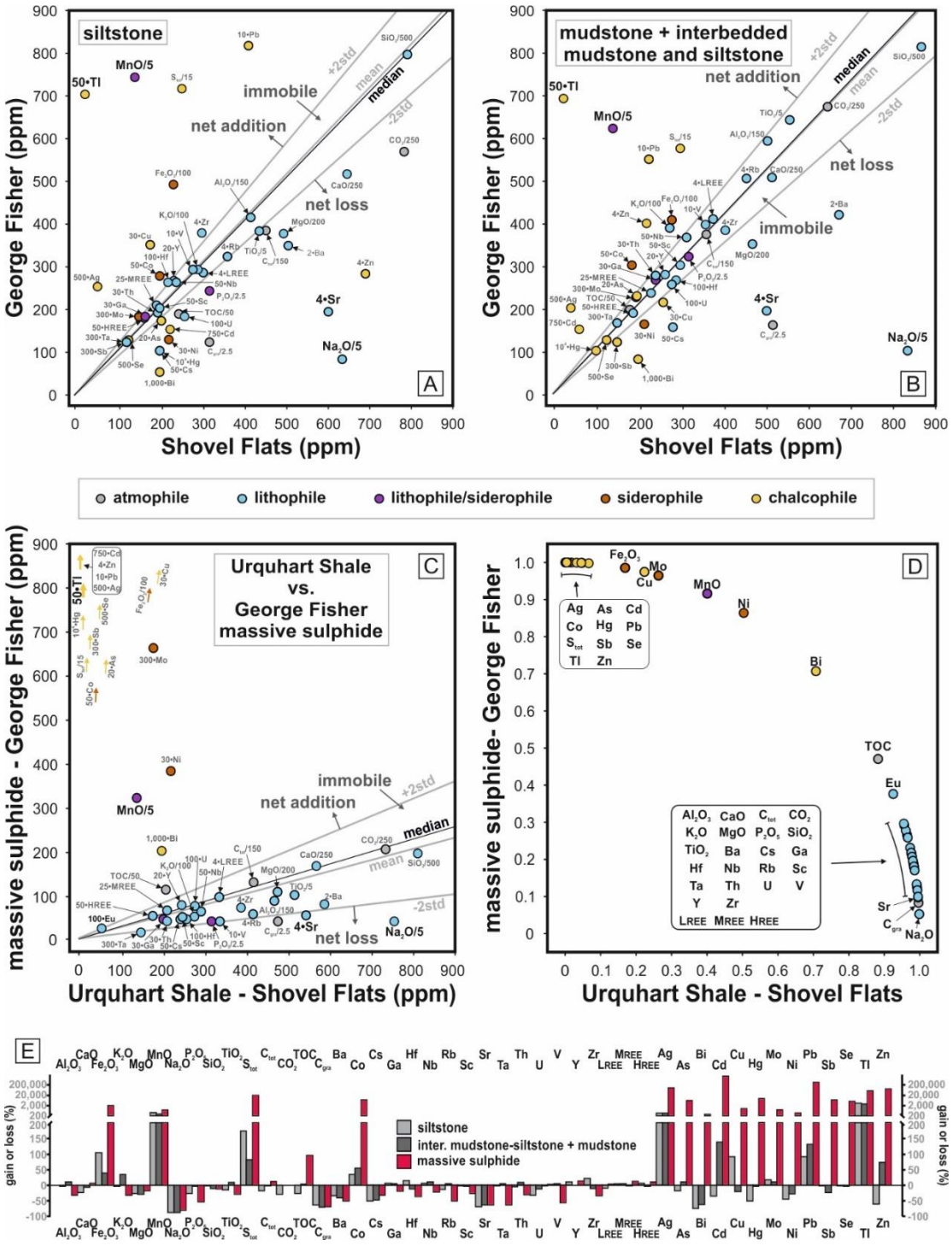

Fig. 3-13 Isocon diagrams for samples from the Shovel Flats drill core and the George Fisher deposit separated by lithology: (A) Background (below alteration indexes) siltstone vs. George Fisher siltstone. (B) Background (below alteration indexes) combined mudstone and mudstone-siltstone vs. George Fisher combined mudstone and mudstone-siltstone samples. (C) Combined Background Urquhart Shale samples vs. George Fisher massive sulphide samples. (D) Modified isocon diagram of C. with data scaled to a distance of 1 from the origin. Data in (A-C) are arbitrarily scaled to plot major and trace elements in a single diagram. (A-C) include the mean and median values and ±2 standard deviation (2std) values for the isocon line defining a field of immobile behaviour. All elements are grouped according to their geochemical behaviour. (E) Element mass gain and loss calculated for Shovel Flats vs. George Fisher samples shown in (A-D) for siltstone, combined mudstone and mudstone-siltstone, and for massive sulphide respectively.

The ratios of the immobile elements (Si, Al, Ti, Sc, Nb, Th, Y, and REE) in both lithological subgroups preserve evidence of a small bulk mass loss (ΔM) of 2 % (siltstones) and 4 % (combined mudstones and siltstones) in the George Fisher samples (relative to unaltered Shovel Flats samples). The largest element gains (> 50 %) are Tl, Ag, Mn, S, Pb; Fe and Cu for the siltstones, and Zn and Co for combined mudstones and siltstones. Cobalt, Zr, Mo, and Hf are moderately enriched (50 % to 2 standard deviations of *isocon* line) in the siltstones, and Fe and K are moderately enriched in combined mudstone and siltstone samples respectively.

There is a large depletion (>50 %) in Na, Sr and C_{gra} for both lithological sub-groups, and for Zn and Cs in siltstones. Barium, Mg and Ni are moderately depleted (50 % to 2 standard deviations of *isocon* line) in both sub-groups; Cs, Sb, and Cu in the combined mudstones and siltstones, and; U, CO2, TOC, P, Ca, As and C_{tot} in the siltstones.

Overall, the bulk mass loss and the enrichment or depletion factors of the most enriched or depleted elements (e.g., Tl, Mn, Ag, Na, Sr) and the immobile elements (Si, Al, Ti, Sc, Nb, Th, Y, and REE) are similar for both lithology sub-groups (Fig. 3-13A, B, E). For comparison with the ore samples from the George Fisher deposit, both lithologies for unaltered samples (n = 21) from the Shovel Flats drill core were, therefore, combined to identify the most enriched and most depleted elements (Fig. 3-13C, D).

The bulk mass change ($\Delta M = 100 * [\frac{c_{i\_GF} - c_{i\_SF}}{c_{i\_GF}}]$) of the ore samples relative to the unaltered Urquhart Shale samples indicates a large mass gain of 283 %. Chalcophile (Cd, Zn, Pb, Ag, Hg, Tl, S, Sb, Se, As, Cu) and siderophile elements (Co, Fe, Mo) are strongly enriched (>1000 %). Furthermore, Mn and Ni are enriched (> 500 – 1000 %) and TOC and Eu are slightly enriched (500 % to 2 standard deviations of *isocon* line) in the ore samples relative to the background Urquhart Shale samples. Element depletion (>2 standard deviations of *isocon* line) is indicated for Na, Cgra, Sr, Ta, V, and P. Overall, the elements, which show the greatest variability between the Shovel Flats drill-hole and the George Fisher deposit are Zn, Pb, Na, Mn, Sr, and Tl (Fig. 3-9).

George Fisher Index

The elements for which there is the greatest difference between Shovel Flats and George Fisher (Zn, Pb, Na, Mn, Sr and Tl) are all relatively uniform in total concentration in the Shovel Flats samples (Fig. 3-9). The one exception is in the uppermost 200 m, where concentrations of Mn and Tl are slightly elevated and Na and Sr are present at slightly lower concentrations. This variability also corresponds with scatter in the SEDEX AI values.

The non-base metal elements within this sub-group (Na, Mn, Sr and Tl) have been used to formulate an alteration index for the George Fisher deposit (GF Index). Element factors have been applied to obtain 1:1 proportion between Tl and Mn, and between Sr and Na for the Urquhart Shale samples, $i.e.\ 10\left(\frac{400Tl+Mn}{10Sr+Na}\right)$. The Shovel Flats samples preserve the lowest index values (median = 1.9), although they are slightly elevated in the upper 100 m of the drill core. The GF Index is highest in the mineralized samples from George Fisher, whereas the unmineralized samples have intermediate values (Fig. 3-14). Overall, the GF Index provides improved sensitivity for differentiating between the sample subgroups (Fig. 3-14) when compared to the existing SEDEX AI's (Fig. 3-11).

There is a negative correlation between Sr and Mn, whereby the highest Sr/Ca ratios and lowest Mn/Ca ratios are preserved in Shovel Flats samples and lowest Sr/Ca ratios and highest Mn/Ca ratios in George Fisher samples (Fig. 3-15). Thallium concentrations covary strongly with pyrite abundance and Tl/pyrite ratios (ppm/wt.%) are generally high in Urquhart Shale and ore stage 1 and 2 samples at George Fisher and low in Shovel Flats samples and samples from ore stage 3 (Fig. 3-16). Similarly, Ag concentrations covary with pyrite abundance and preserve elevated Ag/pyrite ratios for all George Fisher samples relative to Shovel Flats. Notably, the highest Ag/pyrite values are preserved by ore stage 2 samples, which also preserve the highest concentrations of Zn and Pb (Fig. 3-11B, C).

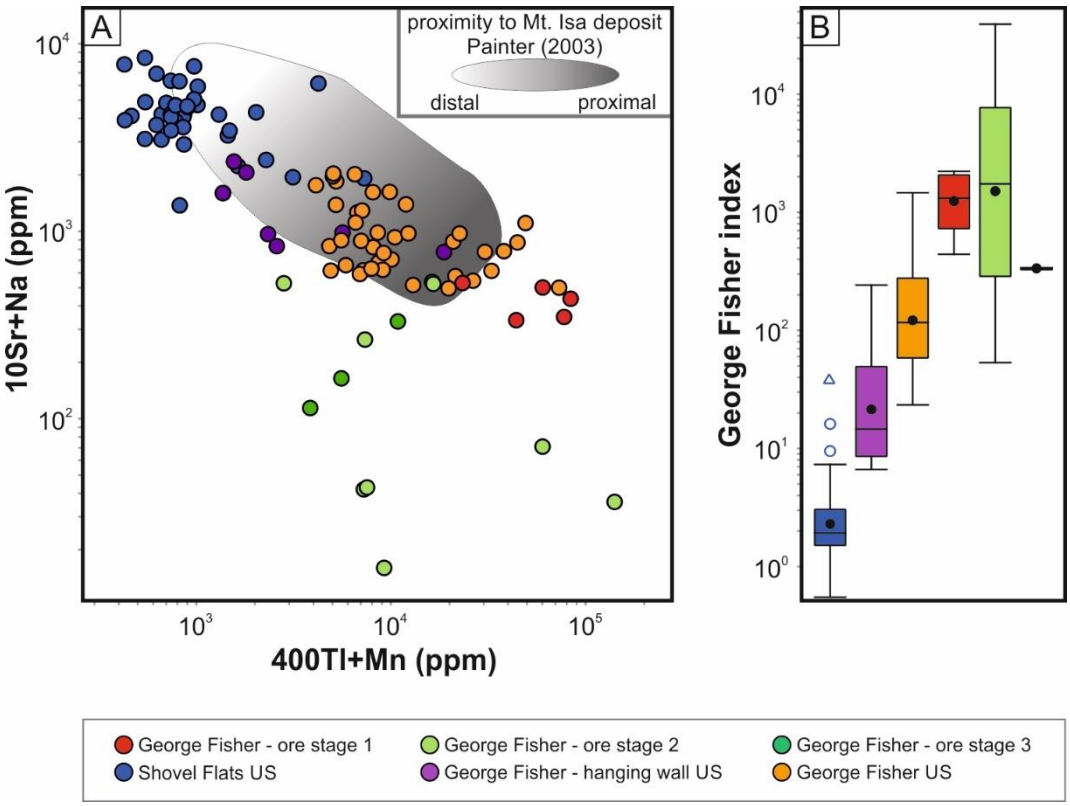

Fig. 3-14 George Fisher Index for samples from the Shovel Flats drill core and the George Fisher deposit. (A) 400Tl+Mn vs. 10Sr+Na plot. The grey field represents Urquhart Shale samples distal (white) to proximal (dark grey) to the Mount Isa deposit (data from Painter 2003). (B) George Fisher index (10 (400Tl+Mn)/(10Sr+Na)) box and whisker plot. For details of the statistical method for box and whisker plots see Fig. 3-7B.

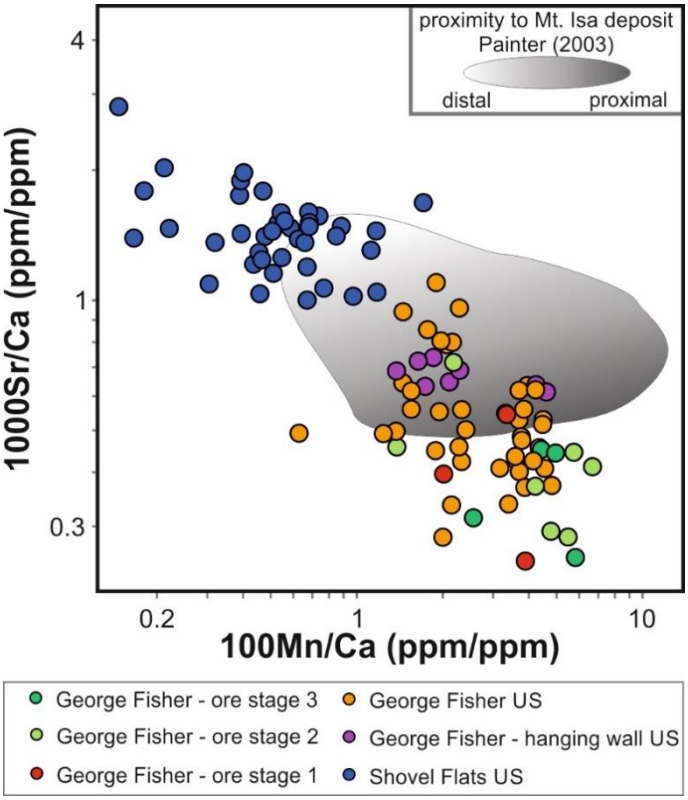

Fig. 3-15 Scatter plot of 100Mn/Ca vs. 1000Sr/Ca for samples from the Shovel Flats drill core and the George Fisher deposit. The grey field represents Urquhart Shale samples distal (white) to proximal (dark grey) to the Mount Isa deposit (data from Painter 2003).

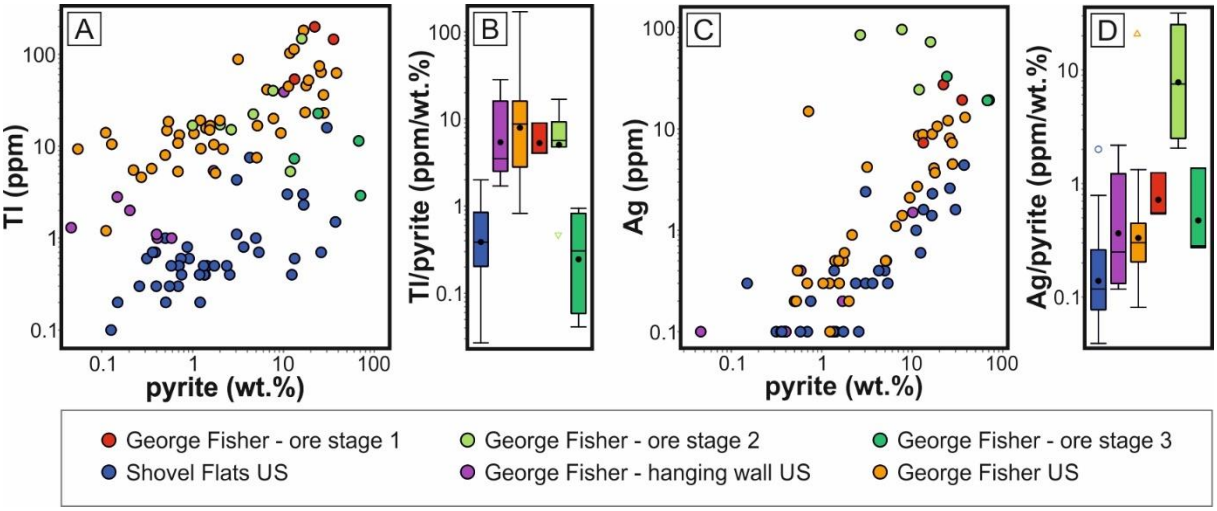

Fig. 3-16 (A) Scatter plot of pyrite (wt. %) vs. Tl (ppm) for samples from the Shovel Flats drill core and the George Fisher deposit. (B) Box and whisker plot of the Tl/pyrite ratio. (C) Scatter plot of pyrite (wt. %) vs. Ag (ppm) for samples from the Shovel Flats drill core and the George Fisher deposit. (D) Box and whisker plot of the Ag/pyrite ratio. For details of the statistical method for box and whisker plots see Fig. 3-7B.

3.6. Discussion

3.6.1. Unaltered composition of the Urquhart Shale Formation

It is essential to define the mineralogical composition of the unaltered protolith when developing accurate hydrothermal alteration models. For the George Fisher system, the unaltered protolith is represented by samples from the Shovel Flats drill-hole, which is located approximately 5 km away from the deposit (Fig. 3-2). The deposits in the northern Carpentaria Province are typically hosted within subbasins that represent localized fault-bound depocenters (e.g., Large et al. 2005), which preserve considerable lateral variability in the thickness and sedimentary facies of syn-tectonic depositional sequences (e.g., McGoldrick et al. 2010). In the Mount Isa Group there is similar evidence of syn-tectonic deposition in the form of variable formation thicknesses (e.g., Smith 1969; Derrick 1982). This sedimentological complexity makes precise stratigraphic correlations challenging, which in the southern Carpentaria has been further compounded by tectonic overprint (Valenta 1994). Nevertheless, the Urquhart Shale samples from Shovel Flats, George Fisher (this study) and from the wider Mount Isa area (Neudert 1983; Painter 2003) do preserve overlapping detrital components (e.g., quartz and feldspars), authigenic components (e.g., diagenetic pyrite and carbonate), and phyllosilicate phases (e.g., muscovite, illite, and phlogopite) that justify this

comparison (Fig. 3-5, Fig. 3-6, Fig. 3-7, Fig. 3-8). These mineralogical similarities are further supported by overlapping major and trace element compositions (e.g., Fig. 3-10, Fig. 3-11, Fig. 3-12, Fig. 3-15).

Detrital constituents of sedimentary rocks represent the cumulative effect of a range of weathering, transport and depositional processes (Rimstidt et al. 2017) and provide the framework for all subsequent diagenetic reactions (Bjørlykke 2014). During the Proterozoic it is generally accepted that low pO2 limited terrestrial weathering to mostly physical processes, resulting in relatively immature siliciclastic input to sedimentary basins (Rafiei and Kennedy 2019). The high abundance of feldspar in the Urquhart Shale is broadly similar to that described for the Barney Creek Formation in the McArthur Basin (Baruch et al. 2015), which is typical of chemically immature Precambrian sedimentary rocks (Kennedy et al. 2006). That said, the higher quartz/feldspar ratios in this study may imply a slightly different sediment source or deposition under deeper water conditions, which is consistent with the interpretation of deeper water rhythmite sedimentation for the Urquhart Shale Formation (Domagala et al. 2000).

Biogenic and authigenic constituents in marine sediments are primarily associated with biological productivity in the water column and subsequent organic matter degradation during early diagenesis (Rimstidt et al. 2017). The consumption of oxygen during oxygenic photosynthesis and subsequent organic matter degradation typically results in reducing depositional redox conditions. Paleoredox proxies such as sulphur isotope values or Mo concentrations in sedimentary rocks can then be used to investigate the depositional and early diagenetic conditions that occurred in sedimentary basins. In unrestricted basins, for example, euxinic conditions ($H_2S > Fe^{2+}$) typically results in Mo concentrations (Mo >100 ppm; Scott and Lyons 2012) that are enriched above crustal values (1-2 ppm; Taylor and McLennan 1995). In Shovel Flats and George Fisher samples, low Mo concentrations (Fig. 3-12) indicate either a strong degree of water mass restriction or that euxinic conditions were not a widespread feature. Notably, the $\delta^{34}S$ values of fine-grained diagenetic pyrite (pre-ore) are consistent with open system conditions during microbial sulphate reduction (Rieger et al. 2020),

meaning that low levels of Mo enrichment are consistent with predominantly ferruginous conditions (i.e. $H_2S < Fe^{2+}$) during deposition of the Urquhart Shale Formation.

There is moderate enrichment of total organic carbon (TOC) in samples from the Urquhart Shale (1-2 wt. %), which is similar to other Proterozoic fine-grained carbonaceous sedimentary rock units throughout the Carpentaria province (e.g., Baruch et al. 2015; Revie and Normington 2020). With sufficient availability of organic matter and oxidants (e.g., sulphate, Fe-hydroxides, or Mn-oxides) microbial reactions during early diagenesis produce a number of reduced species (e.g., HS^-, Fe^{2+} and Mn^{2+}) and bicarbonate ions (HCO_3^-) and result in the formation of pyrite and carbonate. The formation of nodular carbonates in the Urquhart Shale is generally interpreted due to diagenetic processes (Painter et al. 1999; Domagala et al. 2000) and this is consistent with their pre-ore paragenetic timing at George Fisher (Fig. 3-6). As such, the pyrite and carbonate associated elements (Fe and S, and Ca, Mg, Sr, Mn and Fe respectively) in the unmineralized Urquhart Shale are considered to largely represent biogenic and authigenic processes.

Phyllosilicate phases generally form in response to increasing pressures and temperatures during burial diagenesis (e.g., Bjørlykke 2014; Rimstidt et al. 2017). These reactions involve the transformation of early diagenetic and detrital clay minerals (e.g., kaolinite, smectite) through intermediate clay mineral phases, such as mixed-layered clay minerals (e.g., illite-smectite) and illite, to more crystalline phyllosilicate minerals such as muscovite or chlorite (for reviews see e.g., Héroux et al. 1979; Lynch et al. 1997; Beaufort et al. 2015). The preservation of illite in the Urquhart Shale is consistent with sub-greenschist facies conditions (< 300 °C; Merriman and Frey 1999). Moreover, asymmetric illite reflections may indicate the presence of very small amounts of illite-smectite interlayers (Fig. 7-5; see asymmetric illite-smectite reflections in (Lanson and Champion 1991; Lanson and Besson 1992). Illite-smectite interlayers are not preserved above burial temperatures of 220 °C (Day-Stirrat et al. 2010), which is consistent with previous bitumen reflectance and illite crystallinity data from the Urquhart Shale (ca. 200 °C; (McClay 1979; Chapman 1999).

Chlorite has previously been used as an indicator mineral for greenschist facies metamorphic conditions (> 300 °C) in the Urquhart Shale Formation and deposits of the Mount Isa area (Wilson 1972; Rubenach 1992; Large et al. 2005). In the unmineralized Shovel Flats drill-hole, however, the preservation of illite (and illite-smectite; Fig. 7-5) and the absence of a well-developed metamorphic fabric are inconsistent with conditions of metamorphic chlorite formation. Rather, the fine-grained (<10 µm; Fig. 3-5, Fig. 7-5) interstitial nature of chlorite in the Urquhart Shale Formation is consistent with diagenetic formation (e.g., Beaufort et al. 2015). It should be noted that the diagenetic chlorite is distinct from the coarser grained chlorite that is more closely associated with Cu mineralization in a number of the deposits in the Mount Isa area and is presumably hydrothermal in origin (Valenta 1988; Waring 1990; Chapman 1999; Cave et al. 2020).

The main pathways of diagenetic chlorite formation involve the transformation of precursor phases such as trioctahedral smectite or serpentine (e.g., berthierine; reaction I; Beaufort et al. 2015).

I) $2\ (Fe^{II},Mg,Al)_3(Si,Al)_2O_5(OH)_4 \rightarrow (Fe^{II},Fe^{III},Mg,Al)_6(Si,Al)_4O_{10}(OH)_8$ *(background diagenesis)*

berthierine *chlorite*

In modern estuarine and shelf environments berthierine formation has been linked to a suite of precursor phases (e.g., glauconite and odinite) formed from Fe-rich pore fluids during transgressive and highstand system tracts (e.g., Odin and Matter 1981; Morad et al. 2010; Virolle et al. 2019). It has also been suggested that under the ferruginous conditions that were characteristic of the Precambrian oceans, berthierine formation may have been widespread (e.g., Tang et al. 2017; Johnson et al. 2020). The diagenetic transformation of berthierine to chamosite (Fe-rich chlorite) is normally complete by 70 °C (e.g., Hornibrook and Longstaffe 1996), meaning the chlorite in the Urquhart Shale Formation could have formed during burial diagenesis rather than metamorphism. Chlorite is also present in un-metamorphosed sedimentary rocks throughout the Tawallah, McArthur, Nathan, and Roper Groups of the McArthur Basin (Revie and Normington 2020), which further supports such a diagenetic model for chlorite formation in the Proterozoic Carpentaria province.

3.6.2. Defining hydrothermal anomalism in the Urquhart Shale Formation

None of the published geochemical element ratios and alteration indices are particularly effective in differentiating between the Urquhart Shale Formation at the George Fisher deposit and the background Urquhart Shale Formation from the Shovel Flats drill core (Fig. 3-11). Covariation between pyrite abundance in the Shovel Flats samples and the SEDEX AI, SEDEX AI 3 and SEDEX AI 4 values indicates this alteration index is strongly dependent on pyrite abundance (Fig. 3-11). As there is considerable variability in background levels of pyrite (Rieger et al. 2020), however, the SEDEX alteration indexes are susceptible to false positive values.

The SEDEX metal index values appear to be much more independent of pyrite abundance, although there is no clear differentiation between the background Urquhart Shale samples from the Shovel Flats drill core and the Urquhart Shale samples from the George Fisher deposit (Fig. 3-11). It is unlikely, therefore, that the ore forming metals are widely dispersed within the Urquhart Shale Formation at George Fisher. This lack of metal dispersion is consistent with the model of Zn ore formation in the sub-surface during diagenesis (Chapman 1999, 2004; Rieger et al. 2020) rather than the exhalation of the hydrothermal fluids on the seafloor.

In contrast, the GF Index discriminates between Urquhart Shale samples from the background drill core, hanging wall samples from the George Fisher deposit, inter-mineralization Urquhart Shale samples and massive sulphide samples (Fig. 3-14). The elements in the GF Index are associated with the 3 major mineralogical constituents (silicates, carbonates, sulphides) of the Urquhart Shale Formation, meaning it is necessary to consider the alteration reactions involving these phases.

3.6.3. Hydrothermal alteration at George Fisher

The Cu-mineralization at the George Fisher deposit is a minor component and more spatially restricted than at the Mount Isa and Hilton deposits (Chapman 1999). As such, the host rocks at the George Fisher deposit should preserve the geochemical footprint of the stratabound Zn-Pb mineralization (ore stage 1) more effectively than the Mount Isa or Hilton deposits, where this earlier mineralisation may be more minor or absent.

The greater abundances of dolomite and phyllosilicates at George Fisher relative to unmineralized Shovel Flats samples (Fig. 3-7) are broadly comparable to previous alteration models (cf. Chapman 1999, 2004). The main difference from earlier work is the absence of barium-(K-)feldspar, which was not detectable in any of the bulk rock mineralogical analysis. Furthermore, Ba is slightly depleted in mudstones and siltstones in George Fisher samples relative to Shovel Flats samples (Fig. 3-13). This may either indicate that (1) Ba-feldspar was dissolved or replaced during mineralization at George Fisher, or that (2) Ba-feldspar alteration was spatially restricted on a deposit scale. We consider (2) as being more likely, considering the observation that Ba-feldspar alteration is found mostly in the deeper parts of the deposit (Chapman 1999).

The depletion of chlorite and albite in George Fisher samples relative to unmineralized Shovel Flats samples (Fig. 3-7) has not previously been described. As discussed earlier, the unmineralized host rocks to the George Fisher deposit likely contained diagenetic chlorite which is distinct from the hydrothermal chlorite that is more spatially restricted in association with the later Cu event (Fig. 3-7; Chapman 1999). There are two options for the lack of chlorite in the George Fisher samples: (1) chlorite was never formed in the host rocks at George Fisher; or (2) hydrothermal processes have removed chlorite precursor phases (e.g., berthierine) or chlorite from the host rocks at the George Fisher deposit. There is no supporting evidence that protolith composition was substantially different in order to account for a contrasting diagenetic assemblage in the George Fisher samples (i.e. option 1). Instead, it is worth considering how alteration reactions involving the prograde diagenetic reaction sequence might control the mineralogy assemblage developed with ore stage 1. For example, the alteration of berthierine/chlorite, albite, and calcite during TSR (reaction II) would result in the formation of muscovite/phlogopite (reaction III), dolomite (reaction IV) and pyrite (reaction V).

This alteration reaction is consistent with the depletion of albite, chlorite, and calcite, and the greater abundances of muscovite/phlogopite and dolomite in samples from George Fisher (Fig. 3-7). The preservation of K-feldspar also suggests a high K^+/H^+ ratio in the fluid (relatively high pH), near the muscovite/K-feldspar stability boundary.

The magnesium released during berthierine/chlorite alteration (reaction III), combined with bicarbonate from TSR (II), could have resulted in hydrothermal dolomite formation (IV), which is consistent with the higher dolomite abundance at George Fisher relative to Shovel Flats Urquhart Shale samples (Fig. 3-7). Dolomitization of calcite typically results in changes in the trace element composition; for example, neo-formed dolomite is commonly enriched in Mn and/or Fe and depleted in Sr relative to precursor calcite (Brand and Veizer 1980; Kah 2000). These trace element changes are due to the incompatibility of the larger Sr^{2+}-ion compared to the smaller Mn^{2+}- or Fe^{2+}-ions in the dolomite structure (e.g., Kretz 1982). The inverse relationship of Mn and Sr in Shovel Flats and George Fisher samples (Fig. 3-15) is consistent with hydrothermal dolomitization at the George Fisher deposit. Nodular carbonates at George Fisher also preserve evidence of replacement by sphalerite (Fig. 3-6; (Chapman 2004).

The changes in whole rock carbonate mineralogy (calcite vs. dolomite) and replacement textures of dolomite by sphalerite likely indicate that mineralization has resulted in complex carbonate replacement and dissolution-precipitation reactions at George Fisher, although further studies on the carbonate chemistry are needed to test this hypothesis.

Reactive Fe from berthierine/chlorite (reaction III) and the hydrothermal fluid would have combined with reduced S (TSR; reaction II) to form hydrothermal pyrite (reaction V). Whole-rock Tl concentrations have previously been identified to be an important pathfinder for CD-type systems in the Carpentaria province (e.g., Lambert and Scott 1973; Large and McGoldrick 1998; Whitbread 2004) and in other sedimentary basins (e.g., Slack et al. 2004; Gadd et al. 2016). Pyrite at George Fisher contains higher concentrations of Tl and Ag than pyrite from unmineralized samples (Fig. 3-16). Recently, high-resolution element mapping of pyrite aggregates has shown that Tl-enriched pyrite formed after fine-grained pyrite in the McArthur River deposit (Spinks et al. 2019). At George Fisher, samples that are dominated by ore stage 1 preserve the highest whole rock Tl concentrations and have similar morphologies to McArthur River Tl-rich pyrites (Eldridge et al. 1993; Spinks et al. 2019; Rieger et al. 2020).

II) $SO_4^{2-} + CH_4 \rightarrow HS^- + HCO_3^- + H_2O$ **(TSR)**

sulphate methane hydrogen sulphide bicarbonate water

III) $(Fe^{II},Mg,Al)_3(Si,Al)_2O_5(OH)_4 / (Fe^{II},Fe^{III},Mg,Al)_6(Si,Al)_4O_{10}(OH)_8 + NaAlSi_3O_8 + 8H^+ + K^+ \rightarrow$

berthierine chlorite albite hydrogen potassium

$KAl(AlSi_3O_{10})(OH)_2 / KMg_3(AlSi_3O_{10})(OH)_2 + Al(OH)_3 + Si(OH)_4 + Na^+ + Fe^{2+} + Mg^{2+}$ **(muscovite / phlogopite alteration)**

muscovite phlogopite aluminium hydroxide silicic acid sodium iron magnesium

IV) $Mg^{2+} + CaCO_3 + HCO_3^- \rightarrow CaMg(CO_3)_2 + H^+$ **(dolomite formation)**

magnesium calcite bicarbonate dolomite hydrogen

V) $Fe^{2+} + Zn^{2+} + Pb^{2+} + 4\ HS^- \rightarrow FeS_2 + ZnS + PbS + 4H^+$ **(sulphide formation)**

iron zinc lead hydrogen sulphide pyrite sphalerite galena hydrogen

In contrast, the Tl/pyrite ratios of ore stage 3 (Cu-mineralization) are lower and are similar to background Urquhart Shale ratios (Fig. 3-16). Overall, the reaction sequence described by reactions (II)-(V) is consistent with lower chlorite albite, and calcite contents, higher phyllosilicate and dolomite abundances, and formation of hydrothermal pyrite at George Fisher and the element changes described by the GF index.

3.6.4. Implications

Considering the petrographic and mineralogical evidence that parts of the Urquhart Shale Formation did not reach greenschist facies (this study; McClay 1979; Chapman 1999) we would argue that the chlorite formed during diagenesis. It is possible, therefore, that compositional and isotopic data generated on samples from the Urquhart Shale Formation near the George Fisher deposit could be used to investigate the Paleoproterozoic depositional and diagenetic environment in this part of the Carpentaria province.

In terms of the sulphide mineralization at the George Fisher deposit, there is robust petrographic evidence that ore stage 1 (Zn-dominated, stratabound) post-dated the formation of diagenetic pyrite formed during the earliest stages of diagenesis (Rieger et al. 2020). If so, it may have occurred either before, or after, diagenetic chlorite formation (i.e. < 70 °C, transformation of berthierine to chlorite). If the mineralization pre-dated diagenetic chlorite formation, this must have occurred within the upper 2-3 km of the basin (assuming a normal geothermal gradient). This is consistent with recent paragenetic models for mineralization at other deposits in the Carpentaria Province (e.g., Teena, Magnall et al. 2020b). Alternatively, if ore stage 1 mineralization post-dated diagenetic chlorite formation, this may have occurred during late diagenesis (e.g., >3 km burial depth; cf. George Fisher, Chapman 2004; Mount Isa, Painter 2003). This would be consistent with ore formation models for the Century deposit, which likely formed during the onset of basin inversion (Broadbent et al. 1998; Broadbent 2002). Notably, the depletion of albite and chlorite during hydrothermal activity has also been reported for the Century deposit (Whitbread 2004).

Considering these mineralogical similarities, it is worth exploring the broader application of the GF index in the Carpentaria district. When applied to the Mount Isa and Century deposits the GF index can discriminate between the background protolith and the altered host rocks within approximately 2 km and 800 m of the respective deposits (Fig. 17). Irrespective of the different paragenetic models that exist for the Carpentaria CD-type deposits, therefore, it is clear that alteration models should incorporate aspects of the sulphide, carbonate, and (phyllo)silicate assemblages; this will be most effectively achieved by combining petrographic, mineralogical, and bulk geochemical techniques.

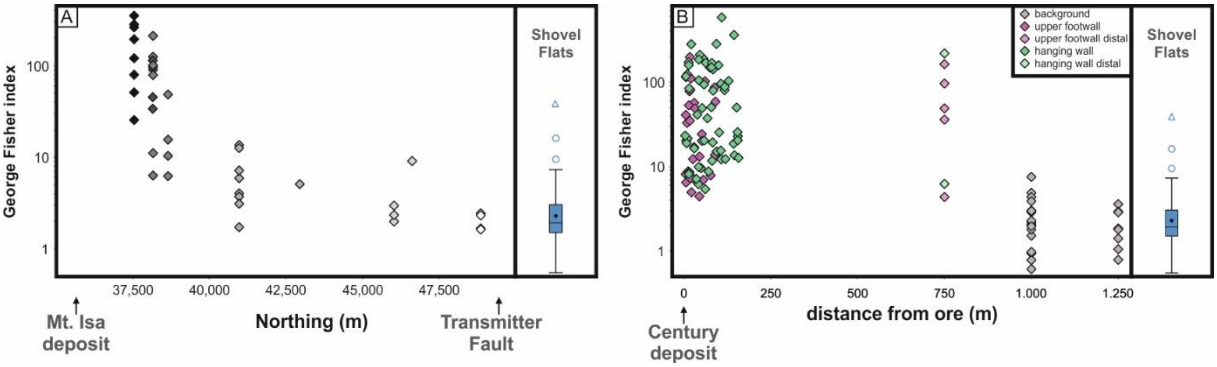

Fig. 3-17 George Fisher index values for the Urquhart Shale Formation north of the Mount Isa deposit (A; data compiled from Painter 2003) and for the Century deposit (B; data compiled from Whitbread 2004). George Fisher index values for the Shovel Flats samples (this study) are shown for reference.

3.7. Conclusions

The Urquhart Shale Formation is host to the world class George Fisher Zn deposit (165 Mt at 9.1 % Zn, 3.4 % Pb, and 55 g/t Ag; Glencore 2019) and consists of carbonaceous, variably dolomitic or calcareous siltstones and mudstones; unmineralized mudstones and siltstones contain a variety of detrital and authigenic mineral phases (quartz, feldspars, phyllosilicates, calcite, dolomite, and pyrite). The occurrence of fine-grained chlorite in pores spaces with illite, the lack of well-developed metamorphic fabric, and low temperatures indicated by illite crystallinity are consistent with a sub-greenschist facies metamorphic grade. This implies that unmineralized Urquhart Shale samples preserve a combination of detrital, authigenic and diagenetic components (including chlorite).

Hydrothermal alteration processes during ore stage 1 (Zn-dominated, stratabound) at the George Fisher deposit resulted in lower chlorite, albite, and calcite abundances, higher concentrations of dolomite and phyllosilicate minerals (e.g., muscovite or phlogopite), and the formation of sulphide minerals (pyrite, sphalerite, and galena). These mineralogical changes are consistent with a hydrothermal event either before, or after, the formation of diagenetic chlorite from berthierine. This may have occurred in the upper 2-3 km of the basin or during later diagenesis (e.g., at the onset of basin inversion). During this hydrothermal event, the dissolution of albite, the replacement of calcite by dolomite, and the formation of hydrothermal pyrite has resulted in minor and trace element depletion (Sr and Na) and enrichment (Tl and Mn), which were used to formulate an alteration index for the George Fisher deposit (GF index, 10((400Tl+Mn)/(10Sr+Na))). This alteration index is highly effective in differentiating between the unmineralized background Urquhart Shale Formation and the mineralized Urquhart Shale Formation at George Fisher. It may, therefore, be useful in future geochemical exploration programmes in the Mount Isa area. Moreover, similar mineralogical and element changes in other CD-type massive sulphide deposits may indicate that hydrothermal alteration reactions were broadly comparable throughout the Carpentaria province. Overall, the combination of petrographic, lithogeochemical, and mineralogical techniques has proved to be effective in determining the background composition of the Urquhart Shale Formation and the alteration footprint of the ore-forming system at George Fisher.

3.8. Acknowledgments

We would like to thank the geology teams at Mount Isa Mines George Fisher operation and Mount Isa Mines Resource Development for support during field work and for access to drill cores. Moreover, we would like to thank P. Rea from Mount Isa Mines Resource Development for insightful discussions and his review of this manuscript. Funding for this project was provided by a Helmholtz recruitment initiative grant to S. Gleeson. Furthermore, we acknowledge H. Liep, U. Dittmann, and E. Lewerenz for sample preparation; and F. Wilke for assistance with BSE imaging.

4. Rare earth element and yttrium fractionation in carbonates at the George Fisher deposit, Australia

Differentiating between hydrothermal and diagenetic carbonates using rare earth element and yttrium (REE+Y) geochemistry: A case study from the George Fisher massive sulphide deposit

Rieger P.[1,2], Magnall J.M.[1], Gleeson S.A.[1,2], Oelze M.[1], Wilke F.[1], Lilly R.[3]

[1]GFZ German Research Centre for Geosciences, Telegrafenberg, 14473 Potsdam, Germany
[2]Freie Universität Berlin, Institute for Geological Sciences, Malteserstraße 74-100, 12249 Berlin, Germany
[3]School of Earth and Environmental Sciences, University of Adelaide, Adelaide, South Australia 5005, Australia

This manuscript is an earlier version of a manuscript that has been submitted to Mineralium Deposita.

4.1. Abstract

Carbonate mineral phases are ubiquitous in most sediment-hosted mineral deposits. These deposits can comprise a variety of carbonate types (detrital, primary, diagenetic, hydrothermal, and/or metamorphic), which typically have complex paragenetic relationships. Recent developments in laser ablation-inductively coupled plasma-mass spectroscopy (LA-ICP-MS) analysis allow for the generation of high-resolution *in situ* rare earth element and yttrium (REE+Y) data from carbonate minerals. When normalized to chondritic values (CN), REE+Y_{CN} can be used to constrain fluid chemistry and fluid-rock interaction processes in both low, and high, temperature settings. Unlike other phases (e.g., pyrite), however, the application of *in situ* LA-ICP-MS data to differentiate between pre-ore and hydrothermal carbonates remains relative untested. To assess the potential applicability of carbonate *in situ* REE+Y data, we combined transmitted light and cathodoluminescence (CL) petrography with LA-ICP-MS analysis of carbonate mineral phases from (1) the Proterozoic George Fisher clastic dominated (CD-type) massive sulphide deposit and from (2) correlative, barren host rock lithologies (Urquhart Shale Formation). Pre-ore calcite preserves homogenous CL signals and light rare earth element (LREE) enriched REE+Y_{CN} profiles. Together with variable super-chondritic Y/Ho ratios and variable Ce/Ce^* values (~ 1), the REE+Y_{CN} compositions provide evidence that pre-ore carbonates formed during diagenesis from diagenetic pore fluids derived from anoxic seawater, which is consistent with the ferruginous conditions that likely dominated the Proterozoic oceans. Hydrothermal and hydrothermally altered dolomite and calcite from the George Fisher deposit can be differentiated from pre-ore calcite both petrographically (by dull CL signals) and by their REE+Y compositions. Relative to shale reference values, whole rock REE concentrations, and to pre-ore calcite, the George Fisher calcites and dolomites are generally LREE depleted. We suggest this is the result of hydrothermal alteration by saline Cl-rich mineralizing fluids. The difference between the carbonate *in situ* and whole rock REE+Y_{CN} signatures suggests that the carbonate REE+Y composition is more sensitive to hydrothermal alteration relative to the whole rock REE+Y composition. Furthermore, the presence of both positive and negative Eu/Eu^* values in calcite and dolomite

indicates that the mineralizing fluids were relatively hot (>250 °C) and cooled below 200-250 °C during ore formation. This study confirms the hypothesis that *in situ* REE+Y data can be used to both differentiate between pre-ore and hydrothermal carbonate mineral phases and provide important constraints on the physicochemical conditions of ore formation.

4.2. Introduction

In many mineral systems, carbonate minerals constitute a significant proportion of the host rock and gangue mineralogy. Sediment hosted ore deposits can comprise a variety of carbonate types (Cline et al. 2005; Hitzman et al. 2005; Leach et al. 2005): detrital carbonates, primary carbonates, diagenetic carbonates, hydrothermal carbonates, and tectonic or metamorphic carbonates. Such carbonate-rich ore systems also typically lack an extensive alteration footprint due to the effective buffering of acidic hydrothermal fluids by carbonate-rich lithologies. The complex carbonate paragenesis and the limited alteration footprint are major challenges when investigating, and exploring for, ore systems in carbonate-rich rocks; therefore, there is a need for new tools to differentiate alteration halos from background lithologies.

Recent analytical developments are providing exploration geoscientists with new techniques for confronting these challenges. For example, new techniques that enable the generation of large C and O isotope datasets have shown how alteration halos in carbonate-hosted mineral systems may extend beyond bulk rock lithogeochemical anomalies (e.g., off-axis integrated cavity output spectroscopy; Barker et al. 2013). As a result of being generated using bulk rock techniques, such isotopic datasets may need to be supplemented by *in situ* techniques in order to constrain hydrothermal and background processes in samples with a complex paragenetic history. In low temperature (e.g., marine or diagenetic) environments, *in situ* trace element analysis of carbonate minerals (e.g., laser ablation ICP-MS) has attracted increasing usage (e.g., Webb et al. 2009; Himmler et al. 2010). For example, the partitioning of rare earth elements and yttrium (REE+Y) between fluids and carbonate minerals is well constrained (e.g., Morgan and Wandless 1980; Tanaka and Kawabe 2006; Voigt et al. 2017) and REE+Y fractionate systematically in aqueous solutions in response to

physicochemical conditions (pH, temperature, ligand type, or fluid-rock interaction) as a function of ionic radius and charge (e.g., Bau 1991; Bau and Möller 1992). Altogether, there is potential for the REE+Y systematics of diagenetic and hydrothermal carbonates in constraining key aspects of fluid chemistry (Debruyne et al. 2016; Smrzka et al. 2019). Until relatively recently, however, the potential to use *in situ* REE+Y analysis of carbonate minerals has remained relatively untested for hydrothermal mineral systems, and few studies have used *in situ* REE+Y data to interpret the conditions of hydrothermal carbonate formation (e.g., Magnall et al. 2016a; Vaughan et al. 2016).

The need to differentiate between pre-ore and hydrothermal carbonate signatures is particularly relevant in the Carpentaria province (Fig. 4-1), where several of the world's largest clastic-dominated (CD-type) Zn-Pb massive sulphide deposits are hosted in sedimentary rocks with multiple types of carbonate (e.g., Perkins and Bell 1998; Large et al. 2005; McGoldrick et al. 2010). Previous bulk rock lithogeochemical studies have found large-scale (several km) halos of carbonate-associated elements (Mn and Fe) related to these hydrothermal systems (Large and McGoldrick 1998; Large et al. 2000). However, both Fe and Mn can also be enriched in carbonate minerals by background processes in marine or diagenetic environments (e.g., Brand and Veizer 1980; Kah 2000; Wittkop et al. 2020). As a result, bulk rock and *in situ* major element analyses alone may not be sufficient to differentiate between hydrothermal and background carbonate signatures.

In this study, we test the hypothesis that *in situ* REE+Y data can be used to differentiate diagenetic and hydrothermal carbonate mineral phases. We combine transmitted light and cathodoluminescence (CL) petrography with LA-ICP-MS trace element analyses of carbonates from drill core samples through the main ore bodies at the southern Carpentaria George Fisher deposit (165 Mt at 9.1 % Zn, 3.4 % Pb, and 55 g/t Ag; Glencore 2019) and from a drill-hole that intersected correlative, unmineralized host rock lithologies (Urquhart Shale Formation). The resultant *in situ* data are then compared to REE+Y compositions from whole rock data from the same samples.

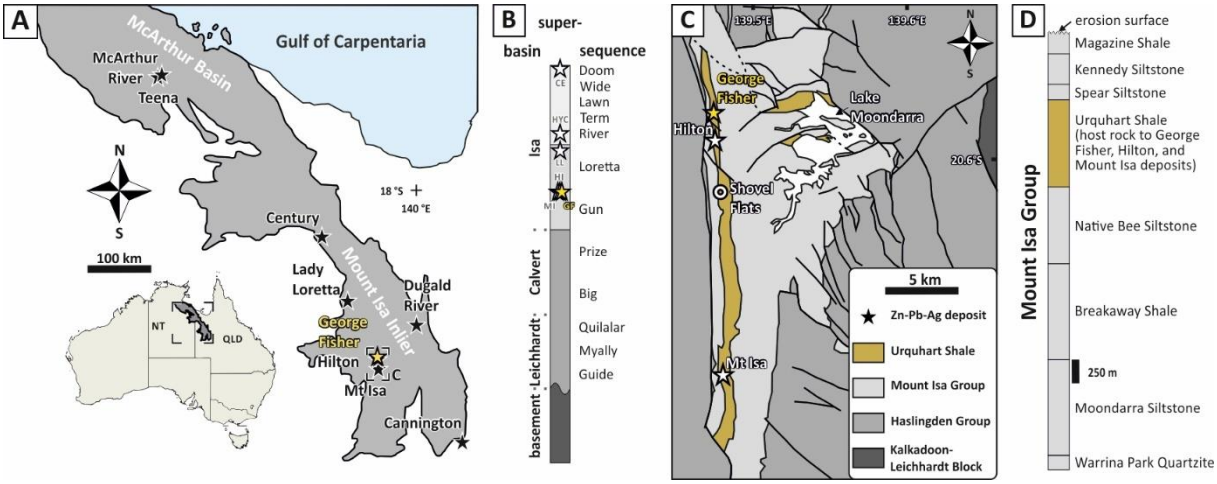

Fig. 4-1 (A) A map showing the Carpentaria province. Major Zn-Pb deposits in the Mount Isa Inlier and in the McArthur basin are denoted by stars. (B) Simplified superbasin stratigraphy for the Mount Isa Inlier (after Southgate et al. 2000). Stars denote approximate locations of the George Fisher (GF), Hilton (HI), Mount Isa (MI), Lady Loretta (LL), McArthur River (HYC), and Century (CE) clastic-dominated Zn-Pb massive sulphide deposits. (C) A map of the Mount Isa area showing simplified bedrock geology (after Gibson et al. 2017). The locations of the George Fisher, Hilton, and Mount Isa deposits and the unmineralized drill-hole (Shovel Flats) are denoted by stars and a circle respectively. (D) The stratigraphy of the Mount Isa Group (approximate formation thicknesses adapted from Neudert 1983).

4.3. Rare earth elements and yttrium (REE+Y)

The REE+Y are hard cations (high charge/radius ratio) and all have broadly similar chemical behaviour, although subtle differences in solubility occur due to decreasing ionic radii from the light to the heavy REE+Y (e.g., Bau 1991; Migdisov et al. 2009; Williams-Jones et al. 2012). As a consequence of the Oddo-Harkins effect, elements with even atomic numbers are more abundant than those with uneven atomic numbers; therefore, the REE+Y are typically normalized to reference values (e.g., post-Archean Australian shale - PAAS, McLennan 1989; chondrite, McDonough and Sun 1995), which allows for better evaluation of the relative fractionation from different reservoirs and among individual REE+Y subgroups (light, middle, and heavy rare earth elements; LREE, MREE, and HREE). This fractionation can then be used to trace biogeochemical processes and to constrain fluid chemistry in low and high temperature settings (for reviews see Debruyne et al. 2016 and Smrzka et al. 2019).

The REE+Y are mostly trivalent (3^+), apart from Ce (3^+, 4^+), Eu (2^+, 3^+), and Yb (2^+, 3^+), which are redox sensitive. The redox sensitivity of Yb is only important at high temperatures (> 420 °C), whereas Ce and Eu can undergo valence changes at ambient and lower hydrothermal temperatures under geochemically reasonable fO_2 conditions

(Fig. 4-2B). The fractionation of Ce and Eu relative to their neighbouring REE can, therefore, be used to constrain fluid redox conditions (e.g., De Baar et al. 1983; Sverjensky 1984; Bau and Möller 1992). This contrasting behaviour is expressed as empirical anomalies relative to reference values, which can either be determined linearly or geometrically (e.g., Lawrence et al. 2006). The Ce anomalies (Ce/Ce^*_N) are typically shale-normalized (e.g., to PAAS; Ce/Ce^*_{SN}) in order to evaluate seawater or pore water redox, whereas Eu anomalies are commonly chondrite-normalized (Eu/Eu^*_{CN}) to avoid overestimation of Eu/Eu^* values due to the negative Eu anomaly of PAAS (Fig. 4-2A).

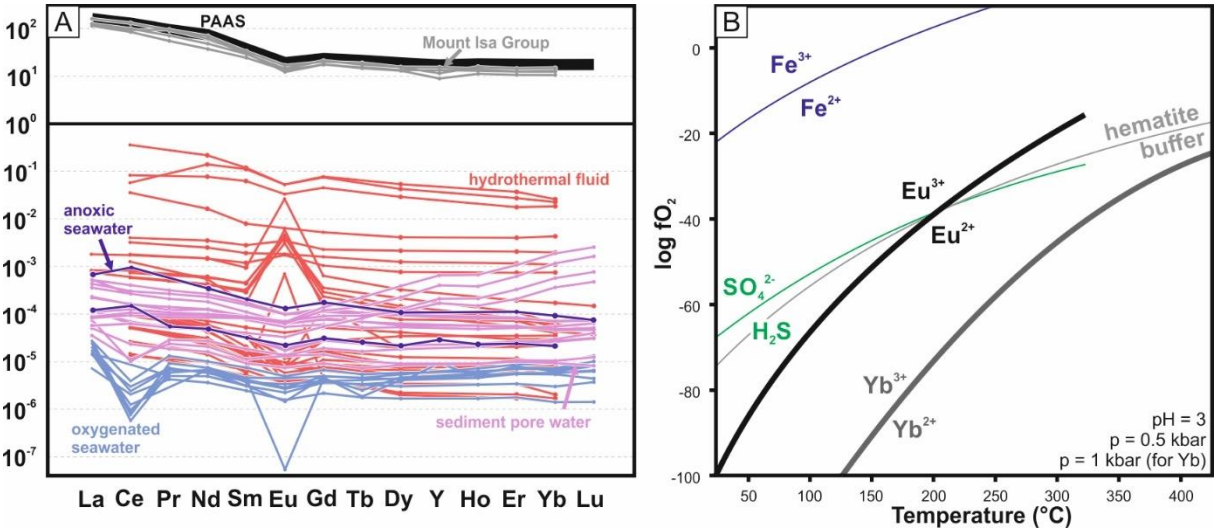

Fig. 4-2 (A) The chondrite normalized (McDonough and Sun 1995) rare earth element and Y patterns for: the post-Archean Australian shale reference material (black; PAAS, McLennan 1989), the Mount Isa Group (grey; Breakaway Shale, Native Bee Siltstone, Spear/Kennedy Siltstone, Magazine Shale; Nance and Taylor 1976), hydrothermal fluid literature data (red; Michard and Albarède 1986; Michard 1989; James et al. 1995; James and Elderfield 1996; Bau and Dulski 1999), modern oxygenated seawater data (light blue; James et al. 1995; Alibo and Nozaki 1999; Haley et al. 2004; Deng et al. 2017), modern anoxic seawater data (dark blue; Schijf et al. 1995; Bau et al. 1997), and modern sediment pore water data (light purple; Haley et al. 2004; Soyol-Erdene and Huh 2013; Deng et al. 2017). (B) Redox equilibria for Eu^{3+}/Eu^{2+}, Yb^{3+}/Yb^{2+}, Fe^{3+}/Fe^{2+}, and SO_4^{2-}/H_2S as a function of temperature and oxygen fugacity (after Bau and Möller 1992).

Yttrium and Ho exhibit similar geochemical behaviour, although Ho is preferentially complexed and removed from fluids by Fe-oxides and organic particles; consequentially, seawater, and seawater-derived fluids, preserve super-chondritic (>28) Y/Ho values, whereas crustal fluids have chondritic Y/Ho (Zhang et al. 1994; Nozaki et al. 1997; Bau and Dulski 1999). Similarly, there are subtle differences in the adsorption of LREE, MREE, HREE, and Ce onto organic particles, oxide phases, or mineral phases (e.g., German and Elderfield 1989; Sholkovitz et al. 1994; Alibo and Nozaki 1999). These

differences affect the absolute and relative abundances of REE+Y in seawater as a function of redox state and water depth; further modification can then occur due to mineral formation or redox reactions in early diagenetic pore waters (e.g., Haley et al. 2004; Abbott et al. 2019; for REE+Y reference profiles see Fig. 4-2A and for a recent review on REE+Y fractionation see Smrzka et al. 2019).

The REE+Y partition strongly into carbonate minerals (e.g., Tanaka and Kawabe 2006; Voigt et al. 2017), are enriched in crustal rocks (>chondrite) and occur only as trace components in fluids (<chondrite; Fig. 4-2A). As a consequence, high fluid-rock ratios are necessary to alter whole rock REE+Y budgets, whereas fluid REE+Y compositions can be strongly affected even at low fluid rock ratios (Michard and Albarède 1986; Bau 1991). Therefore, REE+Y signatures of marine and diagenetic carbonate mineral phases are good archives of fluid chemistry and generally unaffected by later diagenesis (e.g., Webb et al. 2009; Liu et al. 2019).

Ligand concentration, pH, and temperature can have strong effects on REE+Y solubility in aqueous solutions (e.g., Michard 1989; Craddock et al. 2010; Williams-Jones et al. 2012) and the REE+Y composition of hydrothermal fluids can be extremely variable (Fig. 4-2A). Fluid-mineral interactions under hydrothermal conditions can also modify the REE+Y signatures of carbonate mineral phases (Vaughan et al. 2016). Commonly, hydrothermal fluids have positive Eu/Eu^* and $REE+Y_{CN}$ profiles that are LREE enriched, which has been interpreted to directly result from dissolution of plagioclase during fluid-rock interaction (e.g., Klinkhammer et al. 1994; Douville et al. 1999). Alternatively, empirical and experimental studies suggest that both the LREE and Eu^{2+} are more soluble in high temperature Cl-rich fluids (Migdisov et al. 2009; Craddock et al. 2010; Williams-Jones et al. 2012). Because of the higher solubility of Eu^{2+} relative to Eu^{3+}, the temperature-dependent redox sensitivity of Eu has a strong effect on Eu/Eu^*; for example, under geochemically reasonable fO_2 the more soluble Eu^{2+} is only dominant over Eu^{3+} at temperatures above 200-250 °C (Fig. 4-2B; Sverjensky 1984; Bau 1991; Bilal 1991). As a consequence, positive Eu/Eu^* can only develop in hot (>200-250 °C) hydrothermal fluids. Divalent Eu is, however, not readily incorporated into the carbonate crystal lattice, which is why positive Eu/Eu^* can only develop in carbonate

mineral phases that formed from hot fluids that cooled below 200-250 °C in order to stabilize Eu^{3+} (Bau and Möller 1992). Many hydrothermal carbonates also preserve LREE depletion relative to PAAS (e.g., Roberts et al. 2009; Debruyne et al. 2013; Magnall et al. 2016a). Such LREE depleted REE+Y signatures in hydrothermal precipitates have been interpreted to result from co-precipitation with LREE-enriched phases (Roberts et al. 2009), LREE scavenging by fluid-mineral interaction along the fluid pathway (e.g., by monazite; Debruyne et al. 2016), inherited REE+Y signatures from fluid-rock interaction (Lüders et al. 1993; Hecht et al. 1999), or LREE retention in the fluid by Cl-complexes (Craddock et al. 2010; Magnall et al. 2016a).

4.4. Geological Background

The Carpentaria Province comprises the Mount Isa Inlier and the McArthur Basin, which formed in an intracontinental setting during the Paleo- to Mesoproterozoic (Betts et al. 2002, 2016; Giles et al. 2002). During this time, three unconformity bound superbasins formed due to episodic rifting, sag phase, and basin inversion; those superbasins can be further subdivided into twelve supersequences (Fig. 4-1; e.g., Jackson et al. 2000; Southgate et al. 2000, 2013). The George Fisher, Hilton, and Mount Isa massive sulphide deposits are hosted by the Urquhart Shale Formation, which is part of the Mount Isa Group of the Isa Superbasin (Southgate et al. 2000, 2013). Closure of the superbasins was initiated by the onset of the Isan orogeny (ca. 1600 Ma), in which the rocks of the Mount Isa Inlier have undergone multiple phases of deformation in at least four separate north-south or east-west directed deformation events (Page and Bell 1986; Connors and Page 1995; Bell and Hickey 1998).

The Urquhart Shale Formation was deposited at ca. 1652 ± 7 Ma and comprises mainly laminated to bedded mudstones and siltstones, which are variably calcareous, dolomitic, carbonaceous, and pyritic (Page and Sweet 1998; Painter et al. 1999; Page et al. 2000). The depositional environment of the Urquhart Shale Formation was interpreted as either a carbonate slope (Neudert 1983; Painter 2003) or deeper water environment (Domagala et al. 2000). Moderate concentrations of organic carbon (< 2 wt. %) and Mo (< 30 ppm) are consistent with anoxic and ferruginous seawater, which

is further supported by sulphur isotope values of diagenetic pyrite that do not preserve evidence of extreme sulphate limitation under euxinic conditions (Rieger et al. 2020).

Carbonates are major rock forming mineral phases in the Urquhart Shale. There are several types of detrital, diagenetic, and hydrothermal calcite and dolomite. Zoned, porous, silt-sized detrital calcite and dolomite were deposited together with other clastic mineral grains (Painter et al. 1999) and potentially entirely replaced by diagenetic carbonate (Chapman 1999). Diagenetic carbonates comprise calcareous and dolomitic cements, which was interpreted as supratidal crusts (e.g., Neudert 1983; Painter et al. 1999), as seafloor cementation (Domagala et al. 2000), or as carbonate alteration (Chapman 1999). Furthermore, nodular carbonates have been interpreted as diagenetic precipitates (e.g., Chapman 1999, 2004; Domagala et al. 2000; Painter 2003), as diagenetic pseudomorphs after sulphate minerals (e.g., van den Heuvel 1969; McClay and Carlile 1978; Painter et al. 1999), or as hydrothermal replacement textures (Perkins 1997; Perkins and Bell 1998). In and around the George Fisher, Hilton, and Mount Isa deposits there are several types of calcite, dolomite, and siderite veins, infill, and breccias associated with the Zn-Pb and Cu ore systems (e.g., Waring 1990; Valenta 1994; Chapman 1999). Generally, carbonate mineral phases are more dolomitic, and Fe- and Mn-bearing at the Mount Isa and George Fisher deposits relative to the unmineralized Urquhart Shale (Painter 2003; Chapter 3). Furthermore, the ore forming systems have likely produced ^{18}O-depleted carbonate haloes around the mineral deposits in the Urquhart Shale Formation beyond visible alteration (Waring 1990; Chapman 1999). Besides differences in carbonate mineralogy and isotopic composition, the footprints of these CD-type massive sulphide deposits are evident from element enrichment (e.g., Tl, Mn, Ag) and depletion (e.g., Na, Sr) in whole rock data (Painter 2003; Chapter 3). The main sulphide minerals at George Fisher are pyrite, sphalerite, galena, and pyrrhotite, and chalcopyrite occurs only in minor quantities; these sulphides occur in multiple generations (Chapman 1999, 2004; Murphy 2004; Rieger et al. 2020). Recently, Rieger et al. (2020) described pre-ore diagenetic fine-grained pyrite followed by three ore stages: (1) stratabound sphalerite + pyrite ± galena, (2) breccia-hosted galena + sphalerite + pyrite + pyrrhotite, and (3) vein and breccia-hosted pyrite + pyrrhotite + chalcopyrite ± galena and sphalerite.

A whole rock lithogeochemistry study on Urquhart Shale samples from an unmineralized drill-core and from the George Fisher deposit has shown that REE+Y, Si, Al, Ti, Sc, Nb, and Th were immobile during hydrothermal alteration, and that mineralization at George Fisher resulted in dilution of these immobile elements (Chapter 3). The nature of any REE+Y fractionation was not discussed in chapter 3 and so the data are presented here in Fig. 4-3 and in the electronic appendix, and fully discussed below. The REE+Y_{CN} profiles for Urquhart Shale and massive sulphide samples are LREE enriched, and have relatively flat MREE and HREE profiles, as well as negative Eu/Eu^{*} and chondritic Y/Ho (Fig. 4-3). These REE+Y_{CN} profiles are generally very similar to PAAS and to other formations from the Mount Isa Group, yet, are offset to lower concentrations (Fig. 4-3; Nance and Taylor 1976; McLennan 1989).

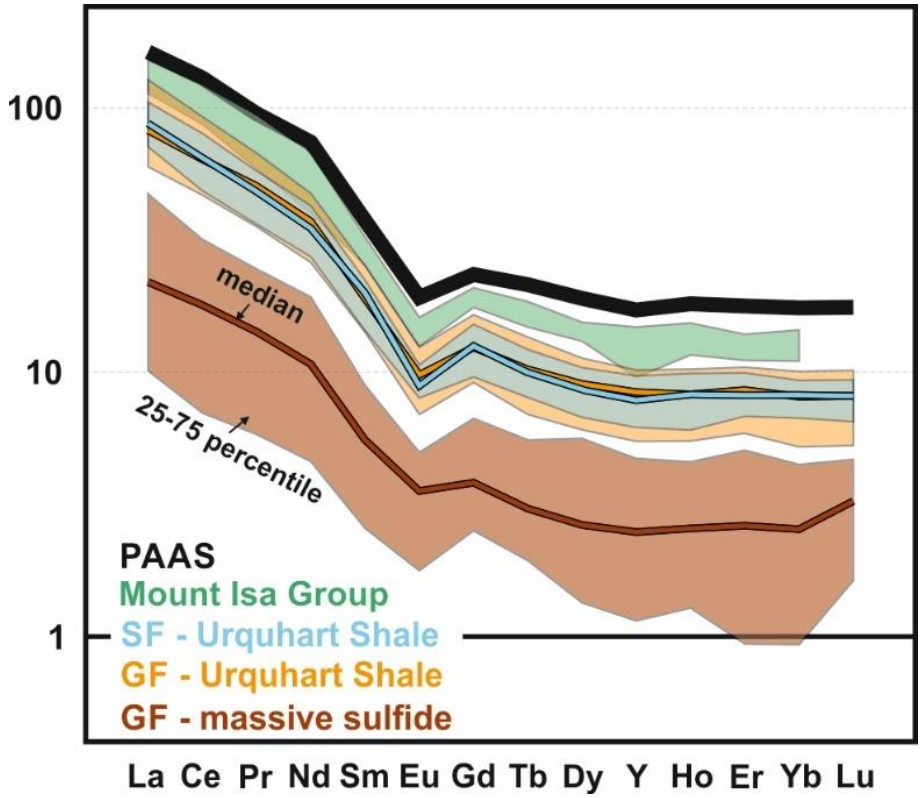

Fig. 4-3 The chondrite normalized (McDonough and Sun 1995) rare earth element and Y reference patterns for: PAAS (black; McLennan 1989), the Mount Isa Group (green; Breakaway Shale, Native Bee Siltstone, Spear/Kennedy Siltstone, Magazine Shale; Nance and Taylor 1976), whole rock data from unmineralized Urquhart Shale (blue; Shovel Flats; Chapter 3), whole rock data from mineralized Urquhart Shale (orange; George Fisher; Chapter 3), and whole rock data from massive sulphides (dark red; George Fisher; Chapter 3).

4.5. Methods

4.5.1. Sampling and petrography

Representative samples were selected from a drill-core that intersected unmineralized Urquhart Shale (Shovel Flats drill-hole; n = 91) and from 4 drill-holes that intersected mineralized Urquhart Shale at the George Fisher deposit (drill-hole 8C K751, n = 61; 10C K795, n = 77; 10C K798, n = 57; 12C I797, n = 30). At George Fisher, representative samples were taken from the main ore bodies, weakly mineralized sections, barren siltstones or mudstones, and from sections of stratigraphically continuous hanging wall stratigraphy.

Drill-core samples were examined using a binocular microscope and key samples were selected for polished thin section preparation (n= 95). Thin sections were further examined using transmitted and reflected light microscopy and representative carbonate samples were selected for cathodoluminescence (CL) petrography (n = 30). The hot-cathode optical CL system was operated at 14 keV and 0.15-0.20 mA. To capture zonation and differences in luminescence, exposure times were varied and quartz grains were used as reference for luminescence intensity, because quartz is characterized by very low CL relative to carbonates or feldspars (Marshall 1988).

4.5.2. Electron probe micro-analyser (EPMA)

Quantitative wavelength dispersive spectrometry (WDS) was performed on a JEOL Superprobe JXA 8230, Hyperprobe JXA 8500F and Hyperprobe JXA-8530Fplus. The samples were coated with a 20 nm thick carbon film and quantified for Mg, Ca, Fe, Mn, Sr, and partly Ba and Zn in carbonates using an acceleration voltage of 15 kV, a beam current of 10 nA, a probe size of 5-40 µm depending on the grain size and relative short measurement times between 10 to 50 sec (for background and peak). Those analytical parameters are reported as optimal for precise electron probe micro analyses of carbonates (Zhang et al. 2019). The $\phi(\rho Z)$ matrix correction scheme (CITZAF; Armstrong 1995) was applied and natural standards were analysed during the course of the analytical sessions to ensure the quality of measured data. Standards were Calcite (Ca), Dolomite (Ca, Mg), Siderite (Fe), Strontianite (Sr), Rhodonite (Mn), $BaSi_2O_5$ for

Ba and ZnS for Zn. Under these conditions, analytical errors (2σ) and detection limits were 1.5 % and 300 ppm for Ca, 0.4 % and 300 ppm for Mg, Mn, and Fe, 0.1 % and 200 ppm for Zn and Sr, and 0.1 % and 350 ppm for Ba.

4.5.3. Mass spectroscopy (LA-ICP-MS)

Laser ablation ICP-MS of 19 polished thin sections was carried out using the Analyte Excite 193 nm ArF* excimer-based laser ablation (LA) system (Teledyne Photon Machines, Bozeman, MT, USA), coupled to the quadrupole-ICP-MS iCAP from Thermo Scientific. The LA-system is equipped with a HelEx II 2-volume ablation cell. Helium was used as a carrier gas for aerosol transport from the sample surface to the ICP and was mixed downstream with Ar as a make-up gas before entering the plasma. Operational parameters of the ICP-MS instrument and LA-unit were tuned for maximum sensitivity, low oxide formation based on the $^{232}Th^{16}O/\ ^{232}Th$ ratio and low laser-induced elemental fractionation based on the $^{232}U/\ ^{232}Th$ ratio using NIST SRM 610. We used ^{43}Ca as internal standard and the certified reference material NIST610 for calibration for all elements. Samples were ablated with a spot size of 50 µm, for 30 s with a repetition rate of 10Hz and an energy density of 2-3 J/cm^2. Time intervals for data reduction were selected by visual inspection of each spectrum using Iolite™ (Paton et al. 2011) and the data reduction scheme X_trace_elemets_IS (Woodhead et al. 2007). Uncertainty estimates for the elements measured are based on repeated measurement of the reference material MACS-3 and ECRM-752 and are in general below 10 %. Data were then screened for contamination by other mineral phases than carbonates (e.g., silicates, phosphates, sulphides) by using the elements Al, K, P, S, Si, and Ti. Data with high concentrations of these elements (Al + K + P + S + Si + Ti > 1000 ppm) were then rejected.

The Ce/Ce* and Eu/Eu* values were calculated geometrically (cf. Lawrence et al. 2006):

$$Eu/Eu^*_{CN} = \left(\frac{Eu}{(Sm^2 * Tb)^{\frac{1}{3}}}\right)_{CN} \text{ and } Ce/Ce^*_{SN} = \left(\frac{Ce}{Pr*(\frac{Pr}{Nd})}\right)_{SN}$$

Lanthanum was not used to calculate Ce* in order to avoid the influence of La anomalies on Ce/Ce* values (cf. Bau and Dulski 1996).

4.6. Results

4.6.1. Carbonate in the Urquhart Shale Formation

Detrital carbonate grains are most abundant in siltstone lithologies and preserve similar grain size (≤ 20 μm) and morphology (sub-rounded to angular) to detrital feldspar and quartz grains. Micritic calcite and dolomite is common throughout all lithologies and is very fine-grained (< 5 μm). These detrital and micritic carbonates were too fine grained for LA-ICP-MS analyses and will not be discussed further. Carbonate nodules are interbedded with laminated, pyritic, carbonaceous siltstones. Nodules are, typically, several cm long and wide in the lateral and vertical direction (Fig. 4-4A, B). Calcite is the dominant carbonate phase in the carbonate nodules and calcite grains are anhedral to subhedral and >10 μm. Coarse-grained (>100 μm) calcite veins cross-cut all lithologies and often contain euhedral pyrite. Where the veins cross-cut carbonate nodules, euhedral pyrite can occur in the nodules.

4.6.2. Carbonate at the George Fisher deposit

Both calcite and dolomite have been observed in the paragenesis at the George Fisher deposit. When calcite and dolomite occur together, calcite can be differentiated by a brighter luminescence, whereas dolomite commonly has a red, low intensity luminescence signal (Fig. 4-4I). Nodular carbonates at George Fisher have similar morphologies to those from Shovel Flats samples, but comprise mostly anhedral to subhedral finer grained dolomite and minor amounts of coarser grained calcite. The edges of carbonate nodules are also commonly replaced by sphalerite (Fig. 4-4H).

Within the sulphide paragenesis described by Rieger et al. (2020; i.e. ore stages 1, 2, and 3), there are multiple phases of hydrothermal carbonate. The most abundant type of this carbonate is anhedral, coarse-grained (>100 μm), and Fe-rich dolomite; it is generally observed with anhedral quartz, and is in textural disequilibrium with sphalerite and galena, which is indicated by irregular grain boundaries and partial replacement of the sulphides after dolomite (e.g., Fig. 4-5H, I). The dolomites, therefore, likely formed before sulphide precipitation of the individual ore stages.

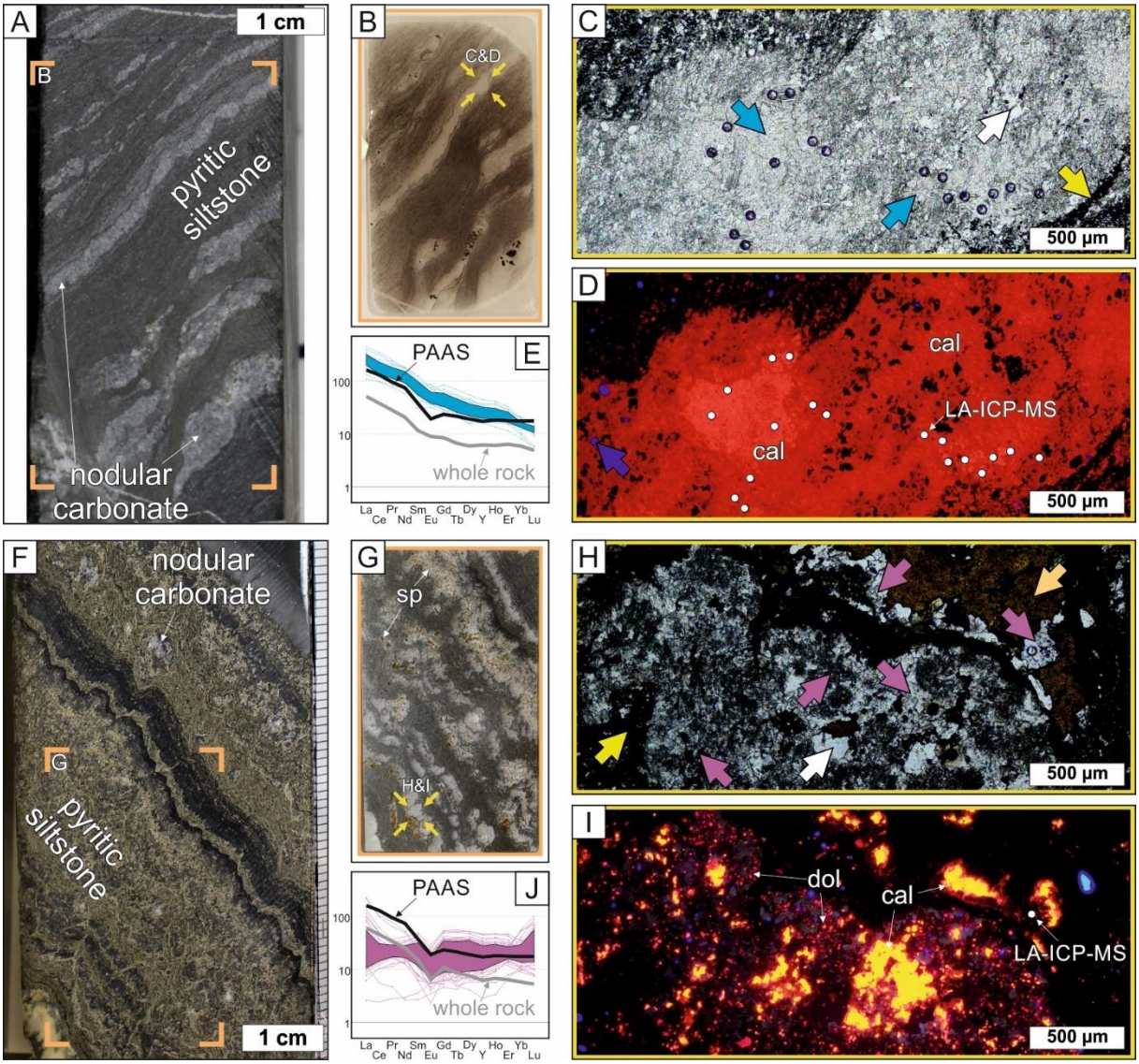

Fig. 4-4 (A-E) An unmineralized nodular carbonate sample from the background drill-core. (A) A hand sample photograph. (B) A thin section photograph. (C) A transmitted light microphotograph; the arrows indicate respective mineral phases (blue = calcite; white = quartz; yellow = pyrite). (D) A cathodoluminescence microphotograph of the area shown in C, white circles indicate LA-ICP-MS analysis spots in calcite and the blue arrow indicates a K-feldspar grain with blue luminescence. (E) The chondrite-normalized REE+Y patterns of calcite from this sample (PR832SF080). (F-I) A mineralized nodular carbonate sample from George Fisher. (F) A hand sample photograph. (G) A thin section photograph. (H) A transmitted light microphotograph; the arrows indicate respective mineral phases (purple = dolomite and calcite; white = quartz; yellow = pyrite; light orange = sphalerite). (I) A cathodoluminescence microphotograph of area shown in H; the white circle indicates a LA-ICP-MS analysis spot. Note the strong difference in the luminescence signal between bright, yellow calcite and dull, red dolomite. (J) The chondrite-normalized REE+Y pattern of calcite and dolomite from this sample (PRK751017).

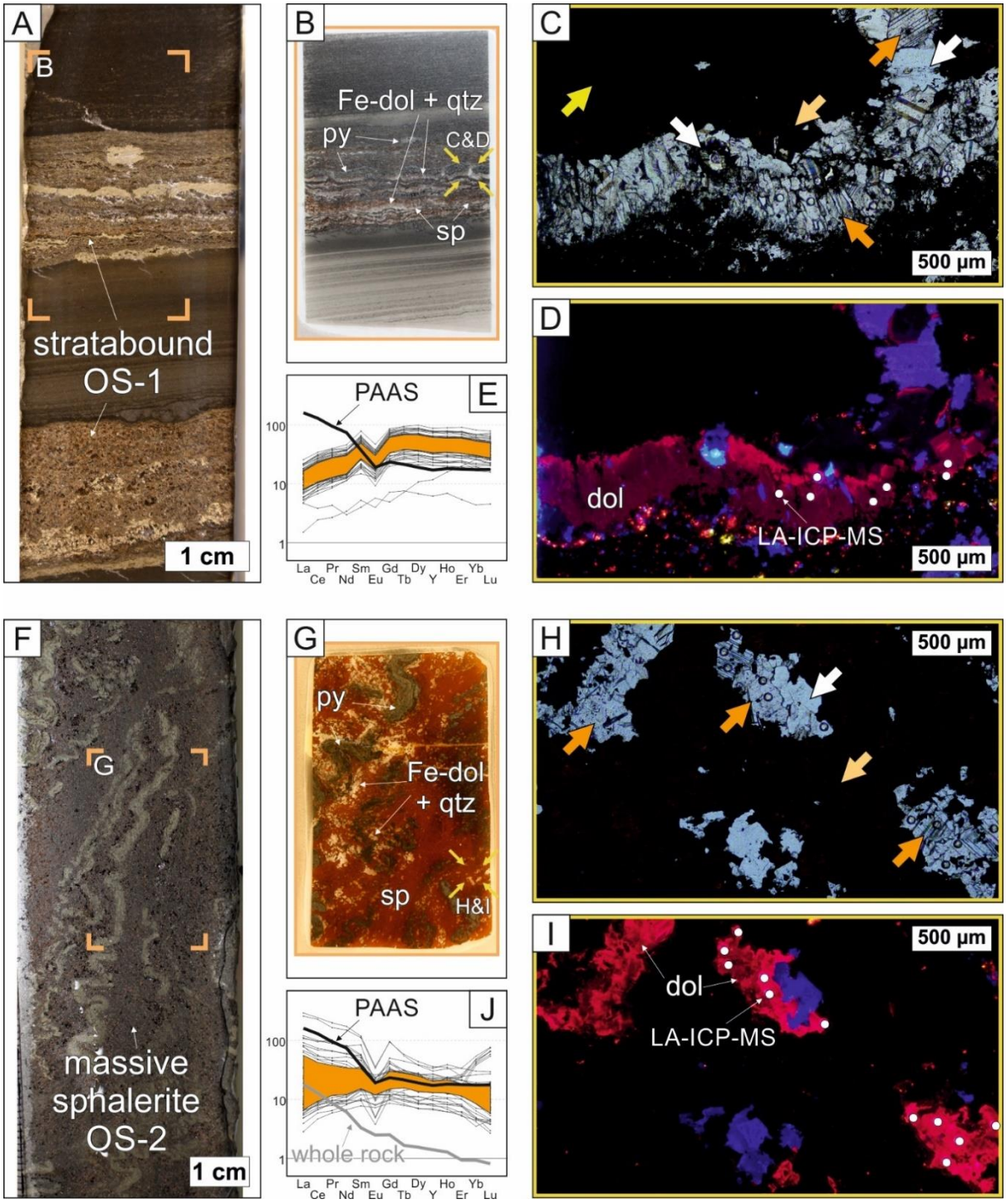

Fig. 4-5 (A-E) Carbonate in a stratabound massive sulphide sample from ore stage 1. (A) A hand sample photograph. (B) A thin section photograph. (C) A transmitted light microphotograph, the arrows indicate respective mineral phases (orange = dolomite; white = quartz; yellow = pyrite; light orange = sphalerite). (D) A cathodoluminescence microphotograph of the area shown in C; the white circles indicate LA-ICP-MS analysis spots in dolomite. (E) The chondrite-normalized REE+Y patterns of dolomite from this sample (PRK798C014). (F-I) Carbonate in a massive sulphide breccia sample from ore stage 2. (F) A hand sample photograph. (G) A thin section photograph. (H) A transmitted light microphotograph; the arrows indicate respective mineral phases (orange = dolomite; white = quartz; light orange = sphalerite). (I) A cathodoluminescence microphotograph of the area shown in H; the white circles indicate LA-ICP-MS analysis spots in dolomite. (J) The chondrite-normalized REE+Y patterns of dolomite from this sample (PRK751024).

In ore stage 1, this Fe-rich dolomite occurs in stratabound veins together with massive sulphide (e.g., Fig. 4-5C, D). In the later ore stages 2 and 3, this dolomite occurs as irregular clasts in massive sulphide breccias (e.g., Fig. 4-5H, I). The other, less abundant, types of carbonate that are associated with massive sulphides are calcites and dolomites that have planar crystal faces at 120° with quartz and sphalerite; they were, therefore, formed in textural equilibrium with quartz and sphalerite directly from the hydrothermal fluid (Fig. 4-6D, E). In the samples studied here, these calcites and dolomites have only been found associated with ore stage 2. They are coarse-grained (> 100 µm) and occur in cross-cutting, mineralized carbonate-quartz veins or in carbonate-quartz infill adjacent to massive sulphide (Fig. 4-6). For the purpose of further discussion, these carbonates that are associated with the massive sulphides will be grouped into two types: hydrothermal dolomite type A, which comprises the dolomites that are in textural disequilibrium with sulphide minerals; and hydrothermal calcite and dolomite type B, which comprises the carbonates that are in textural equilibrium with sulphide minerals.

There are also barren veins with coarse-grained calcite (> 100 µm) at George Fisher that cross-cut massive sphalerite of ore stage 1. In the samples studied here, the paragenetic relationship of these barren calcite veins with ore stage 2 and 3 could not be observed.

4.6.3. Major element data – electron probe micro-analyser (EPMA)

Major element data for carbonates plot between the endmember compositions of calcite, dolomite and ankerite (Fig. 4-7). Calcite grains plot near the modal composition of calcite with $MgCO_3$, $FeCO_3$, and $MnCO_3$ concentrations generally below 1.6 wt.%, 1.5 wt.%, and 1.1 wt.% respectively. Dolomite and ankerite grains plot between the endmember modal compositions of the two minerals and preserve a range of $MgCO_3$, $FeCO_3$, and $MnCO_3$ concentrations between 9-46 wt.%, 2-37 wt.%, and 0.2-9 wt.% respectively. Overall, the carbonate major element data from this study are consistent with data for the George Fisher and Hilton deposits from other studies (Fig. 4-7; Valenta 1988; Chapman 1999; Murphy 2004).

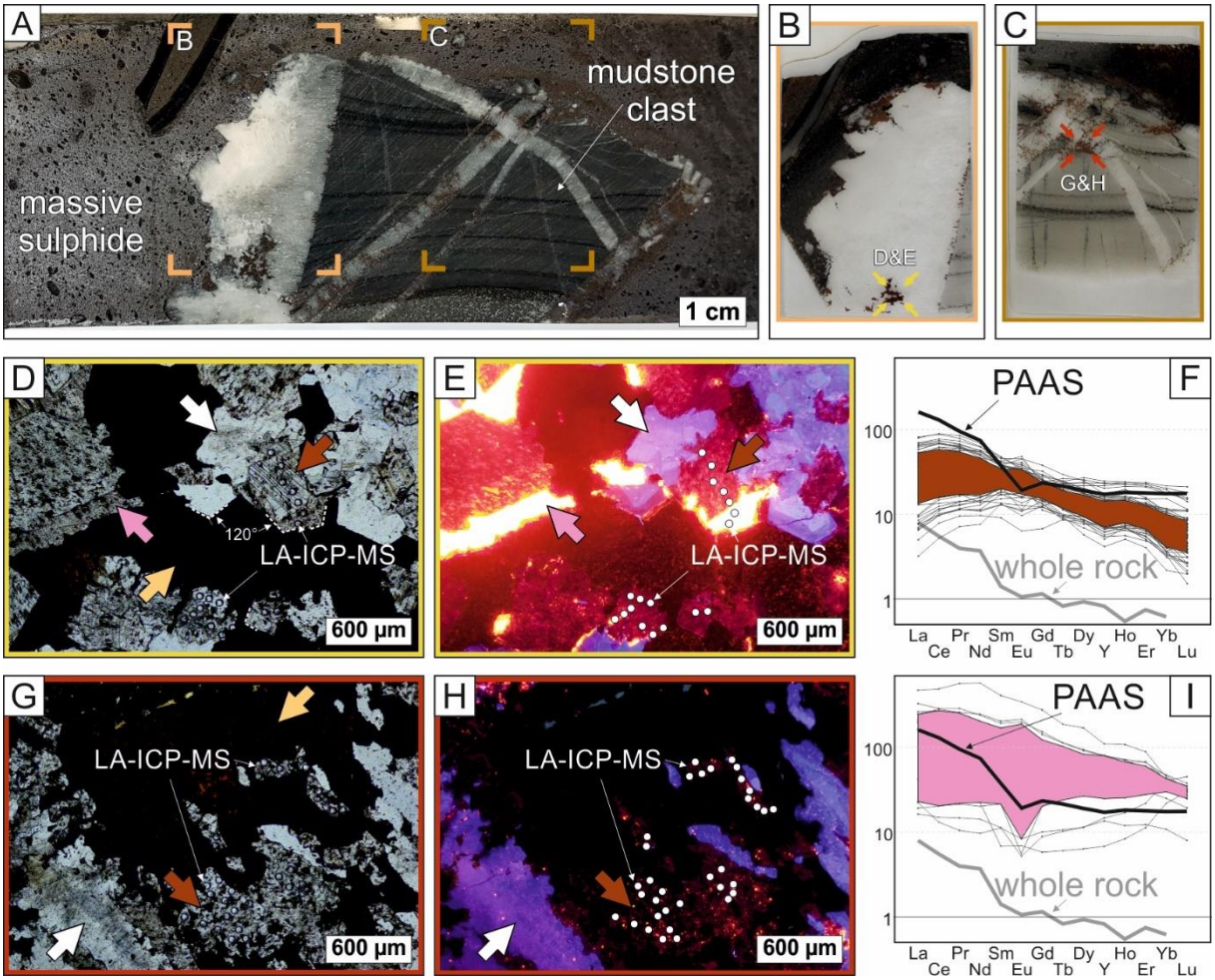

Fig. 4-6 (A-I) Carbonate veins and infill in a massive sulphide breccia sample from ore stage 2 (sample PRK7952037). (A) A hand sample photograph. (B) A thin section photograph. (C) A thin section photograph. (D) A transmitted light microphotograph of the area indicated in B; the arrows indicate respective mineral phases (dark red = dolomite; pink = calcite; white = quartz; light orange = sphalerite). A textural equilibrium of carbonate and quartz phases with ore-stage sphalerite is indicated by planar crystal faces orientated at 120°. (E) A cathodoluminescence microphotograph of the area shown in D; the white circles indicate LA-ICP-MS analysis spots in dolomite and calcite. (F) The REE+Y data of dolomite from this sample. (G) A transmitted light microphotograph of the area indicated in C; the arrows indicate respective mineral phases (dark red = dolomite; white = quartz; light orange = sphalerite). (H) A cathodoluminescence microphotograph of the area shown in G; the white circles indicate LA-ICP-MS analysis spots in dolomite. (I) The REE+Y data of calcite from this sample.

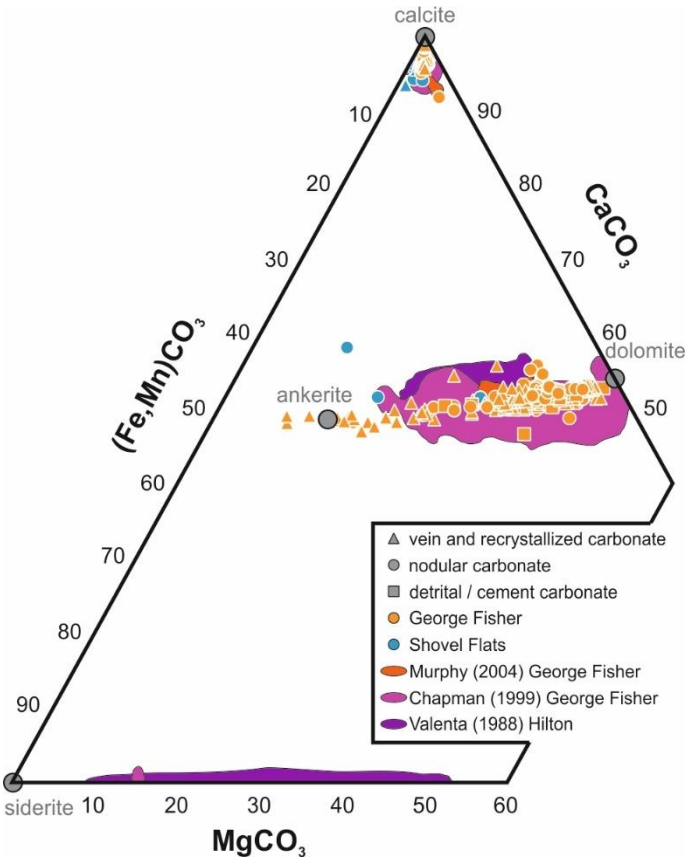

Fig. 4-7 A $CaCO_3$-$MgCO_3$-$(Fe,Mn)CO_3$ ternary diagram of carbonates from the George Fisher deposit and the Shovel Flats drill core. The coloured fields denote EPMA carbonate data from Murphy (2004), Chapman (1999), and Valenta (1988). Endmember compositions of calcite, dolomite, ankerite, and siderite are shown in grey.

4.6.4. Rare earth elements and Yttrium (REE+Y) – laser-ablation ICP-MS (LA-ICP-MS)

Total rare earth element concentrations (ΣREE) of carbonates are generally within one order of magnitude of the post-Archean Australian shale (PAAS; Fig. 4-8, Fig. 4-9C), and several times higher than REE concentrations in modern seawater, diagenetic pore fluids, and hydrothermal fluids (cf. Fig. 4-2).

Generally, the nodular calcites from Shovel Flats samples have $REE+Y_{CN}$ profiles similar to PAAS (Fig. 4-8A), whereas nodular calcites and dolomites at George Fisher have more variable $REE+Y_{CN}$ profiles (Fig. 4-8C). Hydrothermal dolomites type A from ore stages 1, 2, and 3 have $REE+Y_{CN}$ profiles that are LREE depleted and preserve negative Eu/Eu^* (Fig. 4-8D). Hydrothermal calcite and dolomite type B also have $REE+Y_{CN}$ profiles that are depleted in LREE, but preserve positive Eu/Eu^* (Fig. 4-8E, F). The highest Eu/Eu^* values are preserved in hydrothermal carbonate type B (calcite and dolomite; Fig. 4-8E, F, Fig. 4-9E) and in calcite veins from the Shovel Flats drill hole (Fig. 4-8B, Fig. 4-9E). The Ce/Ce^* values are distributed around unity and are slightly skewed to negative anomalies (Fig. 4-9B). The Y/Ho values are variable, but are generally

distributed between 15 and 50, Pr/Yb_{SN} values are typically below 1 in George Fisher dolomite and calcite, and the greatest variability in both Y/Ho and Pr/Yb_{SN} is preserved in nodular dolomite and calcite from George Fisher samples (Fig. 4-9D, E).

The *in situ* composition of nodular calcite from Shovel Flats samples preserves overall higher REE+Y concentrations than whole rock samples, whereas carbonates at George Fisher are generally LREE depleted (Fig. 4-10A). When the data are normalized to the respective whole rock REE+Y value, the *in situ* carbonate data from George Fisher is LREE depleted, whereas Shovel Flats nodular calcite REE+Y profiles are relatively flat (Fig. 4-10B).

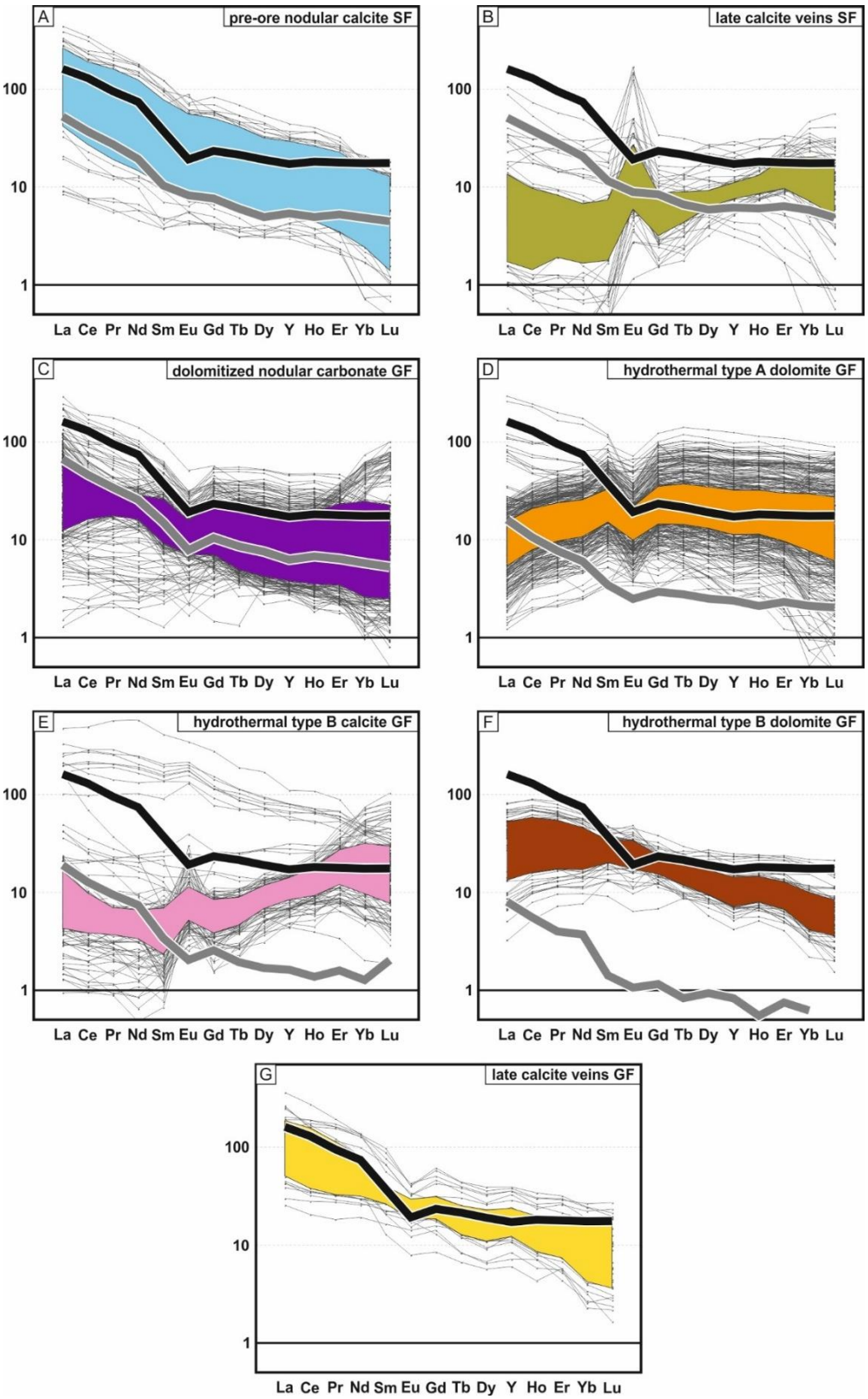

Fig. 4-8 (A-G) The chondrite normalized (McDonough and Sun 1995) REE+Y data for different carbonate sub-groups from the George Fisher deposit and the Shovel Flats drill-core. (A) Nodular carbonate (calcite) from the Shovel Flats drill core. (B) Late calcite veins from the Shovel Flats drill-core. (C) Nodular carbonate (calcite and dolomite) from George Fisher. (D) Hydrothermal type A dolomite from George Fisher. (E) Hydrothermal type B calcite from George Fisher. (F) Hydrothermal type B dolomite from George Fisher. (G) Late calcite veins from George Fisher. The coloured fields in A-G denote the 25-75 percentile for the respective sub-groups, thin black lines are the REE+Y patterns of individual analyses, thick black lines are PAAS (McLennan 1989), and grey lines are median values of REE+Y whole rock data of the respective samples that in situ data was generated from (whole rock data from chapter 3).

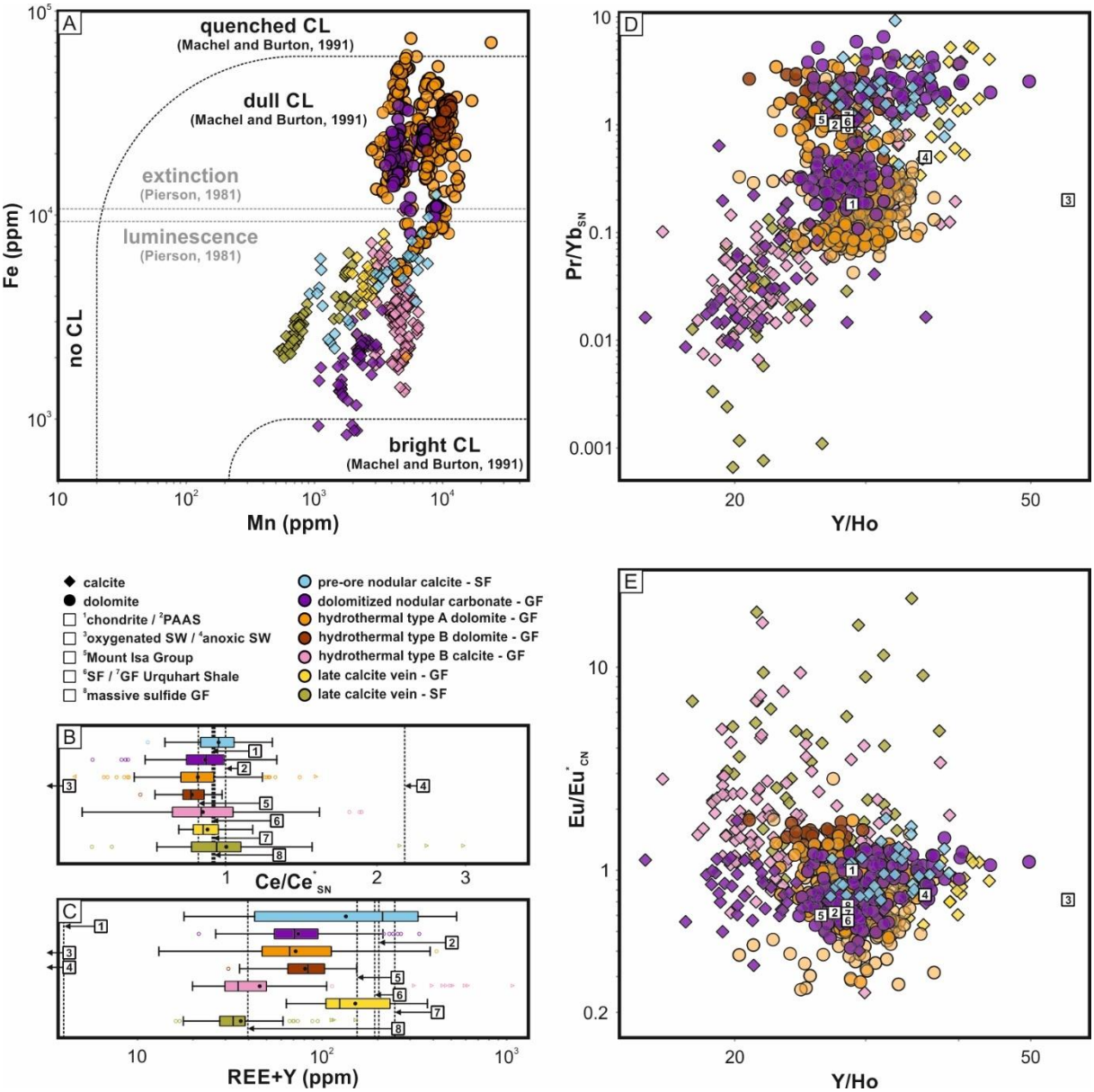

*Fig. 4-9 (A) The Mn and Fe concentrations of calcite and dolomite from the Shovel Flats drill core and the George Fisher deposit. Dashed lines denote expected cathodoluminescence signal of carbonate phases as a function of Fe and Mn concentration (fields after Pierson 1981; Machel and Burton 1991). (B) Box and whisker plot of Ce/Ce$_{SN}$ for individual carbonate sub-groups. Boxes are 50 % of the data (Q1 to Q3), black lines and balls indicate median and mean values respectively, whiskers denote extreme values, and circles and triangles are outliers with >1.5*Q3-Q1 and >3*Q3-Q1 respectively. (C) Box and whisker plot of REE+Y concentrations for individual carbonate sub-groups. (D) The ratios of Y/Ho and Pr/Yb$_{SN}$ for calcite and dolomite from the Shovel Flats drill core and the George Fisher deposit. (E) The ratio of Y/Ho and Eu/Eu*$_{CN}$ values of calcite and dolomite from the Shovel Flats drill core and the George Fisher deposit. Figures (B-E) also show reference values of chondrite (1; McDonough and Sun 1995), PAAS (2; McLennan 1989), oxygenated seawater (3; Alibo and Nozaki 1999), anoxic seawater (4; Bau et al. 1997), the median value of the Mount Isa Group (5; Nance and Taylor 1976), and the whole rock median values of Urquhart Shale from the unmineralized Shovel Flats drill-core (6), from the George Fisher deposit (7), and from massive sulphide samples from George Fisher (8; chapter 3). Note that values of #3, and #3 and #4 are lower than the plotted x-axis for (B) and (C).*

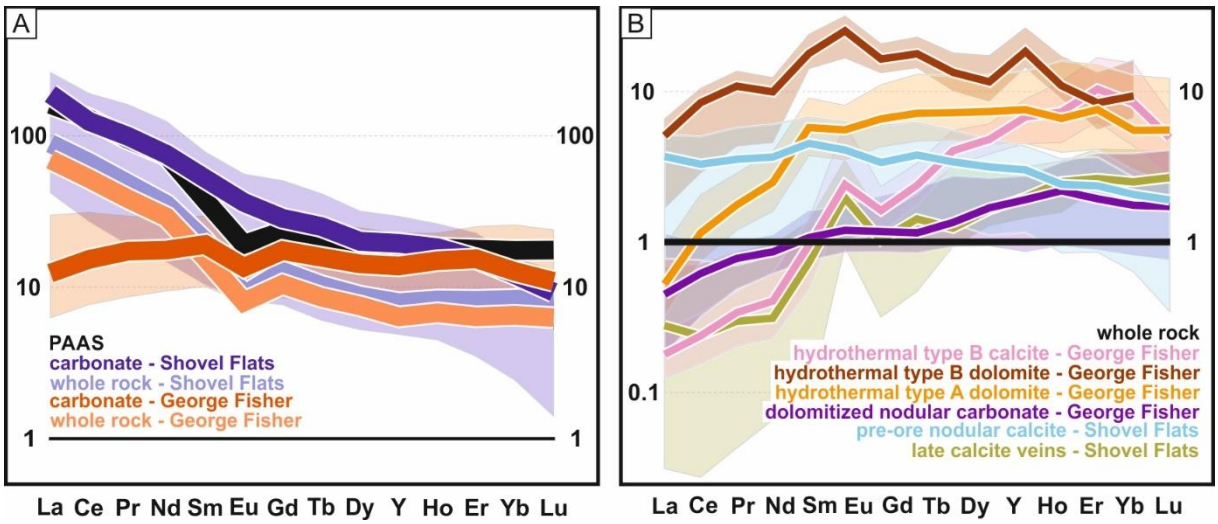

Fig. 4-10 (A) The chondrite normalized REY data for samples from the Shovel Flats drill-core and the George Fisher deposit. The lines denote median values for in situ carbonate data from the Shovel Flats drill core (dark blue) and from the George Fisher deposit (red), and for whole rock REE+Y data from the Shovel Flats drill core (light blue; n = 41) and from the George Fisher deposit (orange; Urquhart Shale and massive sulphide; n = 69); the light purple (Shovel Flats) and light red (George Fisher) fields denote the 25-75 percentiles of the in situ carbonate REE+Y data. For more detailed whole rock data see Fig. 3. (B) The REE+Y data (medians and 25-75 percentiles) for individual carbonate sub-groups from the Shovel Flats drill-core and the George Fisher deposit normalized to respective whole rock REE+Y data of the respective sample that in situ data was generated from.

4.7. Discussion

4.7.1. Pre-ore carbonate

The unmineralized Paleoproterozoic Urquhart Shale Formation consists of carbonate-rich siltstones and mudstones that comprise detrital, micritic, and nodular carbonates (e.g., Neudert 1983; Chapman 1999; Painter et al. 1999). The detrital and micritic carbonate is fine grained (≤ 20 µm) and not amenable to laser ablation studies, but the nodular carbonates are coarser grained and occur both in the barren Urquhart Shale at Shovel Flats and in the George Fisher deposit. In the mineralized units the nodular carbonates pre-date the first phase of mineralization (Fig. 4-4; Chapman 2004; Chapter 3), and therefore, provide constraints on carbonate formation under pre-ore conditions.

The nodular carbonates in the Urquhart Shale have been interpreted as pseudomorphs after sulphate evaporites (e.g., Painter et al. 1999) or as diagenetic precipitates (cf. Domagala et al. 2000; Chapman 2004). Indicators for shallow-water, evaporitic conditions, such as halite casts and stromatolites, are preserved in other

formations of the Mount Isa Group (McClay and Carlile 1978; Neudert and Russell 1981; Neudert 1983). However, sulphur isotope values of early diagenetic pyrite (cf. Painter et al. 1999; Rieger et al. 2020) indicate that open-system conditions with respect to sulphate availability were dominant during deposition and early diagenesis of the Urquhart Shale. Such conditions are inconsistent with the closed system conditions typical of evaporite formation and more typical of diagenetic carbonate precipitation (cf. Domagala et al. 2000; Chapman 2004). The composition of the nodular carbonates from the Urquhart Shale Formation is, therefore, considered representative of diagenetic pore fluids, which predated the hydrothermal system at George Fisher.

The REE+Y systematics in seawater and diagenetic pore fluids are typically controlled by redox processes (for a review see Smrzka et al. 2019). Unlike the modern oxygenated oceans, Mid- and Paleoproterozoic oceans were mostly ferruginous (anoxic, non-sulphidic), with euxinic conditions spatially and temporally restricted to highly productive margins and oxygenated conditions only developed in surface waters (e.g., Canfield 1998; Planavsky et al. 2011; Lyons et al. 2014). Indeed, the REE+Y compositions of Proterozoic carbonates are consistent with REE+Y systematics observed in modern anoxic basins (cf., Bau et al. 1997; Tang et al. 2016; Bellefroid et al. 2019). Such REE+Y systematics are characterized by variable Ce/Ce^*_{SN} and Eu/Eu^*_{CN} values around unity, variable chondritic to super-chondritic Y/Ho, $REE+Y_{CN}$ profiles that are similar to PAAS (e.g., Planavsky et al. 2010; Tang et al. 2016; Bellefroid et al. 2019). Compared to oxygenated seawater (Fig. 4-2A), these contrasting REE+Y signatures are likely the result (1) of the dissolution of LREE-, Ce-, and Ho-enriched phases, such as Mn-oxides, at the chemocline between oxidizing and reducing seawater, and (2) enhanced solubility of Eu^{2+} under reducing conditions (Planavsky et al. 2010). In this context, the distribution of Ce/Ce^*_{SN} and Eu/Eu^*_{CN} values slightly above or below unity together with Y/Ho between chondritic and super-chondritic values (Fig. 4-9B, E), and $REE+Y_{CN}$ profiles similar to PAAS (Fig. 4-4E, Fig. 4-8A) in nodular calcites are consistent with pore waters derived from anoxic bottom waters during the deposition of the Urquhart Shale Formation. The existence of ferruginous conditions is supported by the sulphur isotope values of early diagenetic pyrite and Mo concentrations from the Urquhart Shale (Rieger et al. 2020; Chapter 3) and concurs with growing evidence for wide-spread ferruginous

conditions in Proterozoic oceans (e.g., Poulton et al. 2010; Planavsky et al. 2011; Song et al. 2017). As such, the nodular carbonate chemistry from the unmineralized Urquhart Shale Formation preserves normal background marine and early-diagenetic signatures for the Proterozoic.

4.7.2. Carbonate at George Fisher

The George Fisher deposit was formed from a multi-stage mineralizing system (Chapman 2004; Rieger et al. 2020), and it is possible that multiple processes contributed to the trace element composition of George Fisher carbonates. The deposit comprises a number of different carbonate generations (this study; Chapman 1999) and, generally, hydrothermal alteration has resulted in dolomitization of pre-ore calcite (chapter 3). For example, nodular carbonates from unmineralized (Fig. 4-4A-E; Shovel Flats) and mineralized (Fig. 4-4F-J; George Fisher) Urquhart Shale samples are considerably different in that the George Fisher nodular carbonate samples can be partially replaced by sphalerite and have higher dolomite/calcite ratios (Fig. 4-4G, H; chapter 3). Furthermore, nodular carbonates from the unmineralized rocks have homogenous CL signals (Fig. 4-4D), whereas those at George Fisher have irregular signals with relatively bright CL of calcite compared to dull and quenched CL of dolomite (Fig. 4-4I). Such dull and quenched luminescence is characteristic of carbonate minerals with high Mn and Fe concentrations (Pierson 1981; Machel and Burton 1991; Baele et al. 2019), which is also consistent with the major element chemistry of George Fisher and Shovel Flats carbonates (Fig. 4-7, Fig. 4-9A). These irregular CL signals (Fig. 4-4I) and variable Fe and Mn concentrations (Fig. 4-9A), together with higher whole rock dolomite/calcite ratios (chapter 3), are consistent with dolomitization of pre-ore calcite that was associated with the mineralization at George Fisher. Similar to calcite and dolomite in nodular carbonate samples at George Fisher, type A dolomite has dull to quenched luminescence (Fig. 4-5C, H). It is, therefore, likely that dolomitization was associated with all stages of mineralization at George Fisher.

The sulphide replacement textures and irregular grain boundaries with sphalerite (Fig. 4-4G-I, Fig. 4-5C, D, H, I) are indicative of a pre-sphalerite timing for some dolomitization at the onset of mineralization. Notably, such a timing for dolomitization

is consistent with carbonate formation at the onset of mineralization suggested by Chapman (1999). If dolomitization took place at the onset of mineralization, the REE+Y data of these pre-sphalerite dolomites can provide constraints on the hydrothermal fluids that caused the alteration of pre-ore calcites before the precipitation of base metal sulphides. The dolomite and calcite from type B formed in textural equilibrium with sphalerite (Fig. 4-6D, E). The composition of this type B calcite and dolomite may, therefore, provide constraints on the hydrothermal fluids during sphalerite formation. In order to constrain the syn-sphalerite end-member of the hydrothermal fluid the REE+Y composition of this type B carbonate is discussed first.

Type B calcite and dolomite is characterized by (1) LREE depletion relative to PAAS, respective whole rock, and pre-ore calcite, (2) chondritic and sub-chondritic Y/Ho, and (3) Eu/Eu^* values >1 (Fig. 4-6F, I, Fig. 4-8E, F Fig. 4-9D, E). Light rare earth element fractionation is a common feature of hydrothermal fluids and there are a number of processes that could have produced the $REE+Y_{CN}$ profiles in the type B carbonates (Fig. 4-6F, I, Fig. 4-8E, F). A mineralogical control on this LREE fractionation is unlikely because both calcites and dolomites are, overall, LREE depleted relative to pre-ore calcite (Fig. 4-8A, E, F). This observation is consistent with other studies on hydrothermal gangue carbonates that indicate no significant REE+Y fractionation between calcite and dolomite (e.g., Hecht et al. 1999; Roberts et al. 2009). Light rare earth element-depleted $REE+Y_{CN}$ profiles in carbonate mineral phases can also be inherited from complexation-controlled REE+Y-leaching from crustal source rocks (e.g., Lüders et al. 1993) or from LREE-scavenging by mineral phases with high REE-partition coefficients (e.g., monazite) along the fluid pathways (e.g., Debruyne et al. 2013, 2016). The source rocks for the mineralization are unknown at George Fisher. Equally, whether the footwall units could contain significant amounts of phosphatic minerals is also unknown. However, if the REE+Y signatures were inherited from the metal source or fluid-rock interaction along the flow pathway, they would likely be more homogeneous than the variability preserved in the REE+Y profiles of hydrothermal calcite and dolomite at George Fisher (Fig. 4-6F, I, Fig. 4-8E, F). Notably, the rocks of the Mount Isa Group and of the unconformably underlying Eastern Creek Volcanics have LREE enriched $REE+Y_{CN}$ profiles (Fig. 4-3; Nance and Taylor 1976; Hannan et al. 1993); as a

consequence, a hydrothermal fluid buffered by these rocks would most likely not be LREE depleted. Instead, the observed variability may result from closed system Rayleigh fractionation during carbonate precipitation, which is consistent with variable LREE concentrations in type B calcites (e.g., Fig. 4-6I).

Fluid composition and temperature also provide a major control on REE+Y fractionation (e.g., Michard 1989; Craddock et al. 2010; Williams-Jones et al. 2012). Unfortunately, there are no direct constraints on the composition of the mineralizing fluids at George Fisher (e.g., fluid inclusions). Based on the basin fill in the stratigraphy below the Carpentaria CD-type deposits, Cooke et al. (2000) suggested that the mineralizing fluids were likely oxygenated, neutral to mildly acidic, and saline brines (ca. 25 wt. % $NaCl_{equiv}$), which would have been highly effective in transporting Zn and Pb at moderate temperatures (150 °C). Fluid inclusion data from the relatively undeformed Century deposit do indicate relatively low temperature (<125 °C) and high salinity fluids (ca. 23 wt. % $NaCl_{equiv}$; Polito et al. 2006). Notably, salinity can have a strong effect on REE+Y solubility and fractionation. For example, experimental studies and numerical modelling of REE+Y partitioning and solubility in hydrothermal fluids suggest that chlorides are the dominant ligands for REE+Y-complexation at hydrothermal temperatures and that Cl-ligands form the strongest complexes with the REE+Y with the lowest charge/radius ratios (Eu^{2+} and LREE; e.g., Migdisov et al. 2009; Williams-Jones et al. 2012; Perry and Gysi 2018). If the mineralizing fluids for the George Fisher deposit were saline (cf. Cooke et al. 2000; Polito et al. 2006), Cl-complexes were likely the dominant ligands for REE+Y-complexation. Under such conditions, LREE are more soluble, which could have resulted in stronger LREE-retention in the fluid during carbonate precipitation. Consequently, $REE+Y_{CN}$ profiles of syn-ore carbonates should be LREE depleted.

A second common signature of type B carbonates at George Fisher are chondritic and sub-chondritic Y/Ho ratios (Fig. 4-9D, E). Chondritic Y/Ho ratios are typical of hydrothermal fluids (Bau and Dulski 1999; Douville et al. 1999), whereas sub-chondritic Y/Ho may indicate further fractionation of Y relative to Ho. Experiments at ambient temperatures suggest that Ho partitions more strongly into calcite than Y (e.g., Tanaka

and Kawabe 2006). Such differential partitioning is consistent with sub-chondritic Y/Ho ratios in type B carbonates at George Fisher. There is, however, no experimental data available for Y/Ho fractionation during carbonate precipitation at hydrothermal temperatures. If future experiments show differential fractionation of Y and Ho into carbonate minerals at hydrothermal temperatures, sub-chondritic Y/Ho values may be a distinguishing criterium for hydrothermal carbonates.

A third dominant feature of type B carbonates at George Fisher are Eu/Eu^* values >1 (Fig. 4-6F, I, Fig. 4-8E, F, Fig. 4-9B). The major control on Eu/Eu^* is temperature (Fig. 4-2; Sverjensky 1984; Bau 1991; Bilal 1991). In oxidized hydrothermal fluids, such as those suggested for the Carpentaria CD-type deposits ($SO_4^{2-} > H_2S$; Cooke et al. 2000), Eu/Eu^* values >1 can only develop at high temperatures, because the more soluble Eu^{2+} is only stable at temperatures >200-250 °C (Fig. 4-2B; Sverjensky 1984; Bau 1991; Bilal 1991). It is, therefore, unlikely that the George Fisher deposit formed from fluids that were initially cooler than 200 °C, which is in contrast to fluid temperatures suggested by Cooke et al. (2000). Divalent Eu is, however, not readily incorporated into the crystal lattice of carbonate minerals (Bau and Möller 1992); and therefore, such hot, Eu^{2+}-dominated hydrothermal fluids (>200-250 °C) must have cooled significantly in order to stabilize sufficient Eu^{3+} to produce Eu/Eu^* values >1 in the type B calcites and dolomites at George Fisher. Such cooling of initially hot fluids is consistent with thermodynamic models for sulphide formation (Rieger et al. 2020), calcite twinning temperatures (Murphy 2004) at George Fisher, and also with overall temperature constraints for the Urquhart Shale Formation (see summary for temperature constraints in chapter 3). Furthermore, this is consistent with Eu/Eu^* values <1 preserved by type A dolomites from ore stage 2 (Fig. 4-5J). These Eu/Eu^* values <1 in type A dolomites concur with the hypothesis that the hydrothermal fluids were hot at the onset of mineralization, and then cooled below 200-250 °C before type B calcite and dolomite formation.

Dolomites that formed from dolomitization of pre-ore calcite at the onset of mineralization are preserved both in samples of mineralized nodular carbonate and in massive sulphide samples at George Fisher (Fig. 4-4F-I, Fig. 4-5A-I). Partially mineralized nodular carbonates preserve the highest textural variability, together with

the highest variability in the REE+Y composition (Fig. 4-4E, J, 8C, 9B-D). Therefore, they likely comprise mixed REE+Y compositions from pre-ore diagenetic and hydrothermal end members, which is consistent with the large ranges of LREE depletion relative to pre-ore calcite and the large variability of Y/Ho values (Fig. 4-8C, Fig. 4-9D). The REE+Y data of type A dolomites at George Fisher are slightly more homogenous than those of mineralized nodular carbonates (Fig. 4-8D, Fig. 4-9D), and this may indicate that the REE+Y data are more dominated by hydrothermal signatures as a result of more dolomitization. The $REE+Y_{CN}$ profiles of type A dolomites are LREE depleted relative to PAAS, pre-ore calcite, and to whole rock REE+Y profiles (Fig. 4-4J, Fig. 4-5E, J, Fig. 4-8D, Fig. 4-10B). This LREE depletion is similar to $REE+Y_{CN}$ profiles of type B calcite and dolomite and consistent with Cl-complexation and LREE-retention in the fluid (see discussion above).

Chemical alteration and dissolution-reprecipitation of carbonates are not limited to the high grade domains of ore deposits, and chemical and isotopic changes in carbonates can be traced beyond zones of visible alteration (e.g., Barker et al. 2013; Vaughan et al. 2016). In fact, isotopic studies indicate that large scale ^{18}O-depletion in carbonates is associated with the Mount Isa Cu-system (Waring 1990; Waring et al. 1998a), and similarly, ^{18}O-depletion has also been reported for carbonates from the George Fisher Zn-Pb system (Chapman 1999). There is, therefore, the potential that the mineralizing fluids at George Fisher have also produced alteration of the REE+Y signatures beyond the highly mineralized zones. For example, sulphide formation resulted in a fluid that was metal depleted and that had a higher availability of chloride (e.g., $ZnCl_2 + HS^- \rightarrow ZnS + H^+ + 2Cl^-$). Such a fluid would have caused even higher solubilities of LREE as Cl-complexes, which could have resulted in LREE depletion along the fluid migration pathway beyond visible alteration.

Post-dating the Zn mineralization there are late calcite veins that cross-cut stratabound mineralization at George Fisher, and late calcite veins that cross-cut all lithologies, and are coeval with euhedral pyrite, in the unmineralized Shovel Flats drill-core. Cross-cutting calcite veins have also been described before at Mount Isa and George Fisher (e.g., Waring et al. 1998b; Murphy 2004). The calcite veins at George

Fisher preserve REE+Y signatures similar to the pre-ore calcites and to PAAS (Fig. 4-8G, Fig. 4-9), which may indicate that they are rock buffered. The late calcite veins from Shovel Flats preserve REE+Y signatures that are more similar to type B calcites (Fig. 4-8B, Fig. 4-9). Therefore, they may represent distal expressions of a hydrothermal system. The differential REE+Y data clearly suggest that there are, at least, two generations of late calcite veins. These veins were, however, not the focus of this study and future work is needed to understand their significance and relationship to mineralization.

Overall, the Y/Ho ratios, Eu/Eu^* values, and LREE depleted $REE+Y_{CN}$ profiles that are characteristic of George Fisher calcite and dolomite are consistent with interaction of a hot, saline (Cl-rich) hydrothermal fluid that subsequently cooled to temperatures below 200-250 °C during fluid-rock interaction. Notably, such conditions correspond well with other CD-type systems, for which the thermal evolution of the hydrothermal fluids is well constrained (e.g., MacMillan Pass; Magnall et al. 2016a).

4.7.3. Implications for the application of *in situ* REE+Y carbonate data

In this study, we present very detailed *in situ* REE+Y data on a small number of samples from the mineralized and unmineralized Urquhart Shale Formation. The sample coverage is not sufficient to evaluate the 3D REE+Y footprint of the mineralizing system at George Fisher. However, the *in situ* REE+Y carbonate data documented here do have important implications for ore formation and for future exploration programs.

The George Fisher deposit formed from a multi-stage system and all mineralization post-dates the deposition of the host rock (Chapman 2004; Rieger et al. 2020). Therefore, the mineralizing fluids must have replaced the host rock, or at least parts of it, in order to create sufficient porosity for fluid flow and base metal sulphide precipitation. The fractionation between whole rock REE+Y data and carbonate *in situ* REE+Y data (Fig. 4-10A, B) indicates that (1) carbonate mineral phases were more sensitive to REE+Y alteration relative to the whole rock, and that (2) fluid-rock ratios were not high enough to alter whole rock REE+Y compositions (cf. Michard and Albarède 1986; Bau and Möller 1992). This suggests that the hydrothermal fluids at George Fisher were highly selective in replacing and altering pre-ore carbonate mineral

phases. It is, therefore, possible that fluid-rock interaction of the Urquhart Shale Formation at George Fisher with hot, acidic, saline, and base metal-bearing hydrothermal fluids has resulted in the replacement and dolomitization of pre-ore calcite, which led to the development of secondary porosity, fluid cooling, and pH increase. This would have resulted in lower solubilities of base metals and subsequent sulphide precipitation. Such a diagenetic carbonate replacement model is consistent with (1) carbonate replacement textures (e.g., Fig. 4-4; Chapman 2004; chapter 3), with (2) fluid cooling indicated by Eu/Eu^{*} <1 in type A dolomites opposed to Eu/Eu^{*} >1 in type B dolomites and calcites (Fig. 4-8D-F, Fig. 4-9E), and with (3) Cl-rich hydrothermal fluids indicated by LREE depleted $REE+Y_{CN}$ profiles in George Fisher carbonates (Fig. 4-4J, Fig. 4-5E, J, Fig. 4-6F, I, Fig. 4-8C-F, Fig. 4-10). Notably, carbonate replacement was reported for a number of other CD-type massive sulphide systems in the Carpentaria province (Eldridge et al. 1993; Perkins and Bell 1998; Chapman 2004; Spinks et al. 2019; Magnall et al. 2020b), which highlights the importance of the reactive carbonate-rich host rocks throughout the province.

It is generally accepted that base metal deposits in sedimentary basins form from saline hydrothermal brines (Bodnar et al. 2014; Heinrich and Candela 2014); and indeed, previous studies on Zn-Pb- and Cu-systems in the Carpentaria province suggest that saline fluids were responsible for base metal transport (Heinrich et al. 1989; Cooke et al. 2000; Polito et al. 2006). At George Fisher, the LREE depleted $REE+Y_{CN}$ profiles in calcite and dolomite (Fig. 4-4J, Fig. 4-5E, J, Fig. 4-6F, I, Fig. 4-8C-F, Fig. 4-10A, B) are consistent with LREE-retention in such Cl-rich saline hydrothermal fluids (see discussion above). In fact, there is evidence that LREE depletion is a common feature of carbonate mineral phases from a number of mineral deposits that formed from saline fluids (Roberts et al. 2009; Debruyne et al. 2013; Genna et al. 2014; Magnall et al. 2016a), whereas LREE depletion is not evident from carbonates that precipitated from low-salinity fluids that were dominated by S- or CO_3-complexes (Maskenskaya et al. 2015; Vaughan et al. 2016). As a consequence, LREE depletion in calcites or dolomites relative to background REE+Y profiles may be an effective tracer for fluid-rock interaction involving saline hydrothermal fluids. So, if this hypothesis is supported by future studies, the analysis of REE+Y in carbonate mineral phases could be useful for future exploration

programs in sedimentary basins in order to identify hydrothermally altered carbonate-rich lithologies.

In summary we show that LA-ICP-MS analyses of REE+Y in carbonate minerals can distinguish hydrothermal carbonate from pre-existing diagenetic carbonate, and this may be a useful exploration tool in combination with whole rock and isotope geochemistry in sediment hosted mineral deposits. Future studies should test this hypothesis by systematically sampling the 3D grid around an (undeformed) deposit to assess the nature of the distal footprint on carbonate REE+Y systematics.

4.8. Conclusions

Like many sediment-hosted massive sulphide deposits, the George Fisher deposit (165 Mt at 9.1 % Zn, 3.4 % Pb, and 55 g/t Ag; Glencore 2019) comprises several types of carbonate mineral phases. Pre-ore nodular calcite likely formed via diagenetic processes from ferruginous (anoxic, non-sulphidic) Proterozoic seawater. Interaction of a hot (>200-250 °C) hydrothermal fluid with the host rocks at George Fisher caused selective dolomitization and replacement of pre-ore calcite, fluid cooling and base metal sulphide precipitation. Evidence for these processes is preserved by dull CL signals, fractionated $REE+Y_{CN}$ profiles (LREE-depletion), and by both positive and negative Eu/Eu^* values in calcite and dolomite. The difference in REE+Y signatures between *in situ* data from calcite and dolomite at George Fisher and respective whole rock data also indicates that carbonate mineral phases are more sensitive to hydrothermal REE+Y alteration. Furthermore, the LREE depleted $REE+Y_{CN}$ profiles preserved in carbonates at George Fisher may be a common feature of hydrothermal carbonates in base metal deposits that formed from saline Cl-rich fluids. Overall, this study shows that *in situ* REE+Y analysis of carbonate mineral phases combined with petrographic techniques can be used to differentiate between pre-ore and hydrothermally altered carbonate-rich lithologies.

4.9. Acknowledgment

We would like to thank the geology teams at Mount Isa Mines George Fisher operation and Mount Isa Mines Resource Development for support during field work and for access to drill cores. Funding for this project was provided by a Helmholtz recruitment initiative grant to S. Gleeson. Furthermore, we acknowledge U. Dittmann and E. Lewerenz for sample preparation.

5. Conclusions

This thesis had two main aims. Firstly, to identify the accumulation processes of reduced sulphur at the George Fisher deposit, and secondly, to constrain the mineralogical and geochemical footprint of the mineralizing system at George Fisher. In order to understand the processes responsible for mineralization at George Fisher, and the mineralogical and geochemical anomalies they produced, it was essential to understand the mineralogical, and whole rock and isotope geochemical background composition of the unmineralized Urquhart Shale Formation.

This chapter highlights the new findings presented in chapters 2-4 and the implications they have for (1) the depositional environment and the background composition of the Urquhart Shale Formation, for (2) the mineralizing system at George Fisher, and for (3) the identification of CD-type massive sulphide footprints for future exploration programmes in the Carpentaria province. Furthermore, I give some suggestions on future research that could improve the understanding of the mineralizing system at George Fisher, and that could help to refine exploration models in the Carpentaria province.

5.1. The unmineralized Urquhart Shale Formation

As outlined in chapter 3, the Urquhart Shale consists of relatively immature siliciclastic components (e.g., a high abundance of feldspar), which is characteristic for Precambrian sedimentary rocks, because of limited chemical weathering due to low atmospheric pO_2 at that time (Rafiei and Kennedy 2019); and notably, the mineralogical composition of the Urquhart Shale Formation is very similar to other late Paleoproterozoic and early Mesoproterozoic fine-grained sedimentary rocks of the Carpentaria province (e.g., Barney Creek Formation; Baruch et al. 2015; Revie and Normington 2020). Moderate enrichment of total organic carbon (1 to 2 wt.%) in the siltstones and mudstones from the Urquhart Shale Formation provided sufficient reductants for the early diagenetic redox reactions (e.g., microbial sulphate reduction, MSR) that resulted in the formation of reduced sulphur and bicarbonate (chapter 2). Together with reactive Fe and Ca, this reduced sulphur and bicarbonate reacted to diagenetic pyrite and nodular calcite (chapter 2, 3, and 4). The pre-ore timing of these diagenetic mineral phases suggests that their trace element and isotope geochemistry can be used to constrain paleoredox conditions during sedimentation and early diagenesis of the Urquhart Shale. The $\delta^{34}S$ values of this early diagenetic pyrite are significantly offset to more negative $\delta^{34}S$ values relative to Paleoproterozoic seawater sulphate ($\Delta^{34}S$ = 6.2–33.1 ‰; chapter 2). This offset implies that open-system MSR was responsible for sulphate reduction, which means that the deposition and diagenesis of the Urquhart Shale Formation was dominated by open-system conditions with respect to sulphate availability. Such conditions are inconsistent with a euxinic water column ($H_2S > SO_4^{2-}$, and $H_2S > Fe^{2+}$), which concurs with non-euxinic conditions indicated by low Mo concentrations in the mudstone and siltstone samples from the Urquhart Shale Formation (chapter 3). Further paleoredox constraints from the REE+Y composition of nodular calcite suggest that these carbonates formed from diagenetic fluids derived from anoxic seawater (chapter 4). The anoxic, non-euxinic conditions inferred from these redox proxies are, furthermore, consistent with the presence of fine-grained chlorite in pore spaces of the unmineralized Urquhart Shale Formation; as this chlorite likely formed diagenetically from Fe-silicate precursor phases, which are characteristic of

ferruginous pore waters during early diagenesis (chapter 3). Notably, the diagenetic formation of fine-grained chlorite concurs with temperature indicators, which imply that the Urquhart Shale Formation at this location, has not undergone greenschist facies metamorphism (chapter 3).

The new paleoredox proxies for the Urquhart Shale Formation from this study are consistent with the current understanding of the Proterozoic ocean redox conditions. For example, the data presented here overlaps with sulphur isotope values in Proterozoic diagenetic pyrite (Eldridge et al. 1993; Canfield and Farquhar 2009; Fike et al. 2015; Magnall et al. 2020b), with REE+Y data of Proterozoic carbonate (Tang et al. 2016; Bellefroid et al. 2019), and concurs with growing evidence for widespread ferruginous conditions for the Paleoproterozoic oceans (Poulton et al. 2010; Poulton and Canfield 2011; Tang et al. 2017).

In summary, the new mineralogical data together with the new whole rock, *in situ* trace element, and *in situ* isotope geochemical data presented in chapters 2-4 are (1) compositionally similar to other fine-grained sedimentary rocks from the Carpentaria province, (2) indicate that the Urquhart Shale has not undergone regional greenschist metamorphism in this part of the Mount Isa area, and (3) are consistent with the current understanding of the global ocean redox conditions during the Proterozoic.

5.2. The mineralizing system(s) at George Fisher and in the Carpentaria province

5.2.1. The mineralizing system at George Fisher

There is relatively minor Cu mineralization at the George Fisher deposit, and based on structural, petrographic, and geochemical data, models for ore formation have mainly focussed on whether the majority of Zn-Pb mineralization occurred during diagenesis (Chapman 1999, 2004) or during orogenesis (Murphy 2004). The George Fisher deposit is highly deformed and structural observations have been interpreted to suggest a relatively early, or late, timing of mineralization; there is, however, general agreement that mineralization took place over a prolonged period of time and likely during multiple events (syn-diagenetic + multiple syn-deformation events, Chapman

1999, 2004; minor to no syn-diagenetic + multiple syn-deformation events, Murphy 2004).

The sulphide paragenesis and replacement textures of diagenetic carbonate by sphalerite observed in this study suggest that the first stage of mineralization at George Fisher post-dated the formation of both early diagenetic fine-grained pyrite (chapter 2) and diagenetic nodular calcite (chapter 3 and 4). It is, therefore, unlikely that mineralization occurred due to hydrothermal fluid exhalation during sedimentation (SEDEX; cf. Large et al. 1998). This interpretation is consistent with the lack of widely dispersed trace metals in the Urquhart Shale at George Fisher (chapter 3). In this study we did not produce any absolute timing constraints for the Zn-Pb mineralization. However, the sulphide paragenesis and *in situ* $\delta^{34}S$ values of paragenetically constrained pyrite ($\delta^{34}S_{pyrite}$ values) in chapter 2 indicate that multiple processes were involved in the accumulation of reduced sulphur for base metal sulphide precipitation. During stratabound mineralization in ore stage 1, reduced sulphur was likely derived via thermochemical sulphate reduction (TSR); and during later vein- and breccia-hosted mineralization in ore stage 2 reduced sulphur from pre-ore and ore stage 1 pyrite was recycled at different redox and/or temperature conditions, which is consistent with replacement textures of pyrite by sphalerite and galena and also with the occurrence of pyrrhotite in ore stage 2. The $\delta^{34}S_{pyrite}$ values in later ore stage 3 pyrite suggest that another stage of TSR was responsible for sulphate reduction at higher temperatures. Overall, these $\delta^{34}S_{pyrite}$ values, together with the sulphide paragenesis presented in chapter 2, strongly suggest a multi-stage mineralizing system at George Fisher.

Further constraints for the first phase of mineralization may be derived from Pb-model ages (ca. 1653 Ma; Chapman 1999), which are slightly younger than the depositional age of the Urquhart Shale Formation (1654 ±5 Ma; Page and Sweet 1998). Assuming sedimentation rates similar to modern marine sedimentary basins (ca. 1 cm/yr; median value of data compiled by Egger et al. 2018) and considering that mineralization post-dated early diagenetic pyrite and carbonate (see above), mineralization at George Fisher at 1653 Ma would have taken place within the upper 6 km of the sedimentary basin. Such burial depths would concur with temperatures

≤180°C of the Urquhart Shale at George Fisher (assuming a normal geothermal gradient). These temperatures are (1) consistent with reduced sulphur derived from TSR similar to natural gas reservoirs (chapter 2), are (2) within the maximum temperature constraints for the Urquhart Shale Formation (chapter 3), and are also (3) consistent with the earliest phase of mineralization either before, or after, the formation of diagenetic chlorite from precursor phases (chapter 3).

All mineralization at George Fisher post-dates the deposition of the Urquhart Shale Formation, and, therefore, all mineralization (syn-diagenetic and syn-orogenic) is epigenetic. It is generally accepted that porosity decreases strongly as a function of burial depth within sedimentary basins (Baldwin and Butler 1985), which is why during epigenetic mineralization (parts of) the host rock at George Fisher must have been replaced in order to produce secondary porosity (and permeability) for fluid flow and sulphide precipitation. The petrographic, whole rock mineralogical and geochemical, and *in situ* REE+Y carbonate data in chapters 3 and 4 suggest that dolomitization and replacement of pre-ore carbonate resulted from fluid-rock interaction of the Urquhart Shale Formation with hot (>200-250 °C), saline, potentially acidic hydrothermal fluids during mineralization. This fluid-rock interaction would have created sufficient secondary porosity, and would have also led to changing fluid chemistry and metal solubility (e.g., pH increase and fluid cooling; chapter 4). At such conditions and given the availability of sufficient reduced sulphur (from, e.g., TSR or sulphur recycling; chapter 2), base metal sulphides would have been able to precipitate. So, pre-ore diagenetic carbonate together with sufficient availability of reduced sulphur, or of reactants for sulphate reduction, were likely important components of the reactive host rock at George Fisher. Notably, reactive carbonate and a source of reduced sulphur in the Urquhart Shale Formation was likely available over a protracted period of time (early diagenesis to orogenesis), and, therefore, fluid-rock interaction coupled with carbonate replacement and TSR or recycling of reduced sulphur could have occurred at George Fisher at different times. In fact, carbonate replacement has been reported for a number of CD-type deposits throughout the Carpentaria province and irrespective of the timing proposed in respective studies (e.g., Eldridge et al. 1993; Perkins and Bell 1998; Chapman 2004; Magnall et al. 2020b).

5.2.2. Multi-stage vs. single-stage mineralization

It is relatively well accepted that mineralization at George Fisher formed over a prolonged time period by multiple events (this study; Chapman 1999, 2004; Murphy 2004), whereas there is considerable debate over whether the Zn-Pb- and the Cu-systems at the Mount Isa and Hilton deposits have formed from a single-stage or multi-stage system. In summary, for these deposits, proposed ore formation models range from (1) single-stage SEDEX ± syn-diagenetic Zn+Pb+Cu formation (e.g., Mathias and Clark 1975; McGoldrick and Keays 1990), over (2) single-stage syn-orogenic Zn+Pb+Cu formation (e.g., Perkins 1997; Davis 2004; Cave et al. 2020), to (3) multi-stage SEDEX or syn-diagenetic Zn+Pb and later syn-orogenic Cu±Zn±Pb (e.g., Heinrich et al. 1989; Valenta 1994; Waring et al. 1998b; Chapman 1999; Painter 2003). Considering this range of ore formation models, the possible timing of mineralization is constrained by (1) the deposition of the Urquhart Shale Formation (ca. 1654±5 Ma; zircon U-Pb-dating; Page and Sweet 1998), and by (2) the late-orogenic timing of Cu-mineralization (ca. 1523 Ma; Ar-Ar-dating of biotite alteration associated with Cu-mineralization; Perkins et al. 1999). Overall, this encloses a period of ca. 130 Myr during which mineralizing events can have occurred in the Mount Isa area.

In general, the formation of sediment-hosted base metal deposits requires a number of key components (e.g., Leach et al. 2005; Hitzman et al. 2010; Heinrich and Candela 2014): (1) metal source rocks (e.g., basement rocks or reactive basal sedimentary rocks); (2) saline Cl-rich fluids capable of base metal transport; (3) temperature gradients to produce fluid buoyancy; (4) fault-systems providing fluid conduits; (5) reactive host rocks to trap metals; and (6) a source of reduced sulphur. All these geological requirements are met in the Carpentaria province, and specifically in the Mount Isa area. Firstly, the basins are located at the edge of a thick, stable craton, which allowed for the development of prolonged temperature gradients in order to leach and transfer metals from deeper parts into shallower parts of the basins (Hoggard et al. 2020). Secondly, fluid conduits were provided by deep crustal-scale fault systems, such as the Mount Isa-Paroo Fault system (Murphy et al. 2011). Thirdly, fluids were likely saline (Heinrich et al. 1989; Cooke et al. 2000; Polito et al. 2006), and Cl-rich fluids were

likely available over a prolonged time period; for example, even throughout higher grade metamorphism in the Eastern Mount Isa Inlier (Morrissey and Tomkins 2020). Finally, reactive, calcareous, carbonaceous, and sulphur-bearing rock units, such as the Urquhart Shale Formation were available throughout the province (Hutton et al. 2012).

In summary, all the key components that are necessary to form base metal sulphide deposits existed in the Mount Isa area and Carpentaria province. Therefore, it is necessary to consider the processes that led to the fluid movement that formed the deposits. In sediment-hosted mineral systems, faults are the key fluid pathways to connect the metal source with the depositional site; this can occur either actively, during fault activity, or passively along inactive fault systems (Walsh et al. 2018). Within the geological time frame for mineralization in the Mount Isa area (ca. 1650-1520 Ma; deposition of Urquhart Shale to Cu-mineralization, see above), there were ca. 50 Myr of basin tectonics (extension, sag-phases, basin inversion; e.g., Southgate et al. 2013; Gibson et al. 2017), followed by ca. 80 Myr of compressional tectonics after the onset of the Isan orogeny at ca. 1600 Ma (e.g., Connors and Page 1995; Bell and Hickey 1998; Page et al. 2000). This means that there was a time span of 130 Myr to connect metal source and depositional site via tectonic processes (cf. Walsh et al. 2018). The longevity and earthquake frequency of the fault systems that were the main fluid conduits for Zn-Pb mineralization (e.g., Mount Isa-Paroo Fault system) are unknown. In modern analogues, the earthquake frequency is ca. 0.0001-0.00007 yr^{-1} in extensional settings (e.g., Basin and Range Province; Pérouse and Wernicke 2017), and ca. 0.003 yr^{-1} in both compressional settings (e.g., Himalayan frontal thrust; Kumar et al. 2001) and transformational plate boundary settings (e.g., Alpine Fault, New Zealand; Berryman et al. 2012). Assuming modern earthquake frequencies and using a conservative time span for the fault activity of 1 % (1.3 Myr) for the Mount Isa-Paroo Fault zone, the fault system could have been active >2500 times. There were, therefore, >2500 tectonic events that could have potentially provided both the fluid pathway and the fluid driver for mineralization in the Mount Isa area. Given (1) these theoretical constraints for fluid event frequency, (2) the availability of all other key components necessary for ore formation, and (3) the presence of three world-class, structurally and paragenetically complex base metal deposits within a distance of ca. 20 km (Fig. 5-1), it is entirely

possible that the ore deposits in the Mount Isa area did not form in a single giant Cu-Zn-Pb mineralizing event but multiple overprinting events. We would suggest that the preservation of these events differs from deposit to deposit e.g., George Fisher preserves more of the early diagenetic mineralization whereas at Mount Isa the later syn-deformation Cu-Pb-Zn system dominates. In fact, multiple major fluid flow events were very common in Proterozoic sedimentary basins (Kyser et al. 2000); and there is a growing body of evidence that many of the world's most metal endowed sedimentary basins have experienced multiple economic phases of mineralization (e.g., Athabasca basin, Alexandre et al. 2009; Zechstein basin, Alderton et al. 2016; Katangan basin, Selley et al. 2005; Muchez et al. 2015).

Finally, it has to be noted that these conclusions do not eliminate the possibility of a giant single-stage ore forming event. However, a single-stage ore formation model would need to explain, why only one event was able to transport and precipitate Cu, Zn, and Pb, when all other key components for ore formation (reactive host rock, sulphur source, fault system, saline fluids, geodynamic setting, source of metals) were available for a prolonged period of time.

5.3. The footprint of the mineralizing system at George Fisher and its implications for exploration

In this study, new mineralogical, geochemical, and isotopic data were produced using a variety of whole rock and *in situ* techniques. These data were combined with petrographic observation across from the hand specimen to the µm-scale. The resulting insights did not only provide new insights into the background composition of the Urquhart Shale Formation (chapter 5.1) and into the ore forming processes at the George Fisher deposit (chapter 5.2), the data also allowed for a refined understanding of the mineralogical and geochemical footprint of the George Fisher deposit. Fig. 5-1 highlights the most important geochemical and mineralogical differences between the unmineralized Urquhart Shale Formation (Shovel Flats drill core) and the George Fisher deposit presented in chapters 2, 3, and 4.

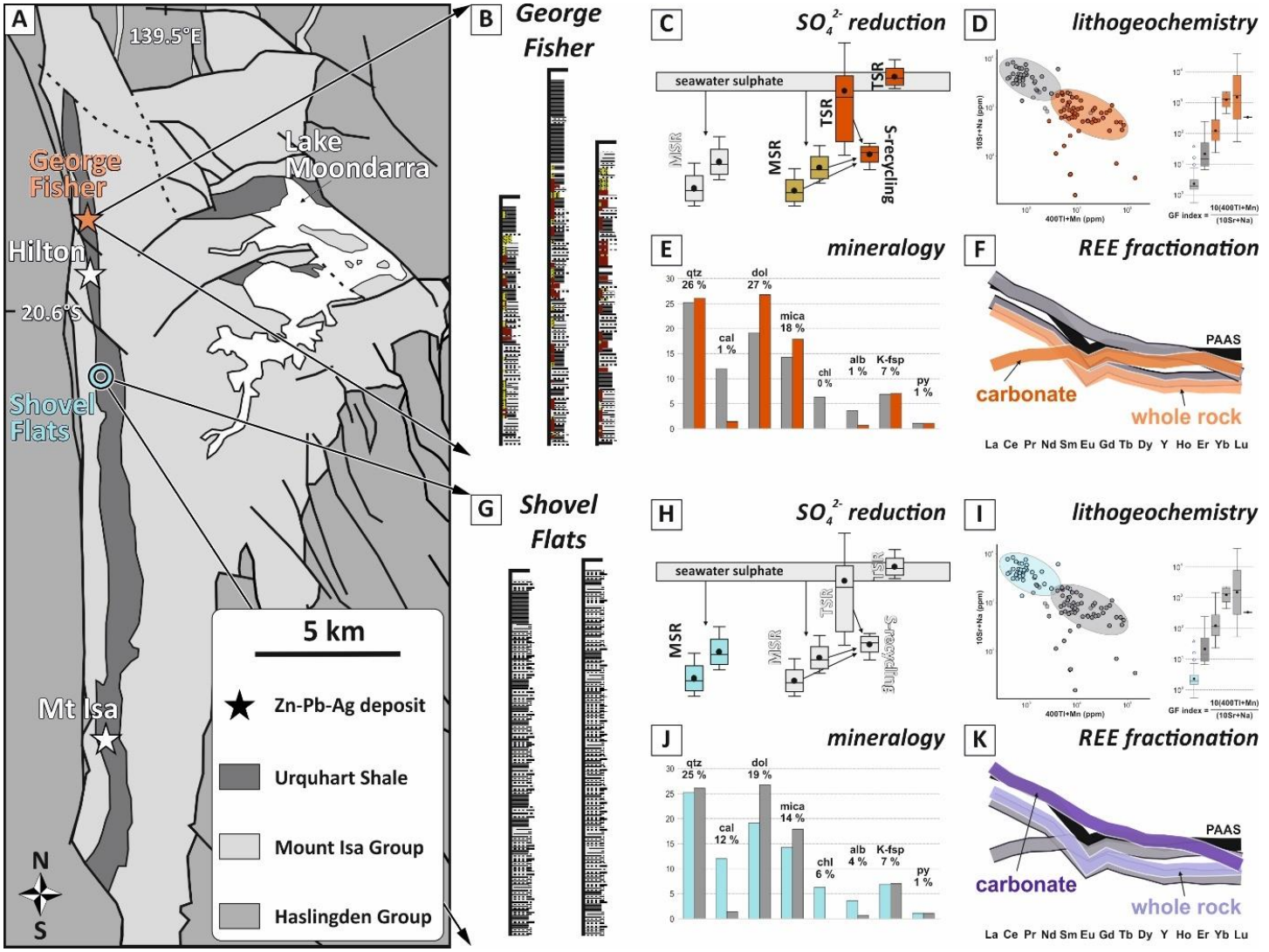

Fig. 5-1 (A) Geological map of the Mount Isa area; (B) lithological logs of drill cores from the George Fisher deposit; (C) schematic $\delta^{34}S$ values of paragenetically constrained pyrite, coloured boxes show data from George Fisher and respective accumulation processes for reduced sulphur; (D) whole rock lithogeochemical data of the most enriched and most depleted elements at George Fisher and George Fisher index values; (E) quantitative XRD data for the main mineral phases at George Fisher; (F) schematic REE+Y_{CN} profiles of whole rock and in situ carbonate data from George Fisher samples; (G) lithological log of the Shovel Flats drill core; (H) schematic $\delta^{34}S$ values of paragenetically constrained pyrite, coloured boxes show data from the Shovel Flats drill core and respective accumulation processes for reduced sulphur; (I) whole rock lithogeochemical data of the most enriched and most depleted elements at George Fisher and George Fisher index values from the Shovel Flats drill core; (J) quantitative XRD data for the main mineral phases from the Shovel Flats samples; (F) schematic REE+Y_{CN} profiles of whole rock and in situ carbonate data from Shovel Flats samples.

The presence of multiple generations of pyrite with distinct $\delta^{34}S$ values (chapter 2; Fig. 5-1C, H) is a reliable proxy that several processes were involved in the accumulation of reduced sulphur; and this may be characteristic for prospective lithologies. On the whole rock scale, mineralization at George Fisher has resulted in a number of geochemical and mineralogical changes compared to unmineralized Urquhart Shale (Fig. 5-1D, E, I, J). For example, there is significant enrichment of Tl and Mn, and depletion of Na and Sr, in whole rock data from George Fisher; and when combined, a ratio of these elements (George Fisher index = $10\left(\frac{400Tl+Mn}{10Sr+Na}\right)$) is highly effective in differentiating mineralized from unmineralized Urquhart Shale (chapter 3). These geochemical changes also correspond well with lower albite, calcite, and chlorite abundances and higher abundances of dolomite, muscovite and phlogopite, and hydrothermal pyrite at George Fisher (chapter 3). The geochemical footprint of the George Fisher deposit can be further defined by *in situ* REE+Y data of dolomite and calcite (chapter 4). Carbonate *in situ* $REE+Y_{CN}$ profiles from George Fisher are LREE depleted relative to whole rock and pre-ore carbonate $REE+Y_{CN}$ profiles (Fig. 5-1; chapter 4); and this LREE depletion in carbonate minerals may be an indicative feature of the interaction of saline (Cl-rich) hydrothermal fluids with carbonate-rich lithologies (chapter 4).

In summary, the findings from this study provide further geochemical and mineralogical constraints on the footprints of CD-type massive sulphide systems that can be tested in future exploration programmes in the Carpentaria Province.

5.4. Future work

This study has provided new petrographic, mineralogical, geochemical, and isotopic data that help to understand (1) the background composition of the Urquhart Shale Formation, (2) the mineralizing system at George Fisher, and (3) the footprint of this mineralizing system. Nevertheless, there are many opportunities for future research projects to gain further insights from the rocks of both the Urquhart Shale Formation and the George Fisher deposit.

Firstly, this study has shown that not all of the Urquhart Shale Formation has been affected by regional greenschist metamorphism, and that unmineralized Urquhart Shale preserves geochemical signatures that are characteristic of Proterozoic sedimentary basins (chapters 2, 3, 4, and 5.1). Future studies should, therefore, focus on investigating the unmineralized Urquhart Shale in greater detail in order to refine and add to the knowledge of the Proterozoic oceans and atmosphere. For example, such work could apply a variety of redox proxies (e.g., Mo, Cr, I, U concentrations, Fe speciation, Fe, I, Mo isotopes; e.g., Lyons et al. 2009; Hardisty et al. 2017) and could also investigate organic matter and biogeochemically reactive elements (e.g., N, P; e.g., Cox et al. 2019; Johnson et al. 2020).

Secondly, future investigations on the unmetamorphosed and unmineralized Urquhart Shale, and potentially other Mount Isa Group lithologies, should refine the diagenetic history and paragenesis. For example, such work could apply high-resolution petrographic techniques (e.g., backscatter electron or transmission electron microscopy) in combination with whole rock quantitative mineralogy in order to understand and quantify the diagenetic formation or dissolution of mineral phases such as feldspar, carbonate, quartz, berthierine, chlorite, illite, or pyrite. Such studies could help to understand the evolution of the reactive metal trap; and furthermore, better understanding of the diagenetic evolution could help to constrain the destruction and/or preservation of porosity and permeability that enhanced or reduced fluid flow during the mineralizing events in the area (cf. Storvoll et al. 2002; Golding et al. 2006; Stricker and Jones 2018).

Thirdly, this study has shown that *in situ* isotopic and geochemical data can help to understand a paragenetically complex mineral system (chapters 2 and 4). Future studies should apply *in situ* trace element analysis of base metal sulphides in order to further constrain fluid evolution and sulphide precipitation at George Fisher. For example, the analysis of trace elements in sphalerite can help to constrain fluid temperatures and fluid compositions (e.g., Frenzel et al. 2016, 2020). These data could then be combined with carbonate REE+Y data and with fluid inclusion studies of suitable, paragenetically constrained mineral phases, such as quartz, carbonate,

sphalerite, or pyrite (cf. Magnall et al. 2016a; Korges et al. 2019). Future *in situ* trace element studies of pyrite could also help to understand Tl enrichment at George Fisher (cf. Spinks et al. 2019), and such trace element data could then be combined with $\delta^{34}S_{pyrite}$ data (chapter 2) or with microstructural data (e.g., EBSD analysis; e.g., Yang et al. 2019) in order to constrain processes responsible for element distribution. There is also indication of hydrocarbon mobility at George Fisher (Chapman 1999) and future studies could investigate the involvement of hydrocarbons for metal solubility and precipitation (e.g., Sanz-Robinson and Williams-Jones 2019).

Fourthly, there are mineral phases that were previously described at George Fisher, which could not be identified in this study (e.g., hyalophane, celsian; Chapman 2004). Such Ba-feldspar minerals have been linked with pseudomorphs after sulphate minerals in unmineralized Urquhart Shale (Painter 2003), and barite has been reported from the Mount Isa and Hilton deposits (Perkins and Bell 1998). Future studies could, therefore, investigate the potential origin and relationship of these mineral phases. For example, barite can form during diagenetic processes and can be part of the reactive host rock in CD-type systems (e.g., Macmillan Pass; Magnall et al. 2016b, 2020a).

Fifthly, future studies should focus on collecting geochronological data on paragenetically constrained sulphide minerals, gangue minerals, and/or alteration minerals in order to constrain the timing of the mineralizing events at George Fisher (e.g., U-Pb in hydrothermal zircon, Ar-Ar in phyllosilicates, Re-Os in sulphide minerals; e.g., Schaltegger 2007; Cloutier et al. 2011; Muchez et al. 2015).

Finally, this study has provided new data and interpretations for the footprint of CD-type deposits in the Carpentaria province (chapters 3 and 4). Future studies should test these hypotheses in un-deformed CD-type systems, which can allow for better constraints on the 3D distribution of the alteration system around Carpentaria deposits.

6. References

Abbott AN, Löhr S, Trethewy M (2019) Are clay minerals the primary control on the oceanic rare earth element budget? Front Mar Sci 6:504

Alderton DHM, Selby D, Kucha H, Blundell DJ (2016) A multistage origin for Kupferschiefer mineralization. Ore Geol Rev 79:535–543

Alexandre P, Kyser K, Thomas D, et al (2009) Geochronology of unconformity-related uranium deposits in the Athabasca Basin, Saskatchewan, Canada and their integration in the evolution of the basin. Miner Depos 44:41

Alibo DS, Nozaki Y (1999) Rare earth elements in seawater: particle association, shale-normalization, and Ce oxidation. Geochim Cosmochim Acta 63:363–372

Andrew AS, Heinrich CA, Wilkins RWT, Patterson DJ (1989) Sulfur isotope systematics of copper ore formation at Mount Isa, Australia. Econ Geol 84:1614–1626

Aplin AC, Macquaker JHS (2011) Mudstone diversity: Origin and implications for source, seal, and reservoir properties in petroleum systems. Am Assoc Pet Geol Bull 95:2031–2059

Armstrong JT (1995) Citzaf-a package of correction programs for the quantitative Electron Microbeam X-Ray-Analysis of thick polished materials, thin-films, and particles. Microbeam Anal 4:177–200

Baele J, Decrée S, Rusk B (2019) Cathodoluminescence applied to ore geology and exploration. Ore Depos Orig Explor Exploit 131–161

Baldwin B, Butler CO (1985) Compaction curves. Am Assoc Pet Geol Bull 69:622–626

Barker SLL, Dipple GM, Hickey KA, et al (2013) Applying stable isotopes to mineral exploration: Teaching an old dog new tricks. Econ Geol 108:1–9

Baruch ET, Kennedy MJ, Löhr SC, Dewhurst DN (2015) Feldspar dissolution-enhanced porosity in Paleoproterozoic shale reservoir facies from the Barney Creek Formation (McArthur Basin, Australia). Am Assoc Pet Geol Bull 99:1745–1770

Bau M (1991) Rare-earth element mobility during hydrothermal and metamorphic fluid-rock interaction and the significance of the oxidation state of europium. Chem Geol 93:219–230

Bau M, Dulski P (1999) Comparing yttrium and rare earths in hydrothermal fluids from the Mid-Atlantic Ridge: implications for Y and REE behaviour during near-vent mixing and for the Y/Ho ratio of Proterozoic seawater. Chem Geol 155:77–90

Bau M, Dulski P (1996) Distribution of yttrium and rare-earth elements in the Penge and Kuruman iron-formations, Transvaal Supergroup, South Africa. Precambrian Res 79:37–55

Bau M, Möller P (1992) Rare earth element fractionation in metamorphogenic hydrothermal calcite, magnesite and siderite. Mineral Petrol 45:231–246

Bau M, Möller P, Dulski P (1997) Yttrium and lanthanides in eastern Mediterranean seawater

and their fractionation during redox-cycling. Mar Chem 56:123–131

Beaufort D, Rigault C, Billon S, et al (2015) Chlorite and chloritization processes through mixed-layer mineral series in low-temperature geological systems–a review. Clay Miner 50:497–523

Bell TH, Hickey KA (1998) Multiple deformations with successive subvertical and subhorizontal axial planes in the Mount Isa region; their impact on geometric development and significance for mineralization and exploration. Econ Geol 93:1369–1389

Bellefroid EJ, Planavsky NJ, Hood AVS, et al (2019) Shallow water redox conditions of the mid-Proterozoic Muskwa Assemblage, British Columbia, Canada. Am J Sci 319:122–157

Bennett EM (1965) Lead-zinc-silver and copper deposits of Mount Isa. Geol Aust Ore Depos Mc Andrew, J (Ed), Eighth Commonw Min Metall Congr Melb 2:233–246

Berryman K, Cooper A, Norris R, et al (2012) Late Holocene Rupture History of the Alpine Fault in South Westland, New ZealandLate Holocene Rupture History of the Alpine Fault in South Westland, New Zealand. Bull Seismol Soc Am 102:620–638

Betts PG, Armit RJ, Stewart J, et al (2016) Australia and nuna. Geol Soc London, Spec Publ 424:47–81

Betts PG, Giles D, Lister GS (2003) Tectonic environment of shale-hosted massive sulfide Pb-Zn-Ag deposits of Proterozoic northeastern Australia. Econ Geol 98:557–576

Betts PG, Giles D, Lister GS, Frick LR (2002) Evolution of the Australian lithosphere. Aust J Earth Sci 49:661–695

Bilal BA (1991) Thermodynamic study of Eu3+/Eu2+ redox reaction in aqueous solutions at elevated temperatures and pressures by means of cyclic voltammetry. Zeitschrift für Naturforsch A 46:1108–1116

Bjørlykke K (2014) Relationships between depositional environments, burial history and rock properties. Some principal aspects of diagenetic process in sedimentary basins. Sediment Geol 301:1–14

Blake DH (1987) Geology of the Mount Isa inlier and environs, Queensland and Northern Territory. Australian Bureau of Mineral Resources Bulletin, 225, p. 83

Blanchard R, Hall G (1937) Mount Isa [Queensland] ore deposition. Econ Geol 32:1042–1057

Bodnar RJ, Lecumberri-Sanchez P, Moncada D, Steele-MacInnis M (2014) 13.5—Fluid inclusions in hydrothermal ore deposits. Treatise Geochemistry, Second Ed edn Elsevier, Oxford 119–142

Borowski WS, Rodriguez NM, Paull CK, Ussler III W (2013) Are 34S-enriched authigenic sulfide minerals a proxy for elevated methane flux and gas hydrates in the geologic record? Mar Pet Geol 43:381–395

Brand U, Veizer J (1980) Chemical diagenesis of a multicomponent carbonate system; 1, Trace elements. J Sediment Res 50:1219–1236

Broadbent G (2002) A decade of new ideas: Geology and exploration history of the Century Zn-

Pb-Ag deposit, Northwestern Queensland, Australia. In Integrated methods for discovery: Global exploration in the twenty-first century. Econ Geol Spec Publ 9:119–140

Broadbent GC, Myers RE, Wright J V (1998) Geology and origin of shale-hosted Zn-Pb-Ag mineralization at the Century deposit, northwest Queensland, Australia. Econ Geol 93:1264–1294

Cai C, Worden RH, Bottrell SH, et al (2003) Thermochemical sulphate reduction and the generation of hydrogen sulphide and thiols (mercaptans) in Triassic carbonate reservoirs from the Sichuan Basin, China. Chem Geol 202:39–57

Canfield DE (1998) A new model for Proterozoic ocean chemistry. Nature 396:450–453

Canfield DE, Farquhar J (2009) Animal evolution, bioturbation, and the sulfate concentration of the oceans. Proc Natl Acad Sci 106:8123–8127

Cave B, Lilly R, Barovich K (2020) Textural and geochemical analysis of chalcopyrite, galena and sphalerite across the Mount Isa Cu to Pb-Zn transition: Implications for a zoned Cu-Pb-Zn system. Ore Geol Rev

Chapman LH (2004) Geology and mineralization styles of the George Fisher Zn-Pb-Ag deposit, Mount Isa, Australia. Econ Geol 99:233–255

Chapman LH (1999) Geology and genesis of the George Fisher Zn-Pb-Ag deposit Mount Isa, Australia. Unpubl. PhD Thesis, James Cook University, p. 315

Cline JS, Hofstra AH, Muntean JL, et al (2005) Carlin-type gold deposits in Nevada: Critical geologic characteristics and viable models. Econ Geol 100th Anniv Vol 451:484

Cloutier J, Kyser K, Olivo GR, Brisbin D (2011) Geochemical, isotopic, and geochronlologic constraints on the formation of the Eagle Point basement-hosted uranium deposit, Athabasca Basin, Saskatchewan, Canada and recent remobilization of primary uraninite in secondary structures. Miner Depos 46:35–56

Cloutier J, Piercey SJ, Layne G, et al (2015) Styles, textural evolution, and sulfur isotope systematics of Cu-rich sulfides from the Cambrian Whalesback volcanogenic massive sulfide deposit, central Newfoundland, Canada. Econ Geol 110:1215–1234

Connors KA, Page RW (1995) Relationships between magmatism, metamorphism and deformation in the western Mount Isa Inlier, Australia. Precambrian Res 71:131–153

Cook NJ, Hoefs J (1997) Sulphur isotope characteristics of metamorphosed Cu□(Zn) volcanogenic massive sulphide deposits in the Norwegian Caledonides. Chem Geol 135:307–324

Cooke DR, Bull SW, Large RR, McGoldrick PJ (2000) The importance of oxidized brines for the formation of Australian Proterozoic stratiform sediment-hosted Pb-Zn (Sedex) deposits. Econ Geol 95:1–18

Cox GM, Sansjofre P, Blades ML, et al (2019) Dynamic interaction between basin redox and the biogeochemical nitrogen cycle in an unconventional Proterozoic petroleum system. Sci Rep 9:1–11

Craddock PR, Bach W, Seewald JS, et al (2010) Rare earth element abundances in hydrothermal

fluids from the Manus Basin, Papua New Guinea: Indicators of sub-seafloor hydrothermal processes in back-arc basins. Geochim Cosmochim Acta 74:5494–5513

Craig JR, Vokes FM (1993) The metamorphism of pyrite and pyritic ores: an overview. Mineral Mag 57:3–18

Crowe DE, Vaughan RG (1996) Characterization and use of isotopically homogeneous standards for in situ laser microprobe analysis of 34S/32 S ratios. Am Mineral 81:187–193

Davis TP (2004) Mine-scale structural controls on the Mount Isa Zn-Pb-Ag and Cu orebodies. Econ Geol 99:543–559

Day-Stirrat RJ, Dutton SP, Milliken KL, et al (2010) Fabric anisotropy induced by primary depositional variations in the silt: clay ratio in two fine-grained slope fan complexes: Texas Gulf Coast and northern North Sea. Sediment Geol 226:42–53

De Baar HJW, Bacon MP, Brewer PG (1983) Rare-earth distributions with a positive Ce anomaly in the Western North Atlantic Ocean. Nature 301:324–327

Debruyne D, Balcaen L, Vanhaecke F, Muchez P (2013) Rare earth element and yttrium characteristics of carbonates within the sediment-hosted Luiswishi and Kamoto Cu-Co deposits, Katanga Copperbelt (Democratic Republic of Congo-DRC). Geol Belgica 16:76–83

Debruyne D, Hulsbosch N, Muchez P (2016) Unraveling rare earth element signatures in hydrothermal carbonate minerals using a source–sink system. Ore Geol Rev 72:232–252

Deng Y, Ren J, Guo Q, et al (2017) Rare earth element geochemistry characteristics of seawater and porewater from deep sea in western Pacific. Sci Rep 7:1–13

Derrick GM (1974) Stratigraphic and palaeogeographic evolution and revolution in the Mount Isa area. In: Regional Meeting Pap Austra] as Inst Min Metall NW Queensland Branch (Aug. 1974). pp 177–187

Derrick GM (1982) A PROTEROZOIC RIFT-ZONE AT MOUNT-ISA, QUEENSLAND, AND IMPLICATIONS FOR MINERALIZATION. BMR J Aust Geol Geophys 7:81–92

Doebelin N, Kleeberg R (2015) Profex: a graphical user interface for the Rietveld refinement program BGMN. J Appl Crystallogr 48:1573–1580

Domagala J, Southgate PN, McConachie BA, Pidgeon BA (2000) Evolution of the Palaeoproterozoic Prize, Gun and lower Loretta Supersequences of the Surprise Creek Formation and Mt Isa Group. Aust J Earth Sci 47:485–507

Douville E, Bienvenu P, Charlou JL, et al (1999) Yttrium and rare earth elements in fluids from various deep-sea hydrothermal systems. Geochim Cosmochim Acta 63:627–643

Egger M, Riedinger N, Mogollón JM, Jørgensen BB (2018) Global diffusive fluxes of methane in marine sediments. Nat Geosci 11:421–425

Eldridge CS, Compston W, Williams IS, et al (1988) Sulfur isotope variability in sediment-hosted massive sulfide deposits as determined using the ion microprobe SHRIMP; I, An example from the Rammelsberg orebody. Econ Geol 83:443–449

Eldridge CS, Williams N, Walshe JL (1993) Sulfur isotope variability in sediment-hosted massive sulfide deposits as determined using the ion microprobe SHRIMP; II, A study of the HYC Deposit at McArthur River, Northern Territory, Australia. Econ Geol 88:1–26

Elshkaki A, Graedel TE, Ciacci L, Reck BK (2018) Resource demand scenarios for the major metals. Environ Sci Technol 52:2491–2497

Fallick AE, Ashton JH, Boyce AJ, et al (2001) Bacteria were responsible for the magnitude of the world-class hydrothermal base metal sulfide orebody at Navan, Ireland. Econ Geol 96:885–890

Fike DA, Bradley AS, Rose C V (2015) Rethinking the ancient sulfur cycle. Annu Rev Earth Planet Sci 43:593–622

Finlow-Bates T, Croxford NJW, Allan JM (1977) Evidence for, and implications of, a primary FeS phase in the lead-zinc bearing sediments at Mount Isa. Miner Depos 12:143–149

Frenzel M, Cook NJ, Ciobanu CL, et al (2020) Halogens in hydrothermal sphalerite record origin of ore-forming fluids. Geology

Frenzel M, Hirsch T, Gutzmer J (2016) Gallium, germanium, indium, and other trace and minor elements in sphalerite as a function of deposit type—A meta-analysis. Ore Geol Rev 76:52–78

Gadd MG, Layton-Matthews D, Peter JM, et al (2017) The world-class Howard's Pass SEDEX Zn-Pb district, Selwyn Basin, Yukon. Part II: the roles of thermochemical and bacterial sulfate reduction in metal fixation. Miner Depos 52:405–419

Gadd MG, Layton-Matthews D, Peter JM, Paradis SJ (2016) The world-class Howard's Pass SEDEX Zn-Pb district, Selwyn Basin, Yukon. Part I: trace element compositions of pyrite record input of hydrothermal, diagenetic, and metamorphic fluids to mineralization. Miner Depos 51:319–342

Gellatly AM, Lyons TW (2005) Trace sulfate in mid-Proterozoic carbonates and the sulfur isotope record of biospheric evolution. Geochim Cosmochim Acta 69:3813–3829

Genna D, Gaboury D, Roy G (2014) Evolution of a volcanogenic hydrothermal system recorded by the behavior of LREE and Eu: Case study of the Key Tuffite at Bracemac–McLeod deposits, Matagami, Canada. Ore Geol Rev 63:160–177

German CR, Elderfield H (1989) Rare earth elements in Saanich Inlet, British Columbia, a seasonally anoxic basin. Geochim Cosmochim Acta 53:2561–2571

Gibson GM, Henson PA, Neumann NL, et al (2012) Paleoproterozoic-earliest Mesoproterozoic basin evolution in the Mount Isa region, northern Australia and implications for reconstructions of the Nuna and Rodinia supercontinents. Episodes 35:131–141

Gibson GM, Hutton LJ, Holzschuh J (2017) Basin inversion and supercontinent assembly as drivers of sediment-hosted Pb–Zn mineralization in the Mount Isa region, northern Australia. J Geol Soc London 174:773–786

Gibson GM, Meixner AJ, Withnall IW, et al (2016) Basin architecture and evolution in the Mount Isa mineral province, northern Australia: Constraints from deep seismic reflection profiling and implications for ore genesis. Ore Geol Rev 76:414–441

Giles D, Betts P, Lister G (2002) Far-field continental backarc setting for the 1.80–1.67 Ga basins of northeastern Australia. Geology 30:823–826

Glencore (2019) Resources and reserves report: December 31, 2019, p. 71, https://www.glencore.com/dam/jcr:0e7b6c0f-e670-49fe-9048-8582e7530dab/GLEN_2019_Resources_Reserves_Report--.pdf.

Glencore (2018) Resources and reserves report: December 31, 2018, p. 67, www.glencore.com/dam/jcr:ae4466b47ef44407ae006ca55b694028/GLEN_2018_Resources_Reserves_Report-.pdf.

Glikson M, Mastalerz M, Golding SD, McConachie BA (2000) Metallogenesis and hydrocarbon generation in northern Mount Isa Basin, Australia: implications for ore grade mineralization. In: Organic Matter and Mineralisation: Thermal Alteration, Hydrocarbon Generation and Role in Metallogenesis. Springer, pp 149–184

Goldhaber MB, Kaplan IR (1975) Controls and consequences of sulfate reduction rates in recent marine sediments. Soil Sci 119:42–55

Goldhaber MB, Orr WL (1995) Kinetic controls on thermochemical sulfate reduction as a source of sedimentary H2S. ACS Publications

Golding SD, Uysal IT, Glikson M, et al (2006) Timing and chemistry of fluid-flow events in the Lawn Hill platform, northern Australia. Econ Geol 101:1231–1250

Gomes ML, Hurtgen MT (2015) Sulfur isotope fractionation in modern euxinic systems: implications for paleoenvironmental reconstructions of paired sulfate–sulfide isotope records. Geochim Cosmochim Acta 157:39–55

Grant JA (1986) The isocon diagram; a simple solution to Gresens' equation for metasomatic alteration. Econ Geol 81:1976–1982

Grant JA (2005) Isocon analysis: A brief review of the method and applications. Phys Chem Earth, Parts A/B/C 30:997–1004

Grondjis HF, Schouten C (1937) A study of the Mount Isa ores. Econ Geol 32:407–450

Haley BA, Klinkhammer GP, McManus J (2004) Rare earth elements in pore waters of marine sediments. Geochim Cosmochim Acta 68:1265–1279

Hannan KW, Golding SD, Herbert HK, Krouse HR (1993) Contrasting alteration assemblages in metabasites from Mount Isa, Queensland; implications for copper ore genesis. Econ Geol 88:1135–1175

Hardisty DS, Lu Z, Bekker A, et al (2017) Perspectives on Proterozoic surface ocean redox from iodine contents in ancient and recent carbonate. Earth Planet Sci Lett 463:159–170

Hecht L, Freiberger R, Gilg HA, et al (1999) Rare earth element and isotope (C, O, Sr) characteristics of hydrothermal carbonates: genetic implications for dolomite-hosted talc mineralization at Göpfersgrün (Fichtelgebirge, Germany). Chem Geol 155:115–130

Heinrich CA, Andrew AS, Wilkins RWT, Patterson DJ (1989) A fluid inclusion and stable isotope study of synmetamorphic copper ore formation at Mount Isa, Australia. Econ Geol 84:529–550

Heinrich CA, Candela PA (2014) Fluids and ore formation in the Earth's crust. In: Treatise on Geochemistry (Second Edition). Elsevier, pp 1–28

Héroux Y, Chagnon A, Bertrand R (1979) Compilation and correlation of major thermal maturation indicators. Am Assoc Pet Geol Bull 63:2128–2144

Himmler T, Bach W, Bohrmann G, Peckmann J (2010) Rare earth elements in authigenic methane-seep carbonates as tracers for fluid composition during early diagenesis. Chem Geol 277:126–136

Hitzman M, Kirkham R, Broughton D, et al (2005) The sediment-hosted stratiform copper ore system. Econ Geol 100:609–642

Hitzman MW, Selley D, Bull S (2010) Formation of sedimentary rock-hosted stratiform copper deposits through Earth history. Econ Geol 105:627–639

Hoggard MJ, Czarnota K, Richards FD, et al (2020) Global distribution of sediment-hosted metals controlled by craton edge stability. Nat Geosci 13:504–510

Hornibrook ERC, Longstaffe FJ (1996) Berthierine from the lower cretaceous Clearwater formation, Alberta, Canada. Clays Clay Miner 44:1–21

Humphris SE, Alt JC, Teagle DAH, Honnorez JJ (1998) Geochemical changes during hydrothermal alteration of basement in the stockwork beneath the active TAG hydrothermal mound. In: PROCEEDINGS-OCEAN DRILLING PROGRAM SCIENTIFIC RESULTS. National Science Foundation, pp 255–276

Hutton LJ, Denaro TJ, Dhnaram C, Derrick GM (2012) Mineral Systems in the Mount Isa Inlier. Episodes 35:120–130

Ireland T, Large RR, McGoldrick P, Blake M (2004) Spatial distribution patterns of sulfur isotopes, nodular carbonate, and ore textures in the McArthur River (HYC) Zn-Pb-Ag deposit, Northern Territory, Australia. Econ Geol 99:1687–1709

Jackson MJ, Muir MD, Plumb KA (1987) Geology of the southern McArthur Basin, Northern Territory. Australian Government Publishing Service

Jackson MJ, Scott DL, Rawlings DJ (2000) Stratigraphic framework for the Leichhardt and Calvert Superbasins: review and correlations of the pre-1700 Ma successions between Mt Isa and McArthur River. Aust J Earth Sci 47:381–403

James RH, Elderfield H (1996) Chemistry of ore-forming fluids and mineral formation rates in an active hydrothermal sulfide deposit on the Mid-Atlantic Ridge. Geology 24:1147–1150

James RH, Elderfield H, Palmer MR (1995) The chemistry of hydrothermal fluids from the Broken Spur site, 29 N Mid-Atlantic Ridge. Geochim Cosmochim Acta 59:651–659

Johnson BR, Tostevin R, Gopon P, et al (2020) Phosphorus burial in ferruginous SiO2-rich Mesoproterozoic sediments. Geology 48:92–96

Johnson CA, Slack JF, Dumoulin JA, et al (2018) Sulfur isotopes of host strata for Howards Pass (Yukon–Northwest Territories) Zn-Pb deposits implicate anaerobic oxidation of methane, not basin stagnation. Geology 46:619–622

Jørgensen BB, Böttcher ME, Lüschen H, et al (2004) Anaerobic methane oxidation and a deep H2S sink generate isotopically heavy sulfides in Black Sea sediments. Geochim Cosmochim Acta 68:2095–2118

Kah LC (2000) Depositional δ18O signatures in Proterozoic dolostones: constraints on seawater chemistry and early diagenesis. SEPM Spec Publ 67:345–360

Kaplan IR, Emery KO, Rittenbebg SC (1963) The distribution and isotopic abundance of sulphur in recent marine sediments off southern California. Geochim Cosmochim Acta 27:297–331

Kaplan IR, Rittenberg SC (1964) Microbiological fractionation of sulphur isotopes. Microbiology 34:195–212

Kelley KD, Leach DL, Johnson CA, et al (2004) Textural, compositional, and sulfur isotope variations of sulfide minerals in the Red Dog Zn-Pb-Ag deposits, Brooks Range, Alaska: Implications for ore formation. Econ Geol 99:1509–1532

Kendrick MA, Duncan R, Phillips D (2006) Noble gas and halogen constraints on mineralizing fluids of metamorphic versus surficial origin: Mt Isa, Australia. Chem Geol 235:325–351

Kennedy M, Droser M, Mayer LM, et al (2006) Late Precambrian oxygenation; inception of the clay mineral factory. Science (80-) 311:1446–1449

King HE, Walters CC, Horn WC, et al (2014) Sulfur isotope analysis of bitumen and pyrite associated with thermal sulfate reduction in reservoir carbonates at the Big Piney–La Barge production complex. Geochim Cosmochim Acta 134:210–220

Kiyosu Y, Krouse HR (1990) The role of organic acid in the abiogenic reduction of sulfate and the sulfur isotope effect. Geochem J 24:21–27

Klinkhammer GP, Elderfield H, Edmond JM, Mitra A (1994) Geochemical implications of rare earth element patterns in hydrothermal fluids from mid-ocean ridges. Geochim Cosmochim Acta 58:5105–5113

Korges M, Weis P, Lüders V, Laurent O (2019) Sequential evolution of Sn–Zn–In mineralization at the skarn-hosted Hämmerlein deposit, Erzgebirge, Germany, from fluid inclusions in ore and gangue minerals. Miner Depos 1–16

Kretz R (1982) A model for the distribution of trace elements between calcite and dolomite. Geochim Cosmochim Acta 46:1979–1981

Kumar S, Wesnousky SG, Rockwell TK, et al (2001) Earthquake recurrence and rupture dynamics of Himalayan Frontal Thrust, India. Science (80-) 294:2328–2331

Kyser K, Hiatt E, Renac C, et al (2000) Diagenetic fluids in Paleo-and Meso-Proterozoic sedimentary basins and their implications for long protracted fluid histories. Mineral Assoc Canada Short Course 28:225–262

Lambert IB, Scott KM (1973) Implications of geochemical investigations of sedimentary rocks within and around the McArthur zinc-lead-silver deposit, Northern Territory. J Geochemical Explor 2:307–330

Lanson B, Besson G (1992) Characterization of the end of smectite-to-illite transformation:

Decomposition of X-ray patterns. Clays Clay Miner 40:40–52

Lanson B, Champion D (1991) The I/S-to-illite reaction in the late stage diagenesis. Am J Sci 291:473–506

Large RR, Bull SW, Cooke DR, McGoldrick PJ (1998) A genetic model for the HYC Deposit, Australia; based on regional sedimentology, geochemistry, and sulfide-sediment relationships. Econ Geol 93:1345–1368

Large RR, Bull SW, McGoldrick PJ (2000) Lithogeochemical halos and geochemical vectors to stratiform sediment hosted Zn–Pb–Ag deposits: part 2. HYC deposit, McArthur River, Northern Territory. J Geochemical Explor 68:105–126

Large RR, Bull SW, McGoldrick PJ, Walters SG (2005) Stratiform and strata-bound Zn-Pb-Ag deposits in Proterozoic sedimentary basins, northern Australia. Econ Geol 100:931–963

Large RR, McGoldrick PJ (1998) Lithogeochemical halos and geochemical vectors to stratiform sediment hosted Zn–Pb–Ag deposits, 1. Lady Loretta Deposit, Queensland. J Geochemical Explor 63:37–56

Lawrence MG, Greig A, Collerson KD, Kamber BS (2006) Rare earth element and yttrium variability in South East Queensland waterways. Aquat Geochemistry 12:39–72

Leach DL, Bradley DC, Huston D, et al (2010) Sediment-hosted lead-zinc deposits in Earth history. Econ Geol 105:593–625

Leach DL, Sangster DF, Kelley KD, et al (2005) Sediment-hosted lead-zinc deposits: A global perspective. Econ Geol 100:561–607

Li C, Planavsky NJ, Love GD, et al (2015) Marine redox conditions in the middle Proterozoic ocean and isotopic constraints on authigenic carbonate formation: insights from the Chuanlinggou Formation, Yanshan Basin, North China. Geochim Cosmochim Acta 150:90–105

Lin Z, Sun X, Peckmann J, et al (2016) How sulfate-driven anaerobic oxidation of methane affects the sulfur isotopic composition of pyrite: a SIMS study from the South China Sea. Chem Geol 440:26–41

Liu X-M, Hardisty DS, Lyons TW, Swart PK (2019) Evaluating the fidelity of the cerium paleoredox tracer during variable carbonate diagenesis on the Great Bahamas Bank. Geochim Cosmochim Acta 248:25–42

Lüders V, Moeller P, Dulski P (1993) REE fractionation in carbonates and fluorites. In: Formation of Hydrothermal Vein Deposits. A case study of the Pb-Zn-, barite and fluorite deposits of. Gebrüder Borntraeger, pp 133–150

Lynch FL, Mack LE, Land LS (1997) Burial diagenesis of illite/smectite in shales and the origins of authigenic quartz and secondary porosity in sandstones. Geochim Cosmochim Acta 61:1995–2006

Lyons TW (1997) Sulfur isotopic trends and pathways of iron sulfide formation in upper Holocene sediments of the anoxic Black Sea. Geochim Cosmochim Acta 61:3367–3382

Lyons TW, Anbar AD, Severmann S, et al (2009) Tracking euxinia in the ancient ocean: a

multiproxy perspective and Proterozoic case study. Annu Rev Earth Planet Sci 37:507–534

Lyons TW, Luepke JJ, Schreiber ME, Zieg GA (2000) Sulfur geochemical constraints on Mesoproterozoic restricted marine deposition: lower Belt Supergroup, northwestern United States. Geochim Cosmochim Acta 64:427–437

Lyons TW, Reinhard CT, Planavsky NJ (2014) The rise of oxygen in Earth's early ocean and atmosphere. Nature 506:307–315

Machel HG (2001) Bacterial and thermochemical sulfate reduction in diagenetic settings—old and new insights. Sediment Geol 140:143–175

Machel HG, Burton EA (1991) Factors governing cathodoluminescence in calcite and dolomite, and their implications for studies of carbonate diagenesis. SEPM Spec Publ 37–57

Machel HG, Krouse HR, Sassen R (1995) Products and distinguishing criteria of bacterial and thermochemical sulfate reduction. Appl geochemistry 10:373–389

Magnall JM, Gleeson SA, Blamey NJF, et al (2016a) The thermal and chemical evolution of hydrothermal vent fluids in shale hosted massive sulphide (SHMS) systems from the MacMillan Pass district (Yukon, Canada). Geochim Cosmochim Acta 193:251–273

Magnall JM, Gleeson SA, Creaser RA, et al (2020a) The Mineralogical Evolution of the Clastic Dominant-Type Zn-Pb±Ba Deposits at Macmillan Pass (Yukon, Canada)—Tracing Subseafloor Barite Replacement in the Layered Mineralization. Econ Geol 115:961–979

Magnall JM, Gleeson SA, Hayward N, Rocholl A (2020b) Massive sulfide Zn deposits in the Proterozoic did not require euxinia. Geochemical Perspect Lett 13:19–24

Magnall JM, Gleeson SA, Stern RA, et al (2016b) Open system sulphate reduction in a diagenetic environment–Isotopic analysis of barite (δ34S and δ18O) and pyrite (δ34S) from the Tom and Jason Late Devonian Zn–Pb–Ba deposits, Selwyn Basin, Canada. Geochim Cosmochim Acta 180:146–163

Marshall B, Gilligan LB (1987) An introduction to remobilization: information from ore-body geometry and experimental considerations. Ore Geol Rev 2:87–131

Marshall DJ (1988) Cathodoluminescence of geological materials. Unwin Hyman

Maskenskaya OM, Drake H, Mathurin FA, Åström ME (2015) The role of carbonate complexes and crystal habit on rare earth element uptake in low-temperature calcite in fractured crystalline rock. Chem Geol 391:100–110

Mathias B V, Clark GJ (1975) Mount Isa copper and silver-lead-zinc orebodies—Isa and Hilton mines. Econ Geol Aust Papua New Guinea Aust Inst Min Metall 1:351–372

McClay KR (1979) Folding in silver-lead-zinc orebodies, Mount Isa, Australia. Trans Inst Min Metall Sect B-APPLIED EARTH Sci 88:B5–B14

McClay KR, Carlile DG (1978) Mid-proterozoic sulphate evaporites at Mount Isa mine, Queensland, Australia. Nature 274:240–241

McDonough WF, Sun S-S (1995) The composition of the Earth. Chem Geol 120:223–253

McGoldrick P, Winefield P, Bull S, et al (2010) Sequences, synsedimentary structures, and sub-basins: the where and when of SEDEX zinc systems in the southern McArthur Basin, Australia. Soc Econ Geol Spec Publ 15:1–23

McGoldrick PJ, Keays RR (1990) Mount Isa copper and lead-zinc-silver ores; coincidence or cogenesis? Econ Geol 85:641–650

McLennan SM (1989) Rare earth elements in sedimentary rocks: influence of provenance and sedimentary processes. Geochemistry Mineral Rare Earth Elem Rev Mineral 21 169–200

Mering JA, Barker SLL, Huntington KW, et al (2018) Taking the temperature of hydrothermal ore deposits using clumped isotope thermometry. Econ Geol 113:1671–1678

Merriman RJ, Frey M (1999) Patterns of very low-grade metamorphism in metapelitic rocks. In: Low-Grade Metamorphism (Eds M. Frey and D. Robinson). 61–107

Michard A (1989) Rare earth element systematics in hydrothermal fluids. Geochim Cosmochim Acta 53:745–750

Michard A, Albarède F (1986) The REE content of some hydrothermal fluids. Chem Geol 55:51–60

Migdisov AA, Williams-Jones AE, Wagner T (2009) An experimental study of the solubility and speciation of the Rare Earth Elements (III) in fluoride-and chloride-bearing aqueous solutions at temperatures up to 300 C. Geochim Cosmochim Acta 73:7087–7109

Moore DM, Reynolds Jr RC (1997) X-ray Diffraction and the Identification and Analysis of Clay Minerals (2nd ed.): Oxford University Press. Oxford University Press, Oxford, England, p. 378

Morad S, Al-Ramadan K, Ketzer JM, De Ros LF (2010) The impact of diagenesis on the heterogeneity of sandstone reservoirs: A review of the role of depositional facies and sequence stratigraphy. Am Assoc Pet Geol Bull 94:1267–1309

Morgan JW, Wandless GA (1980) Rare earth element distribution in some hydrothermal minerals: evidence for crystallographic control. Geochim Cosmochim Acta 44:973–980

Morrissey LJ, Tomkins AG (2020) Evaporite-bearing orogenic belts produce ligand-rich and diverse metamorphic fluids. Geochim Cosmochim Acta 275:163–187

Muchez P, André-Mayer A-S, El Desouky HA, Reisberg L (2015) Diagenetic origin of the stratiform Cu–Co deposit at Kamoto in the Central African Copperbelt. Miner Depos 50:437–447

Mudd GM, Jowitt SM, Werner TT (2017) The world's lead-zinc mineral resources: Scarcity, data, issues and opportunities. Ore Geol Rev 80:1160–1190

Murphy FC, Hutton LJ, Walshe JL, et al (2011) Mineral system analysis of the Mt Isa–McArthur River region, Northern Australia. Aust J Earth Sci 58:849–873

Murphy TE (2004) Structural and stratigraphic controls on mineralization at the George Fisher Zn-Pb-Ag Deposit, northwest Queensland, Australia. Unpubl. PhD Thesis, James Cook University, p. 403

Nance WB, Taylor SR (1976) Rare earth element patterns and crustal evolution—I. Australian post-Archean sedimentary rocks. Geochim Cosmochim Acta 40:1539–1551

Nesbitt Hw, Young GM (1982) Early Proterozoic climates and plate motions inferred from major element chemistry of lutites. Nature 299:715–717

Neudert M (1983) A depositional model for the Upper Mount Isa Group and implications for ore formation. Unpubl. PhD Thesis, Australian National University, p. 538

Neudert MK, Russell RE (1981) Shallow water and hypersaline features from the middle Proterozoic Mt Isa Sequence. Nature 293:284–286

Neumann NL, Southgate PN, Gibson GM, McIntyre A (2006) New SHRIMP geochronology for the Western Fold Belt of the Mt Isa Inlier: developing a 1800–1650 Ma event framework. Aust J Earth Sci 53:1023–1039

Nozaki Y, Zhang J, Amakawa H (1997) The fractionation between Y and Ho in the marine environment. Earth Planet Sci Lett 148:329–340

Odin GS, Matter A (1981) De glauconiarum origine. Sedimentology 28:611–641

Page RW, Bell TH (1986) Isotopic and structural responses of granite to successive deformation and metamorphism. J Geol 94:365–379

Page RW, Jackson MJ, Krassay AA (2000) Constraining sequence stratigraphy in north Australian basins: SHRIMP U–Pb zircon geochronology between Mt Isa and McArthur River. Aust J Earth Sci 47:431–459

Page RW, Sweet IP (1998) Geochronology of basin phases in the western Mt Isa Inlier, and correlation with the McArthur Basin. Aust J Earth Sci 45:219–232

Painter MGM (2003) The geochemical and mineralogical haloes around the Mt Isa base metal orebodies. Unpubl. PhD Thesis, University of Queensland, p. 478

Painter MGM, Golding SD, Hannan KW, Neudert MK (1999) Sedimentologic, petrographic, and sulfur isotope constraints on fine-grained pyrite formation at Mount Isa Mine and environs, Northwest Queensland, Australia. Econ Geol 94:883–912

Parkhurst DL, Appelo CAJ (2013) Description of input and examples for PHREEQC version 3: a computer program for speciation, batch-reaction, one-dimensional transport, and inverse geochemical calculations. US Geological Survey

Paton C, Hellstrom J, Paul B, et al (2011) Iolite: Freeware for the visualisation and processing of mass spectrometric data. J Anal At Spectrom 26:2508–2518

Perkins C, Heinrich CA, Wyborn LAI (1999) 40 Ar/39 Ar geochronology of copper mineralization and regional alteration, Mount Isa, Australia. Econ Geol 94:23–36

Perkins WG (1997) Mount Isa lead-zinc orebodies: Replacement lodes in a zoned syndeformational copper-lead-zinc system? Ore Geol Rev 12:61–110

Perkins WG (1984) Mount Isa silica dolomite and copper orebodies; the result of a syntectonic hydrothermal alteration system. Econ Geol 79:601–637

Perkins WG (1998) Timing of formation of Proterozoic stratiform fine-grained pyrite; post-diagenetic cleavage replacement at Mount Isa? Econ Geol 93:1153–1164

Perkins WG, Bell TH (1998) Stratiform replacement lead-zinc deposits; a comparison between Mount Isa, Hilton, and McArthur River. Econ Geol 93:1190–1212

Pérouse E, Wernicke BP (2017) Spatiotemporal evolution of fault slip rates in deforming continents: The case of the Great Basin region, northern Basin and Range province. Geosphere 13:112–135

Perry EP, Gysi AP (2018) Rare earth elements in mineral deposits: speciation in hydrothermal fluids and partitioning in calcite. Geofluids 2018:1–19

Pierson BJ (1981) The control of cathodoluminescence in dolomite by iron and manganese. Sedimentology 28:601–610

Planavsky N, Bekker A, Rouxel OJ, et al (2010) Rare earth element and yttrium compositions of Archean and Paleoproterozoic Fe formations revisited: new perspectives on the significance and mechanisms of deposition. Geochim Cosmochim Acta 74:6387–6405

Planavsky NJ, McGoldrick P, Scott CT, et al (2011) Widespread iron-rich conditions in the mid-Proterozoic ocean. Nature 477:448–451

Polito PA, Kyser TK, Golding SD, Southgate PN (2006) Zinc deposits and related mineralization of the Burketown mineral field, including the world-class Century deposit, northern Australia: Fluid inclusion and stable isotope evidence for basin fluid sources. Econ Geol 101:1251–1273

Poulton SW, Canfield DE (2011) Ferruginous conditions: a dominant feature of the ocean through Earth's history. Elements 7:107–112

Poulton SW, Fralick PW, Canfield DE (2010) Spatial variability in oceanic redox structure 1.8 billion years ago. Nat Geosci 3:486–490

Present TM, Paris G, Burke A, et al (2015) Large carbonate associated sulfate isotopic variability between brachiopods, micrite, and other sedimentary components in Late Ordovician strata. Earth Planet Sci Lett 432:187–198

Rafiei M, Kennedy M (2019) Weathering in a world without terrestrial life recorded in the Mesoproterozoic Velkerri Formation. Nat Commun 10:1–9

Raiswell R, Berner RA (1985) Pyrite formation in euxinic and semi-euxinic sediments. Am J Sci 285:710–724

Revie D, Normington VJ (2020) Shale resource data from the greater McArthur Basin. Northern Territory, Geological Survey, Digital Information Package DIP 014. Version January 2020

Riciputi LR, Cole DR, Machel HG (1996) Sulfide formation in reservoir carbonates of the Devonian Nisku Formation, Alberta, Canada: An ion microprobe study. Geochim Cosmochim Acta 60:325–336

Rieger P, Magnall JM, Gleeson SA, et al (2020) Sulfur Isotope Constraints on the Conditions of Pyrite Formation in the Paleoproterozoic Urquhart Shale Formation and George Fisher Zn-Pb-Ag Deposit, Northern Australia. Econ Geol 115:1003–1020

Rimstidt JD, Chermak JA, Schreiber ME (2017) Processes that control mineral and element abundances in shales. Earth-Science Rev 171:383–399

Roberts S, Palmer MR, Cooper MJ, et al (2009) REE and Sr isotope characteristics of carbonate within the Cu–Co mineralized sedimentary sequence of the Nchanga Mine, Zambian Copperbelt. Miner Depos 44:881

Rubenach MJ (1992) Proterozoic low-pressure/high-temperature metamorphism and an anticlockwise P–T–t path for the Hazeldene area, Mount Isa Inlier, Queensland, Australia. J Metamorph Geol 10:333–346

Rudnick RL, Gao S (2003) Composition of the continental crust. The crust 3:1–64

Rudnicki MD, Elderfield H, Spiro B (2001) Fractionation of sulfur isotopes during bacterial sulfate reduction in deep ocean sediments at elevated temperatures. Geochim Cosmochim Acta 65:777–789

Sanz-Robinson J, Williams-Jones AE (2019) Zinc solubility, speciation and deposition: A role for liquid hydrocarbons as ore fluids for Mississippi Valley Type Zn-Pb deposits. Chem Geol 520:60–68

Schaltegger U (2007) Hydrothermal zircon. Elements 3:51–79

Schieber J (1990) Pyritic shales and microbial mats: Significant factors in the genesis of stratiform Pb-Zn deposits of the Proterozoic? Miner Depos 25:7–14

Schieber J (1989) Pyrite mineralization in microbial mats from the mid-Proterozoic Newland Formation, Belt Supergroup, Montana, USA. Sediment Geol 64:79–90

Schijf J, De Baar HJW, Millero FJ (1995) Vertical distributions and speciation of dissolved rare earth elements in the anoxic brines of Bannock Basin, eastern Mediterranean Sea. Geochim Cosmochim Acta 59:3285–3300

Schodde R (2017) Challenges of Exploring Under Deep Cover. In: AMIRA International's 11th Biennial Exploration Managers Conference 28th–31st March

Scott C, Lyons TW (2012) Contrasting molybdenum cycling and isotopic properties in euxinic versus non-euxinic sediments and sedimentary rocks: Refining the paleoproxies. Chem Geol 324:19–27

Selley D, Broughton D, Scott RJ, et al (2005) A new look at the geology of the Zambian Copperbelt. Soc Econ Geol Inc 100:965–1000

Sholkovitz ER, Landing WM, Lewis BL (1994) Ocean particle chemistry: the fractionation of rare earth elements between suspended particles and seawater. Geochim Cosmochim Acta 58:1567–1579

Slack JF, Kelley KD, Anderson VM, et al (2004) Multistage hydrothermal silicification and Fe-Tl-As-Sb-Ge-REE enrichment in the Red Dog Zn-Pb-Ag district, northern Alaska: geochemistry, origin, and exploration applications. Econ Geol 99:1481–1508

Smith WD (1969) Penecontemporaneous faulting and its likely significance in relation to Mount Isa ore deposition. Spec Publ Geol Soc Aust 2:225–235

Smrzka D, Zwicker J, Bach W, et al (2019) The behavior of trace elements in seawater, sedimentary pore water, and their incorporation into carbonate minerals: a review. Facies 65:41

Solomon PJ (1965) Investigations into sulfide mineralization at Mount Isa, Queensland. Econ Geol 60:737–765

Song H, Jiang G, Poulton SW, et al (2017) The onset of widespread marine red beds and the evolution of ferruginous oceans. Nat Commun 8:1–7

Southgate PN, Neumann NL, Gibson GM (2013) Depositional systems in the Mt Isa Inlier from 1800 Ma to 1640 Ma: Implications for Zn–Pb–Ag mineralisation. Aust J Earth Sci 60:157–173

Southgate PN, Scott DL, Sami TT, et al (2000) Basin shape and sediment architecture in the Gun Supersequence: a strike-slip model for Pb–Zn–Ag ore genesis at Mt Isa. Aust J Earth Sci 47:509–531

Soyol-Erdene T-O, Huh Y (2013) Rare earth element cycling in the pore waters of the Bering Sea Slope (IODP Exp. 323). Chem Geol 358:75–89

Spinks SC, Peare M, Ryan C, et al (2019) Carbonate replacement and thallium enrichment: ultra-high-resolution trace element mapping, and the origin of Proterozoic sediment-hosted Zn-Pb deposits. Proc 15th SGA Bienn Meet Vol 2 Life with Ore Depos Earth, 15th Bienn Meet Soc Geol Appl to Miner Depos (Glasgow, Scotl 2019)

Storvoll V, Bjørlykke K, Karlsen D, Saigal G (2002) Porosity preservation in reservoir sandstones due to grain-coating illite: a study of the Jurassic Garn Formation from the Kristin and Lavrans fields, offshore Mid-Norway. Mar Pet Geol 19:767–781

Strauss H (1993) The sulfur isotopic record of Precambrian sulfates: new data and a critical evaluation of the existing record. Precambrian Res 63:225–246

Strauss H, Schieber J (1990) A sulfur isotope study of pyrite genesis: the Mid-Proterozoic Newland Formation, Belt Supergroup, Montana. Geochim Cosmochim Acta 54:197–204

Stricker S, Jones SJ (2018) Enhanced porosity preservation by pore fluid overpressure and chlorite grain coatings in the Triassic Skagerrak, Central Graben, North Sea, UK. Geol Soc London, Spec Publ 435:321–341

Sverjensky DA (1984) Europium redox equilibria in aqueous solution. Earth Planet Sci Lett 67:70–78

Sweeney RE, Kaplan IR (1973) Pyrite framboid formation; laboratory synthesis and marine sediments. Econ Geol 68:618–634

Tanaka K, Kawabe I (2006) REE abundances in ancient seawater inferred from marine limestone and experimental REE partition coefficients between calcite and aqueous solution. Geochem J 40:425–435

Tang D, Shi X, Jiang G, et al (2017) Ferruginous seawater facilitates the transformation of glauconite to chamosite: An example from the Mesoproterozoic Xiamaling Formation of North China. Am Mineral 102:2317–2332

Tang D, Shi X, Wang X, Jiang G (2016) Extremely low oxygen concentration in mid-Proterozoic

shallow seawaters. Precambrian Res 276:145–157

Taylor SR, McLennan SM (1995) The geochemical evolution of the continental crust. Rev Geophys 33:241–265

Toland WG (1960) Oxidation of organic compounds with aqueous sulfate. J Am Chem Soc 82:1911–1916

Toulmin III P, Barton Jr PB (1964) A thermodynamic study of pyrite and pyrrhotite. Geochim Cosmochim Acta 28:641–671

Valenta R (1994) Deformation of host rocks and stratiform mineralization in the Hilton Mine area, Mt Isa. Aust J Earth Sci 41:429–443

Valenta RK (1988) Deformation, fluid flow and mineralization in the Hilton area, Mt Isa, Australia. Unpub. PhD Thesis, Monash University, p. 284

van den Heuvel BH (1969) Sedimentation, stratigraphy and post-depositional changes in the sediments of the upper formations of the Mount Isa group, North-West Queensland. Unpubl. PhD Thesis, University of Queensland, p. 195

Vaughan JR, Hickey KA, Barker SLL (2016) Isotopic, chemical, and textural evidence for pervasive calcite dissolution and precipitation accompanying hydrothermal fluid flow in low-temperature, carbonate-hosted, gold systems. Econ Geol 111:1127–1157

Vine JD, Tourtelot EB (1970) Geochemistry of black shale deposits; a summary report. Econ Geol 65:253–272

Virolle M, Brigaud B, Bourillot R, et al (2019) Detrital clay grain coats in estuarine clastic deposits: origin and spatial distribution within a modern sedimentary system, the Gironde Estuary (south-west France). Sedimentology 66:859–894

Voigt M, Mavromatis V, Oelkers EH (2017) The experimental determination of REE partition coefficients in the water-calcite system. Chem Geol 462:30–43

Wagner T, Boyce AJ (2006) Pyrite metamorphism in the Devonian Hunsrück Slate of Germany: Insights from laser microprobe sulfur isotope analysis and thermodynamic modeling. Am J Sci 306:525–552

Walsh JJ, Torremans K, Güven J, et al (2018) Fault-controlled fluid flow within extensional basins and its implications for sedimentary rock-hosted mineral deposits: Society of Economic Geologists Special Publications, v. 21. Spec Publ 21:237–269

Waring CL (1990) Genesis of the Mount Isa copper ore system. Unpub. PhD Thesis, Monash University, p. 295

Waring CL, Andrew AS, Ewers GR (1998a) Use of O, C, and S stable isotopes in regional mineral exploration. AGSO J Aust Geol Geophys 17:301–313

Waring CL, Heinrich CA, Wall VJ (1998b) Proterozoic metamorphic copper deposits. AGSO J Aust Geol Geophys 17:239–246

Webb GE, Nothdurft LD, Kamber BS, et al (2009) Rare earth element geochemistry of scleractinian coral skeleton during meteoric diagenesis: a sequence through

neomorphism of aragonite to calcite. Sedimentology 56:1433–1463

Whitbread MAI (2004) Lithogeochemical Alteration Around the Century and Elura Zn-Pb-Ag Deposits: Detecting Alteration Expressions in the Deep and Near Surface Environments. Unpub. PhD Thesis, University of Canberra, p. 410

Wilkinson JJ, Crowther HL, Coles BJ (2011) Chemical mass transfer during hydrothermal alteration of carbonates: Controls of seafloor subsidence, sedimentation and Zn–Pb mineralization in the Irish Carboniferous. Chem Geol 289:55–75

Williams-Jones AE, Migdisov AA, Samson IM (2012) Hydrothermal mobilisation of the rare earth elements–a tale of "ceria" and "yttria." Elements 8:355–360

Williams N, Rye DM (1974) Alternative interpretation of sulphur isotope ratios in the McArthur lead-zinc-silver deposit. Nature 247:535–537

Williams PJ (1998) An introduction to the metallogeny of the McArthur River-Mount Isa-Cloncurry minerals province. Econ Geol 93:1120–1131

Wilson CJL (1972) The stratigraphic and metamorphic sequence west of Mount Isa, and associated igneous intrusions. Proc Aust Inst Min Metall 243:27–44

Wittkop C, Swanner ED, Grengs A, et al (2020) Evaluating a primary carbonate pathway for manganese enrichments in reducing environments. Earth Planet Sci Lett 538:116201

Woodhead JD, Hellstrom J, Hergt JM, et al (2007) Isotopic and elemental imaging of geological materials by laser ablation inductively coupled plasma-mass spectrometry. Geostand Geoanalytical Res 31:331–343

Wyborn LAI, Page RW, McCulloch MT (1988) Petrology, geochronology and isotope geochemistry of the post-1820 Ma granites of the Mount Isa Inlier: mechanisms for the generation of Proterozoic anorogenic granites. Precambrian Res 40:509–541

Yang M, Li J, Zhao X, et al (2019) Electron back-scattered diffraction and LA-ICP-MS analysis of pyrite from the Dahu lodegold deposit, southern North China craton: Insights into geochemistry and distribution of trace element connection to microstructure of pyrite. Ore Geol Rev 115:103164

Zhang J, Amakawa H, Nozaki Y (1994) The comparative behaviors of yttrium and lanthanides in the seawater of the North Pacific. Geophys Res Lett 21:2677–2680

Zhang X, Yang S, Zhao H, et al (2019) Effect of Beam Current and Diameter on Electron Probe Microanalysis of Carbonate Minerals. J Earth Sci 30:834–842

Zhu G, Zhang S, Liang Y, et al (2005) Isotopic evidence of TSR origin for natural gas bearing high H 2 S contents within the Feixianguan Formation of the northeastern Sichuan Basin, southwestern China. Sci China Ser D Earth Sci 48:1960

7. Appendix

The electronic appendix comprises: (a) the *in situ* sulphur isotope data from pyrite presented in chapter 2; (b) the whole rock mineralogical and lithogeochemical data presented in chapter 3; and (c) the *in situ* trace element data from carbonate minerals presented in chapter 4.

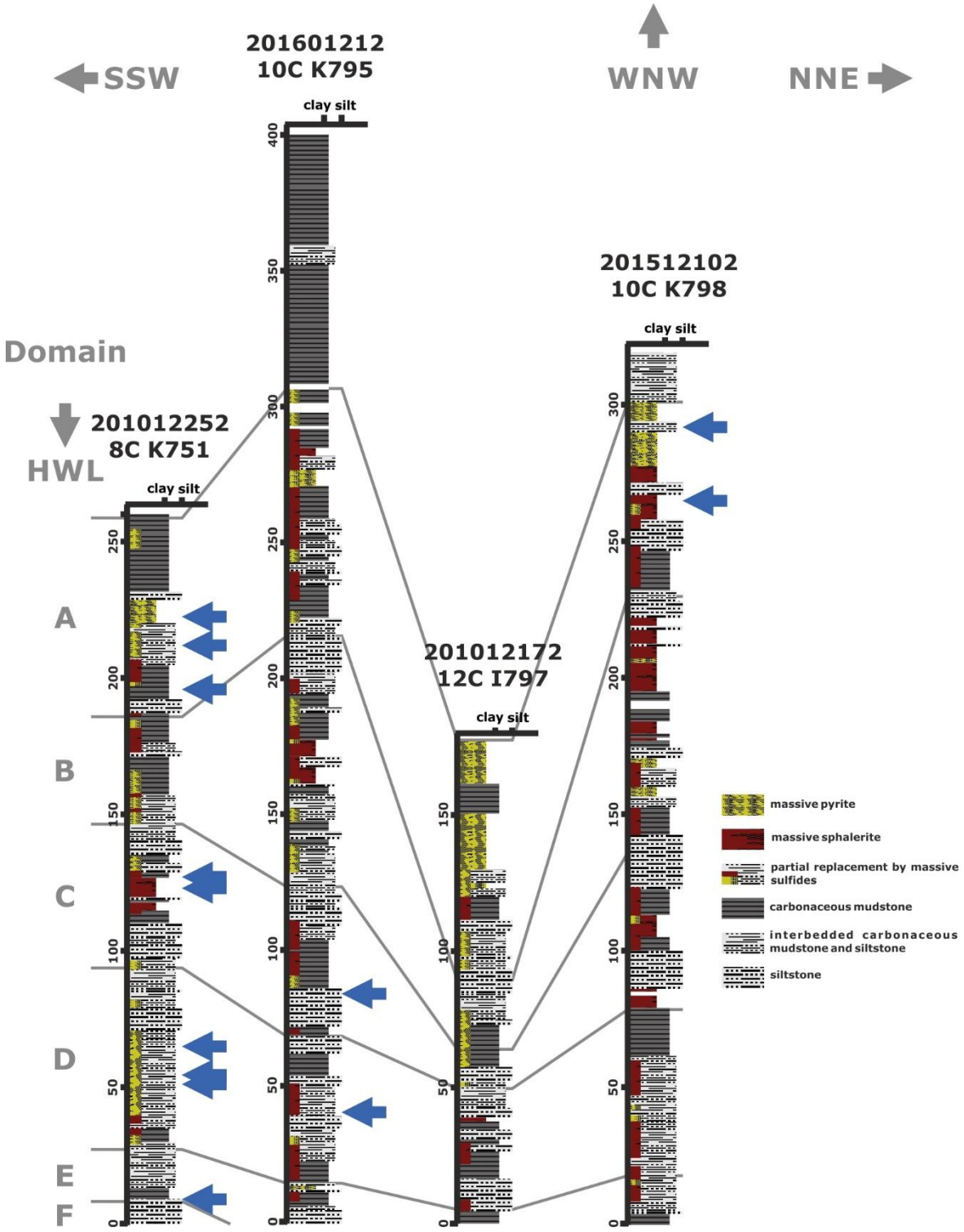

Fig. 7-1 Lithological logs of four drill cores from the George Fisher deposit; the blue arrows annotate samples that were used for isotopic analysis in this study; grey characters indicate in-mine ore body domains (A to F; HWL = hanging wall).

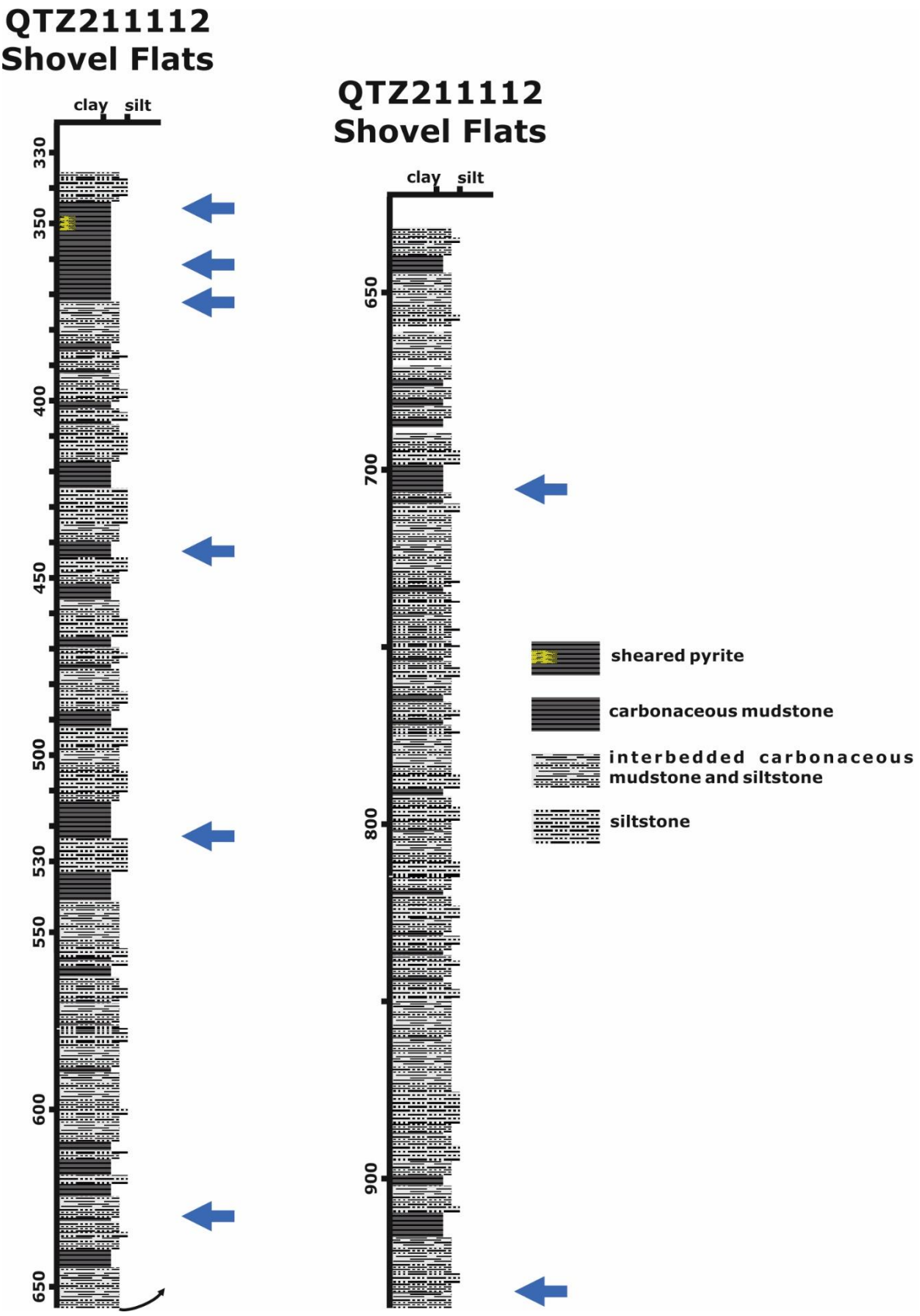

Fig. 7-2 Lithological log of the Shovel Flats drill core; the blue arrows annotate samples that were used for isotopic analysis in this study.

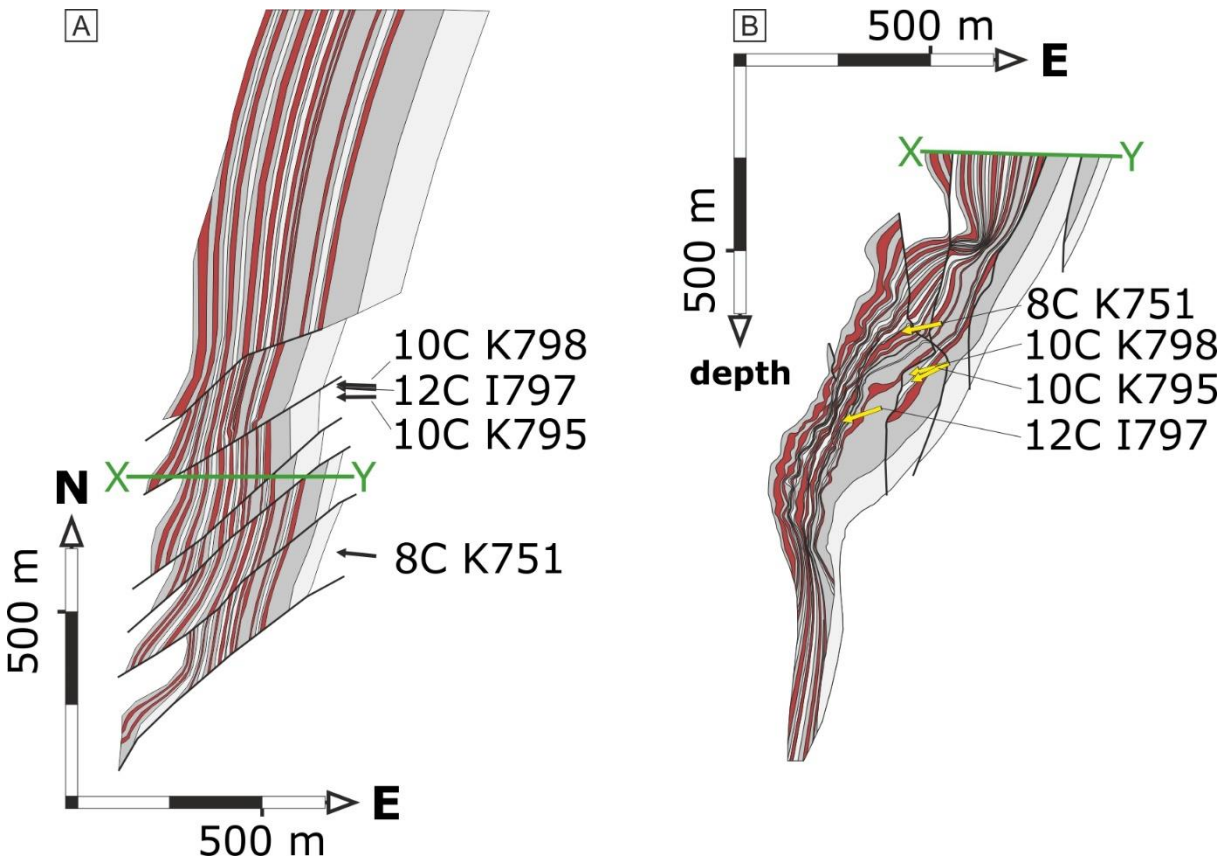

Fig. 7-3 The mine geology of the George Fisher deposit. The red, dark grey and light grey units represent the respective ore domains, mudstone units and siltstone units. Black and yellow arrows indicate locations and dips of drill cores 8C K751, 10C K795, 10C K798 and 12C I797. (A) Top view of the deposit. The green line indicates the location of the cross section shown in B. (B) Cross section X-Y of George Fisher deposit.

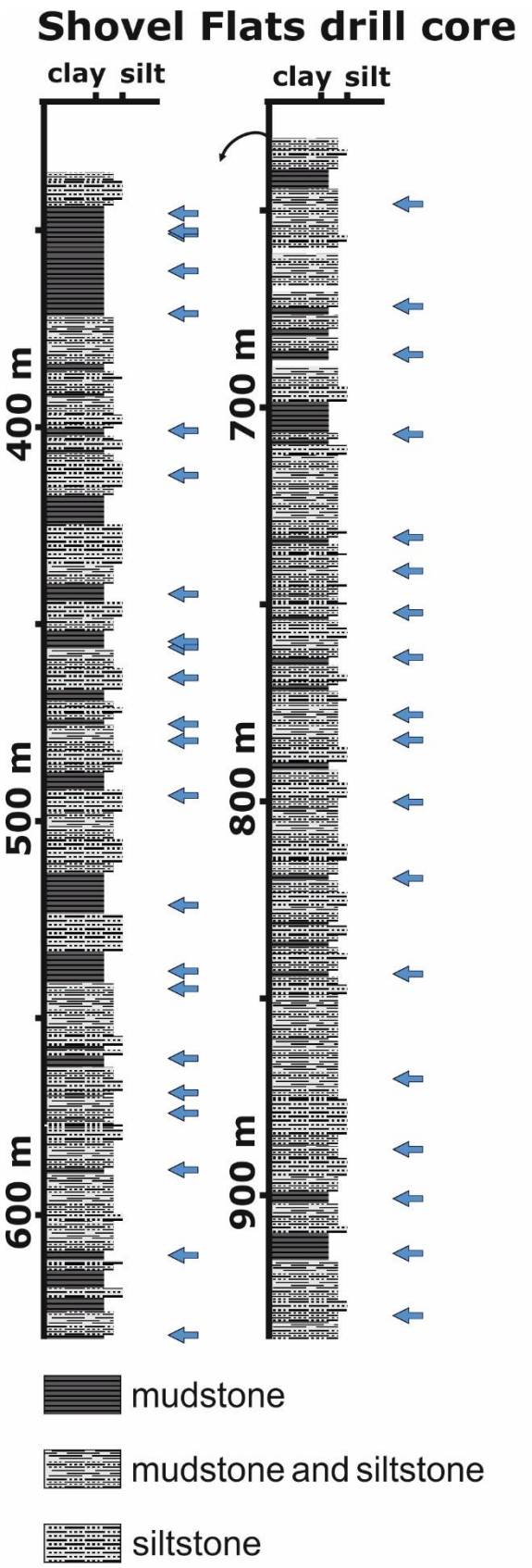

Fig. 7-4 A lithological log of the Shovel Flats drill core (see Fig. 3-2 for location) and individual samples analysed in this study (blue arrows).

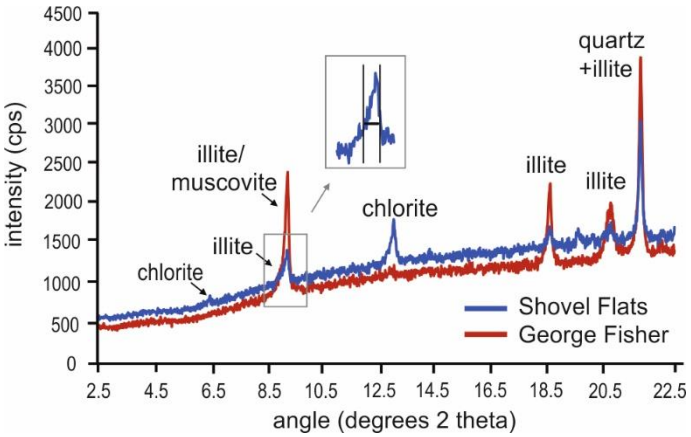

Fig. 7-5 X-ray diffraction patterns of two representative clay-fraction separates from both the Shovel Flats drill core and the George Fisher deposit; notice the asymmetric 001 reflection of illite in the inset.